

Electrocatalysis and its application towards overall ammonia synthesis and Zn-air batteries

A Thesis Submitted

In the fulfillment for the degree of

Doctor of Philosophy

by

Divyani Gupta

2018CYZ0010



**Department of Chemistry
Indian Institute of Technology Ropar
India**

May 2023

Declaration

*I hereby declare that this thesis entitled "**Electrocatalysis and its application towards overall ammonia synthesis and Zn-air batteries**" is the outcome of original research work performed by me under the able guidance of Dr. Tharamani C. N., Associate Professor at the Department of Chemistry, Indian Institute of Technology Ropar. I solemnly declare that the contents of this thesis both in part or complete has not been submitted elsewhere for the award of any degree or diploma.*

Divyani Gupta
24/7/23
Divyani Gupta

(2018CYZ0010)

**Department of Chemistry
Indian Institute of Technology Ropar**

Certificate

This is to certify that the thesis entitled "Electrocatalysis and its application towards overall ammonia synthesis and Zn-air batteries" submitted by Ms. Divyani Gupta for the award of the degree of "Doctor of Philosophy" in Chemistry is based on the results of studies carried out by her under my guidance and supervision.

The thesis or any part thereof has not been previously submitted for the award of any other degree or diploma.



Dr. Tharamani C.N.

Associate Professor
Department of Chemistry
Indian Institute of Technology Ropar
Rupnagar-140001
Punjab, INDIA

Coursework Certificate

This is to certify that Ms. Divyani Gupta has undertaken the following coursework for the fulfillment of the degree of Doctor of Philosophy;

CY423	Solid State Chemistry
CY511	Instrumentation Analysis
CY613	Chemistry of Metal-Carbon bond
CY701	Molecular Spectroscopy
CY622	Applied Electrochemistry



Dr. Tharamani C.N.

**Associate Professor
Department of Chemistry
Indian Institute of Technology Ropar
Rupnagar-140001
Punjab, INDIA**



Dedicated to my beloved family

This thesis is dedicated to my mother and sister, Veenu Gupta and Divyanshi Gupta for supporting me and motivating me to achieve the goals that I had targeted for. I am forever thankful to both of them for standing beside me as strong pillars and letting me achieve my goals by sacrificing their own. This thesis and resulting doctoral degree is a symbol of what we have accomplished as a family. This one is for us!

Acknowledgments

First and foremost, I wish to express my heartfelt thanks to my beloved family who motivated me and gave me the strength and encouragement throughout this journey to complete my research work.

My words fail to express my deep gratitude to my research supervisor, Dr. Tharamani C. N., Associate Professor, IIT Ropar, for providing me with a life-changing opportunity to explore the scientific world in such a prestigious institute. Thank you Ma'am for showing your deep faith in me and motivating me, even when I didn't believe myself. I remember your first words when I joined your group that "Life won't be the same after joining Ph.D., it is a totally different journey of life where you will learn a number of things and make sure you get the best out of it and assure you give a better future to your family". Thank you for always believing in me and supporting me through all the ups and downs in this roller coaster journey on both professional as well as personal level. I am not the same girl who joined here, I have grown as a more confident and matured person, and this is only because of you and your faith that you have shown in me. Thank you for correcting me always till today and pushing me to go beyond my limits and achieve my goals. Your never give up attitude, great enthusiasm towards work, leadership quality and personal care is what makes you different from others. You have provided me with insightful and constructive comments on my research that have been a substantial aid in this accomplishment. You have taught me how to deal with the failures and nourished my research throughout this beautiful journey. Without your guidance and persistent support, I would never have been able to complete my thesis. I hope I was able to meet up to your expectations a bit and I will try to follow the things that I have learnt from you and carry forward the same in future also. I also want to thank Dr. Vasanth Kumar for his support, love, care and the cheerful moments. My deepest thank you goes to Avish for all the love and

care and I will cherish and going to miss the fun moments that we have shared during this period.

I want to express my sincere gratitude to Dr. Debaprasad Mandal, Associate Professor, IIT Ropar, for his guidance, livelihood, and constructive criticism from the very beginning of my Ph.D. journey. I was fortunate enough to learn a lot from you, which has promoted my research skills and thinking abilities. I am certainly obliged to him for his collaboration and support. I wish to express my thanks to my doctoral committee: Dr. T. J. Dhilip Kumar, Dr. Anupam Bandyopadhyay and Dr. Dhiraj Mahajan for their inspiration, praise and valuable feedback. I want to thank Prof. Rajeev Ahuja and Dr. Sudip Chakraborty for their guidance and research collaboration. I want to acknowledge all the faculty members in Department of Chemistry, IIT Ropar, who have encouraged me during various stages of this research tenure. I also want to express my gratitude to all the staff members Ms. Poonam, Mr. Sushil, Mr. Nagendra, Ms. Samita, Mr. Manish, Mr. Amit, Ms. Hanspreet, Ms. Gurprakash for always co-operating and supporting me whenever required. Your contribution has played a huge role in completion of my research work. My special thank goes to Dr. Suman from my secondary school, thank you Ma'am. You are the reason why I had interest in Chemistry, you made the subject so lively and interesting that made me pursue my research career in this field. I want to express my gratitude to Dr. Balwinder Singh, my M.Sc. project mentor who supported me and guided me to enter this Ph.D. journey and introduced me to the research before joining IIT Ropar.

My acknowledgment will not be completed without thanking my lovely lab mates with whom I was fortunate enough to meet and build a family. The healthy environment, the fun moments and the cooperation that you all have given is the reason behind my successful completion of thesis. You all have played a different role in my life and my acknowledgment will be incomplete without mentioning your names. My heartfelt thank goes to Daisy Mehta for the days that we had spent together like a family. Those were the times when every activity we used to do

together be it fun, having food, gossips and lots of notorious things. All those memories are going to last forever and once again thank you for your encouragement, honest concerns, care, love and support from the beginning of my journey. The difficult times that we have faced as well as the beautiful memories that we have created will always be treasured. My special thanks goes to Dr. Neha Thakur and Dr. Mukesh Kumar, whom I can call my loved ones. Thank you for the love, care, encouragement and support that you have provided me during this journey. Dr. Neha, my dearest, has always motivated me and supported me both on personal as well as professional level. Her well-determined nature, leadership quality, caring and loving nature has inspired me a lot. I found an elder brother in Dr. Mukesh, I will never forget your funny pranks you did to tease me, and brought out the real funny character out of me. His dedication, hard-work and patience towards the research has taught me a lot which I would wish to implement in my research also. Together we all have shared a lot of memories, some serious, funny as well as notorious ones. Our tea breaks, “Tapri ki chai and chai pe charcha” in winters will stay with me forever. Thank you both for being a support system and gem of a friend.

A very special thanks to my buddy Man Singh. Thank you for the respect that you have given me always in every aspect that I might not have expressed during this journey. His never ending pranks made sure that I am feeling lively in the lab. His curiosity for research, hard-working nature and composed attitude is an inspiration to me. I wish to have the scientific and constructive research discussions with him in future also. I want to thank him for making me learn the things which I didn't know and inspiring me to think out of the box. I extend my thanks to Akansha Chaturvedi for the good company, wonderful memories and her support during this journey which I will never forget. My heartfelt thanks goes to Sukhjot Kaur for her sincerity, continuous support, help and respect that she has given to me. She has always helped me whenever required both professionally as well as personally, and always inspired me to work hard. I am whole-heartedly grateful to her. I want to

thank Shivangi Mehta and Kalpana Garg for their respect, care, fun memories, love and support during my research journey. I want to thank Sukhdeep Singh, Devyani Dahare and Sameer for the respect, care and support due to which I was able to finalize my thesis. I thank Naresh Bhatia Sir for his motivation, care, blessings and inspiring me to achieve my goals in life. My acknowledgment would be incomplete without thanking my senior Dr. Vikram Singh for his guidance, assistance and introducing me to the lab culture and research work at initial stage of my Ph.D. journey. I express my special gratitude to Dr. Sinchan Maji, Dr. Subhasis Das Adhikary, Dr. Anil Kumar Padhan, Dr. Gaje Singh, Diksha, Ganga, Tino, Aayushi, and Rahul for their motivation, care and cherished memories at IIT Ropar. I want to thank Naina Goyal, Pooja Kulashri, and Rahul for their respect and love. A special thanks goes to my much-loved Bhawana, who has always respected me, listened to me sincerely and cared for me till now. Finally, I thank my friends and colleagues at IIT Ropar for their care and support.

I fail to express my gratitude to my best friend and research partner Mr. Alankar Kafle. I was fortunate enough to start my Ph.D. journey and pursue my research with you. I have just not found a research partner and a friend in you, I see a fatherly figure in you who has always motivated me, supported me, scolded me and shown me the right path to follow whenever I was getting demotivated. I am lucky to learn so much from you, be it the research knowledge and attitude especially handling the failures and never giving up, or the dignity and how to maintain the relationships. Without you and your support it would have been impossible for me to make it this far in this research journey. You have supported and motivated me in every possible way on both personal and professional levels and I am wholeheartedly grateful to you for the love you have bestowed on me. Thank you for always standing by my side no matter how hard the time was. I also want to thank Sandhya Subedi for her sweet gestures, care, love and support in this period. My thanks and love goes to Maitreyee and Vaidehee for all the sweet memories. I express my love and thanks to my bestie Neha Rani. We started our Ph.D. journey

together but at different places, but her continuous support, love and care regardless of the distance between us has made my journey more easy and lively.

My special thanks goes to my beloved best friend, support system and companion for life, Mohit, who always stood by me and motivated me. His contribution is immense and the eternal support that he has given to me during this journey has made these five years more memorable. Whenever I got low and disappointed, he was there to motivate me on both professional and personal level. He believed in me and made me realize that I can accomplish my goals in life. His enthusiasm, positive attitude and dedication to achieve his aims has taught me a lot. Thank you for your encouragement and care in accomplishing my research and finalizing my thesis. I cannot express more, as my words may fall short to thank him for the love, care and support he has sprinkled on me.

Last but not the least, I want to thank my lifelines, my mother Veenu Gupta and my sister (second mother) Divyanshi Gupta. They are the reason behind whatever I am able to achieve today. Their motivation, understanding, encouragement, love, care and support has made me come this far in life. I can never express my gratitude and love to my mother, she is the backbone of my life. She has struggled and sacrificed her whole life to see me in this position today. Especially during this journey, she has supported me immensely, handled my mood swings when I was depressed, took care of my health when I was low, never expressed herself if she wants to have a conversation with me. She supported me in every way possible. Her contribution to my thesis and research journey is utmost. I want to thank my elder sister for believing in me, motivating me and supporting me always. I cannot forget the sacrifices that she has made due to which I have come this far. Her love, care and support is indispensable which has made me strong enough to reach this far in life. I hope I have made you both proud, and want to thank you again for being my role models and support system. My acknowledgement would be incomplete without thanking my little angel Kamakshi (Pari). She made me lively

and happy when I was low and discouraged. I also want to thank Mr. Nitish Juneja for his love, care and support during this journey.

I thank all those whose names may have escaped attention here but have contributed to my work. I am grateful to all those who have helped me throughout the journey.

Divyani Gupta

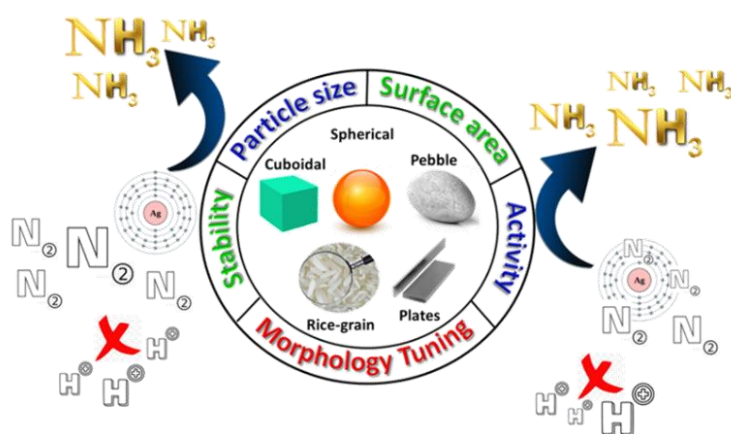
Preface

The world's population is sought to reach upto 9 billion in the next 35 years and with this gigantic upsurge in human population, the pressure to meet the three primary rations for life on earth viz. food, water and energy will increase abruptly. Especially, in an over populated country like India, the food production needs a boost of upto 70% by 2030 according to the Food and Agriculture Organization (FAO). About 40–60% of global food production is tied to the usage of commercial fertilizers which involve fossil fuels as the major feedstock. Unfortunately, the looming perils of the fossil fuels induce greenhouse gas emissions, climate change, rise in sea level, health hazards while their escalating depletion and limited reserves impose a serious concern. Thus, the use of alternative sustainable methodologies in fertilizer industry is obligatory to diminish the dependence over fossil fuels.

Ammonia (NH_3) makes an indispensable contribution to the agricultural avenue through its application in fertilizer industry. It is also considered as a green energy carrier and is used in production of nitric acid, nylon, pharmaceuticals, explosives, dyes, refrigerants, etc. Ammonia production currently relies on energy intensive Haber-Bosch process which is generally powered by fossil fuels and accounts for more than 2% of global CO_2 emissions (2.16 tonne CO_2 /tonne NH_3) and 2-3% of total energy (30 GJ/tonne NH_3) & natural gas consumption. For sustainable NH_3 production and transformation of the H-B industry, one of the most green and viable substitute is electrochemical nitrogen reduction reaction (NRR) which uses water as a proton source and can be operated under mild conditions with zero carbon emissions. However, electrochemical reduction of the N_2 molecule necessitates clogging of certain bottlenecks *i.e.* $\text{N}\equiv\text{N}$ triple bond activation & adsorption and the competition with hydrogen evolution reaction (HER). In addition, with global transition from fossil fuels to renewable energy sources, there is an increasing necessity for energy storage solutions that can cover the timeframes

for storing the excess energy produced from the renewables which can later be used for powering the ammonia production. Therefore the objectives of this thesis include the design and development of various classes of electrocatalysts including noble metals, non-noble metals and carbonaceous materials which exhibit activity towards NRR, O_2 evolution and O_2 reduction reactions as well. The scope of this thesis is very broad and paves the pathway for future green ammonia production at reduced cell voltages and by green routes over conventional methods. Also, a new integrated system *viz.* Zn-air battery powered NH_3 synthesis is presented to eliminate the reliance over renewables.

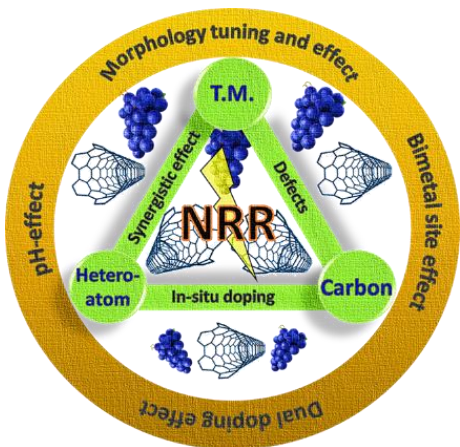
Chapter 1 of my thesis briefly introduces the population growths and challenges associated with consumption of fossil fuels to meet the water-energy-food demands, followed by the green ammonia production to lead a sustainable life on earth. Afterwards the significance of electrochemical pathways to produce ammonia, challenges associated with the same and development of electrocatalysts for overall ammonia synthesis and Zn-air batteries powered NH_3 production have been detailed. The second chapter describes the details of the synthesis methods involved, material and electrochemical characterization techniques, formula for calculations, basic terminologies as well as product quantification methods used in the current thesis.



One of the objectives of this thesis (Chapters 3^{4, 5} and 4⁶) is to develop highly efficient noble-metal, non-noble metal and metal-free

electrocatalysts exhibiting morphology dependent activity which will effectively carry out NRR and suppress HER. Ag metal based composites are explored for

effective N₂ reduction and HER suppression in Chapter 3 where the morphology tuning is carried out by varying the reaction time and synthesis routes. The stability of Ag metal is enhanced in alkaline media by alloying it with phosphate unit while

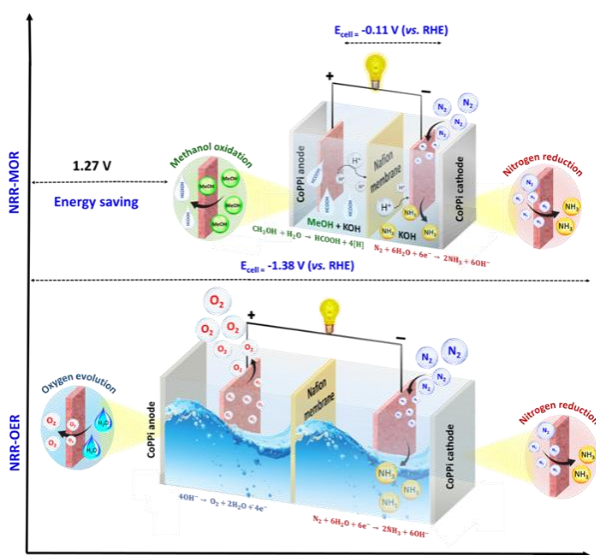


the incorporation of secondary metal like Vanadium is introduced to improve the conductivity and thus NRR activity.

A more economical way is to utilise earth abundant and non-expensive transition metal based and metal-free electrocatalysts for the same. In this regard, in Chapter 4 the synthesis of dual heteroatom containing carbon materials

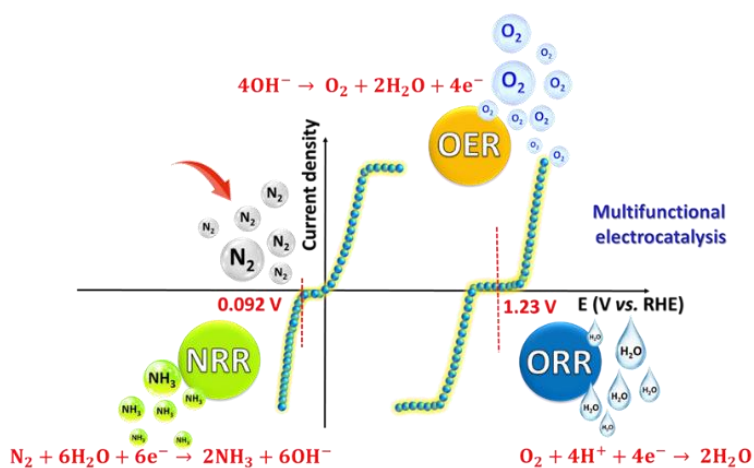
and transition metal based catalyst with well defined morphology is designed and explored towards NRR. The theoretical investigations are also performed in this chapter to affirm the actual active site and role of Cu-metal as a dopant in metal borides is also investigated.

For practical implementation *i.e.* NH₃ synthesis under full cell conditions, the anodic half-cell reaction (O₂ evolution, OER) cannot be ignored. The performance of overall ammonia synthesis device is utterly reliant on the activity and durability of NRR-OER catalysts, where both involve different mechanisms and hence different catalysts are employed to achieve better activity and performance. The development of a bifunctional catalyst can simplify the cell setup and reduce the cost of overall cell with maximum utilization of electrocatalyst. Therefore, in Chapter 5A, our



objective is to design a cost-effective, non-precious metal based electrocatalyst which exhibits bifunctional activity towards NRR and OER to produce ammonia under full-cell configuration. Also, the poor kinetics of OER reduces the overall energy efficiency of the device and results into large cell voltages, and therefore it can be replaced with an alternative anode reaction with faster kinetics, thermodynamically feasibility which can yield a value-added product. As a consequence, another objective of our thesis is to replace the sluggish OER with methanol oxidation reaction (MOR) at anode during NH_3 synthesis in Chapter 5B⁷ to reduce the cell voltage and produce value-added industrial intermediates/products such as formic acid or formate at anode.

In addition, with global transition from fossil fuels to renewable energy sources, there is an increasing necessity for energy storage solutions that can cover the



timeframes for storing the excess energy produced from the renewables which can later be used for powering the ammonia production. Since the reliance over the renewable

energy sources impose disadvantages like dependency on the weather, the development integrated energy systems (IES) such as combined solar cell and lithium storage unit, water splitting powered by solar cells/metal-air batteries is significant. Zn-air batteries have demonstrated their potential as the power source due to earth abundancy, economical and environment friendly nature and its high theoretical energy density (1216 Wh kg^{-1}). Integration of ZAB in electrochemical NH_3 production will also provide cumulative efficiency compared to its individual device and thus we have aimed at a more economical way to produce ammonia

without the use of any external power source. And so, the final objective of our thesis includes designing of multifunctional catalysts for Zn-air batteries and overall ammonia synthesis active towards ORR, OER (air cathode in Zn-air battery) and NRR.⁸ Chapter 6 focuses onto the development of a trifunctional catalysts which can effectively execute self-powered ammonia synthesis under full-cell conditions.

Chapter 7 summarized the overall thesis work and presented the possible future outlook in similar area and new endeavors.

Contents

Chapter 1. Introduction	1
1-1 Population growth and challenges	1
1-2 Dependence over fossil fuels	1
1-3 Renewable sources of energy	4
1-4 Significance of ammonia production	5
1-5 Electrochemical ammonia synthesis	9
1-6 Major challenges in electrochemical N ₂ reduction to NH ₃	12
1-7 Significance of electrocatalysis	15
1-8 Development of bifunctional catalysts	17
1-9 Self-powered ammonia synthesis	18
1-10 Zn-air battery as a power source	19
1-11 Development of trifunctional catalysts	22
1-12 Overall aim and objectives	23
1-13 References	27
Chapter 2. Material design, characterization and instrumentation techniques	31
2-1 Synthetic approach	32
2-1.1 Citrate-complexation method	32
2-1.2 Hydrothermal method	32
2-1.3 High temperature pyrolysis	33
2-1.4 Chemical reduction method	33
2-1.5 Sonochemical method	34
2-1.6 Microwave (MW) method	34
2-2 Material characterization	35

2-2.1	Electron microscopy	35
2-2.1.1	Scanning electron microscopy and field emission scanning electron microscopy	35
2-2.1.1	Transmission electron microscopy and high-resolution TEM	36
2-2.2	Powder X-ray diffraction	36
2-2.3	Fourier transformation Infrared spectroscopy	37
2-2.4	Raman spectroscopy	37
2-2.5	CHNS-O elemental analysis	38
2-2.6	BET surface area analysis	39
2-2.7	Microwave plasma atomic emission spectroscopy	39
2-2.8	Water contact angle	39
2-2.9	UV-visible spectroscopy	40
2-2.10	¹ H-nuclear magnetic resonance spectroscopy	41
2-2.11	Liquid chromatography-mass spectroscopy	41
2-2.12	Gas chromatography and gas chromatography-mass Spectroscopy	42
2-2.13	X-ray photoelectron spectroscopy	43
2-3	Electrochemical measurements	43
2-3.1	Voltammetry	43
2-3.1.1	Cyclic Voltammetry	43
2-3.1.2	Linear sweep voltammetry	44
2-3.2	Rotating disc electrode & rotating ring disc electrode	44
2-3.3	Electrochemical Impedance spectroscopy	45
2-3.4	Electrochemical surface area determination	46
2-3.5	Chronopotentiometry and chronoamperometry	47
2-4	Detection and quantification of products/trace contaminants	48
2-4.1	Quantification of Ammonia	48
2-4.1.1	Indophenol blue method	48
2-4.1.2	Nessler's reagent method	48

2-4.1.3	¹ H-NMR spectroscopy	49
2-4.1.4	LC-MS	49
2-4.2	Quantification of hydrazine	49
2-4.2.1	Watt-Chrisp method	49
2-4.3	Quantification of hydrogen (H ₂) and oxygen (O ₂) by gas chromatography	50
2-4.4	Detection and quantification of trace NO _x and NH ⁴⁺ impurities	50
2-4.4.1	Nitrate (NO ₃ ⁻) and nitrite (NO ₂ ⁻) ion determination	50
2-4.4.2	N ₂ O quantification by gas chromatography-mass spectroscopy (GC-MS)	51
2-5	Theoretical investigations	51
2-6	Zn-O ₂ battery assembly	53
2-7	Basic terminology used in batteries	54
2-7.1	Anode	54
2-7.2	Cathode	54
2-7.3	Electrolyte	54
2-7.4	Separator	54
2-7.5	Open circuit voltage	55
2-7.6	Specific capacity	55
2-7.7	Power density	55
2-7.8	Energy density	55
2-7.9	Cycling stability	55
2-8	Calculations	55
2-9	References	56

Chapter 3. Morphology dependent activity of noble metal based catalysts for electrochemical N₂ conversion to NH₃

59

3A. High yield selective electrochemical conversion of N₂ to NH₃ via morphology controlled silver phosphate under ambient conditions	61
3A-1 Introduction	62
3A-2 Material Synthesis	63
3A-2.1 Synthesis of Ag ₃ PO ₄	63
3A-3 Results and discussion	64
3A-3.1 Mechanism for synthesis and morphology control	64
3A-3.2 Physical characterization	65
3A-3.3 Electrochemical activity towards NRR	66
3A-3.4 Detection/elimination of N-labile impurities	73
3A-3.5 Validation of NH ₃ yield rate	76
3A-3.6 Stability measurements	78
3A-4 Summary	79
3A-5 References	80
 3B. Sustainable ammonia synthesis through electrochemical dinitrogen activation using Ag₂VO₂PO₄ catalyst	 83
3B-1 Introduction	84
3B-2 Material Synthesis	86
3B-2.1 Synthesis of Ag ₂ VO ₂ PO ₄	86
3B-3 Results and discussion	86
3B-3.1 Physical characterization	86
3B-3.2 Electrochemical dinitrogen reduction	89
3B-3.3 Identification/elimination of N-contamination during NRR	94
3B-3.4 Isotope labelling experiments	96
3B-3.5 NRR Stability tests and post-stability material characterizations	98
3B-4 Summary	100
3B-5 References	100

Chapter 4. Development of non-noble metal based & metal-free catalysts for electrochemical synthesis of NH₃ 103

4A. Selective electrochemical conversion of N₂ to NH₃ in neutral media using

B, N containing carbon with nanotubular morphology	105
4A-1 Introduction	106
4A-2 Material synthesis	108
4A-2.1 Synthesis of [BMIM] ⁺ Br ⁻	108
4A-2.2 Synthesis of IL	110
4A-2.3 Synthesis of ZIB-IL	110
4A-2.4 Synthesis of C-BN@T/ C-N@T and C-B@T	111
4A-3 Results and discussion	111
4A-3.1 Physical characterization	111
4A-3.2 Electrocatalytic activity towards NRR	118
4A-3.3 True estimation of NH ₃ yield	123
4A-3.4 Stability studies	125
4A-3.5 Theoretical investigations	128
4A-4 Summary	130
4A-5 References	130

4B. Modification of Ni₄B₃ composite with copper for enhanced electrochemical N₂ reduction to NH₃ 133

4B-1 Introduction	134
4B-2 Material synthesis	136
4B-2.1 Synthesis of Cu-Ni ₄ B ₃	136
4B-3 Results and discussion	136
4B-3.1 Physical characterization	136
4B-3.2 Catalytic activity towards NRR	139
4B-3.3 Role of Cu-modification and optimal metal to precursor	

ratio on electrochemical NRR performance	141
4B-3.4 Detection/Elimination of false positives in NRR	144
4B-3.5 Validation of NH_3 yield rate by isotope labelling experiments	144
4B-3.6 Catalyst stability	145
4B-4 Summary	146
4B-5 References	147

Chapter 5. Designing of high performance bifunctional catalysts for overall ammonia synthesis

149

5A. Bifunctional electrocatalysis towards N_2 reduction and O_2 evolution via Ni_xB_y catalyst for overall NH_3 synthesis

151

5A-1 Introduction	152
5A-2 Material synthesis	155
5A-2.1 Synthesis of Ni_xB_y	155
5A-3 Results and discussion	155
5A-3.1 Physical characterization	155
5A-3.2 Electrocatalytic NRR activity	158
5A-3.3 Electrocatalytic OER activity	163
5A-3.4 Overall ammonia synthesis	164
5A-4 Summary	166
5A-5 References	166

5B. Dinitrogen reduction coupled with methanol oxidation for low overpotential electrochemical NH_3 synthesis over cobalt pyrophosphate as bifunctional catalyst

169

5B-1 Introduction	170
5B-2 Material synthesis	173

5B-2.1 Synthesis of CoPPi	173
5B-3 Results and discussion	173
5B-3.1 Physical characterization	173
5B-3.2 Electrochemical N ₂ reduction	175
5B-3.3 Methanol electro-oxidation	185
5B-3.4 Overall NH ₃ synthesis	190
5B-4 Summary	192
5B-5 References	192

Chapter 6. Trifunctional Co₂B catalyst enables high power density Zn-air batteries to drive the electrochemical NH₃ synthesis

6-1 Introduction	196
6-2 Material synthesis	198
6-2.1 Synthesis of Co ₂ B	198
6-3 Results and discussion	199
6-3.1 Physical characterization	199
6-3.2 Electrochemical dinitrogen reduction (NRR)	203
6-3.3 Theoretical investigations for NRR	208
6-3.4 Oxygen bifunctional activity	212
6-3.5 Self-powered ammonia synthesis	218
6-4 Summary	219
6-5 References	220

Chapter 7. Summary and future perspectives

7-1 Summary	223
7-2 Future perspective	228

Curriculum vitae

Chapter 1

Introduction

1-1 Population growth and challenges

Over the last century, the global population has quadrupled and is estimated to reach around 10 billion by 2050 (Figure 1-1a).¹ The water-food-energy nexus lie at the heart of sustainable life on earth and is anticipated to exacerbate in the near future beneath the pressure of immensely growing population (Figure 1-1b).² Particularly in developing and overpopulated countries, there is a mounting concern and question of “*How to eradicate the human hunger and feed the future population?*”, which is amongst one of the “Sustainable Development Goals” (Figure 1-1c)³. The available data from UNICEF states that more than 800 million people suffered from hunger in 2020 whilst above 30% of the world’s population were adequately fed.⁴ To come across the endeavors of creating a world free of hunger by 2030, agricultural production must increase by about 30-40% which obliges the boost in fertilizer production.⁵ Fertilizers allow the crops to grow bigger, faster, and to produce more food by providing them with essential nutrients such as potassium, phosphorus, and nitrogen. As per the statistics, a marginal increase of 0.5% is witnessed for fertilizer production over 2020-2021 standing with 18.58 million metric tonnes annual fertilizer production value at present.⁶

1-2 Dependence over fossil fuels

The global demands for the water-food-energy nexus are majorly fulfilled by the consumption of fossil fuels *viz.* coal, oil and natural gas, which have been powering economies (energy, agriculture, industries, etc.) for over 150 years (Figure 1-2a).⁶ These fossil fuels are available in limited quantities and usually found in specific regions of the world, making them more abundant in some nations than others.

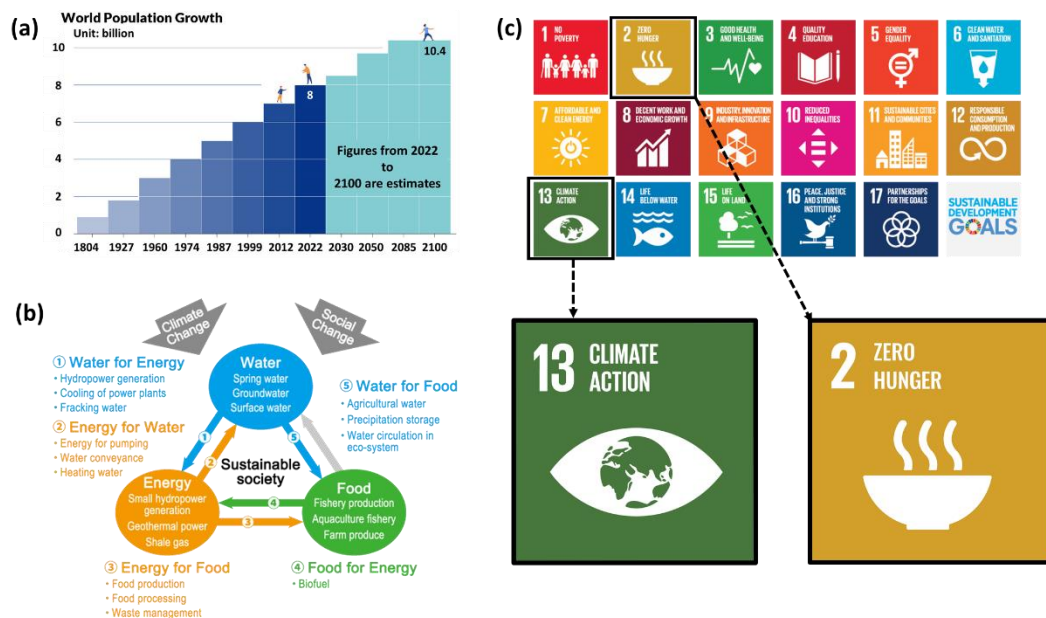


Figure 1-1. (a) Bar graph for global population growth trend¹, (b) water-food-energy nexus for sustainable life on earth² and (c) Sustainable Development Goals proposed by United Nations under “Sustainable Development Agenda by 2030” (Zoomed goals: Goal 13 and Goal 2)³.

Moreover the current depletion rate of fossil fuels and greenhouse gas (GHG) emission upon burning of fossil fuels has raised an alarming situation. Particularly, an excess buildup of GHG (Figure 1-2b) provokes dramatic climate changes such as floods, droughts and warming up the planet. A major part of GHG emission (in million metric tons of carbon dioxide equivalent, MMTCDE) is held by CO₂ (80.14%) with the energy sector being the highest source (5392.27 MMTCDE) followed by agricultural (628.62 MMTCDE) and industrial processes (373.71 MMTCDE).⁷ The rising GHG production and the increase in carbon footprint has increased the earth’s temperature by 0.92 °C between 1880 and 2012 and also increased the degradation rate of the environment in connection with global warming, air pollution, loss of the ozone layer, human health and global sea level rise (increased 3.8 inches after 1993), as shown in Figures 1-2 (c-f).^{5, 8} To address this issue and save lives and livelihood, Goal 13³ (Figure 1-1c) under the Agenda for Sustainable Development by United Nations has been announced which

states “Take urgent action to combat climate change impacts”. To meet this goal, GHG emission must decline by 43% by 2030 and to net zero by 2050, however, in the current scenario it seems somewhat challenging. Henceforth, the overall target is to look for an alternative, since fossil fuels are not the only way to fulfil the water-food-energy demands. There are several options capable enough to transform the fossil fuel economy and one such alternative is renewable energy which can afford a more sustainable system with zero carbon emission.

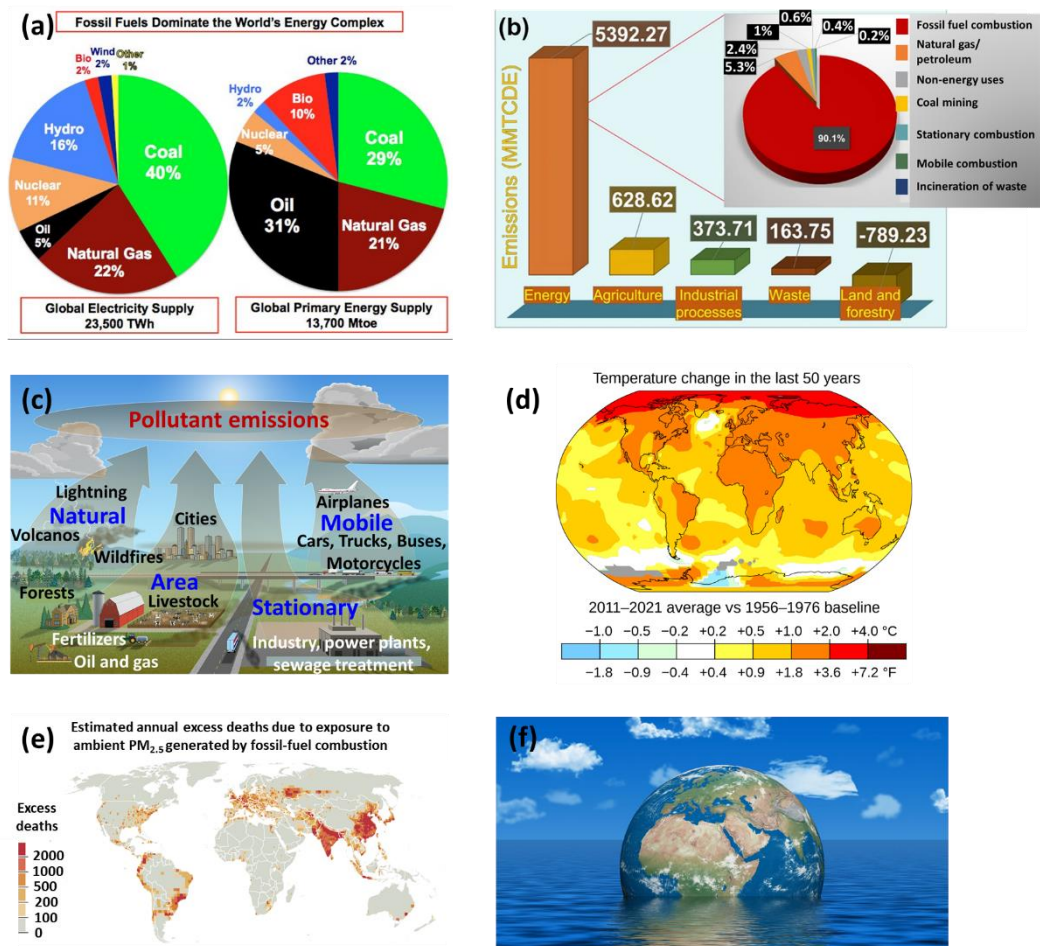


Figure 1-2. (a) Use and consumption of fossil fuels in different sectors⁶, (b) emission of GHGs in the USA by category [Inset in (b): Breakdown of emission in the energy category]⁷. Effect of GHG emission onto the (c) atmosphere⁹, (d) global temperature^{10, 11}, (e) human health¹² and (f) sea level on earth¹¹.

1-3 Renewable sources of energy

Renewable energy from natural sources such as the sun and wind is booming on the pledge of a clean energy future, as they are constantly replenished and do not run out like fossil fuels (Figure 1-3a). They hold the capability to reduce the dependence over the fossil fuels and at the same time can reduce the global CO₂ footprint from the environment and other GHG emission.¹³ Renewable energy sources will be liable for the reduction of almost one-third of carbon emission by 2030 under the *Net Zero Emission* target by 2050 (Figure 1-3b). At present, more than 12% of U.S. energy generation is coming from renewable sources at small and large scales [Figures 1-3(c-d)]. Even the rural areas in U.S. such as Alaska, Kansas, etc. are rigorously exploiting renewable energy for heating and lighting purposes.¹⁴ Renewable energy aims to realize substantial benefits in water-energy-food sector by providing the energy using less resource-intensive processes over conventional fossil-fuel-based technologies. Water is used for the extraction and processing of

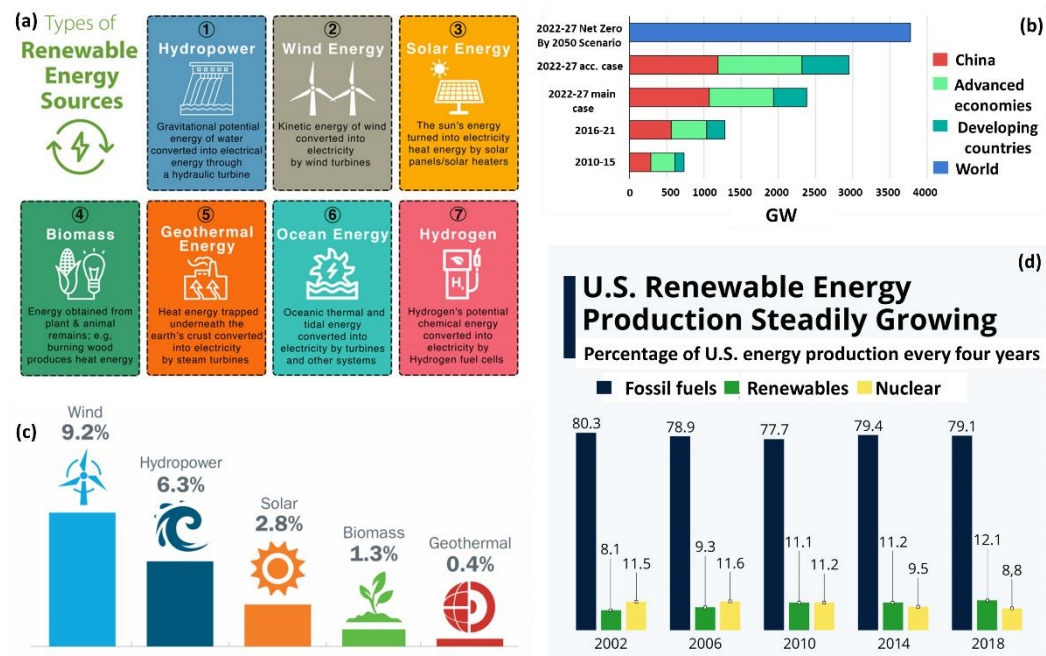


Figure 1-3. (a) Renewable energy sources¹⁵ and (b) renewable capacity growth in the main and accelerated cases (2010-2027)¹⁶, (c) shares of total electricity production in 2021 among the types of renewable power in United States¹⁷ and (d) bar graph showing percentage growth of U.S. renewable energy every four years¹⁸.

fossil fuels and the generation of electricity which accounts for more than 15% of global water consumption. On the other hand, food production accounts for 30% of global energy consumption and is the largest consumer of water resources. By the utilisation of renewable energy sources, electricity generation will become less water-intensive. For instance, solar or wind energy requires upto 200 times less water than a coal power plant to produce the same amount of electricity. In addition, during food production, integration of renewable energy can improve the productivity, post-harvest processing and reduce GHG emission. Interestingly, renewable energy can also be used for on-site energy generation for fertilizer production to improve accessibility and can substitute fossil fuels for the provision of heat, electricity or transportation for food production.⁵

1-4 Significance of ammonia production

Amid the water-food-energy nexus, in developing and overpopulated countries, food production is one of the major sectors which requires a boost of upto 70% by 2050.¹⁹ Around 40-60% of food production is tied with fertilizer production which plays an essential role in providing vital nutrients for crops and increases its productivity (Figure 1-4a). Particularly, nitrogen fertilizers are most frequently used in which ammonia (NH_3) makes an indispensable contribution by forming a bridge between the nitrogen in the air and the food we eat. Ammonia, the second largest produced chemical worldwide after sulfuric acid, has reached a production capacity of 290 million tons annually with India holding a massive share of 25.5 million tons at present (Figure 1-4b).²⁰ A major part of NH_3 *i.e.* 70% is used to produce nitrogen fertilizers with the remainder 30% of global demand is for a wide range of industrial applications. For example, it is used in the production of nitric acid, urea, acrylonitrile, etc. used in the explosives and plastics industry (Figure 1-4c).²¹ Ammonia may also be used as a future low-carbon energy vector or fuel in terms of clean energy transition, since it can store hydrogen indirectly, can be easily liquefied by cooling to $-33\text{ }^\circ\text{C}$ at roughly atmospheric pressure and provides easy transportation owing to its high energy density of 11.5 MJ L^{-1} than liquid hydrogen

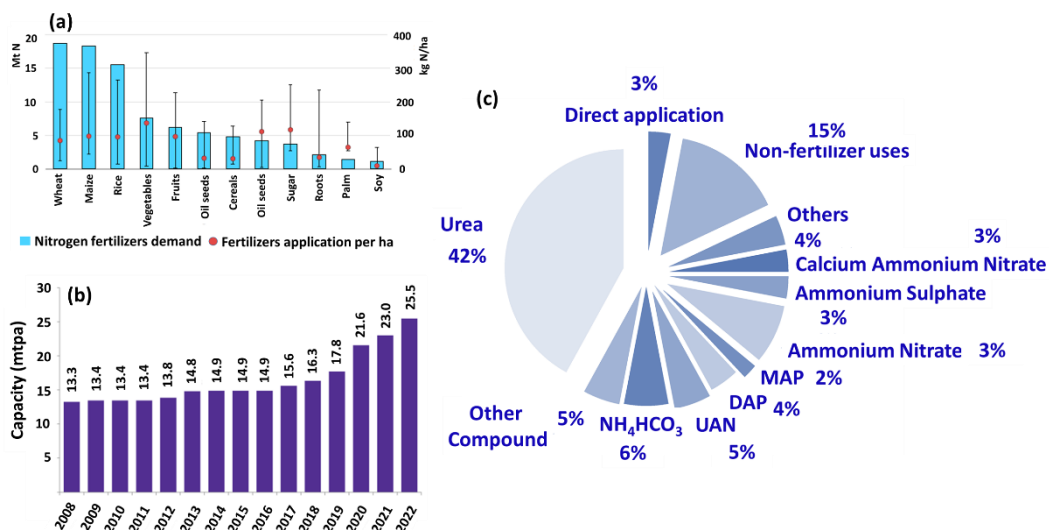
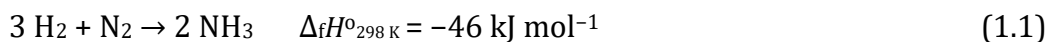


Figure 1-4. (a) Nitrogen fertiliser demand and application rate by crop²², (b) total ammonia plant capacity in India from 2008-2022 and (c) the applications of ammonia in different sectors²¹.

(8.491 MJ L⁻¹).^{23,24,25} The NH₃ production was first carried out by Humphry Davy²⁶ in 1807 by electrolysis of distilled water in the presence of air using gold electrodes and at low current density, but the production yield was found to be very low. Later, another method for ammonia synthesis was invented by Fritz Haber and Robert Le Rossignol in 1909 and scaled up by Carl Bosch at BASF in 1913.²⁷ The first Haber-Bosch commercial plant was opened at Oppau, Germany to react nitrogen (N₂) with hydrogen (H₂) to give ammonia with improved energy efficiency requiring around 100 GJ energy per tonne of ammonia. To date, it is the dominant process for global ammonia production, but it is also a contributor to the global declines in energy and natural gas resources, prevalent air quality glitches and GHG emission across the world. Haber-Bosch process (Figure 1-5a) is energy intensive and operates under harsh conditions of temperature (350-550 °C) and



pressure (100-250 bar) wherein N₂ and H₂ gases react over Fe₃O₄ based catalyst to produce NH₃ (Equation 1.1). H₂, one of the feedstock for this process is obtained from natural gas, coal or oil wherein the methane steam reformation process (use

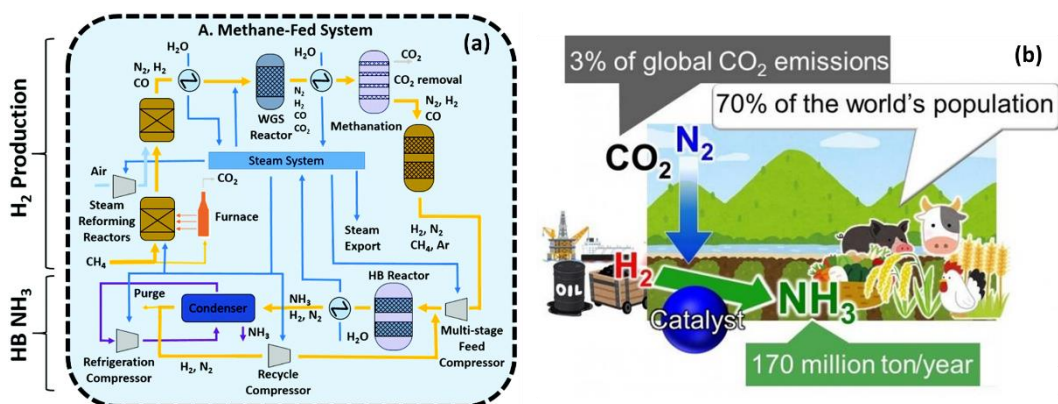


Figure 1-5. (a) Schematic diagram of an energy-intensive Haber Bosch process for ammonia production²⁸ and (b) CO₂ emission associated with the process²⁹.

about 72% for NH₃ synthesis) results in the production of CO₂ (~400 Mt per year) along with NH₃ leading to about 2% of world-wide energy consumption (~34 GJ ton_{NH₃}⁻¹), as shown in Figure 1-5b. Hence, the inclusive ambition of this century is to cut down the consumption of fossil fuels for ammonia synthesis and find a sustainable and economic alternative to it, which will be operated at ambient conditions with diminished CO₂ emission.³⁰

The Net Zero Emission by 2050 aims to transform the Haber-Bosch industry which requires innovation, infrastructure and investment at commercial scale. Based on the carbon emission from the ammonia synthesis processes (Figure 1-6), ammonia can be categorized into the following terms³¹;

Brown ammonia- NH₃ is produced using fossil fuel as the feedstock and associated with higher CO₂ emission. However, most of the energy consumption and more than 90% of carbon emission are due to the H₂ production via the steam methane reformation process.

Blue ammonia- NH₃ is produced using fossil fuels as a feedstock but with carbon capture and storage technology combined with the Haber-Bosch process and allied with reduced CO₂ emission. It involves the sequestration of the emitted CO₂ via carbon capture utilization and storage (CCUS) technology and by planting trees to

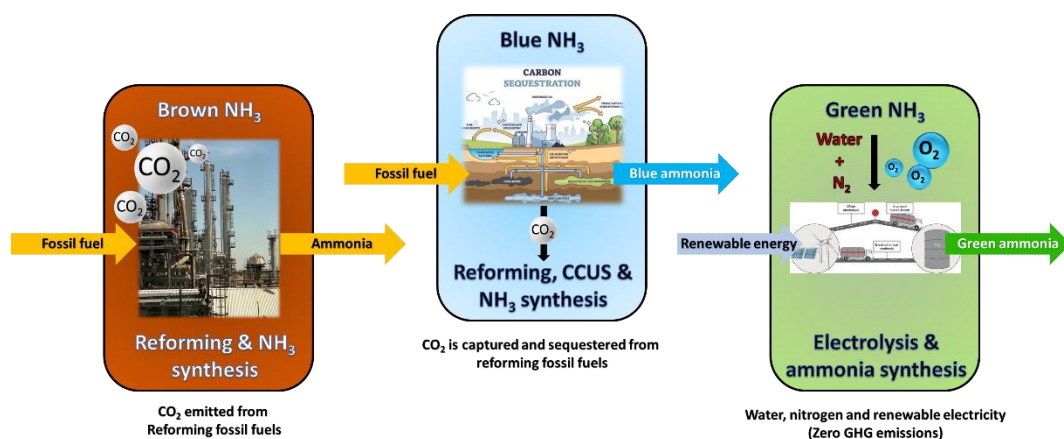


Figure 1-6. Schematic representation of different types of ammonia based on the H_2 production process involved.

reduce the global carbon footprint.

Green ammonia- NH_3 which doesn't involve the use and consumption of fossil fuels and is produced by means of sustainable electricity, water and air. It involves the H_2 production through water electrolysis which combines with N_2 directly from the air using a separation unit to produce ammonia with zero carbon emission³². This process demands 36 GJ of electricity per tonne of NH_3 , where 95% of the electricity is used for H_2 production while 5% to power the air separation and Haber-Bosch units. Although the water-electrolysis coupled with Haber-Bosch plants for ammonia synthesis can cut off the global carbon footprint, but there are also certain challenges associated with this system.³³ The first is the cost of the electricity required to perform water splitting which is not predicted to be cost-competitive with H_2 production by natural gas, while the other challenge is the prerequisite of the continuous high-purity water stream. The global production of NH_3 in 2016 was reported to be 146 million tonnes which will require around 233.6 billion litres of water if produced using a water-electrolysis coupled Haber-Bosch process. In comparison with the H_2 prices produced using the steam reformation process (1.03–2.16 USD $\text{kg}_{\text{H}_2}^{-1}$), the alkaline water electrolyzer can produce H_2 at a cost of 10.79 USD $\text{kg}_{\text{H}_2}^{-1}$ while the proton exchange membrane electrolyzer and solid oxide electrolyzer can produce hydrogen at a price of 13.35 and 14.31 USD

$\text{kg}_{\text{H}_2}^{-1}$ respectively. This production cost is around 5 times higher when compared to the conventional H_2 production by natural gas and can be reduced to 2.16 USD $\text{kg}_{\text{H}_2}^{-1}$ at maximum for alkaline water electrolyzer in 2035 (Figure 1-7).³¹ This necessitates advanced technology for producing green ammonia with reduced energy consumption at the commercial level.

1-5 Electrochemical ammonia synthesis

The overall ambition of this century is to reduce the consumption of fossil fuels for ammonia synthesis and find a sustainable and economic alternative to it which will be operated at ambient conditions with diminished CO_2 emission. Direct electrochemical production of ammonia from water and nitrogen using renewable electricity is one of the most proficient method to produce green ammonia³⁴ (Figure 1-8). More interestingly, there is no separate step involved for green H_2 production

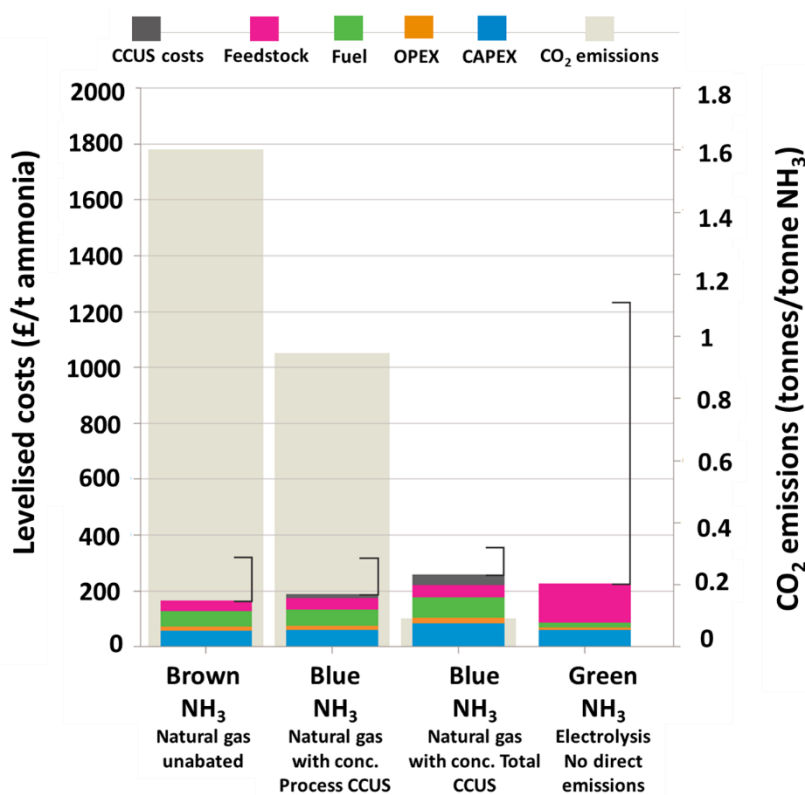


Figure 1-7. Cost comparison of NH_3 produced via different methods.³¹

whereby the required protons (H^+) are generated *in-situ* from water oxidation.³⁵ It enlarges the operating conditions from harsh to mild ones and the reactants involved such as N_2 (78% volume% in air) and H_2O are environmentally benign, abundant and inexpensive.^{30,36} The major advantages of electrochemical ammonia synthesis compared to existing technologies are;

1. **Energy saving**- Less capital-intensive process and holds the potential to achieve higher energy efficiency over thermo-chemical processes as well as water-electrolysis coupled Haber-Bosch process, which is only about 40% energy efficient.
2. **Mild operating conditions**- Can be operated under lower temperatures and pressures, and thus leads to reduced CAPEX (capital expenditure) costs.
3. **Zero carbon emission**- Eliminates the consumption of fossil fuels for H_2 production and uses water as a proton source.
4. **Environment compatible**- Uses renewable sources of energy *viz.* solar, wind to power the process.
5. **Small to medium scale utilization**- Ideal for a more distributed and small-scale ammonia synthesis for on-demand and on-site production.

In due course of electrochemical ammonia synthesis (equation 1.4) in aqueous solutions, N_2 gas is supplied to the cathodic side where its reduction to NH_3 (NRR, equation 1.2) takes place whereas oxygen evolution reaction (OER, equation 1.3) is witnessed at anode due to oxidation of water.³⁷ NRR involves six proton-coupled electron transfer (PCET) processes while OER involves 4 subsequent PCET processes.



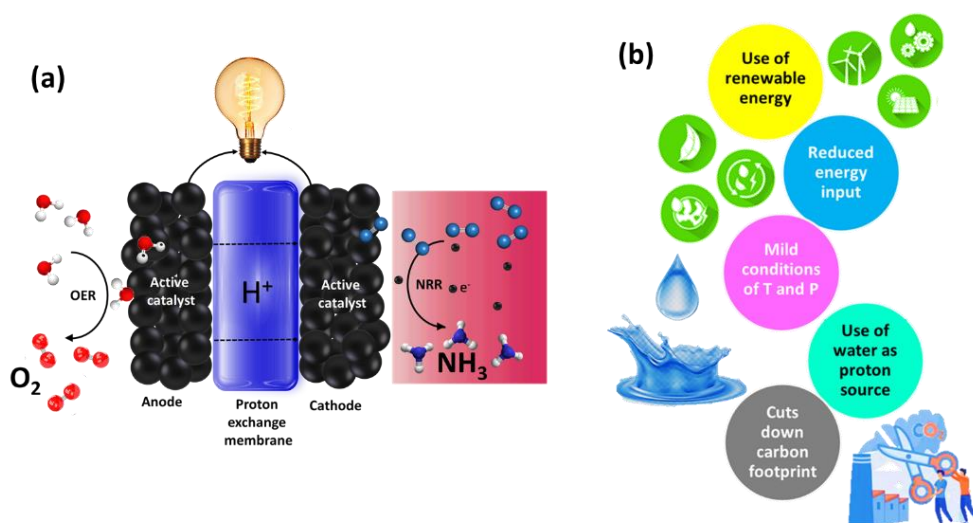


Figure 1-8. (a) Schematic representation of electrochemical ammonia synthesis and (b) its advantages.

NRR is usually classified into two fundamental mechanistic reaction pathways *i.e.* associative and dissociative pathways. The conventional Haber-Bosch process is known to follow a dissociative pathway where the $\text{N}\equiv\text{N}$ triple bond is cleaved first followed by the hydrogenation of the N_2 molecule. On the contrary, adsorption of the N_2 molecule over the catalyst surface is a primary step where the hydrogenation takes place prior to $\text{N}\equiv\text{N}$ bond cleavage, after which NH_3 is produced. Associative NRR pathway can further be subcategorized into distal and alternating based on the addition of H atoms over adsorbed N_2 molecule. During the associative distal pathway by assuming end on adsorption binding mode, N atom far away from the catalytic surface is hydrogenated until one NH_3 molecule is released, followed by hydrogenation of the remaining N atom producing a second NH_3 molecule subsequently. Contrastingly, in the case of the associative alternating pathway, hydrogenation of both the N atoms is accompanied alternatively, followed by PCET to release NH_3 molecules one after another in a sequential manner (Figure 1-9a).³⁸ In addition to it, a new mechanism specific to transition metal nitrides has been proposed *viz.* Mars-van Krevelen (MvK) mechanism.³⁹ It is found to be more favourable over associative and dissociative pathways with reduced overpotentials

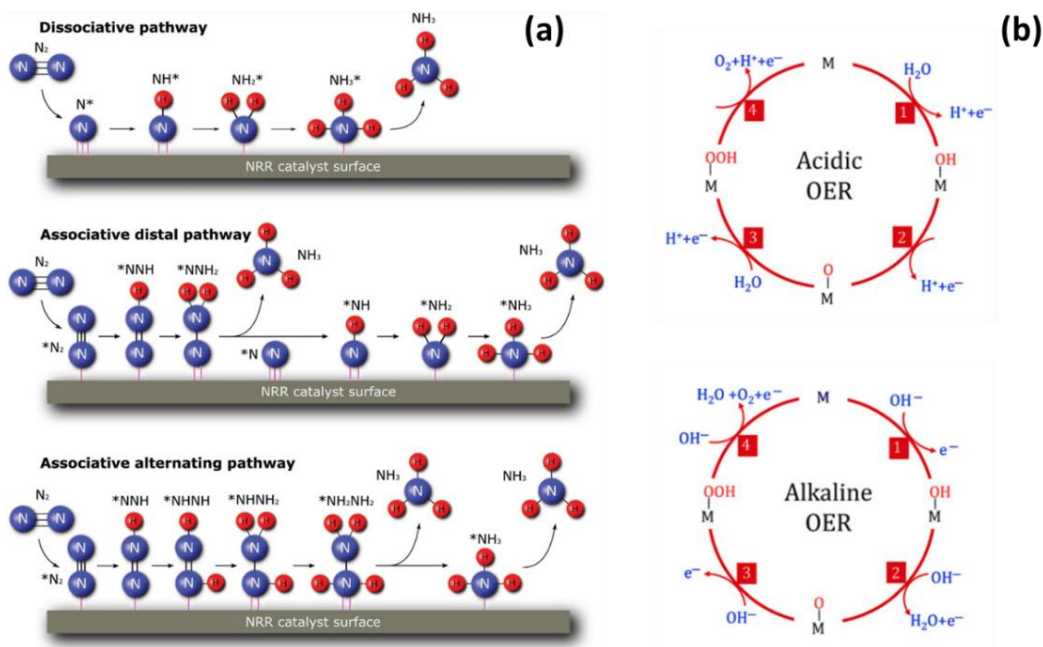


Figure 1-9. (a) Possible NRR pathways over catalyst surface⁴⁰ and (b) OER mechanism under acidic and alkaline electrolyte conditions.⁴¹

due to endothermic N_2 adsorption over nitrides. On the other hand, OER consists of 4 consecutive PCET steps in both acidic and alkaline electrolytes and is dependent on the structure of the electrode surface & pH of the electrolyte.^{42,43} Water undergoes oxidation on reaction with H^+ and e^- pairs in the acidic media to release O_2 while hydroxyl ions (OH^-) are oxidized to give H_2O , O_2 and e^- in alkaline conditions (Figure 1-9b). The reactive intermediates involved during OER like OH^* , O^* , and OOH^* determine the overall kinetics of the catalyst depending on the binding energy of the same over catalyst surface.

1-6 Major challenges in electrochemical N_2 reduction to NH_3

The electrochemical reduction of dinitrogen to ammonia being a multistep PCET process involves the generation of several intermediates and the extra potential required for the hydrogenation of these adsorbed intermediates makes it thermodynamically more difficult resulting in a huge energy barrier for overall electrochemical dinitrogen reduction.^{44,45} Prior to the hydrogenation of the N_2

molecule over the catalyst surface, the adsorption and activation of the same are also critical.⁴⁶ The reason being the high triple bond energy of inert $\text{N}\equiv\text{N}$ triple bond (941 kJ mol^{-1}), HOMO-LUMO energy gap (10.82 eV), negative e^- affinity (-1.8 eV), high ionization potential (15.8 eV), permanent dipole as well as the low solubility of N_2 in water (20 ppm at 20°C , 1 atm).^{47, 48} Besides, its competition with HER in an aqueous medium, which takes place at almost identical potential to that of NRR and is more feasible being a $2e^-$ transfer rather than a $6e^-$ process. This accounts for poor selectivity and hence the poor Faradaic efficiency (F.E.) for ammonia.

In addition to the sluggish kinetics during NRR, the separation of NH_3 produced via NRR from the NH_3 obtained by contaminants is an insurmountable task. It has been realized lately that the interference of trace NO_x and NH_4^+ impurities along with the reducible N species in cell setup (e.g., catalysts, electrolyte, gas supplies) or even in the atmosphere can lead to false-positive or overestimated NH_3 yield rate.^{49, 50} For example,

- ❖ Even the air contains higher concentrations of ammonia in indoor ($\sim 10\text{--}70 \text{ ppb}$) and outdoor ($\sim 50 \text{ ppt}$ to 5 ppb) environments.
- ❖ Human breath can contain $0.3\text{--}3 \text{ ppm}$ of ammonia concentration.
- ❖ The catalyst itself can contain N-labile impurities if the NO_3^- based reactants were used during synthesis while an N-containing catalyst may also participate during NRR.
- ❖ The electrolyte solutions may contain nitrate or nitrite contaminations which are easily reduced to ammonia.
- ❖ The commercial gas supplies even with % a purity as high as 99.999% contain NO_x and NH_4^+ impurities at ppm or sub-ppm levels (~ 0.05 to 2 ppm).

As a corollary, most of the reports in recent years are obscured by these experimental inconsistencies and require a revisit. It underlines the significance of adopting stringent and rigorous experimental protocols to trace and later eliminate

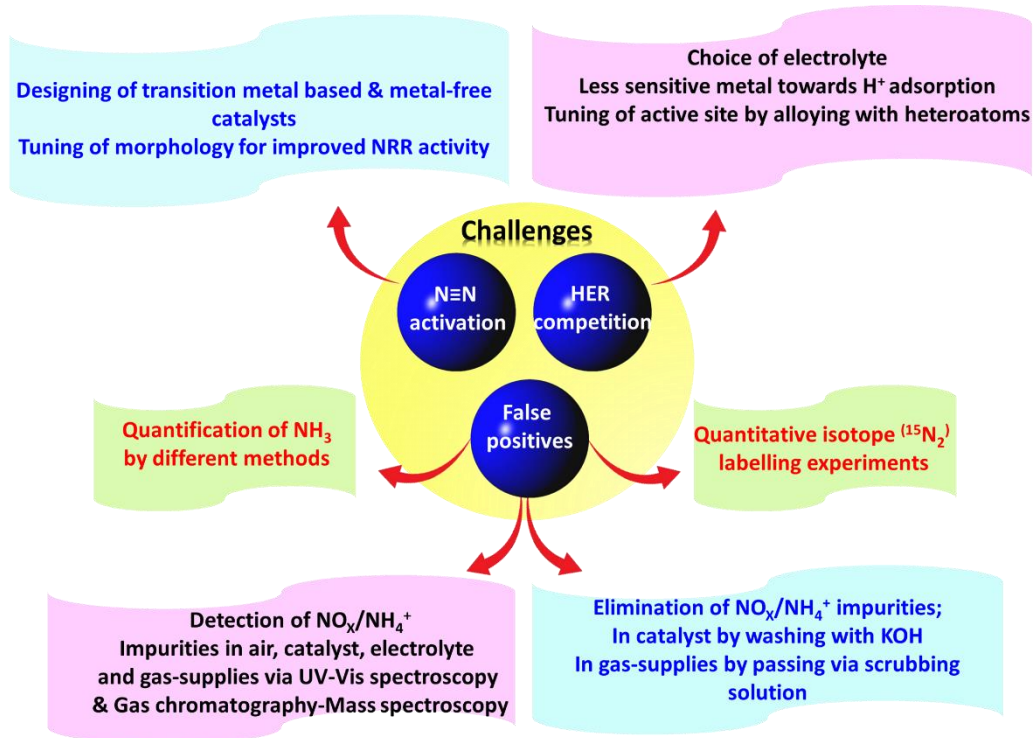


Figure 1-10. Challenges of NRR and probable solutions with rigorous protocol to be followed to avoid false estimation.

or minimize the NO_x and NH_4^+ impurities and then accurately quantify the ammonia concentration in the electrolyte.⁵¹ Indophenol blue method is widely practiced for ammonia quantification after NRR, but it lacks uniformity in terms of the amount of reactants, complexing agents and oxidants which results in inconsistency in quantification at sub-ppm levels. And so, the rigorous isotope labelling experiments emerge as a significant tool to validate the ammonia yield rate and determine the actual source for reduced product devoid of interference from the contaminants. However, the expensiveness, complex procedures and cell setup as well as the not-so-easy availability of $^{15}N_2$ gas supply are certain tailbacks to its extensive use. A single control experiment is not sufficient enough to prove that NH_3 is produced via N_2 reduction and not from any adventitious contamination, plus a single quantification method doesn't validate the reported ammonia yield rate. A rigorous set of control experiments must be performed such as under Ar environments, at open circuit potential (OCP) and over bare electrodes

to see whether the NH_3 is originating from N_2 reduction or contaminations. But the contamination from the gas supplies can also not be neglected for which purification procedures must be adopted.⁵² A scrubbing solution setup involving alkaline KMnO_4 to trap NO_x impurities and an acidic trap to capture NH_4^+ impurities within the gas supplies can be utilised during NRR measurements. Nonetheless, the isotope labelling experiments must be conducted to affirm the origin of ammonia and the $^{15}\text{NH}_4^+$ yield rate must also be in quantitative agreement with $^{15}\text{NH}_4^+$ yield.^{53, 54}

1-7 Significance of electrocatalysis

The major bottlenecks of NRR can be overcome via electrocatalysis by the design and development of an electrocatalyst which can facilitate the electron transfer between the electrode and reactants in electrolyte.⁵⁵ Electrocatalysis put emphasis on reduction of electrode overpotential by means of providing alternate energy pathways depending on the surface adsorption of reactive intermediates.⁵⁶ During the last few decades, electrocatalysis has played a key role in the development of energy conversion and storage devices such as fuel cells, water electrolyzers and batteries. An NRR active electrocatalyst should possess high conductivity, a small activation energy barrier for N_2 adsorption and activation as well as the favorable adsorption energy for reactive intermediates is also a prerequisite for the efficacious synthesis of ammonia.^{57,58}

Various classes of electrocatalysts, typically molecular, homogeneous and heterogeneous catalysts have been explored for electrochemical N_2 reduction to NH_3 .⁵⁹ However, the poor stability and low conductivity of molecular and homogeneous catalysts limit their electrocatalytic NRR performance. On the other hand, the high conductivity and stability of heterogeneous catalysts present them to be the most effectual class of electrocatalysts. Up to the present time, a number of heterogeneous electrocatalysts have been explored towards electrochemical NH_3 synthesis including noble-metal-based, non-noble metal based and even metal-free carbonaceous materials. But unfortunately, they suffer from low ammonia

production yield rates and poor F.E. towards NRR caused by low catalytic efficacy and poor selectivity of electrocatalysts.⁶⁰ U.S. DOE has aimed at the designing and development of exceptionally versatile and robust catalysts with a practical yield rate of 10^{-4} mol h⁻¹ cm⁻¹ and a F.E. of more than 50% to meet the practical expectations.⁶¹ The activity and durability of NRR active electrocatalysts can be boosted by optimizing the morphology (size, shape, etc.), electronic structure, structural phase, exposed facets, surface area and porosity which affect the mass and electron transfer during electrocatalysis. Furthermore, the introduction of heteroatoms, defects, and amorphism can also tune the electron density of the catalyst to achieve high activity during NRR.⁶² To date, quite a lot of sophisticated electrocatalysts have been widely explored to bring about selective NRR, including transition metals-based and metal-free carbon-based catalysts.^{63,57,64} In the midst of existing advances, the transition metal (TM) based catalysts are one of the most likely candidates for NRR due to the availability of vacant *d*-orbitals which facilitates N₂ chemisorption over the catalyst surface and allow the π -back donation of electrons to activate dinitrogen molecule.^{65, 66} The outer *s*-orbital accepts lone pair of electrons from N₂ and eventually downshifts the π^* antibonding orbital of N₂. Thereafter, the metal *d*-orbital transfers the electron to the antibonding π^* N₂ orbital to expedite back bonding and activation of strong N \equiv N bond. Lately, N-doped carbon materials have also attracted widespread consideration by virtue of their ability to modify the electronic properties of the carbon catalyst and enable selective N₂ adsorption.^{67,68} Plenteous work has been over and done with improving the kinetics of NRR by N-doped carbons, while the poor F.E. and yield rate still persist to be an unresolved task. Nowadays, the research is progressing in the direction of enhancing the NRR activity of N-containing carbons via the addition of other heteroatoms including B, S and P due to synergistic effects and co-activation with adjacent carbon.⁶⁹⁻⁷¹ Major part of this thesis is entirely focused on the development of different classes of heterogeneous electrocatalysts for application in NRR via simplified and controlled synthetic procedures to achieve a well-defined morphology.

1-8 Development of bifunctional catalysts

The overall cell potential during ammonia synthesis depends on both anodic and cathodic reactions. The reaction taking place at the cathode is NRR while the OER is witnessed at the anode during ammonia synthesis. We have already discussed the drawbacks associated with NRR and the significance of electrocatalysis to meet practical expectations. In addition, the sluggish kinetics of OER requires high energy input and ultimately the energy efficiency of the NH_3 synthesis device is deprived. In general, IrO_2 and RuO_2 -based catalysts⁷² are considered as benchmark catalysts for OER. Considering the scarcity and high cost of these noble metal catalysts, the overall cost for reactor setups can be a huge challenge at the industrial level. Besides, the lethargic kinetics of both NRR and OER entails the higher overall cell voltage in full cell conditions. Regardless of the exciting efforts being made for the development of separate electrocatalysts for NRR and OER, an appropriate catalyst aiming at the efficient couplings between OER and NRR to execute ammonia production under a full-cell configuration is of vast importance.⁷³ The development of a bifunctional catalyst can simplify the cell setup and decrease the cost of the process and material processing costs with maximum utilization of electrocatalyst.^{74, 75} The performance of NRR-OER coupled overall ammonia synthesis is completely reliant on the activity and robust phase stability of bifunctional NRR-OER catalysts, which is rarely considered. The major task is to accelerate the kinetically sluggish $4e^-$ OER and $6e^-$ NRR which affect the efficiency of the cell system due to which very few reports in this area have been reported so far. Furthermore, due to the high overpotential requirement for OER at the anode and resultant high cell voltage, it can be replaced with an alternative anode reaction which exhibits faster kinetics, more thermodynamic feasibility and formation of value-added product/intermediates used in industries. Henceforth, the below-mentioned strategies (Figure 1-11a);

1. The development of bifunctional electrocatalyst for overall ammonia synthesis can reduce the cost and complexity of the process and

- the replacement of anodic OER with a more feasible reaction to reduce the cell voltage and forming a value-added product on either side,

will definitely pave a floor for the practical implementation of electrochemical NH_3 synthesis route and thus transform the existing Haber-Bosch industry. In this thesis, we have aimed at these two strategies by the development of earth-abundant TM based catalysts with bifunctional activity for overall ammonia synthesis.

1-9 Self-powered ammonia synthesis

Apart from the quest of developing an effective electrocatalyst for ammonia synthesis in aqueous solutions, another major hindrance to its commercialization is the requirement of an external power supply to drive the process. This results in limited mobility and field activities for ammonia production for which it is highly desirable to develop a self-powered electrochemical ammonia synthesis system. The dependence on renewable energy *i.e.* solar energy and wind energy to power the electrochemical device which inflict detriments like reliance on the weather

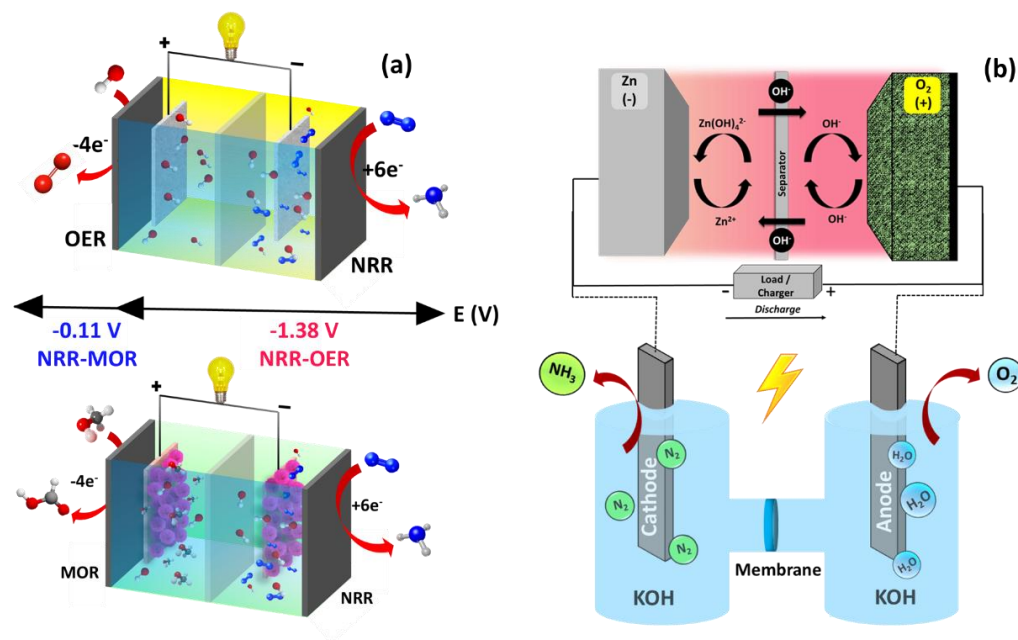


Figure 1-11. (a) Schematic representation of overall ammonia synthesis using NRR-OER and NRR-MOR coupled bifunctional electrocatalysis and (b) Zn-air battery-powered ammonia synthesis.

conditions, high cost and limited production hours. For instance, a decoupled photovoltaic-electrolysis setup to produce H_2 using solar energy gives efficiencies of more than 15% but are associated with high capital and balance of system costs (5-15 \$/kg of H_2) depending on the underlying technology and location.⁷⁶ This has led to the development of clean and renewable energy alternatives like integrated energy systems (IES) such as combined solar cells and lithium storage units, water splitting powered by solar cells/metal-air batteries. Energy systems have progressed from individual and independent ones towards integrated ones for large-scale applications. Brown and Sheen in 1962⁷⁷, proposed the “*self-powered*” concept to eliminate the need for external power supplies, after which several pioneer breakthroughs have been reported. Such as self-powered electrochemical applications including the production of green H_2 , electro-oxidation reactions, etc. have been practiced using triboelectric/piezoelectric nanogenerators or batteries. One successful example of self-powered systems includes the integration of electrocatalytic water splitting with Zn-air batteries, nanogenerators, thermoelectric and solar cells to produce green H_2 using water.⁷⁸ And for that reason, the elimination of the use of any external power supply to power NH_3 production could be stimulating (Figure 1-11b).

1-10 Zn-air battery as a power source

Utilization of high-power density rechargeable metal-air batteries (MAB) for electrochemical ammonia synthesis⁷⁹ would be a game-changing strategy. Strikingly, the MABs provide about 2-10 folds higher theoretical energy density than that of commercial lithium-ion batteries. Integration of MAB in electrochemical NH_3 production will also provide cumulative efficiency compared to individual devices. Metal-air batteries can store and generate electricity thru redox reactions between the metal anode and oxygen from external air at the cathode. In addition, the exploitation of free and lavish air (O_2) as the reactant at the cathode endows lighter weight and lesser cost of the MABs. In particular, Zinc-air batteries (ZABs) demonstrate potent ability since Zn as a metal anode has

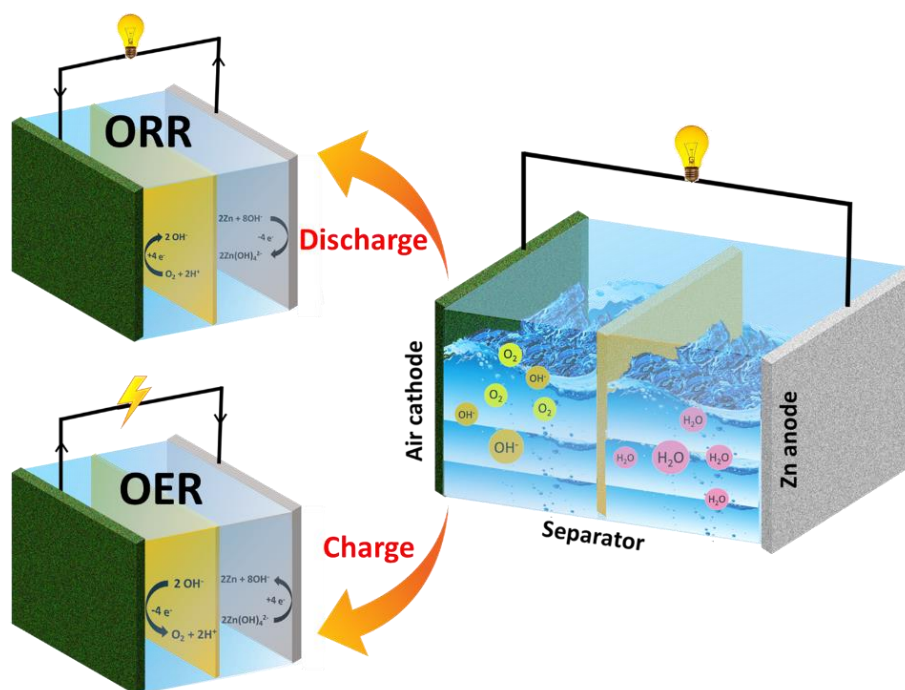


Figure 1-12. (a) Schematic representation of Zn-air battery assembled with Zn anode and air cathode showing charging and discharging process at air cathode.

several advantages over other counterparts such as less corrosion than Aluminium (Al), low cost, abundant reserve in earth's crust, low equilibrium potential, environmental benignity, safety and a long shelf-life.

More interestingly, ZABs can deliver a high theoretical energy density (*ca.* 1216 W h kg⁻¹) and high cell voltage (1.65 V), and thus can be a potential candidate to integrate with ammonia synthesis and eliminate the need for external power supply. ZABs were first reported by Smee in 1840, which entered the market as a century-old technology for application in hearing aid devices. Later in 2012, the first commercial rechargeable ZAB was produced by NantEnergy with an unsatisfactory energy density of just 35 W h kg⁻¹. And so, the research is ongoing to increase the energy density of the rechargeable ZABs. ZABs are constructed using four components, namely the Zn metal anode, air cathode, separator and electrolyte using aqueous alkaline solutions (KOH/NaOH). The reactions involved during the operation of ZAB are summarized as follows;

Zn electrode reaction:**Air electrode reaction:****Overall reaction:**

During discharging, the Zn anode undergoes oxidation and releases Zn^{2+} ions, where e^- travel through the external circuit towards the cathode side. At the cathode the diffusion of O_2 from the air towards the electrode takes place via the gas diffusion layer where its electro-reduction to OH^- is observed i.e. ORR takes place. These OH^- groups pass through the separator to form $\text{Zn}(\text{OH})_4^{2-}$ followed by ZnO formation. Whereas, during charging in rechargeable ZAB, the OER occurs (Figure 1-12). Although the strategy of utilizing ZAB as a power source to conduct overall ammonia synthesis is interesting but at the same time it is very challenging. It is because of several disadvantages allied with ZABs such as drying out of the electrolyte, inadequate performance of air electrodes, water flooding and CO_2 contamination of electrolyte which leads to the deterioration of the battery.⁸⁰ Amongst these, the degradation of air cathodes during consecutive cycling due to the sluggish multielectron ORR-OER process remains a major disadvantage.⁸⁰ The ZAB performance is highly affected by the electrocatalysts applied at the air cathode since the overpotential at the Zn anode is relatively smaller than that at the air cathode reason being the sluggish kinetics of both ORR and OER. For this reason, the research is focused on how to minimize the large overpotential at air cathode reaction by the development of efficient electrocatalysts. The benchmark catalysts for ORR and OER are different, because of the difference in their fundamental mechanisms and different binding energies of the reaction intermediates involved in the rate determining step of individual processes. The precious metal-based catalyst *i.e.* Pt/C can reduce oxygen effectively but is not an optimal catalyst for OER. Instead, $\text{RuO}_2/\text{IrO}_2$ is the benchmark catalyst for OER

but exhibits poor activity for ORR.^{81, 82} Nonetheless, the practical applicability of these devices in commercial markets is still obstructed by the expensive nature of state-of-art catalysts involved, scarcity of the same and poor kinetics for both ORR and OER due to 4 e⁻ transfer. In addition to it, employing two different catalysts at the air cathode increases the complexity, and material processing costs of the battery. For that reason, a groundbreaking approach is necessary to design and develop an oxygen bifunctional catalyst for high-performance ZABs.

1-11 Development of trifunctional catalysts

To accomplish the aforementioned provisions *i.e.* “ZAB powered ammonia synthesis”, the major task is to design and develop extremely competent and robust catalysts active towards NRR and oxygen electrocatalysis *viz.* ORR and OER for ZAB (Figure 1-13).⁸³ However, the existing noble-metal-based state-of-art catalysts for individual reactions are expensive, scarce and put forward poor kinetics and stability, which obstruct their real-time application. This obliges the development of a cost-effective non-noble metal-based electrocatalyst with

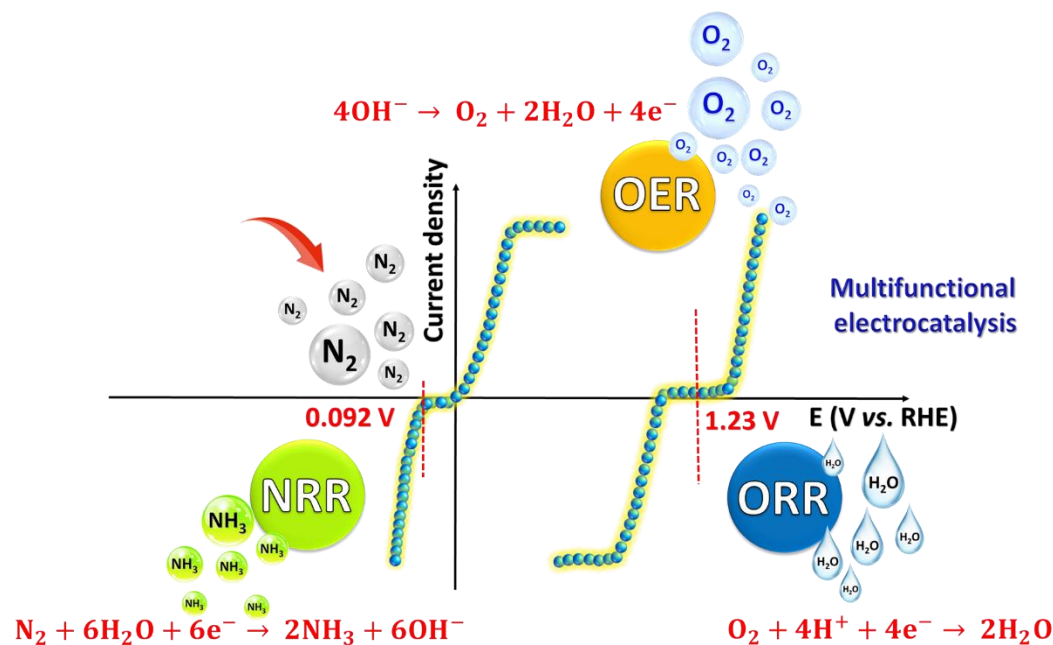


Figure 1-13. Schematic representation of multifunctional electrocatalysis with activity towards NRR, OER and ORR.

trifunctional activity holding the potential to compete or even surpass the activity of benchmark catalysts.^{84,85} Without a doubt, the designing of such a catalyst with plentiful active sites and stability towards three different reactions with completely different fundamental mechanisms is very complicated but the need of the hour.^{86,87,88,89} In the last part of this thesis, we have eliminated the dependence over external power supply to power ammonia synthesis and utilized ZAB as the power source. A trifunctional catalyst active towards NRR, ORR and OER has been designed which can achieve high activity and stability for the self-powered ammonia synthesis system.

1-12 Overall aim and objectives

The present thesis is intended for green NH_3 production via an electrochemical pathway and eliminating the need for an external power supply for ammonia synthesis by integrating Zn-air batteries with NH_3 production devices. This will hit two targets with one arrow *i.e.* achieving two Sustainable Development Goals proposed by United Nations including “Goal 2: Zero Hunger” and “Goal 13: Climate change”. To achieve these goals, the development of novel and efficient electrocatalysts with well-defined morphology is carried out in this thesis via controlled and cost-effective synthesis procedures. The primary objective was to design catalysts for cathodic half-cell reaction during overall ammonia synthesis *viz.* NRR. In order to realize the high activity towards NRR, HER suppression was taken under consideration. Besides, the tuning of morphology towards NRR activity was kept constant during the design of every catalyst. Morphology was tuned by altering the reaction time, temperature, precursor ratio, addition of surfactant and even by changing the synthetic route. All the synthetic procedures adopted here were cost-effective and simplified, amid which the sonochemical synthesis stood out the most owing to its energy efficiency, low time-consuming approach and appropriate control over the morphology.

In the present thesis, the Ag_3PO_4 catalyst was reported with a facile one-pot complexation strategy using trisodium citrate as a complexing agent. The

morphology was tuned by varying the reaction time which resulted into cuboidal-like Ag_3PO_4 particles when the reaction time fixed at 2 h. The choice of Ag as a metal and alkaline electrolyte was based on the HER suppression under applied experimental conditions to preferentially adsorb N_2 molecule. Whilst the inorganic phosphate moiety enhanced the stability of Ag under alkaline environments. Also, the NRR activity of silver phosphate was further improved by incorporation of a secondary metal like vanadium to yield an $\text{Ag}_2\text{VO}_2\text{PO}_4$ catalyst. Since the morphology-dependent activity was observed for Ag_3PO_4 , so we utilized a green, energy-efficient, less time-consuming sonochemical approach to synthesize the same material in a reduced time duration with a well-defined rice-grain-like morphology that too with a narrow particle size. As expected the activity towards NRR was improved and the stability was also retained. The synthesized catalysts demonstrated promising activity, high durability and reliable ammonia production towards NRR. Here, Ag-phosphates were presented as a new class of electrocatalysts which showed impressive morphology-dependent NRR activity and selectivity towards NH_3 which were not explored in this field.

Although, Ag metal is relatively less expensive than other precious metals and reveals low sensitivity towards H^+ adsorption, its low geographical distribution and expensive nature over earth abundant metals demand the development of cost-effective and more sustainable catalysts for NRR. And therefore we have also designed and explored transition metal-based composite and heteroatoms containing carbon catalysts for NRR. Firstly, the B, N-containing carbon catalyst was synthesized via a two-step synthesis procedure where the pyrolysis of Zinc imidazole borate-IL composite (ZIB-IL) at an optimal temperature of 600 °C ensued the formation B, N containing carbon with nanotubular morphology. This is the very first report where the MOF-IL composite was used to synthesize dual heteroatom-containing carbon with nanotubular morphology at a low pyrolysis temperature and explored towards NRR. The catalyst exhibited a high NRR activity in neutral media where the BN bond was predicted to be an active site by experimental and theoretical investigations. Afterwards, a new and underexplored

class of catalysts *i.e.* transition metals borides (TMBs) were explored to serve the same purpose. We have synthesized Ni_4B_3 composite via sonochemical reduction method using cheap precursors and modified the structure of same by addition of a less-HER sensitive metal *i.e.* Cu to improve the selectivity of catalyst towards NRR. The maximum activity was witnessed in acidic media with high durability for the optimal configuration of Cu- Ni_4B_3 (Cu:Ni molar ratio; 1:2) catalyst with grape bunch-like morphology plus pH-universal activity was also exposed. This is the first report where earth-abundant TMBs modified with Cu metal have been explored for NRR and were able to achieve an activity very close to the practical expectations.

In the second part of our thesis, we have aimed at overall ammonia synthesis and elimination of external power supply to realize ammonia production. The first target was achieved by the development of bifunctional catalysts for overall ammonia synthesis which couples NRR at the cathode with OER at the anode. Since both the half-cell reactions involve different fundamental mechanisms, so the catalyst active towards NRR might not be as efficient towards OER. And employing two different catalysts on either side would result in increased complexity, high material processing costs and low efficiency of the overall device. Henceforth, a NRR-OER bifunctional catalyst may open a boulevard of opportunities to overcome these drawbacks and improve the efficiency of the ammonia synthesis device. The Ni_xB_y catalyst has been synthesized via the sonochemical reduction method and then investigated towards NRR-OER bifunctional electrocatalysis which could realize an exceptionally high performance with an impressive NH_3 production yield rate and F.E. of around 49% which is the closest to the targets proposed by US DOE (~50%) in alkaline solutions. In addition to it, the sluggish kinetics of OER at the anode and the requirement of precious metal-based benchmark catalysts for maximum efficiency prompted us to look for an alternate anode reaction with more kinetic and thermodynamic feasibility. We have replaced the OER with “Methanol oxidation reaction” (MOR) owing to its better kinetics and thermodynamic feasibility over

OER. A theoretical voltage of 1.1 V could be saved upon replacing OER with MOR and the production of formic acid/formate ion could be realized at the anode in addition to NH_3 at the cathode. We have designed a $\text{Co}_2\text{P}_2\text{O}_7$ catalyst synthesized by means of surfactant-assisted sonochemical approach to yield a microflower-like morphology assembled from thin and uniform stacked nanosheets. As hypothesized, around 0.2 V of energy could be saved using NRR-MOR coupled ammonia synthesis device along with the production of formic acid due to partial oxidation of MeOH at anode. The development of a bifunctional catalyst for NRR-MOR coupled ammonia synthesis has not been reported earlier and thus could be of great significance in the field of electrochemical ammonia synthesis under practical full-cell conditions. Followed by which, the last goal of this thesis was to realize self-powered ammonia synthesis without the use of any external power source. Zn-air batteries can be integrated with overall ammonia synthesis to exercise the same. In order to practice ZAB-powered ammonia synthesis, an electrocatalyst with trifunctional activity towards NRR, ORR and OER is essential. For ZAB, oxygen bifunctional catalysts (ORR-OER) are required to improve the performance since ORR and OER take place during discharge and charge at air cathode. For ammonia synthesis, NRR-OER bifunctional catalyst is significant and so designing a trifunctional catalyst with activity towards NRR, ORR and OER will put forward a less expensive and less complex system. A single catalyst can be employed as an air cathode in ZABs and the same catalyst can be utilized to perform NRR-OER coupled ammonia synthesis. In the present thesis, a trifunctional Co_2B catalyst was reported with a one-step sonochemical reduction approach to synthesize porous nanosheet like amorphous Co_2B (1:8) with optimized metal to boron ratio. The as-synthesized catalyst was explored for practical application in ZABs and self-powered ammonia synthesis. A high activity with an exceptionally high ammonia yield rate of $1.08 \text{ mg h}^{-1} \text{ mg}_{\text{cat}}^{-1}$ was perceived after 2 h of electrolysis at 1.8 V for Co_2B (1:8) equipped NRR-OER ammonia synthesis device when powered by two Co_2B -based ZABs connected in series. There are just two reports in the literature which explore self-powered ammonia

synthesis in which one report doesn't involve a trifunctional catalyst while the other put forward a high voltage requirement and inferior ammonia yield rate. Therefore, this work designated a remarkable trifunctional activity towards ZAB powered ammonia synthesis which is rarely reported in the literature.

The future advancements in overall ammonia synthesis and self-powered ammonia synthesis by designing novel and efficient multifunctional electrocatalysts would be of great interest. We believe that the strategies adopted in this thesis and the new classes of potential catalysts for ammonia synthesis would definitely offer a broad scope for the future commercialization of green NH_3 by electrocatalytic methods under aqueous conditions.

1-13 References

1. U. N. D. o. Economic and P. D. Social Affairs, 2022.
2. A. Endo, *The Water-Energy-Food Nexus: Human-Environmental Security in the Asia-Pacific Ring of Fire*, 2018, 3-17.
3. U. N. D. o. Economic and S. Affairs, *The Sustainable Development Goals: Report 2022*, UN, 2022.
4. F. IFAD and UNICEF, *The state of food security and nutrition in the world: Transforming food systems for affordable healthy diets. Rome, FAO*, 2020.
5. R. Ferroukhi, D. Nagpal, A. Lopez-Peña, T. Hodges, R. H. Mohtar, B. Daher, S. Mohtar and M. Keulertz, *IRENA, Abu Dhabi*, 2015, 1-125.
6. IEA (2014), *World Energy Outlook 2014*, IEA, Paris. <https://www.iea.org/reports/world-energy-outlook-2014>.
7. J. Rodríguez-Varela, I. L. Alonso-Lemus, O. Savadogo and K. Palaniswamy, *J. Mater. Res.*, 2021, **36**, 4071-4083.
8. R. S. A. Usmani, A. Saeed, A. M. Abdullahi, T. R. Pillai, N. Z. Jhanjhi and I. A. T. Hashem, *Air Quality, Atmosphere & Health*, 2020, **13**, 1093-1118.
9. National Park Service. U.S. Department of the Interior. <https://www.nps.gov/subjects/air/sources.htm>
10. J. Hansen, R. Ruedy, M. Sato and K. Lo, *Global temperature trends*, 2005.
11. E. Kalnay, M. Kanamitsu, R. Kistler, W. Collins, D. Deaven, L. Gandin, M. Iredell, S. Saha, G. White and J. Woollen, *Bull. Am. Meteorol. Soc.*, 1996, **77**, 437-472.
12. K. Vohra, A. Vodonos, J. Schwartz, E. A. Marais, M. P. Sulprizio and L. J. Mickley, *Environ. Res.*, 2021, **195**, 110754.
13. I. Dincer, *Renew. Sustain. Energy Rev.*, 2000, **4**, 157-175.
14. H. Chen, Y. Shi, M. Xu and X. Zhao, *Resour. Policy*, 2022, **77**, 102680.
15. <https://www.sciencefacts.net/types-of-renewable-energy.html>
16. IEA (2021), *Net Zero by 2050*, IEA, Paris. <https://www.iea.org/reports/net-zero-by-2050>.
17. A. Brooks, *Renewable Energy Resource Assessment Information for the United States*, EERE Publication and Product Library, Washington, DC (United States), 2022.
18. <https://www.statista.com/chart/20524/renewable-energy-growth-in-america/> (U.S. Energy Information Administration).
19. I. E. Agency, *Ammonia Technology Roadmap: Towards More Sustainable Nitrogen Fertiliser Production*, OECD Publishing, 2021.

20. D. Kharade, Oil & Gas Analyst at GlobalData. <https://www.globaldata.com/media/press-release/indias-ammonia-capacity-is-expected-to-witness-double-digit-growth-over-the-next-six-years-says-globaldata/>. <https://www.globaldata.com/store/report/ammonia-market-analysis/>.
21. A. I. Amhamed, S. Shuibul Qarnain, S. Hewlett, A. Sodiq, Y. Abdellatif, R. J. Isaifan and O. F. Alrebei, *Fuels*, 2022, **3**, 408-435.
22. P. Heffer, A. Gruère and T. Roberts, *Sci. Data*, 2022, **1**, 9.
23. R. Lan, J. T. Irvine and S. Tao, *Int. J. Hydrogen Energy*, 2012, **37**, 1482-1494.
24. A. Afif, N. Radenahmad, Q. Cheok, S. Shams, J. H. Kim and A. K. Azad, *Renew. Sustain. Energy Rev.*, 2016, **60**, 822-835.
25. W. Avery, *Int. J. Hydrogen Energy*, 1988, **13**, 761-773.
26. H. Davy, *Philos. Trans. Royal Soc.*, 1807, 1-56.
27. G. Leigh, in *Catalysts for nitrogen fixation*, Springer, 2004, pp. 33-54.
28. J. G. Reuvers, J. R. Brightling and D. T. Sheldon, Ammonia Technology Development from Haber-Bosch to Current Times, Proceeding 747, International Fertiliser Society, Colchester, UK, 2014.
29. M. Hattori, S. Iijima, T. Nakao, H. Hosono and M. Hara, *Nat. Commun.*, 2020, **11**, 2001.
30. A. Liu, Y. Yang, X. Ren, Q. Zhao, M. Gao, W. Guan, F. Meng, L. Gao, Q. Yang and T. Ma, *ChemSusChem*, 2020, **13**, 3766.
31. W. David, *Policy Briefing*, The Royal Society, 2020.
32. J. G. Chen, R. M. Crooks, L. C. Seefeldt, K. L. Bren, R. M. Bullock, M. Y. Darensbourg, P. L. Holland, B. Hoffman, M. J. Janik, A. K. Jones, M. G. Kanatzidis, P. King, K. M. Lancaster, S. V. Lyman, P. Pfromm, W. F. Schneider and R. R. Schrock, *Science*, 2018, **360**, eaar6611.
33. S. Giddey, S. Badwal and A. Kulkarni, *Int. J. Hydrogen Energy*, 2013, **38**, 14576-14594.
34. H. Huang, L. Xia, X. Shi, A. M. Asiri and X. Sun, *Chem. Commun.*, 2018, **54**, 11427-11430.
35. C. Du, Y. Gao, J. Wang and W. Chen, *Chem. Commun.*, 2019, **55**, 12801-12804.
36. R. Cai and S. D. Minter, *ACS Energy Lett.*, 2018, **3**, 2736-2742.
37. W. Li, W. Fang, C. Wu, K. N. Dinh, H. Ren, L. Zhao, C. Liu and Q. Yan, *J. Mater. Chem. A*, 2020, **8**, 3658-3666.
38. S. L. Foster, S. I. P. Bakovic, R. D. Duda, S. Maheshwari, R. D. Milton, S. D. Minter, M. J. Janik, J. N. Renner and L. F. Greenlee, *Nat. Catal.*, 2018, **1**, 490-500.
39. C. Doornkamp and V. Poncet, *J. Mol. Catal. A Chem.*, 2000, **162**, 19-32.
40. X. Chen, Y. Guo, X. Du, Y. Zeng, J. Chu, C. Gong, J. Huang, C. Fan, X. Wang and J. Xiong, *Adv. Energy Mater.*, 2020, **10**, 1903172.
41. Z. Yan, H. Liu, Z. Hao, M. Yu, X. Chen and J. Chen, *Chem. Sci.*, 2020, **11**, 10614-10625.
42. K. Zhang, R. Guo, F. Pang, J. He and W. Zhang, *ACS Sustain. Chem. Eng.*, 2019, **7**, 10214-10220.
43. Q. Qin, T. Heil, M. Antonietti and M. Oschatz, *Small Methods*, 2018, **2**, 1800202.
44. Y. Abghoui, A. L. Garden, V. F. Hlynsson, S. Björgvinsdóttir, H. Ólafsdóttir and E. Skúlason, *Phys. Chem. Chem. Phys.*, 2015, **17**, 4909-4918.
45. A. Shilov, *Russ. Chem. Bull.*, 2003, **52**, 2555-2562.
46. A. J. Medford, A. Vojvodic, J. S. Hummelshøj, J. Voss, F. Abild-Pedersen, F. Studt, T. Bligaard, A. Nilsson and J. K. Nørskov, *J. Catal.*, 2015, **328**, 36-42.
47. G. Qing, R. Ghazfar, S. T. Jackowski, F. Habibzadeh, M. M. Ashtiani, C.-P. Chen, M. R. Smith III and T. W. Hamann, *Chem. Rev.*, 2020, **12**, 5437-5516.
48. C. Tang and S.-Z. Qiao, *Chem. Soc. Rev.*, 2019, **48**, 3166-3180.
49. B. H. Suryanto, H.-L. Du, D. Wang, J. Chen, A. N. Simonov and D. R. MacFarlane, *Nat. Catal.*, 2019, **2**, 290-296.
50. C. Tang and S.-Z. Qiao, *Joule*, 2019, **3**, 1573-1575.
51. S. Z. Andersen, V. Čolić, S. Yang, J. A. Schwalbe, A. C. Nielander, J. M. McEnaney, K. Enemark-Rasmussen, J. G. Baker, A. R. Singh and B. A. Rohr, *Nature*, 2019, **570**, 504-508.

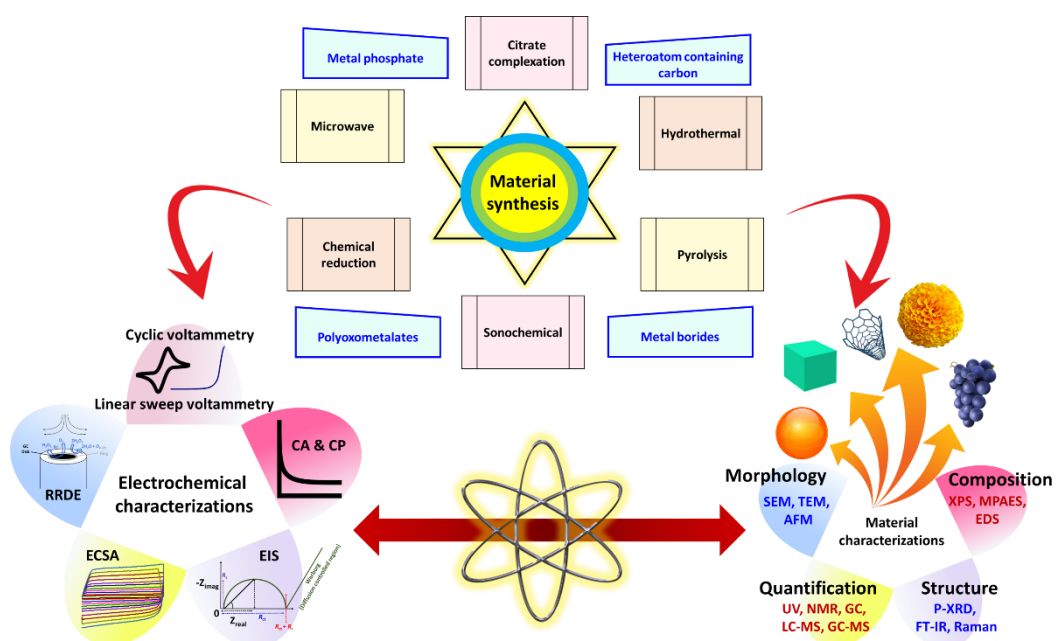
52. J. Choi, H.-L. Du, C. K. Nguyen, B. H. Suryanto, A. N. Simonov and D. R. MacFarlane, *ACS Energy Lett.*, 2020, **5**, 2095-2097.
53. S. E. Saji, H. Lu, Z. Lu, A. Carroll and Z. Yin, *Small Methods*, 2021, **5**, 2000694.
54. J. B. Spinelli, L. P. Kelley and M. C. Haigis, *Sci. Rep.*, 2017, **7**, 1-8.
55. H. Wroblowa, *J. Electroanal. Chem.*, 1964, **7**, 428-451.
56. Z. W. Seh, J. Kibsgaard, C. F. Dickens, I. Chorkendorff, J. K. Nørskov and T. F. Jaramillo, *Science*, 2017, **355**, eaad4998.
57. Y. Yao, S. Zhu, H. Wang, H. Li and M. Shao, *J. Am. Chem. Soc.*, 2018, **140**, 1496-1501.
58. X. Zhao, F. Yin, N. Liu, G. Li, T. Fan and B. Chen, *J. Mater. Sci.*, 2017, **52**, 10175-10185.
59. V. S. Marakatti and E. M. Gaigneaux, *ChemCatChem*, 2020, **12**, 5838-5857.
60. T. Wu, W. Fan, Y. Zhang and F. Zhang, *Mater. Today Phys.*, 2021, **16**, 100310.
61. D. Gupta, A. Kafle, S. Kaur, P. Parimita Mohanty, T. Das, S. Chakraborty, R. Ahuja and T. C. Nagaiah, *J. Mater. Chem. A*, 2022, **10**, 20616-20625.
62. Q. Zhang, Y. Shen, Y. Hou, L. Yang, B. Chen, Z. Lei and W. Zhang, *Electrochim. Acta*, 2019, **321**, 134691.
63. M. Nazemi, S. R. Panikkanvalappil and M. A. El-Sayed, *Nano Energy*, 2018, **49**, 316-323.
64. Z. Wang, Y. Li, H. Yu, Y. Xu, H. Xue, X. Li, H. Wang and L. Wang, *ChemSusChem*, 2018, **11**, 3480-3485.
65. Z. Jiang, W. Lu, Z. Li, K. H. Ho, X. Li, X. Jiao and D. Chen, *J. Mater. Chem. A*, 2014, **2**, 8603-8606.
66. S. Zhao, X. Lu, L. Wang, J. Gale and R. Amal, *Adv. Mater.*, 2019, **31**, 1805367.
67. L. Dai, *Acc. Chem. Res.*, 2013, **46**, 31-42.
68. H. Wang, L. Wang, Q. Wang, S. Ye, W. Sun, Y. Shao, Z. Jiang, Q. Qiao, Y. Zhu and P. Song, *Angew. Chem. Int. Ed.*, 2018, **57**, 12360-12364.
69. C. Lv, Y. Qian, C. Yan, Y. Ding, Y. Liu, G. Chen and G. Yu, *Angew. Chem. Int. Ed.*, 2018, **57**, 10246-10250.
70. W. Qiu, X.-Y. Xie, J. Qiu, W.-H. Fang, R. Liang, X. Ren, X. Ji, G. Cui, A. M. Asiri and G. Cui, *Nat. Commun.*, 2018, **9**, 1-8.
71. S. Xiao, F. Luo, H. Hu and Z. Yang, *Chem. Commun.*, 2020, **56**, 446-449.
72. M. G. Chourashiya and A. Urakawa, *J. Mater. Chem. A*, 2017, **5**, 4774-4778.
73. J.-T. Ren, L. Chen, Y. Liu and Z.-Y. Yuan, *J. Mater. Chem. A*, 2021, **9**, 11370-11380.
74. D. Farrusseng and A. Tuel, *Encapsulated Catal.*, 2017, 335-386.
75. P. Fornasiero and M. Cargnello, *Morphological, Compositional, and Shape Control of Materials for Catalysis*, Elsevier, 2017.
76. F. Gutiérrez-Martín, L. Amodio and M. Pagano, *Int. J. Hydrogen Energy*, 2021, **46**, 29038-29048.
77. D. Brown and E. Sheen, *Health Phys.*, 1963, **9**, 511-521.
78. P. Liu, D. Gao, W. Xiao, L. Ma, K. Sun, P. Xi, D. Xue and J. Wang, *Adv. Funct. Mater.*, 2018, **28**, 1706928.
79. C. Zhao, S. Zhang, M. Han, X. Zhang, Y. Liu, W. Li, C. Chen, G. Wang, H. Zhang and H. Zhao, *ACS Energy Lett.*, 2019, **4**, 377-383.
80. Z. Zhao, X. Fan, J. Ding, W. Hu, C. Zhong and J. Lu, *ACS Energy Lett.*, 2019, **4**, 2259-2270.
81. C. Su, T. Yang, W. Zhou, W. Wang, X. Xu and Z. Shao, *J. Mater. Chem. A*, 2016, **4**, 4516-4524.
82. Y. Gorlin and T. F. Jaramillo, *J. Am. Chem. Soc.*, 2010, **132**, 13612-13614.
83. X. Yang, K. Li, D. Cheng, W.-L. Pang, J. Lv, X. Chen, H.-Y. Zang, X.-L. Wu, H.-Q. Tan and Y.-H. Wang, *J. Mater. Chem. A*, 2018, **6**, 7762-7769.
84. G. Fenya, L. Hongwei, Z. Mengzhe, X. Zhengqi, Z. Yueqing and L. Tingting, *Prog. Chem.*, 2020, **32**, 33.
85. K. Zeng, X. Zheng, C. Li, J. Yan, J. H. Tian, C. Jin, P. Strasser and R. Yang, *Adv. Funct. Mater.*, 2020, **30**, 2000503.
86. Z. Lu, J. Wang, S. Huang, Y. Hou, Y. Li, Y. Zhao, S. Mu, J. Zhang and Y. Zhao, *Nano Energy*, 2017, **42**, 334-340.

Chapter 1

87. S. Ghosh and R. N. Basu, *Nanoscale*, 2018, **10**, 11241-11280.
88. T. Meng, J. Qin, S. Wang, D. Zhao, B. Mao and M. Cao, *J. Mater. Chem. A*, 2017, **5**, 7001-7014.
89. J. Yang, X. Wang, B. Li, L. Ma, L. Shi, Y. Xiong and H. Xu, *Adv. Funct. Mater.*, 2017, **27**, 1606497.

Chapter 2

Material design, characterization and instrumentation techniques



2-1 Synthetic approach

Materials synthesis refers to the fabrication of different materials involving processes such as solution-phase chemistry, polymerization techniques and vapor deposition techniques. Incessant advancements in material synthesis and characterization techniques have presented plentiful means to explore various classes of materials for different applications. In this thesis different materials have been synthesized using simple and facile techniques such as complexation route using a complexing agent, microwave route, hydrothermal approach, chemical and sonochemical reduction methods and high temperature pyrolysis, which are described as follows.

2-1.1 Citrate-complexation method: This synthesis route implicates the use of citrate moiety which can form complexes with metal ions involving adsorption mechanism so that the transition metal ions could be firmly anchored in the precursor structure.^{1, 2} Thus formed metal-citrate complex can be used as a precursor to synthesize metal composites with different inorganic moieties. This method can control the nucleation rate and growth of targeted metal composites via Ostwald ripening process and control the final morphology of the material by varying the reaction conditions such as reaction time, temperature, etc. We have utilized this synthetic method to synthesize metal phosphate complex which is discussed in Chapter 3A.³

2-1.2 Hydrothermal method: Hydrothermal synthesis is one of the standard and important techniques for preparation of various nanomaterials with highly crystalline and powdery nanostructure using water as a primary solvent. This method is extremely prevalent towards controlling the morphology and purity of the product as compared to other conventional methods.⁴ The synthesis is usually performed in a pressurized sealed stainless steel vessel lined with Teflon, known as “autoclave” which can control the temperature as well as pressure. An aqueous mixture of precursors is transferred into an autoclave which enables the synthesis of a crystalline nanostructure upon heating at a specific temperature, time and

autogenous pressure. We have utilized the hydrothermal synthesis to design a variety of precursors as well as final targeted composites in Chapter 3B, 4A and 5A respectively.^{5, 6}

2-1.3 High temperature pyrolysis: Pyrolysis is the process which involves the chemical decomposition of a solid or a liquid into smaller volatile molecules upon heating at high temperatures (400–1000 °C).⁷ It differs from other processes like combustion and hydrolysis since it is carried out under an inert atmosphere *i.e.* in absence of oxygen (O₂, in combustion) or water (in hydrolysis). In this thesis, high temperature pyrolysis is utilized to synthesize heteroatom containing carbon using metal organic framework (MOF) as the novel precursors. This synthetic approach is discussed in detail in Chapter 4A for the synthesis of dual-heteroatom containing carbon.^{6, 8}

2-1.4 Chemical reduction method: It is a traditional method for nanoparticles synthesis which involves the reduction of metal ions by reducing agents where in

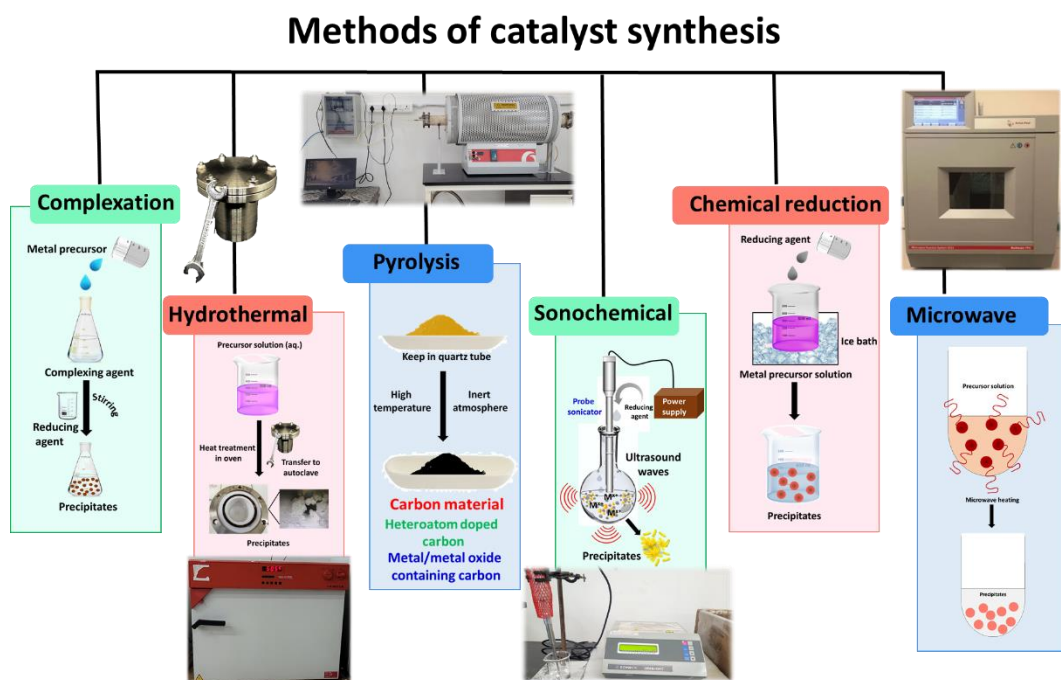


Figure 2-1. Schematic representation of synthetic routes involved for catalyst synthesis.

the size, morphology and other properties can be controlled by using capping agents, surfactants, etc.⁹ The chemical reduction method consists of different stages, initially the metal precursors are dissolved in a suitable solvent to which a reducing agent is added for the reduction of metal ions at first stage of nucleation. The reduced metal ions then combine with other metal ions to form stable nuclei for further growth of nanoparticles. The chemical reduction method is used in Chapter 5A for the synthesis of Ni_xB_y catalyst using Ni^{2+} precursor ions with sodium borohydride as a reducing agent in water solvent.

2-1.5 Sonochemical method: Sonochemistry is a well-defined technique for the fabrication of nanomaterials in which molecules undergo chemical reaction due to the application of powerful ultrasound radiation (20 kHz–10 MHz). The sonochemical synthesis is at the heart of green chemistry as it is an energy efficient alternative to the conventional synthetic methods due to its several advantages such as reduced reaction times, higher yields, lower costs, and mild conditions.¹⁰⁻¹² The reaction conditions and precursor compositions can be varied during sonochemical synthesis to produce a myriad of nanostructured materials with controlled morphologies, structures, and compositions. A nonlinear acoustic phenomena *viz.* acoustic cavitation is involved which can be divided into three distinct stages: (i) formation, (ii) growth and (iii) implosive collapse of bubbles. The sonochemical approach for the synthesis of mono and bimetallic phosphates, metal borides is presented in Chapter 3B, 4B, 5 and 6 respectively, in which the effect of surfactant during sonochemical synthesis is also discussed in Chapter 5B.^{5, 13} The sonochemical synthesis was performed using Sonics Vibra cell instrument with a Ti based horn.

2-1.6 Microwave (MW) method: MW-assisted synthesis has become a robust and efficient technique in the field of green synthetic chemistry which works on the principle of alignment or orientation of molecules by the external electrical field produced by homogeneous microwave electromagnetic radiations which results in the production of internal heat and simultaneously reduce the reaction processing

time and energy required for synthesis.^{14, 15} It can be carried out using standard organic solvents either under open- or sealed-vessel conditions. We have employed the microwave synthesis approach for the synthesis of ionic liquids in Chapter 4A respectively using Anton Paar Multiwave PRO Microwave Reaction System.^{6, 8}

2-2 Material characterization

2-2.1 Electron microscopy: Electron microscopy (EM) is a technique for obtaining high resolution images ranging from manifold bacteria to complex structures of materials, electron microscopy allows us to unravel all the mysteries about the structure, morphology, and composition. The high resolution of EM images results from the use of electrons as the source of illuminating radiation which allows to have a higher resolving power than optical microscopes. A stream of high voltage electrons (usually 5-100 KeV) is emitted by the electron source and accelerated in a vacuum toward the specimen through monochromator using electromagnetic lenses.^{16, 17}

2-2.1.1 Scanning electron microscopy and field emission scanning electron microscopy: The scanning electron microscope (SEM) produces image by scanning the sample with a focused beam of high-energy electrons. When the electron beam hits the surface of the sample, it penetrates the sample to a depth of a few microns, depending on the accelerating voltage and the density of the sample and then produce secondary electrons (produce SEM images), backscattered electrons (determine crystal structures and orientations of minerals), and characteristic X-rays (for elemental analysis via energy dispersive spectroscopy, EDS). It divulges the information about the sample including external morphology (texture), chemical composition, and crystalline structure and orientation of materials making up the sample.¹⁷ Areas ranging from approximately 1 cm to 5 microns in width can be imaged in a scanning mode using conventional SEM techniques (magnification ranging from 20x to approximately 30,000x, spatial resolution of 50 to 100 nm). SEM measurements were carried out using a JEOL,

JSM-6610LV instrument equipped with a thermionic gun as the electron source and EDS was executed via Oxford, INCAx-act, 51-ADD0013 instrument.

On the other hand, a field emission scanning electron microscopy (FESEM) provides topographical and elemental information at a magnifications of 10x to 300000x with resolved, less electrostatically distorted images compared to conventional SEM. In this study, FE-SEM measurements were performed by using CARL ZEISS, ULTRA PLUS and Hitachi, Japan, SU8010 instruments.

2-2.1.2 Transmission electron microscopy and high-resolution transmission electron microscopy: In transmission electron microscopic (TEM) technique, monochromatic beam of electrons is accelerated through a potential of 40 to 100 kV and passed through a strong electromagnetic field. The resolution of a TEM is about 0.2 nanometers (nm). The high energy beam of electrons from the electron gun is focused into a small, thin specimen by the use of the condenser lens after which the parts of beam are transmitted depending upon the thickness and electron transparency of the specimen. The transmitted electrons are focused by objective lens to an image over phosphor screen and passed through the intermediate and projector lenses to obtain an enlarged image in a 2D plane, rather than producing 3D images like in SEM.¹⁸ The TEM can be utilized to observe crystal structure, defects, dislocations, elemental composition, etc. The TEM data were recorded with the help of TEM, JEM 2100, JEOL instrument for the synthesized catalysts.

The high-resolution transmission electron microscopy (HRTEM) uses both the transmitted and the scattered beams to create an interference image. HRTEM is identical to TEM imaging except that the magnifications used are high enough to easily see the lattice spacing of inorganic materials. The HR-TEM data for materials synthesized in this thesis were acquired from the FEI Tecnai (G2 F20) and JEOL, JEM 2100 OLUS instruments operated at 200 keV.

2-2.2 Powder X-ray diffraction: Powder X-ray diffraction (P-XRD) technique is a rapid analytical technique used for structural phase identification of a material.¹⁹ When the filament is heated in a cathode ray tube to produce electrons and further

accelerating the electrons towards a specimen target on application of a voltage, X-rays are generated. The interaction of the incident rays with the target sample leads to constructive interference when Bragg's Law ($n\lambda=2d \sin \theta$) is satisfied and a peak is appeared on the screen after a detector records and processes this X-ray signal/ Copper is the most common target material for single-crystal diffraction, with Cu- K_{α} radiation = 1.5418Å. PANalytical X'Pert Pro diffractometer was utilized to obtain the diffraction patterns of catalysts in this study under the 2θ range of 5-80° at a scan speed of 2° per minute using Cu- K_{α} radiation ($\lambda = 0.1542$ nm, 40 kV, 40 mA). The reference patterns for comparison were obtained from different sources including Inorganic Crystal Structure Database (ICSD) and Joint Committee on Powder Diffraction Standards (JCPDS).

2-2.3 Fourier transformation Infrared spectroscopy: Fourier transformation Infrared (FT-IR) spectroscopy is a technique used to identify the functional groups present in organic and inorganic compounds by measuring their absorption of infrared radiation over a range of wavelengths due to atomic vibrations of a molecule.²⁰ A blackbody source emits IR radiation typically between 4000 and 400 cm^{-1} which then passes through an interferometer to the specimen. An interferogram is recorded consisting of the detector signal as a function of time. The corresponding absorbance spectrum is obtained from a Fourier transform (a mathematical transformation from the time to the frequency domain) of the interferogram. In this study, all the FT-IR spectra were recorded in the range of 600–4000 cm^{-1} using BRUKER TENSOR-27 spectrometer with a spectral resolution of 4 cm^{-1} and number of scans equals to 100. FT-IR data was collected and analyzed by OPUS software.

2-2.4 Raman spectroscopy: Raman spectroscopy is based on the principle of Raman scattering which is defined as the scattering of photons by excited molecules at higher energy levels *i.e.* Raman effect.²¹ When the photons are inelastically scattered by change in the kinetic energy of an incident particle, either Stokes or anti-Stokes lines are observed. Raman spectroscopy observes the shift in

vibration of a functional group from an incident source. Raman spectroscopy was used to relate the electrocatalytic activity with the degree of disorder present using a LabRAM HR Evolution Raman spectrometer (Horiba Scientific). Raman spectra were obtained using a laser of 633 nm as an excitation source in the range of 200-2500 cm^{-1} .

2-2.5 CHNS-O elemental analysis: CHNS-O elemental analysis is a technique based on combustion of organic materials which can determine the amount of carbon (C), hydrogen (H), nitrogen (N), sulfur (S) and oxygen (O) present in a sample. It is a reliable and cost-effective technique used to assess the purity and chemical composition of compounds and can be used on a wide range of different sample types including solid, liquid, volatile and viscous substances. Upon combustion of C, H, N, S, O elements in the material, the gases are generated (e.g. CO_2 , H_2O , NO_2 , etc.) and measured using gas chromatography to determine the ratio of the elements in the original sample via Thermal conductivity detector(TCD). C, H, N and S can all be determined simultaneously whereas O may be analyzed in a second step by pyrolysis. In this work, the amount of C, H, N and O elements in the carbonaceous materials were examined by using CHNS-O CHNS-O elemental analyzer by Thermo Scientific FLASH 2000 model using Elemental analyzer software (Figure 2-2).



Figure 2-2. Image showing the CHNS-O elemental analyzer by Thermo Scientific used for CHNS-O measurements.

2-2.6 BET surface area analysis: Brunauer-Emmett-Teller (BET) surface area analysis method is applied to measure the specific surface area ($\text{m}^2 \text{g}^{-1}$) of target compound (porous and non-porous) via nitrogen adsorption isotherm measurements at 77 K under a relative pressure range from 0.05 to 0.3 and is based on the principle of mono and multilayer adsorption of gas molecules. Moreover, BET analysis can also be applied to measure pore volume and pore size distribution via capillary condensation in pores of the target material. The gas sorption measurements were performed in this study to measure the BET surface area, pore size and volume of the catalysts especially the MOF and carbonaceous materials using a BELSORP MAX (BEL JAPAN) volumetric adsorption analyzer at different temperatures. Ultrapure (99.995%) N_2 gas was used for the adsorption measurements at 77 K temperature. Prior to the adsorption measurement, the sample was ground into a fine powder, evacuated at 393 K for 24 h and purged with ultrapure nitrogen gas on cooling.

2-2.7 Microwave plasma atomic emission spectroscopy: MP-AES is an atomic emission technique which consists of a microwave induced plasma (a high temperature source) interfaced to an atomic emission spectrophotometer (AES) and is used for multi-analyte determination of major and minor elements within a range of ppm to weight percent. It is based on the principle that if once an atom of a specific element is excited, it returns back to the ground state by emitting light in a characteristic pattern of wavelengths.²² The Agilent 4200 instrument was used to detect the amount of different metals present in the catalysts synthesized in this thesis and also to detect the leaching or dissolution of metal species in the electrolyte after electrocatalysis.

2-2.8 Water contact angle: Water contact angle is a measure of wettability of the solid to measure the hydrophobic or hydrophilic properties of the same.^{23, 24} In this study, the water contact angle (WCA) experiments were performed with a First Ten Angstroms (FTA) Contact Angle System using the sessile water drop method at ambient temperature, wherein water was used as a probe liquid in a 0.6 μL volume

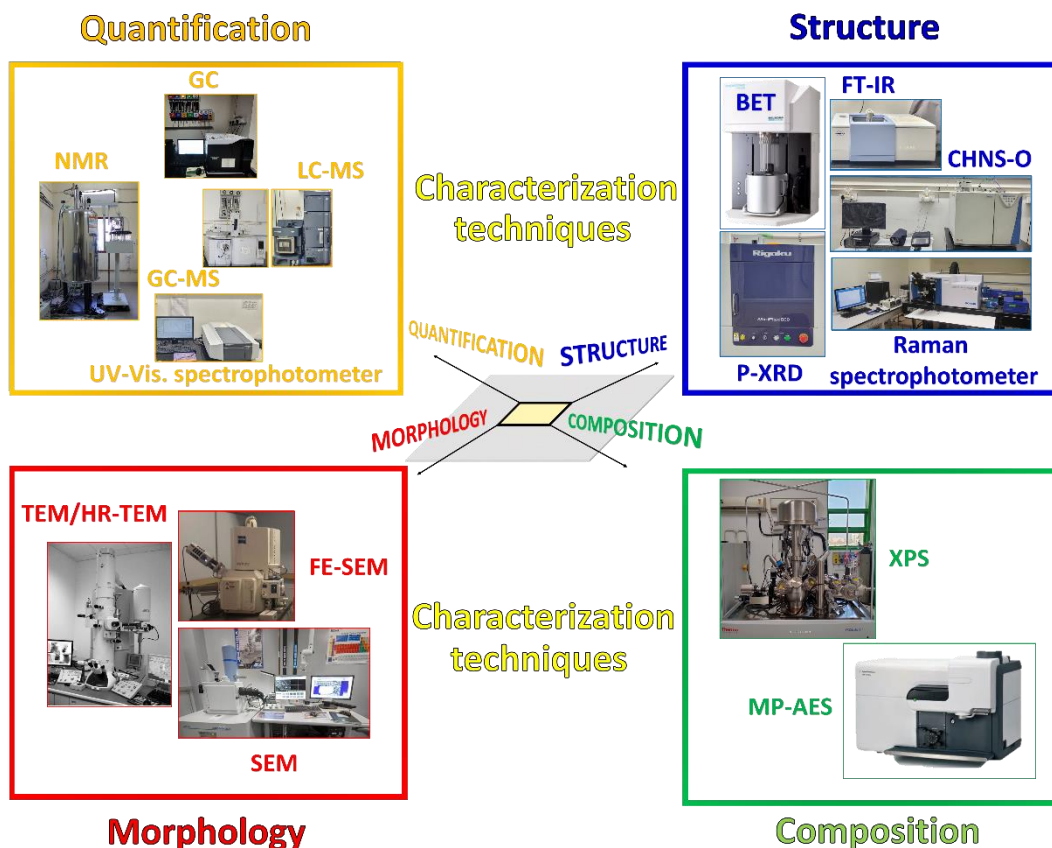


Figure 2-3. Schematic representation of the techniques used for the characterizations of the synthesized materials.

from a 0.305 mm width needle, and the average WCA (θ H₂O) was determined for the different samples. Homogeneous suspension of catalyst (1 mg) mixed with isopropanol (20 μ L) was drop-casted onto the glass slide followed by drying at room temperature. Water drops were deposited with the help of sessile water syringe.

2-2.9 UV-Vis spectroscopy: UV-Vis spectroscopy is an analytical method to measure the wavelengths associated with the maximum absorbance (λ_{\max}) of an analyte under UV or visible light which are absorbed by or transmitted through a sample.²⁵ A light beam from a visible and/or UV light source is separated by a prism or diffraction grating into the relative wavelengths and a monochromator splits it into two equal intensity beams by a half-mirrored device. Electronic

detectors are used to measure the intensities of the light beams where the intensity of reference and sample beam is defined as I_0 and I respectively.²⁶ The ultraviolet (UV) region scanned is normally from 200 to 400 nm, and the visible portion is from 400 to 800 nm. It can be utilized for quantitative measurements based on Beer Lambert's Law;

$$A = \log \frac{I_0}{I} = \epsilon cl \quad (2.1)$$

Where, A is measured absorbance, I_0 denotes the intensity of the incident radiation, I is intensity of transmitted radiation, l describes the path length, c is the concentration of the absorbing species and ϵ stands for extinction coefficient. These measurements were carried out with the UV-Vis spectrophotometer (SEC2000-DH and Shimadzu UV-2600) by taking a typical quartz cuvette (5 ml). In this thesis the UV-Vis spectroscopic technique is widely explored for the analysis of product as well as probable impurities during the course of electrolysis which are briefly described in section 2-3.

2-2.10 ^1H -nuclear magnetic resonance spectroscopy: Nuclear Magnetic Resonance (NMR) technique is a powerful analytical tool to identify the types of nuclei, chemical groups present in a molecule, their binding environment and the chemical structure of compound.^{27, 28} It is based on the principle that under a magnetic field, the nuclei of the molecule resonate at specific frequencies (chemical shift) which are characteristic of their chemical environment. The corresponding peak area acquired in the NMR spectrum can also be utilized for the quantitative analysis based on the peak intensities. In this thesis, NMR is utilized to identify the ammonium yield produced after NRR using NMR 400 MHz, JEOL JNM-ECS-400 and analysis was performed using MestReNova software.

2-2.11 Liquid chromatography-mass spectroscopy: This is an analytical tool to separate, identify and quantify the unknown and known compounds especially small molecules along with their structural and chemical analysis with high sensitivity and selectivity. It is based on the principle of separation of the

components in a mixture followed by its ionization based on their mass/charge ratio. The separated ions are then directed to a photo or electron multiplier tube detector for analysis and quantification of each ion.²⁹ LC-MS technique has been exploited here in for the quantitative estimation of ammonia using HRMS, Waters YEA955.

2-2.12 Gas chromatography and gas chromatography-mass spectroscopy: Gas chromatography (GC) is a separation technique which can separate the chemical components of a sample mixture followed by their determination based on the retention time. However, to identify the unknown compounds, mass spectroscopy (MS) is beneficial which measures the mass-to-charge ratio (m/z) of charged particles and then give the molecular weight and elemental composition of the compound. The mass spectra can identify the compound and the chromatogram can be used for qualitative and quantitative analysis.³⁰ Here in, the GC analysis was performed to detect H_2 and O_2 products after HER and OER while the GC-MS technique was used to determine the trace N_2O amount in commercial gas-supplies viz. N_2 and Ar. The GC analysis was done using Shimadzu GC-2030 instrument with N_2 carrier gas while GC-MS analysis was acquired via Shimadzu QP-2010NC (Ultra) model with He as carrier gas (Figure 2-4).

2-2.13 X-ray photoelectron spectroscopy: X-ray photoelectron spectroscopy (XPS) is a surface-sensitive spectroscopic technique for the chemical analysis of compounds based on the principle of photoelectric effect. It can be used for

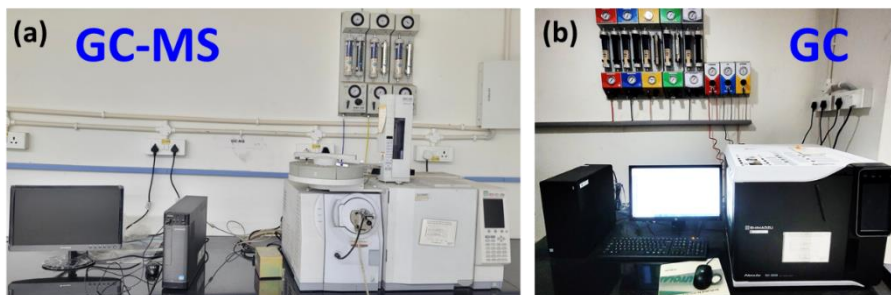


Figure 2-4. Image showing the (a) GC-MS and (b) GC instruments used for quantitative analysis of gaseous products like O_2 , H_2 , CO_2 and N_2O .

qualitative and quantitative estimation of the elemental composition and chemical states by means of peak heights or peak areas and peak positions respectively. The analysis involves the irradiation of sample using monoenergetic soft X-rays such as Mg K α (1253.6 eV) or Al K α (1486.6 eV) with limited penetrating power of 1-10 μm , which upon interaction with surface atoms cause the emission of electrons via photoelectric effect. This is a surface technique since the mean free path of electrons in solids is very small and the electrons can originate from only top few atomic layers. The analysis is done from the plot of number of detected electrons per energy interval versus their kinetic energy.³¹ All the catalytic materials synthesized in this study have been characterized using XPS technique before and after electrocatalysis. XPS measurements were performed with the Thermo scientific NEXSA surface analysis with a micro-focused (400 μm , 72 W, 12000 V) monochromatic Al K α (1486.6 eV) a hemispherical analyser and 128 channel plate detectors under ultrahigh vacuum (UHV 8-10 mbar). The obtained spectra were calibrated with C 1s spectra.

2-3 Electrochemical measurements

2-3.1 Voltammetry

2-3.1.1 Cyclic voltammetry: Cyclic voltammetry (CV) is an electrochemical technique commonly employed to examine the reduction and oxidation processes and measure the current response of a redox active species with respect to cycled potential sweep.³² The potential is swept at a fixed scan rate during the analysis where the faster scan rates result into a thin diffusion layer and therefore give high current response (Figure 2-5). For electrochemically reversible electron transfer processes, the current exhibit a linear relationship with the square root of the scan rate according to the Randles-Sevcik equation (Equation 2.2).

$$I_p = 2.69 \times 10^5 n^{\frac{3}{2}} \nu^{1/2} D^{1/2} A c \quad (2.2)$$

Where, I_p (A) is the peak current, n denotes the number of electrons transferred in a redox reaction, ν (V s^{-1}) is the scan rate, D ($\text{cm}^2 \text{s}^{-1}$) is the diffusion coefficient, A

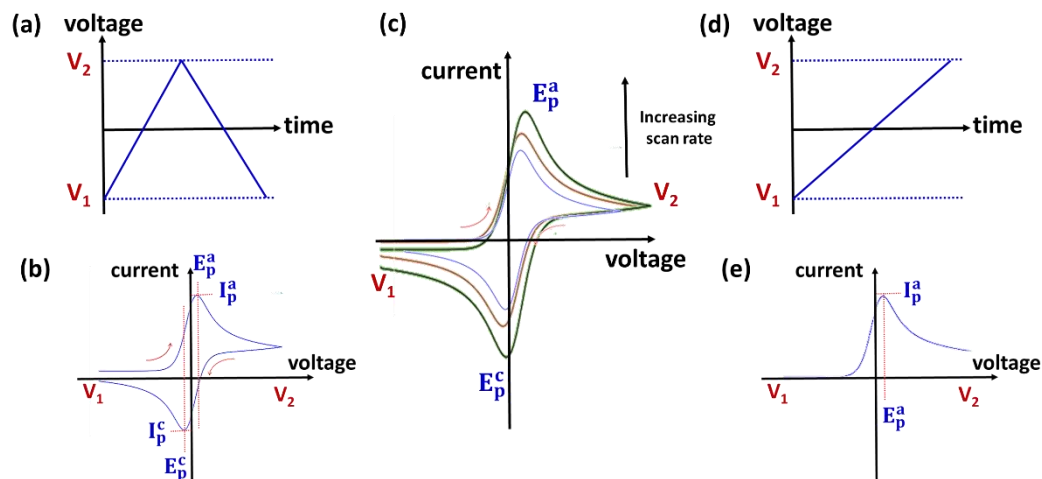


Figure 2-5. (a) A typical representation of triangular waveform during cyclic voltammetry and (b) cyclic voltammogram of a reversible redox system, (c) effect of increasing scan rate on current in cyclic voltammogram, (d) triangular waveform during linear sweep voltammetry and (e) a typical linear sweep voltammogram.

(cm^2) is the area of electrode and c (mol cm^{-3}) is the bulk concentration of analyte.

2-3.1.2 Linear sweep voltammetry: Linear sweep voltammetry (LSV) is equivalent to a one-segment CV measurement where the working electrode potential is swept and current is measured as a function of time (Figure 2-5). Cyclic voltammetry is very similar to LSV. The only difference is that in CV the voltage is swept between two values (V_1 and V_2), however when the voltage reaches V_2 , the scan is reversed and the voltage is swept back to V_1 .³³

2-3.2 Rotating disc electrode & rotating ring disc electrode: Rotating disc electrode & rotating ring disc electrode (RDE & RRDE). RDE is a hydrodynamic (convective-diffusion) electrode method to elucidate the reaction mechanisms in which very rapid and high precision analysis can be made due to the steady-state diffusion where double-layer charging current approaches zero. The reversal techniques are not available with RDE since the products formed are swept away from the surface while the addition of a ring surrounding the disc can provide information equivalent to the reversal techniques at stationary electrodes. The



Figure 2-6. (a) Image representing the RRDE setup connected to Autolab 302 N potentiostat during ORR measurement under hydrodynamic conditions controlled by Pine rotator and (b) schematic representation of RRDE mechanism over rotating-ring disc electrode during ORR.

currents measured at ring can give an idea about what might be occurring at disc electrode, e.g. during oxygen reduction at disc, the ring is held at the oxidation potential of intermediate (typically H_2O_2) and thus the ring current can tell about the ORR pathway as well as the % H_2O_2 produced (Figure 2-6). In this thesis, RRDE and RDE techniques are explored to test the efficacy of catalysts towards oxygen reduction reaction (ORR).³⁴

2-3.3 Electrochemical impedance spectroscopy: Electrochemical impedance spectroscopy (EIS) is a powerful steady-state technique used for the analysis of interactions occurring at the electrode-electrolyte interface e.g., redox species-electrode interactions which includes the concentration of electroactive species, charge-transfer, and mass-transfer from the bulk solution to the electrode surface in addition to the resistance of the electrolyte.^{35, 36} It is characterized by electric circuit where the impedance is measured in ohms. A small signal excitation is applied to measure impedance over a range of applied frequency, from less than 1 mHz to greater than 1 MHz using a potentiostat. Impedance can be divided into a real (Z_{real}) and imaginary part (Z_{imag}) plotted on X-axis and Y-axis respectively to represent a Nyquist plot where the right side of the plot designates low frequency while the left side depicts the higher frequency region. In a three-electrode system,

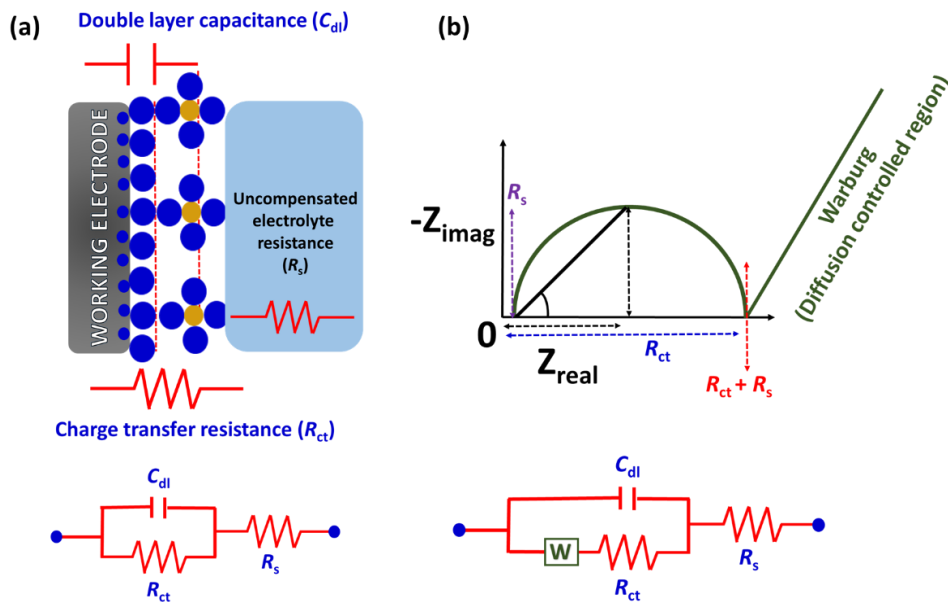


Figure 2-7. (a) Schematic showing the principle of EIS and (b) Nyquist plots acquired after EIS along with their respective circuit diagrams.

an EIS experiments were conducted at a constant applied voltage and the semicircular behavior is witnessed from the Nyquist plot out of which the produced solution resistance (R_s), charge transfer resistance (R_{ct}), and Warburg impedance (W) are collected (Figure 2-7). In this study, a fixed DC potential was applied for different catalysts over an AC perturbation of 10 mV with logarithmic frequency step over a single sine wave for the various frequency in the logarithmic steps. The solution resistance (R_s) was obtained from the point of intersection of the semicircle at the high frequency real axis whereas the polarization resistance (R_p) at the low frequency near the electrode-electrolyte interface. The charge transfer resistance (R_{ct}) was calculated by subtracting the R_s from R_p .

2-3.4 Electrochemical surface area: The electrochemical surface area (ECSA) is a significant descriptor to compare the activity of electrocatalysts during electrochemical reactions. It represents the area of the electrode/catalyst material that is accessible to the electrolyte and is used for charge transfer and/or storage. The more the electrochemically active surface area, the more is the electrocatalytic

performance. In this thesis, the ECSA was determined by calculating the double-layer pseudo capacitance (C_{dl}) in electrolyte. Cyclic voltammograms were recorded in the non-faradaic region at various scan rates from 10 to 320 mV s⁻¹. The resulting pseudo-capacitance was determined as the slope of both anodic and cathodic averaged out current density $\{(I_a+I_c)/2$; ' I_a ' denotes anodic current and ' I_c ' is for cathodic current) at a fixed potential. ECSA was calculated by dividing the obtained C_{dl} with the specific capacitance of the flat standard surface (20-60 $\mu\text{F cm}^{-2}$), which in the present study was considered to be 40 $\mu\text{F cm}^{-2}$. The roughness factor (R_f) was determined by dividing the obtained ECSA with geometrical surface area.³⁷

2-3.5 Chronoamperometry and Chronopotentiometry: Chronoamperometry (CA) is a technique where the potential of the working electrode is held constant and current response is measured as a function of time ($I = f(t)$). On the other hand, in Chronopotentiometry (CP), a current is applied to the electrode and maintained while the changes in potential response are monitored with respect to time ($E = f(t)$). If the potential is stepped from the point where no current is flowing to the potential where electrode reaction is taking place and is diffusion limited, then the current flow will obey the Cottrell equation (Equation 2.3).

$$I(t) = \frac{nFAD_0^{\frac{1}{2}} C_0^*}{\pi^{1/2} t^{1/2}} \quad (2.3)$$

where, I (A) is the current, n represents the no. of electrons required to reduce/oxidize one molecule of analyte, F (96485 C mol⁻¹) stands for the Faraday constant, A (cm²) is the area of electrode, C_0 (mol cm⁻³) is the initial concentration of analyte, D_0 (cm² s⁻¹) is the diffusion coefficient of the species and t (s) stands for time.^{38, 39}

2-4 Detection and quantification of products/trace contaminants

2-4.1 Quantification of Ammonia

2-4.1.1 Indophenol blue method: The final product (*i.e.* NH_3) obtained after electrolysis can be quantified using indophenol blue method with the help of UV-Vis spectroscopy. Firstly, 2 mL of electrolyte sample (after 2 h of chronoamperometry) is collected from the cathodic compartment of H-cell in which 2 mL of solution containing mixture of 5% salicylic acid and 5% trisodium citrate in 1 M KOH is added immediately. Consequently, 1 mL of 0.05 M NaClO and 200 μL of 1% sodium nitroprusside as a colouring agent is added to the same electrolyte sample. The solution is incubated for 2 h to develop stable colour, and absorbance is measured at a wavelength of 655 nm.⁴⁰ The UV-vis spectrum is obtained for different concentrations of NH_3 (0.2, 0.4, 0.8, and 1 ppm) using standard NH_4Cl solution (Figure 2-8) to draw a calibration curve exhibiting a linear relationship between absorbance and concentration value from the fitting curve ($y = 0.285x + 0.109$, $R^2 = 0.99663$).

2-4.1.2 Nessler's reagent method: The preparation of Nessler's reagent is initiated by the addition of 2.5 g of mercuric iodide into 5 mL aq. solution of potassium iodide (2 g in 5 mL deionized water) followed by its dilution upto 20 mL using deionized water. To the above solution, 4 g of NaOH is added thereafter, denoted herein as Nessler's reagent. For quantification of produced ammonia, 5 mL of electrolyte solution obtained after electrolysis is collected to which 0.25 mL of sodium potassium tartrate (500 g L^{-1}) and 0.25 mL of Nessler's reagent is added. The above solution mixture is kept undisturbed for 10 minutes and then measurement was performed using UV-Vis. spectrophotometer at a wavelength (λ)

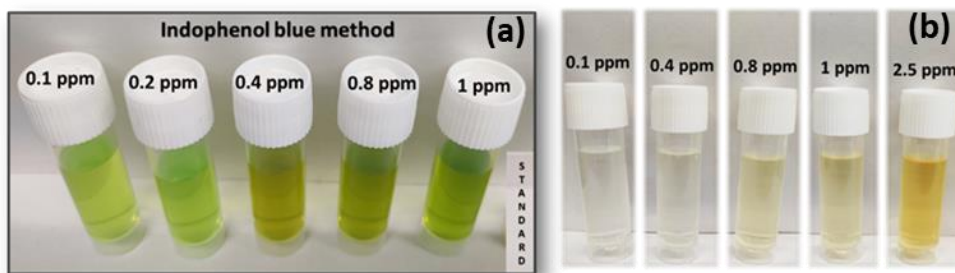


Figure 2-8. Image showing color development in standard NH_4^+ solutions after (a) Indophenol blue test and (b) Nessler's reagent test.

of 420 nm.⁴⁰ The calibration curve is extracted from the different standard NH_4Cl solutions (Figure 2-8) with known NH_4^+ concentrations in the range of 0.1, 0.4, 0.8, 1.0 and 2.5 ppm in a similar way.

2-4.1.3 ^1H -NMR spectroscopy: After NRR, 25 ml of the electrolyte is taken out and mixed with 1M HCl and then concentrated to 1 mL, from which 0.6 ml of the resulting liquid was taken and 0.4 ml of DMSO- d_6 is added as an internal standard. The produced ammonia is confirmed by using proton-nuclear magnetic resonance spectroscopy measurements (^1H NMR)⁴¹ with water gate suppression sequence and a relaxation delay of 3 s, 8000 scans using a pulse sequence by pulse field gradient (PFG) unit.

2-4.1.4 LC-MS: Briefly, 150 μL of phenol solution is mixed with 30 μL of sodium hypochlorite and sodium nitroprusside each. The above solution mixture is then added into 1.5 mL of the NH_4^+ containing standard and sample solution to generate Indophenol blue dye.⁴² After which 15 μL of 10 M HCl is added in order to convert the complex into Indophenol red, which can be extracted by addition of ethyl acetate (1.5 mL) from organic layer. The organic layer is separated from aqueous layer and ethyl acetate is completely evaporated, thereafter the indophenol red is re-dissolved in methanol for LC-MS.

2-4.2 Quantification of hydrazine

2-4.2.1 Watt-Chrisp method: Briefly, 0.3 g of p- $\text{C}_9\text{H}_{11}\text{NO}$ is mixed with 2 mL of HCl and 20 mL of ethanol to obtain the final colouring solution. A series of standard solutions of N_2H_4 (0.1, 0.2, 0.4, 0.8, and 1 ppm) are prepared and 2 mL of which is separately mixed with 2 mL of above prepared colouring solution. Afterwards, the solution is kept under incubation for 20 min. at R.T. to achieve stable color (Figure 2-9) and measure absorbance at a wavelength of 455 nm using UV-Vis spectrometer.⁴³ The as-obtained calibration curve), exhibit a good linear relationship ($y = 0.285 x + 0.109$, $R^2=0.99663$) between absorbance and N_2H_4 concentrations respectively.

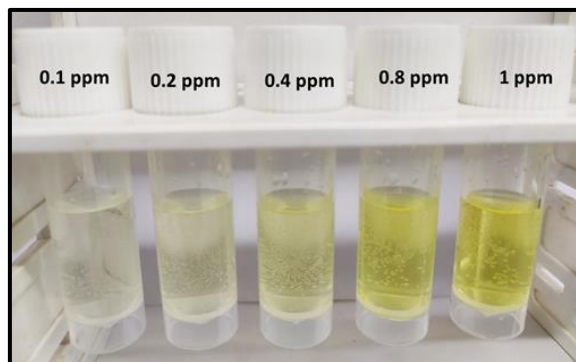


Figure 2-9. Image showing color development in standard N_2H_4 solutions after Watt-Chrisp quantification.

2-4.3 Quantification of hydrogen (H_2) and oxygen (O_2) by gas chromatography

(GC): Evolution of H_2 and O_2 at applied potentials can be detected quantitatively by means of a gas chromatograph (GC, SHIMADZU, GC-2030). A SHIMADZU Rt-Q-BOND column is installed in GC having two detectors, namely, a thermal conductivity detector (TCD) and a flame ionization detector (FID) to measure H_2/O_2 . The carrier gas used is N_2 .³ Below mentioned are the formulas used for quantification of produced gas.

$$\text{Yield rate (mmol mg}^{-1} \text{ h}^{-1}) = \frac{\text{yield (mmol)}}{t \text{ (h)} \times m_{\text{cat.}} \text{ (mg)}} \quad (2.4)$$

$$\text{Selectivity (\%)} = \frac{\text{Experimental} \times 100}{\text{Theoretical}} \quad (2.5)$$

2-4.4 Detection and quantification of trace NO_x and NH_4^+ impurities

2-4.4.1 Nitrate (NO_3^-) and nitrite (NO_2^-) ion determination: For determination of any trace amount of NO_3^- present in the electrolyte, UV-Vis. spectrophotometry is utilised wherein the peak at wavelength of 220 nm correspond to absorption of nitrates. Standard solutions can be prepared using NaNO_3 stock solution with varying concentrations *i.e.* 0.2 ppm to 5 ppm. Subsequently, 5 mL of standard along with sample solution are taken in glass vial to which 0.1 mL of 1 M HCl is added later on with recurrent shaking. The solution is kept undisturbed for 5 min. and UV-

Vis measurement is performed in the range of 200-300 nm from which the calibration curve is acquired.

Additionally, quantification of nitrites can be performed via diazotization reaction by using sulphanilamide under acidic environment followed by coupling with N-(1-Naphthyl) ethylenediamine dihydrochloride which result into formation of pink colored azo dyes with corresponding peak at 540 nm respectively. Initially, standard solutions are prepared using NaNO_2 stock solution with different concentrations *i.e.* 2 to $60 \mu\text{g L}^{-1}$. Afterwards, two reagents are prepared separately, 0.5 g of sulphanilamide in 50 mL of 2 M HCl *i.e.* **A** and 20 mg of N-(1-Naphthyl) ethylenediamine dihydrochloride in 20 mL of deionized H_2O *i.e.* **B**. Briefly, 5 mL of standard or sample solution are taken in glass vials followed by addition of 0.1 mL of A which is then allowed to stand for 10 min. Afterwards, 0.1 mL of B is added to above solution respectively.⁴⁴ The solution mixture is kept undisturbed for 30 min and amount of NO_2^- is estimated under wavelength range of 440-600 nm, from which calibration curves are extracted.

2-4.4.2 N_2O quantification by gas chromatography-mass spectroscopy (GC-MS): The trace N_2O is detected and quantified with the help of GC-MS in SIM (selected ion monitoring) mode by selecting the m/z value of 44 corresponding to N_2O . The parameters to acquire the data can be set with the column oven temperature of 40°C and an injection temperature of 150°C . The column flow is kept at 0.99 mL min^{-1} with an ion source temperature and interface temperature of 200°C and 220°C respectively. The obtained chromatograms are used to draw a calibration curve and calculate the amount of N_2O present in feeding gas-supplies.⁴⁵

2-5 Theoretical investigations

The computations in Chapter 4A are carried out by spin-restricted DFT method including Grimme dispersion corrections, as implemented in DFT code of DMol³ in Material Studio. The generalized gradient approximation with the Perdew-Burke-Ernzerhof functional is employed to describe exchange and correlation

effects. The double numerical plus polarization with addition of diffuse function (DNP+) is chosen as the basis set with all electron core treatment for all the calculations. A conductor-like screening model (COSMO) was used to simulate a H₂O solvent environment throughout the whole process. The adsorption energy (E_{ad}) is defined as:

$$E_{ad} = E_{sub+ads} - E_{sub} - E_{ads} \quad (2.6)$$

where $E_{sub+ads}$ is the total DFT energy of the optimized structure, E_{sub} and E_{ads} are the energies of the catalyst and adsorbate respectively. The Gibbs free energy (G) calculation of the intermediates were performed by using the concept of computational hydrogen electrode (CHE) model. In this method, the chemical potential of the H^+/e^- pair is related to $\frac{1}{2} H_2$ (g) at standard hydrogen electrode (SHE) conditions. The free energy G for each intermediate step can be determined as follows:

$$G = \Delta E - T\Delta S + \Delta ZPE + \Delta G_U \quad (2.7)$$

Where, ΔE , ΔZPE and ΔS are the the electronic energy difference, change in the zero-point energy (ZPE) and entropy change respectively. ZPE and vibrational entropy of adsorbed species are obtained after frequency calculations, and entropies of gas molecules (H_2 , N_2 , and NH_3) were taken from standard values. ΔG_U is the free energy contribution related to applied potential U , which can be determined as

$$\Delta G_U = -eU \quad (2.8)$$

While, in Chapter 6, the density functional theory (DFT) based electronic structure calculations have been executed using Vienna *ab-initio* simulation package (VASP) code throughout the theoretical investigation. The projector augmented-wave (PAW) formalism is used, while the exchange and correlation potential is described through generalized gradient approximation using Perdew-Burke-Ernzerhof (PBE) functional. The kinetic energy cut-off corresponding to the plane wave basis set has been used as 500 eV. All the surface configurations along

with the surface-adsorbate systems are fully relaxed while achieving the minimum-energy criteria until the Hellman-Feynman forces become less than 0.01 eV/\AA .⁴⁶⁻⁴⁹

2-6 Zn-O₂ battery assembly

A home-made Zn-air battery cell was utilized in Chapter 6 to assess the performance of designed catalysts as an air cathode. Air cathode consisted of catalyst layer (CL), nickel foam and gas diffusion layer (GDL) respectively. CL was fabricated using the designed catalyst in N-Methyl-2-pyrrolidone (NMP) solvent. Mixture of polyvinylidene fluoride (PVDF) and Vulcan carbon (VC) (1:1, ratio by weight) were dispersed in NMP after grinding to a fine powder. The dispersion was executed using ultrasonication for 30 min. in bath sonicator and catalyst slurry was coated onto the Ni foam substrate as GDL. On other side of Ni foam substrate, catalyst layer was coated followed by drying and pressing under the pressure of 2.5 MPa by hydraulic press (KBR PRESS 15 ton, Model: M 15). Finally, Zn-air battery was assembled with polished Zn foil (99.5%, extra pure) as the anode, 6 M KOH and 0.2 M Zn(ac)₂ as the electrolyte and prepared air cathode (geometric area of 0.1256 cm², catalyst loading of 2 mg cm⁻² in Chapter 6) in home-made cell setup. For a better comparison, Zn-air battery (Figure 2-10) was

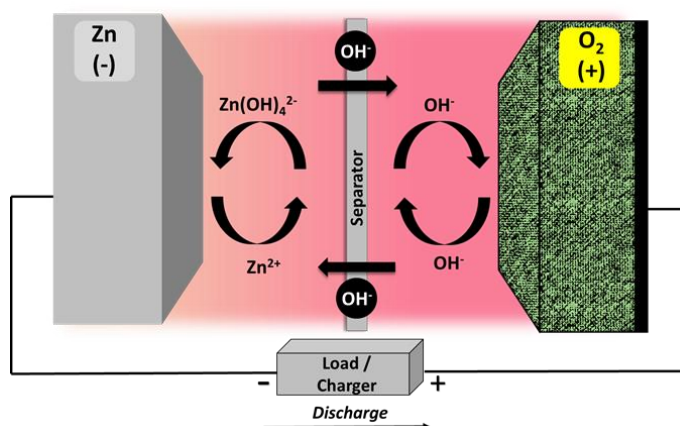


Figure 2-10. (a) Schematic showing the Zn-air battery operation and assembly with Zn anode, air cathode separated by a separator in 6 M KOH + 0.2 M Zn(ac)₂ electrolyte.

assembled using a mixture of commercial Pt/C (20%) and RuO₂ (1:1 ratio by weight) as catalyst layer.^{8, 50} All measurements were carried out under ambient conditions of temperature and pressure using Biologic VSP-300 Battery Cycler.

2-7 Basic terminology used in batteries^{51, 52}

2-7.1 Anode: An anode is a negative electrode and it's one of the essential parts of a battery. It is an oxidizing metal viz. Zn, Li, etc. which loses electrons which move along a conductor to the cathode causing an electrochemical reaction to occur which produces electricity. In this thesis, we have used Zn metal as an anode in Zn-air batteries.

2-7.2 Cathode: A cathode (positive electrode) is capable of gaining electrons i.e. reduction takes place upon receiving the electrons produced from the cathode. Metallic oxides such as copper oxide, lithium oxide, etc. are examples of cathode materials in battery. For this study, three air cathodes have been examined for activity in Zn-air batteries including PVIM-CoPOM/NCNT, Co₂B and the benchmark Pt/C+RuO₂ respectively.

2-7.3 Electrolyte: Both anode and cathode are submerged into an electrolyte, which is a substance that provide ions when dissolved in water or fluids. The electrolyte acts as a medium for transfer of electrical charge between the two terminals of battery in form of ions. The positively charged ions move towards the cathode through electrolyte while the negatively charged ions move towards the anode. 6 M KOH + 0.2 M Zn(ac)₂ has been used as an electrolyte in Zn-air batteries assembled in this work.

2-7.4 Separator: A separator is a porous membrane placed between anode and cathode whose main function is to prevent the electric contact of the electrodes and thus electrical short circuit of the battery. It also allows the rapid transfer of ions to complete the battery circuit. Separators are usually electronic insulators such as cellulose paper, cellophane, ion exchange membranes, polymers, etc. In this thesis, we have used Whatman separator (GE Heathcare, Life Sciences, GF/D 70 mm).

2-7.5 Open circuit voltage (OCV): It is the potential difference between the positive and negative terminals of the assembled cell when no current is flowing and the cell is at rest. The theoretical OCV of Zn-air battery is 1.65 V.

2-7.6 Specific capacity: It can be defined as the amount of electric charge which a material can deliver per gram of the material. It is represented by using the units of milli ampere hours per gram (mA h g^{-1}). The theoretical specific capacity of Zn-air battery is 820 mA h g^{-1} .

2-7.7 Power density: Power density is defined as the amount of power that can be produced per unit mass or volume i.e. it refers to how quickly a device can discharge the energy stored in it. It can be categorized into volumetric and gravimetric power density based on the amount of power supplied per unit volume (W cm^{-3}) and mass (W g^{-1}) respectively.

2-7.8 Energy density: Energy density can be defined as the amount of energy which can be produced per unit mass or volume. If a system has a high energy density then it is able to store a lot of energy in a small amount of mass. A high energy density does not necessarily mean a high power density. It is usually expressed in Watt hours per kilogram (W h kg^{-1}). The theoretical energy density of Zn-air battery is 1218 W h kg^{-1} (excluding O_2).

2-7.9 Cycling stability: It can be defined as the number of charging- or discharging-cycles (usually switching between @ 10 mA cm^{-2} for ORR and @ 10 mA cm^{-2} for OER in Zn-air battery) until its capacity is reduced to a certain amount, typically around 50-80%. This describes the lifetime of a battery and hence is a major descriptor for the commercialization of the same.

2-8 Calculations

F.E. for produced ammonia can be calculated using the formula mentioned below in equation 2.9:

$$\text{F. E. (\%)} = \frac{3 \times F \times V \times C_{\text{NH}_3}}{17 \times Q} \quad (2.9)$$

Rate of NH₃ produced is calculated using the formula given in equation 2.10:

$$\text{Yield rate } (\mu\text{g cm}^{-2} \text{ h}^{-1}) = \frac{V \times C_{\text{NH}_3}}{t \times m_{\text{cat}}} \quad (2.10)$$

Here, F is the Faraday constant, C_{NH3} is the concentration of NH₃ in the electrolyte solution, V is the volume of electrolyte taken in cathode compartment, t is the total time for electrolysis, and m_{cat.} is the amount of catalyst loaded on the WE.

Calculations for specific capacity in Zn-O₂ battery;

$$\text{Specific capacity} = \frac{\text{current} \times \text{discharge time}}{\text{weight of consumed zinc}} \quad (2.11)$$

The energy density for the same is calculated according to following equation:

$$\text{Energy density} = \frac{\text{current} \times \text{discharge time} \times \text{average discharge voltage}}{\text{weight of consumed zinc}} \quad (2.12)$$

TOF_{NRR} calculations for catalysts;

$$\text{Turnover frequency (TOF)} = \frac{\text{Turnover number (TON)}}{\text{Time (h)}} \quad (2.13)$$

$$\text{Turnover number (TON)} = \frac{\text{yield of NH}_3 \text{ obtained after NRR (mg)}}{\text{Loading of catalyst (mg)}} \quad (2.14)$$

Where, time (t in hours) represents the total NRR electrolysis duration.

2-9 References

1. L. Rezaee and M. Haghighi, *RSC Adv.*, 2016.
2. Q. Liang, W. Ma, Y. Shi, Z. Li and X. Yang, *CrystEngComm*, 2012, **14**, 2966-2973.
3. D. Gupta, A. Kafle, S. Kaur, P. Parimita Mohanty, T. Das, S. Chakraborty, R. Ahuja and T. C. Nagaiah, *J. Mater. Chem. A*, 2022, **10**, 20616-20625.
4. A. Rabenau, *Angew. Chem. Int. Ed.*, 1985, **24**, 1026-1040.
5. D. Gupta, A. Kafle and T. C. Nagaiah, *Faraday Discuss.*, 2023, DOI: 10.1039/D2FD00150K..

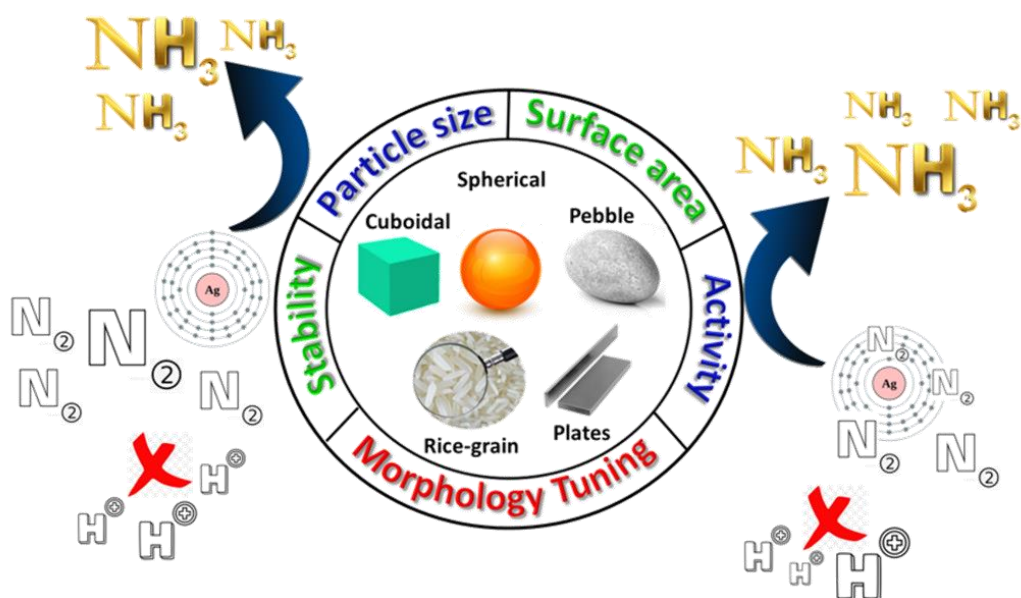
6. D. Gupta, A. Kafle, S. Kaur, T. S Thomas, D. Mandal and T. C. Nagaiah, *ACS Appl. Mater. Interfaces* 2023, **3**, 4033–4043.
7. M. Yang, H. Jin, Z. Sun and R. Gui, *J. Mater. Chem. A*, 2022.
8. T. C. Nagaiah, D. Gupta, S. D. Adhikary, A. Kafle and D. Mandal, *J. Mater. Chem. A*, 2021, **9**, 9228-9237.
9. A.-G. Niculescu, C. Chircov and A. M. Grumezescu, *Methods*, 2022, **199**, 16-27.
10. H. Xu, B. W. Zeiger and K. S. Suslick, *Chem. Soc. Rev.*, 2013, **42**, 2555-2567.
11. S. Anandan, G.-J. Lee and J. J. Wu, *Ultrason. Sonochem.*, 2012, **19**, 682-686.
12. K. S. Suslick, T. Hyeon and M. Fang, *Chem. Mater.*, 1996, **8**, 2172-2179.
13. D. Gupta, A. Kafle and T. C. Nagaiah, *Small*, 2023, 2208272.
14. G. A. Tompsett, W. C. Conner and K. S. Yngvesson, *ChemPhysChem*, 2006, **7**, 296-319.
15. M. Nüchter, B. Ondruschka, W. Bonrath and A. Gum, *Green Chem.*, 2004, **6**, 128-141.
16. R. F. Egerton, *Physical principles of electron microscopy*, Springer, 2005.
17. G. Van Tendeloo, S. Bals, S. Van Aert, J. Verbeeck and D. Van Dyck, *Adv. Mater.*, 2012, **24**, 5655-5675.
18. Z. L. Wang, *Adv. Mater.*, 2003, **15**, 1497-1514.
19. J. Epp, in *Materials characterization using nondestructive evaluation (NDE) methods*, Elsevier, 2016, pp. 81-124.
20. J. S. Gaffney, N. A. Marley and D. E. Jones, *Characterization of materials*, 2002, 1-33.
21. S. P. Mulvaney and C. D. Keating, *Anal. Chem.*, 2000, **72**, 145-158.
22. V. Balaram, *Microchem. J.*, 2020, **159**, 105483.
23. T. Chau, *Miner. Eng.*, 2009, **22**, 213-219.
24. A. Alghunaim, S. Kirdponpattara and B.-m. Z. Newby, *Powder Technol.*, 2016, **287**, 201-215.
25. M. Picollo, M. Aceto and T. Vitorino, *Phys. Sci. Rev.*, 2018, **4**, 20180008.
26. A. Klamt, *J. Phys. Chem.*, 1996, **100**, 3349-3353.
27. P. A. Bottomley, *Rev. Sci. Instrum.*, 1982, **53**, 1319-1337.
28. S. K. Bharti and R. Roy, *Trends Anal. Chem.*, 2012, **35**, 5-26.
29. M. Beccaria and D. Cabooter, *Analyst*, 2020, **145**, 1129-1157.
30. J.-F. Rontani, *Molecules*, 2022, **27**, 1629.
31. M. Seah, *Surf. Interface Anal.*, 1980, **2**, 222-239.
32. J. Heinze, *Angew. Chem. Int. Ed.*, 1984, **23**, 831-847.
33. L. Nadjo and J. Savéant, *J. Electroanal. Chem. Interfacial Electrochem.*, 1973, **48**, 113-145.
34. C. Du, Y. Sun, T. Shen, G. Yin and J. Zhang, *Rotating Electrode Methods and Oxygen Reduction Electrocatalysts*, 2014, 231-277.
35. H. S. Magar, R. Y. Hassan and A. Mulchandani, *Sensors*, 2021, **21**, 6578.
36. Z. He and F. Mansfeld, *Energy Environ. Sci.*, 2009, **2**, 215-219.
37. S. D. Adhikary, A. Tiwari, T. C. Nagaiah and D. Mandal, *ACS Appl. Mater. Interfaces*, 2018, **10**, 38872-38879.
38. N. Walker and J. E. Dick, *Analyst*, 2023, DOI: 10.1039/D3AN00107E..
39. Z. Jin, P. Li, Z. Fang and G. Yu, *Acc. Chem. Res.*, 2022, **55**, 759-769.
40. L. Zhang, X. Ji, X. Ren, Y. Ma, X. Shi, Z. Tian, A. M. Asiri, L. Chen, B. Tang and X. Sun, *Adv. Mater.*, 2018, **30**, 1800191.
41. A. C. Nielander, J. M. McEnaney, J. A. Schwalbe, J. G. Baker, S. J. Blair, L. Wang, J. G. Pelton, S. Z. Andersen, K. Enemark-Rasmussen and V. Colic, *ACS Catal.*, 2019, **9**, 5797-5802.
42. J. B. Spinelli, L. P. Kelley and M. C. Haigis, *Sci. Rep.*, 2017, **7**, 1-8.
43. Y. Zhao, R. Shi, X. Bian, C. Zhou, Y. Zhao, S. Zhang, F. Wu, G. I. Waterhouse, L. Z. Wu and C. H. Tung, *Adv. Sci.*, 2019, **6**, 1802109.
44. L. Li, C. Tang, D. Yao, Y. Zheng and S.-Z. Qiao, *ACS Energy Lett.*, 2019, **4**, 2111-2116.
45. J. Choi, B. H. Suryanto, D. Wang, H.-L. Du, R. Y. Hodgetts, F. M. Ferrero Vallana, D. R. MacFarlane and A. N. Simonov, *Nat. Commun.* 2020, **11**, 1-10.

Chapter 2

- 46. P. Hohenberg and W. Kohn, *Phys. Rev.*, 1964, **136**, B864.
- 47. W. Kohn and L. J. Sham, *Phys. Rev.*, 1965, **140**, A1133.
- 48. J. P. Perdew, K. Burke and M. Ernzerhof, *Phys. Rev. Lett.*, 1996, **77**, 3865.
- 49. H. J. Monkhorst and J. D. Pack, *Phys. Rev. B*, 1976, **13**, 5188.
- 50. X. X. Wang, X. Yang, H. Liu, T. Han, J. Hu, H. Li and G. Wu, *Small Structures*, 2022, **3**, 2100103.
- 51. D. Deng, *Energy Sci. Eng.*, 2015, **3**, 385-418.
- 52. M. Xu, D. Ivey, Z. Xie and W. Qu, *J. Power Sources*, 2015, **283**, 358-371.

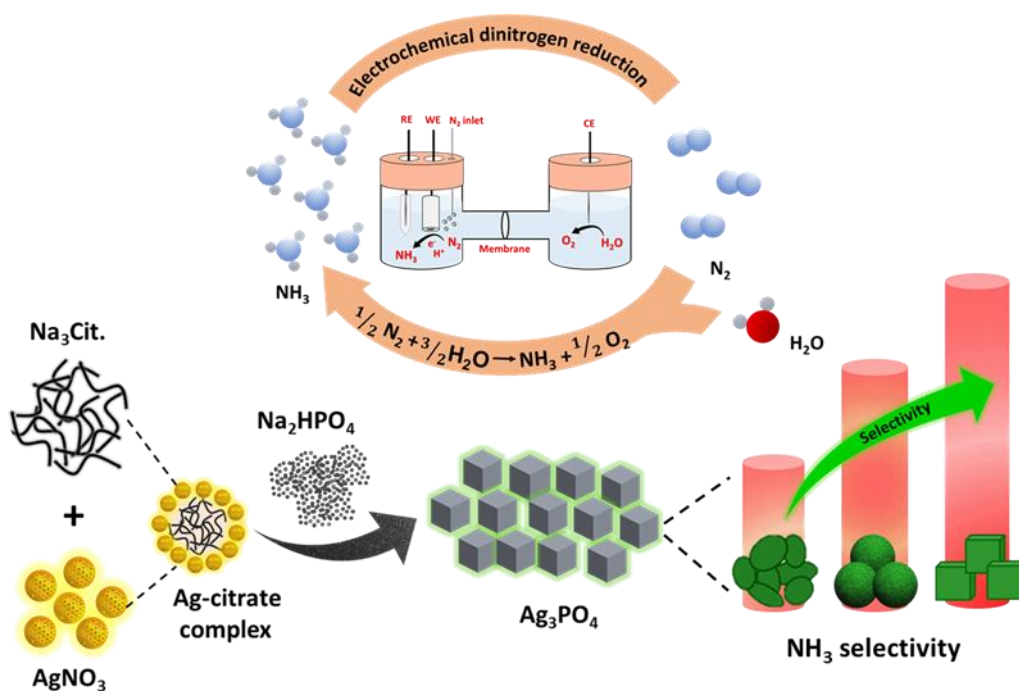
Chapter 3

Morphology dependent activity of noble metal based catalysts for electrochemical N_2 conversion to NH_3



Chapter 3A

High yield selective electrochemical conversion of N_2 to NH_3 via morphology controlled silver phosphate under ambient conditions



3A-1 Introduction

Nitrogen reduction to ammonia is essential due to its dynamic role in chemical industries and fertilizer production.^{1, 2} But, its industrial production via Haber–Bosch process leads to more than 1% and 3-5% of world's overall energy and natural gas consumption respectively along with the 2-3% of global carbon emissions.^{3,4} This demands a search for a green and viable substitute to conventional ammonia synthesis. In this regard, electrochemical energy conversion is a potential approach for clean ammonia production using renewable energy sources under ambient conditions.^{5, 6} However, the activation and electrochemical reduction of the N₂ molecule is difficult due to its high triple bond energy (941 kJ mol⁻¹) and band gap (10.82 eV), for which the development of an efficient electrocatalyst is crucial.^{7, 8}

In past decade, various noble metals (Au, Pd, Pt Ru, Rh etc.) have been examined for N₂ reduction reaction (NRR) to NH₃, but the obtained ammonia yield and Faradaic efficiency (F.E.) is very low to be presented on an industrial scale.⁹⁻¹⁶ The reason being their weak N₂ binding adsorption as well as the competition with hydrogen evolution reaction (HER) since metal d-orbital favors HER over NRR by preferable formation of M-H bonds.^{17, 18} Amid noble metal based catalysts, silver (Ag) is inexpensive, catalytically active^{19, 20, 21} and less sensitive towards HER and so can be a viable choice for selective NH₃ production.²² But then again, a major concern during synthesis of Ag based catalysts is the aggregation of Ag nanoparticles and their poor stability in alkaline media which results into reduced conductivity, low durability and affects the electrocatalytic activity.^{23, 24} Various strategies have been utilised to overcome these issues and improve the activity of Ag based catalysts, like, chemically tethering Ag species to a stable carbon support such as in a report by Li *et al.* where rGO in combination with Ag (111) gave an improved NRR activity due to facilitated electron transfer and increased the number of active sites.²⁵ Other strategy can be alloying or mineralizing it with inorganic phosphate unit.²⁶⁻²⁸

In our work we have explored silver phosphate (Ag_3PO_4) for NRR in alkaline media wherein interaction of phosphorus with metal species could generate more inductive effect, regulate the physicochemical properties and cut down the price of final catalyst. Although silver phosphate is well recognized in pharmaceutical industry and photocatalysis,^{29, 30} but is still underexplored for NRR. Besides, the electrocatalytic activity of noble metal based catalysts is highly dependent on their morphology and composition, and so in the present work we have tuned the morphology of Ag_3PO_4 and consequently its activity towards NRR. A cost-effective complexation methodology is betrothed to bring about the morphology control without the use of expensive templates and structure directing agents.^{31, 32} More interestingly, the NRR studies are carried out under alkaline conditions to effectively suppress the HER near the cathode surface due to increased kinetic overpotential for water dissociation and release of protons.^{33,34} The Ag_3PO_4 catalyst with cuboidal morphology demonstrates a promising NRR activity with a high F.E. (26.67%), yield rate ($456.75 \mu\text{g h}^{-1} \text{mg}^{-1}_{\text{cat}}$) and TOF (0.46 h^{-1}) at 0 V vs. RHE by virtue of its unique electronic structure, well defined morphology, and long-term stability under alkaline conditions.

3A-2 Material synthesis

3A-2.1 Synthesis of Ag_3PO_4 : The synthesis of Ag_3PO_4 has been carried out by slight modification of a previously reported literature.³⁵ A one-pot complexation strategy was utilized where in AgNO_3 and trisodium citrate were used as the metal source and complexing agent respectively. Initially, 10 mL of AgNO_3 (0.08 M) solution was added to a 10 mL of 0.3 M Na_3Cit . solution and which resulted into complexation of Ag salt with trisodium citrate to give turbid silver citrate complex after vigorous stirring for 30 minutes. After that, the dropwise addition of 20 mL of 0.05 M NaH_2PO_4 solution (phosphorization agent) was carried out under constant stirring which led to the formation of Ag_3PO_4 precipitates as a consequence of the replacement of citrate moiety with phosphate. These were allowed to stay at rest for different time durations *ca.* 2, 4 and 6 hours which

resulted into different morphologies. The precipitates obtained after reaction with H_2PO_4^- over an adequate period of time led to the formation of Ag_3PO_4 particles with different morphology due to rearrangement. The Ag_3PO_4 particles were recovered by centrifugation for 5 minutes and later washed with a 1:1 solution mixture of water and ethanol for atleast 5-6 times. Thereafter the product was dried overnight at 60 °C in oven to be used as an electrocatalyst for NRR. The final catalysts are denoted as Ag_3PO_4 (2 h), Ag_3PO_4 (4 h) and Ag_3PO_4 (6 h) respectively depending upon the time duration during synthesis.

3A-3 Results and discussion

3A-3.1 Mechanism for synthesis and morphology control: Initially, the reaction between silver nitrate and trisodium citrate took place which resulted into the formation of silver citrate complex at room temperature by following equation 3.1. This complex acted as a soft-template and upon the addition of NaH_2PO_4 , the silver citrate complex undergo precipitation to Ag_3PO_4 due to reaction with PO_4^{3-} anions (equation 3.2-3.3). The silver citrate complex controlled the nucleation and growth of Ag_3PO_4 particles via Ostwald ripening process where the slow release of PO_4^{3-} ions resulted into formation of Ag_3PO_4 which further underwent deposition and subsequent reaction over citrate complex for further growth of nanoparticles.



The morphology tuning was critically reliant on the reaction time after the addition of NaH_2PO_4 and the morphology restructuring took place after extending the reaction time due to the exfoliation and restructuring of small nanoparticles via hollowing effect by means of a localized Ostwald ripening process in which the Ag_3PO_4 nanoparticles undergo dissolution and subsequent migration from interior to the exterior of aggregates.³⁵

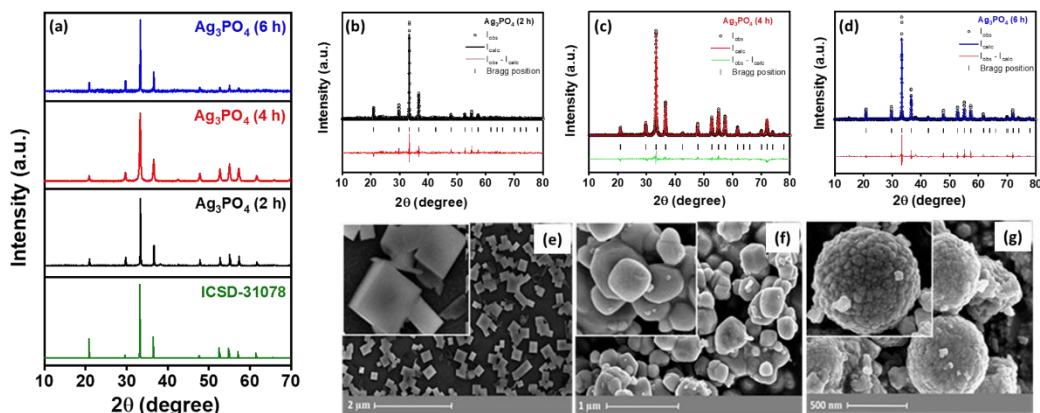


Figure 3A-1. (a) P-XRD patterns for Ag_3PO_4 catalysts compared to reference diffraction pattern of cubic Ag_3PO_4 and (b-d) their respective Rietveld refinement with goodness of fit: 4.986, 3.2 and 8.929 for Ag_3PO_4 (2 h/4 h/6 h) respectively. FE-SEM images of (e) Ag_3PO_4 (2 h), (f) Ag_3PO_4 (4 h) and (g) Ag_3PO_4 (6 h) at different magnifications, respectively (zoomed inset shows a further magnified image).

3A-3.2 Physical characterization: To examine the effect of morphology, microstructure and electronic structure towards NRR, powder X-ray diffraction (P-XRD), field emission- scanning electron microscopy (FE-SEM), transmission electron microscopy (TEM), selected-area electron diffraction (SAED) and X-ray photo- electron spectroscopy (XPS) measurements were carried out. The P-XRD pattern for all Ag_3PO_4 variants shown in Figures 3A-1(a-d) revealed the formation of cubic Ag_3PO_4 (ICSD: 31078) and further confirmed that the structural phase of the catalysts remained unaffected irrespective of the time variation during the synthesis. On the other hand, the morphology was highly affected by the variation of reaction time which was confirmed by means of FE-SEM studies. When the reaction mixture was kept undisturbed for 2 h, the cuboidal Ag_3PO_4 particles were detected (Figure 3A-1e) while pebble-like and spherical morphology was acquired when reaction time was extended upto 4 h and 6 h respectively presumably due to restructuring of the nanoparticles [Figures 3A-1(f-g)]. The histogram profiles of Ag_3PO_4 catalysts presented in Figures 3A-2(a-c) revealed the increase in particle size from 358.34 to 533.31 nm and subsequently to 642.4 nm

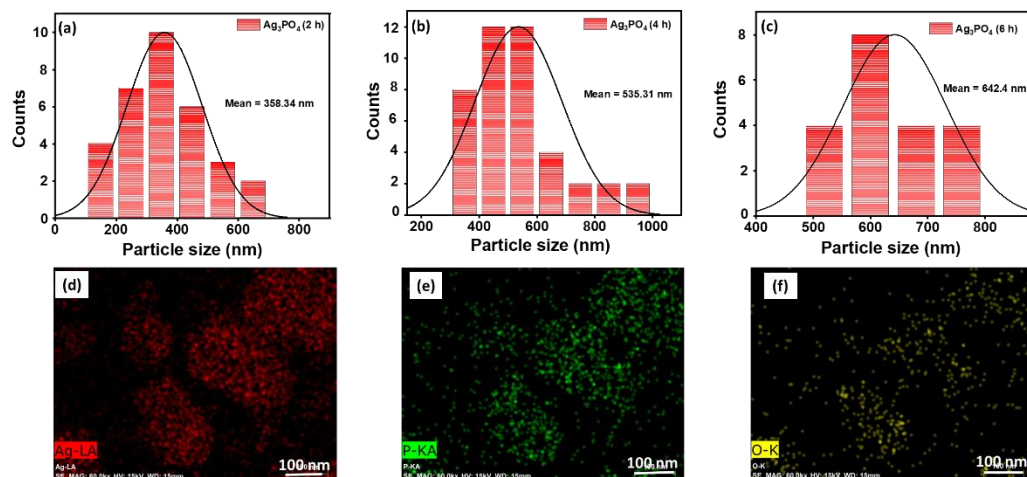


Figure 3A-2. Particle size distribution histogram of (a) Ag_3PO_4 (2 h), (b) Ag_3PO_4 (4 h) and (c) Ag_3PO_4 (6 h) catalyst from corresponding FE-SEM images. (d-f) EDS dot mapping images of Ag, P and O.

upon extending the reaction time from 2 h to 4 h and 6 h respectively and indicated the gradual growth of nanoparticles during extended time duration. Further, the EDS dot mapping images in Figures 3A-2(d-f) confirmed the uniform distribution of Ag, P and O is Ag_3PO_4 (2 h) catalyst whilst Table 3A-1 summarized the detailed elemental composition of all catalyst variants. Further, the TEM image and SAED pattern shown in Figures 3A-3(a-b) evidenced the cuboidal morphology for Ag_3PO_4 (2 h) catalyst with distinct edges and polycrystalline nature with diffused rings showing the presence of (110), (210), (211) and (310) planes of cubic Ag_3PO_4 respectively. Moreover XPS measurements revealed the electronic structure of Ag_3PO_4 (2 h) in which the deconvoluted Ag 3d spectra revealed two peaks due to spin-orbit coupling of $3d_{3/2}$ and $3d_{5/2}$ while P 2p and O 1s spectrum also showed two peaks each related to the formation of phosphate (PO_4^{3-}) moiety and presence of O^{2-} and surface hydroxyl groups respectively [Figures 3A-3(c-e)].

3A-3.3 Electrochemical activity towards NRR: To determine the electrocatalytic activity of the Ag_3PO_4 catalysts towards NRR, LSVs were acquired in Ar- and N_2 -saturated 0.1 M KOH electrolyte at a scan rate of 5 mV s^{-1} . A high net current density ($j_{\text{N}_2} - j_{\text{Ar}}$ @0.4 V vs. RHE) is revealed under N_2 -saturated conditions (Figure

3A-4a) for all the variants confirming the activity towards NRR, with highest net current density of 0.5 mA cm^{-2} in Ag_3PO_4 (2 h) variant. Afterwards, for the probable product estimation, chronoamperometry (CA) was executed at different potentials for 2 h in N_2 - saturated electrolyte [Figures 3A-4(b-d)]. The electrolyte samples collected after 2 h of NRR were then quantified for NH_3 and N_2H_4 production with Indophenol blue and Watt-Chrisp method respectively [Figures 3A-5(a-d)] with the help of UV-Vis

Table 3A-1: Elemental composition analysis for Ag_3PO_4 catalysts.

Element	Ag_3PO_4 (2 h)		Ag_3PO_4 (4 h)		Ag_3PO_4 (6 h)	
	Weight%	Atomic%	Weight%	Atomic%	Weight%	Atomic%
O	23.31	62.14	26.55	66.08	28.47	70.83
P	7.69	10.58	7.43	9.55	3.03	3.90
Ag	69.00	27.28	66.01	24.37	68.50	25.27

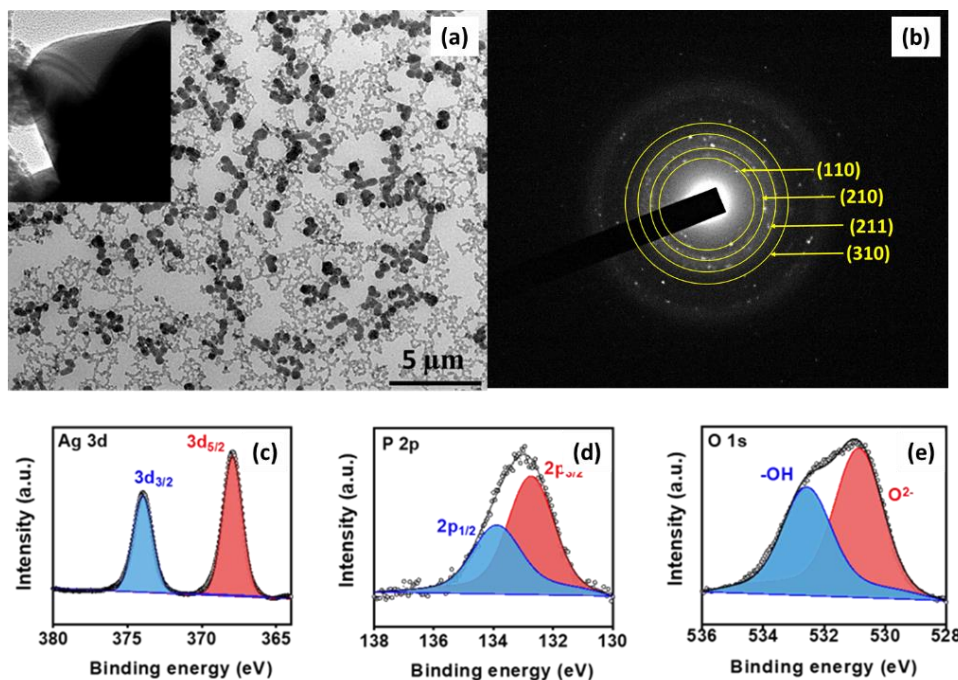


Figure 3A-3. (a) TEM image of the Ag_3PO_4 (2 h) catalyst (inset shows the edge of the cuboid), (b) crystalline SAED pattern showing planes corresponding to Ag_3PO_4 , and XPS deconvoluted spectra for (c) Ag 3d, (d) P 2p and (e) O 1s of Ag_3PO_4 (2 h).

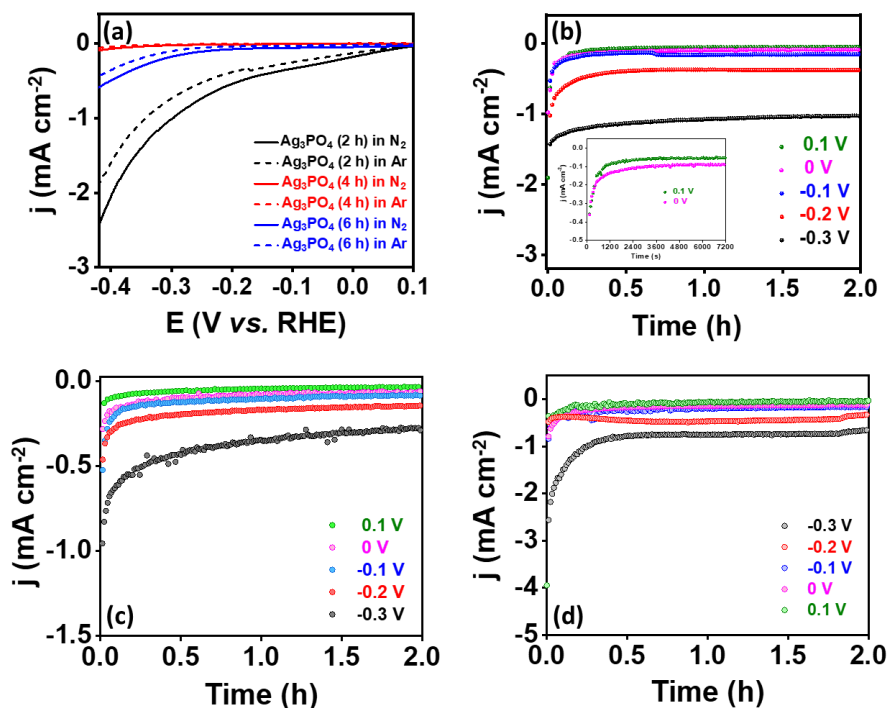


Figure 3A-4. (a) Linear sweep voltammograms for catalysts in N_2 - and Ar saturated 0.1 M KOH, chronoamperometric curves obtained at different potentials by (b) Ag_3PO_4 (2 h), (c) Ag_3PO_4 (4 h) and (d) Ag_3PO_4 (6 h) respectively.

spectroscopy. Figures 3A-6(a-c) asserted the NH_3 production after NRR by all Ag_3PO_4 catalysts at applied potentials while no N_2H_4 production was witnessed in due course of NRR (Figure 3A-6f), and thus put forward high selectivity towards NH_3 production. Among all the variants, Ag_3PO_4 (2 h) revealed superior activity towards NRR with a high F.E. of 26.67%, high NH_3 yield rate of $456.75 \mu\text{g h}^{-1} \text{mg}^{-1} \text{cat}$ and a high TOF of 0.46 h^{-1} at 0 V vs. RHE [Figures 3A-6(d-e)] as compared to other variants under identical conditions which revealed a lower F.E. and yield rate of 14.32%, $239.69 \mu\text{g h}^{-1} \text{mg}^{-1} \text{cat}$ and 20.87%, $527.99 \mu\text{g h}^{-1} \text{mg}^{-1} \text{cat}$ respectively. This huge disparity in NRR activity could be attributed to the difference in the morphology where the cuboidal morphology would provide exposed active sites for N_2 adsorption preferentially by virtue of the surface atoms located at sharp edges, corners or stacking faults which could shift the valence bands upside allowing strong dinitrogen adsorption than surface atoms located at basal planes.³⁶

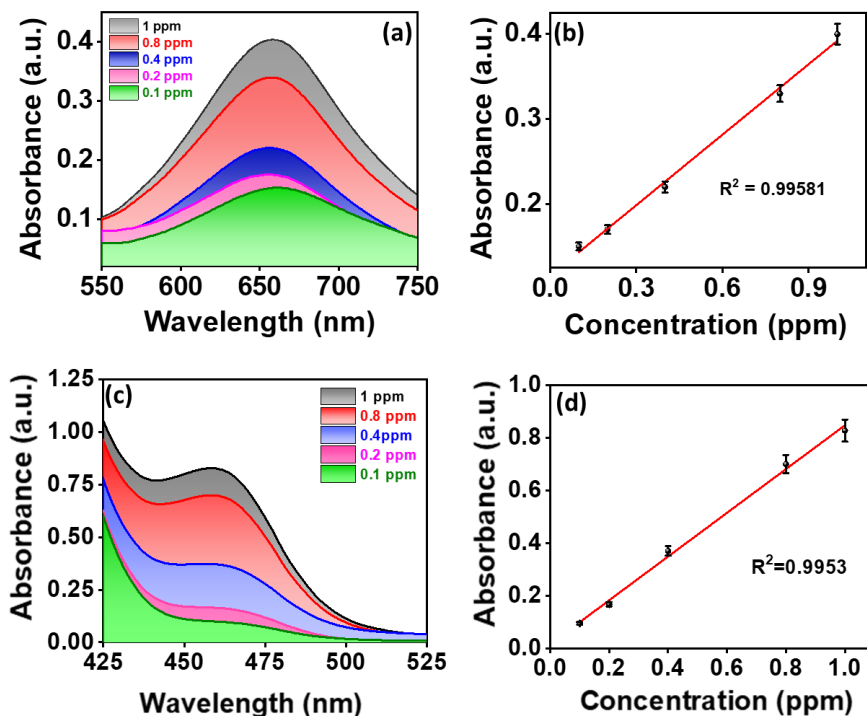


Figure 3A-5. (a) UV-vis spectrum and (b) calibration curve obtained from known concentrations of standard solution of NH_3 using Indophenol blue method. (c) UV-vis spectra of standard N_2H_4 solutions by Watt and Chrisp method and (d) corresponding calibration curve.

Further the activity could also be correlated to the partial positive charge over Ag (+1) in Ag_3PO_4 ²⁷ capable of activation and selective N_2 adsorption as well as its ability to suppress HER since the standard reduction potential of Ag/Ag₃PO₄ couple lies within the reduction potential of H^+ and Ag/AgNO₃ and cannot split water to produce H_2 .³⁷ Notably the phosphate moieties could ease the further hydrogenation of the adsorbed N_2 over Ag^+ active sites and release of ammonia.³⁸ The superior activity of Ag_3PO_4 (2 h) catalyst was then correlated with the lower charge transfer resistance (R_{ct}) value of 70.03 Ω and low Tafel slope values which depict the reaction kinetics at electrode-electrolyte interface (Table 3A-2). Figure 3A-7a showed the Nyquist plots of Ag_3PO_4 catalysts where Ag_3PO_4 (2 h) endured the lowest R_{ct} value of 70.03 Ω defining the formation of thin diffusion layer at interface over other variants. This was found to be in accordance with the lowest Tafel slope value of 229 mV dec^{-1} over other catalysts (Figure 3A-7b).

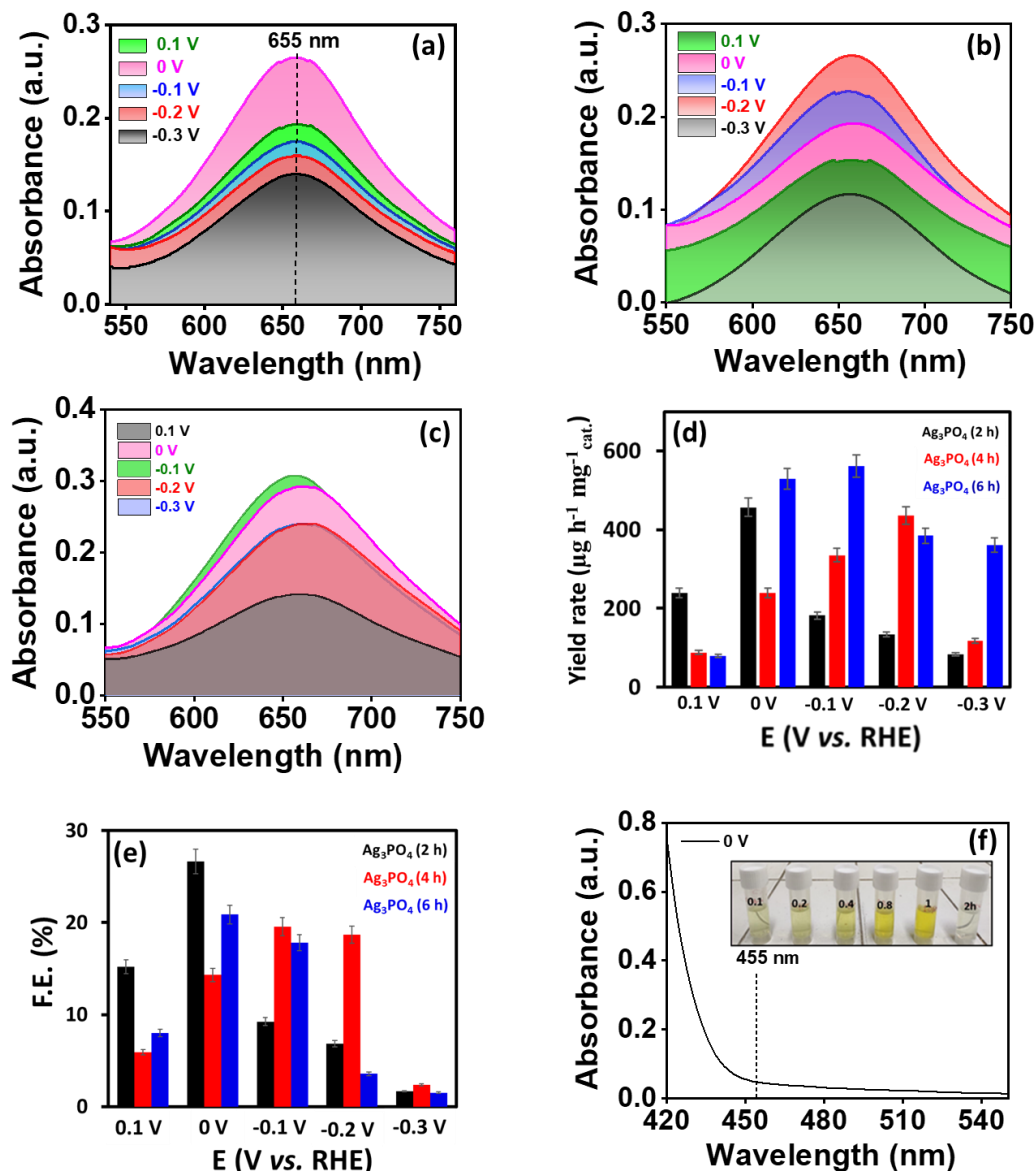


Figure 3A-6. UV-vis spectrum obtained by the indophenol blue method for (a) Ag_3PO_4 (2 h), (b) Ag_3PO_4 (4 h) and (c) Ag_3PO_4 (6 h) respectively. (d) Comparison of FE and the (e) production yield rate of all catalysts at different potentials. (f) UV-vis spectrum of electrolyte sample collected after 2 h chronoamperometry at 0 V vs. RHE by Ag_3PO_4 (2 h) for hydrazine determination.

In contrast the ECSA was utilized to correlate the catalyst activity towards HER for which the CV was executed under the non-faradaic region in Ar-saturated electrolyte at 0 V (vs. RHE) and later the values for C_{dl} and ECSA were calculated

Table 3A-2: EIS and Tafel analysis of Ag₃PO₄ towards NRR.

Electrocatalyst	R_s	R_p	R_{ct}	Tafel slope for NRR
Ag ₃ PO ₄ (2 h)	0.95 Ω	70.98 Ω	70.03 Ω	229 mV dec ⁻¹
Ag ₃ PO ₄ (4 h)	0.12 Ω	108.64 Ω	108.52 Ω	394 mV dec ⁻¹
Ag ₃ PO ₄ (6 h)	0.12 Ω	80.11 Ω	79.99 Ω	297 mV dec ⁻¹

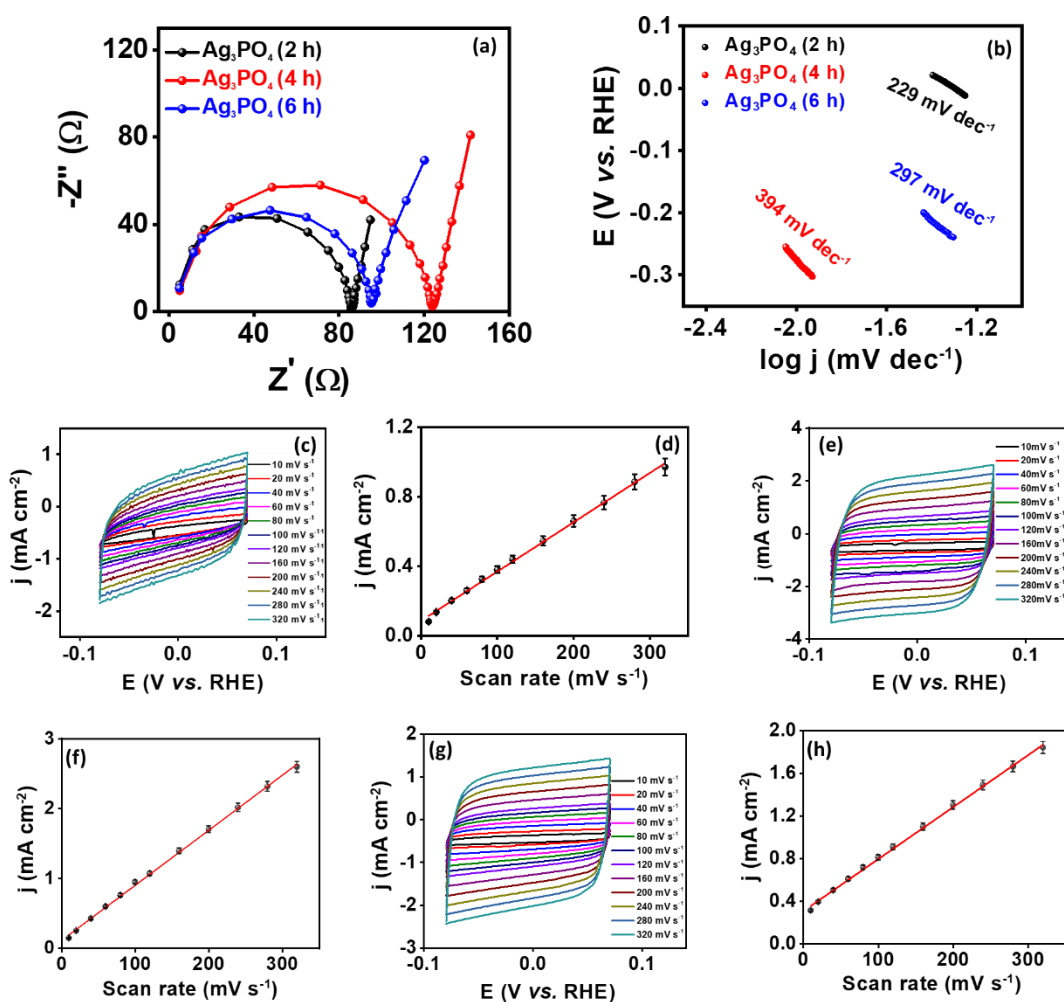


Figure 3A-7. (a) Nyquist plots acquired for Ag₃PO₄ catalysts in 0.1 M KOH, (b) Tafel plots for Ag₃PO₄ catalysts showing NRR kinetics. Cyclic voltammogram for (c) Ag₃PO₄ (2 h), (e) Ag₃PO₄ (4 h), (g) Ag₃PO₄ (6 h) in non-faradaic potential region at various scan rates where (d), (f) & (h) are corresponding average current density versus scan rate plot.

from linear scan rate *vs.* current density curves [Figures 3A-7(c-h)]. The values obtained for C_{dl} and ECSA by Ag_3PO_4 (2 h) were found to be low than other variants and thus indicated the poor intrinsic HER activity and increased F.E. for NRR at similar potential which is parallel to the high Tafel slope of 282 mV dec^{-1} during HER by Ag_3PO_4 (2 h) catalyst (Table 3A-3).

Table 3A-3: ECSA and Tafel analysis for HER.

Electrocatalyst	C_{dl}^*	ECSA	Tafel slope for HER
Ag_3PO_4 (2 h)	2.83 mF	70.75 cm^2	282 mV dec^{-1}
Ag_3PO_4 (4 h)	7.88 mF	197 cm^2	166 mV dec^{-1}
Ag_3PO_4 (6 h)	4.87 mF	121.75 cm^2	218 mV dec^{-1}

This HER suppression by Ag_3PO_4 (2 h) catalyst was authenticated by means of CA measurements at 0 V of applied potential under switching gas-feed environments for 10 h. The current density showed an instant increase and decrease when gas-feed was switched from Ar to N_2 and vice versa (Figure 3A-8a), which indicated the ability of the catalyst to suppress HER and durability of the catalyst. These outcomes were further supported via quantification of products after the aforestated experiments where Figure 3A-8b demonstrated negligible NH_3 production in presence of Ar while GC quantification for H_2 at different applied potentials showed inferior HER at 0 V with an overall H_2 production yield rate of $3.9\text{ }\mu\text{mol h}^{-1}\text{ mg}^{-1}$ and H_2 selectivity of 6.7% respectively [Figures 3A-8(c-e)]. The partial positive charge over the Ag in Ag_3PO_4 catalyst was considered to be an active site for N_2 adsorption which was validated by a control experiment. CV was executed for catalyst coated GCE in 0.1 M KOH electrolyte under N_2 -saturated conditions but with and without the addition of SCN^- (a poison for metal catalysts which selectively coordinate with metal centers) which revealed one reduction peak at 0 V (Ag^+ to Ag (0)) and another at 0.62 V (Ag (0) to Ag^+) respectively when no SCN^- was added. But upon the addition of SCN^- solution in the electrolyte, the peak current decreased and the peak potentials showed shift in the negative region,

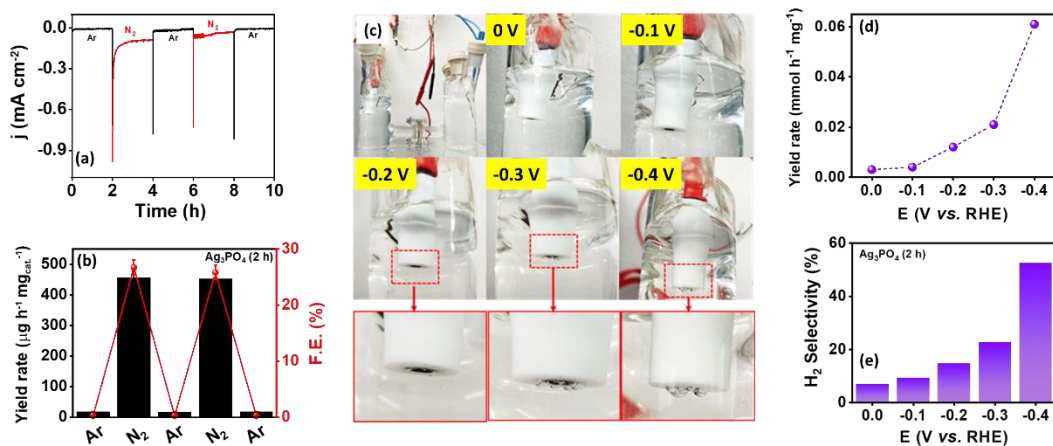


Figure 3A-8. (a) Chronoamperometry measurements in Ar and N₂ saturated 0.1 M KOH, (b) different yield rates and F.E. obtained for Ag₃PO₄ (2 h) in 0.1 M KOH by switching the gas-feed stream every 2 h, (c) Photographs of Ag₃PO₄ (2 h) captured during GC analysis for HER quantification at different potentials, (d) H₂ selectivity of Ag₃PO₄ at different potentials and (e) respective production yield rate for H₂ production.

indicative of the formation of Ag⁺–SCN[–] complex due to poisoning of Ag-metal centres in Ag₃PO₄ catalyst [Figures 3A-9(a-b)]. This was further supported by the decreased NH₃ yield rate of 93.86 μg h⁻¹ mg⁻¹ for the sample collected after 2 h NRR in presence of SCN[–] (Figure 3A-9c). These conclusions confirmed the contribution of Ag as active sites for NRR.

3A-3.4 Detection/elimination of N-labile impurities: The consistency of the produced NH₃ yield rate was established by following rigorous procedures *viz.* cleansing of the gas-feed, electrolyte salt and catalyst itself.^{39, 40} Initially, the catalyst cleansing by alkaline solution was performed to remove any trace NO₃[–] present due to precursor salt, which is proved from the P-XRD pattern of Ag₃PO₄ catalyst where no peak related to silver nitrate could be observed. More interestingly, the reducible and labile N-impurities such as NO_x⁴¹, NH₄⁺ in feeding gases, were eliminated by passing through a scrubbing solution with alkaline KMnO₄ and acid trap consequently. Besides, the electrolyte was also tested for contamination from nitrate (NO₃[–]) and nitrite (NO₂[–]) which upon quantification

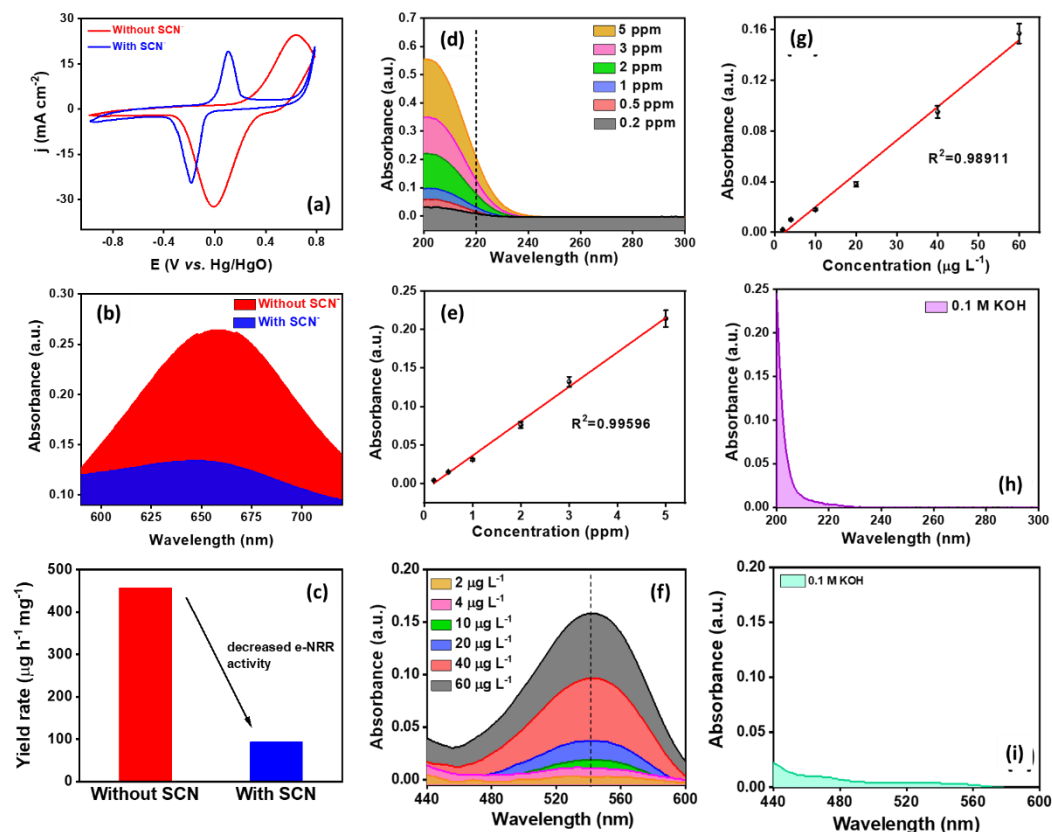


Figure 3A-9. (a) Cyclic voltammograms acquired for Ag_3PO_4 (2 h) catalyst coated GCE, (b) UV-Vis absorbance curves obtained by quantification of samples collected after NRR by Ag_3PO_4 (2 h) and (c) Bar diagram comparison of NH_3 yield rate calculated after NRR control experiments in presence and absence of SCN^- ions. UV-Vis spectrum and corresponding calibration curve for (d-e) nitrate and (f-g) nitrite detection. Detection of amount of (h) NO_3^- and (i) NO_2^- in electrolyte solution.

by spectrophotometric methods didn't show any trace impurities and thus the overestimation of ammonia yield from the electrolyte was also ruled out [Figures 3A-9(d-i)]. The presence of likely interferences were scrutinized by certain control experiments including NRR at open circuit potential (OCP) and over bare GCE and the CA in Ar-saturated electrolyte deliberated the negligible ammonia production which proved that the source of N_2 was only from the feeding gas [Figures 3A-10(a-b)].⁴² In the end, the $^{15}\text{N}_2$ isotope labelling experiments were performed for 2 h and the electrolyte samples were quantified afterwards for NH_4^+ concentration

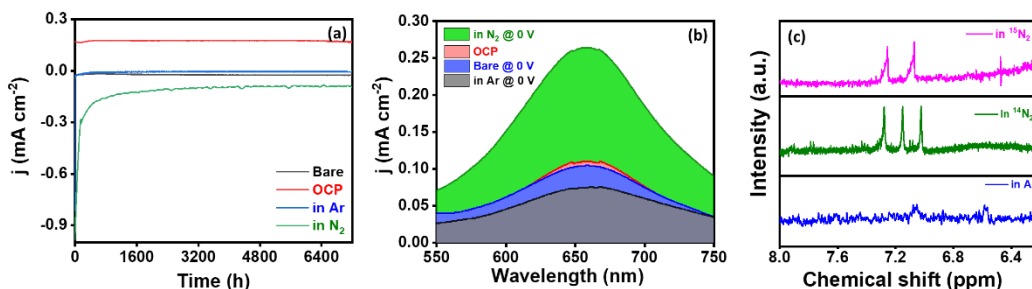


Figure 3A-10. (a) Chronoamperometric curves and (b) UV-vis spectrum of Ag_3PO_4 (2 h) at OCP in N_2 saturated 0.1 M KOH, at 0 V vs. RHE in N_2/Ar saturated electrolyte, and that of bare GC at 0 V vs. RHE in N_2 saturated 0.1 M KOH respectively. (c) ^1H -NMR spectra showing the corresponding $^{14}\text{NH}_4^+$ and $^{15}\text{NH}_4^+$ peaks in the electrolyte sample collected after NRR by Ag_3PO_4 (2 h) catalyst in different gas-feed environments.

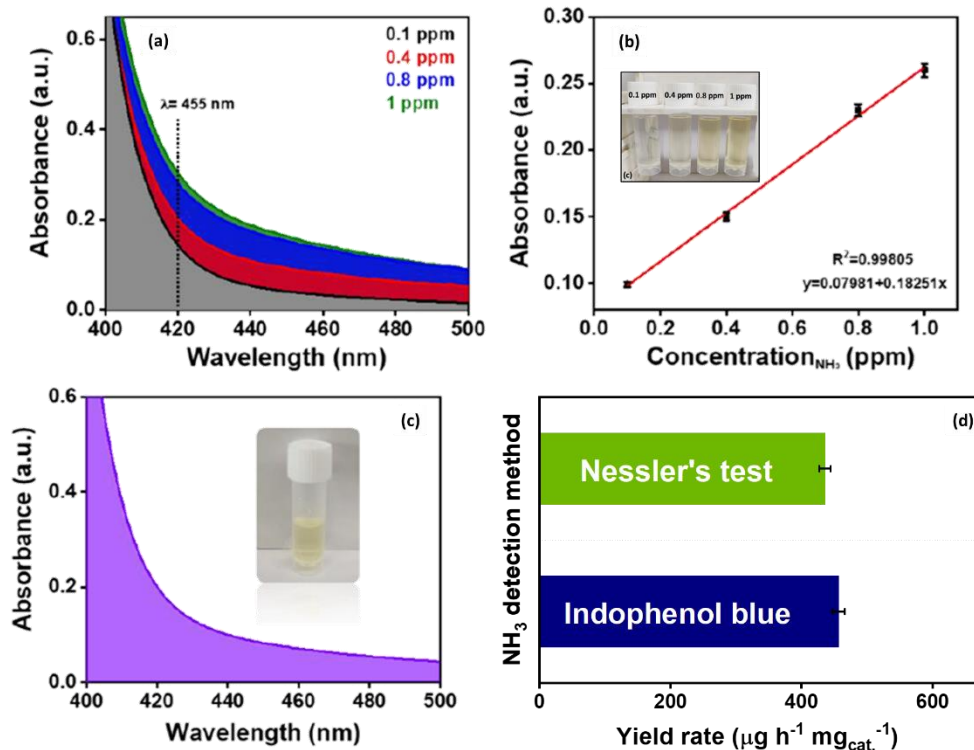


Figure 3A-11. (a) UV-Vis curves for standard NH_4^+ solutions after Nessler's reagent test and (b) corresponding calibration curve. (c) UV-Vis curve for electrolyte solution collected after NRR by Ag_3PO_4 (2 h) quantified by Nessler's test. (d) Bar diagram representing the comparison of the NH_3 yield quantified by different methods after the NRR by Ag_3PO_4 (2 h) at 0 V.

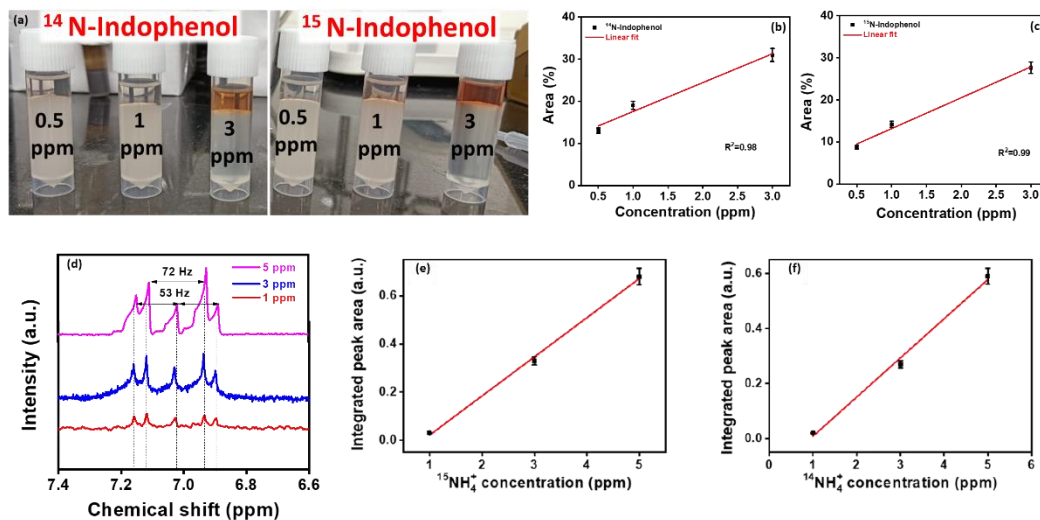


Figure 3A-12. (a) Photographs showing the formation of Indophenol red in organic layer before LC-MS quantification for standard samples, (b-c) calibration curves extracted from LC-MS of standard samples. (d) ^1H -NMR spectra of equimolar mixture of $^{14}\text{NH}_4\text{Cl}$ and $^{15}\text{NH}_4\text{Cl}$ solutions and (e-f) calibration curves for the same.

(Figure 3A-10c), in which a triplet coupling for $^{14}\text{NH}_4^+$ (~53 Hz) and a doublet coupling for $^{15}\text{NH}_4^+$ (~72 Hz) were observed in the ^1H -NMR spectrum obtained after NRR in $^{14}\text{N}_2$ and $^{15}\text{N}_2$ -saturated electrolyte conditions while no labelled $^{14}\text{NH}_4^+$ or $^{15}\text{NH}_4^+$ was observed when Ar was used as gas supply. It underlined the contribution of N atoms in N_2 gas feed stream purged into the electrolyte towards NH_3 production.

3A-3.5 Validation of NH_3 yield rate: The Nessler's reagent test was also performed to validate the NH_3 yield [Figures 3A-11(a-b)], where the analogous yield rate obtained from Indophenol blue and Nessler's method validated the reported yield [Figures 3A-11(c-d)]. In addition to the spectrophotometric validation, the NH_3 yield rate were also validated by ^1H -NMR and LC-MS (Figure 3A-12) for which calibration curves were extracted for different known standard $^{15}\text{NH}_4^+ / ^{14}\text{NH}_4^+$ concentrations. Figures 3A-13(a-b) represented the mass spectrum for electrolyte samples collected after isotope labelling NRR experiments with peaks at m/z value of 197.97 and 198.96 for ^{14}N - and ^{15}N -Indophenol respectively.

The NH_3 yield rates obtained from LC-MS were $479.38 \mu\text{g h}^{-1} \text{mg}^{-1}_{\text{cat}}$ and $455.07 \mu\text{g h}^{-1} \text{mg}^{-1}_{\text{cat}}$ for $^{14}\text{NH}_4^+$ and $^{15}\text{NH}_4^+$ which were in accordance with the yield rates obtained from NMR investigations (460 and $410 \mu\text{g h}^{-1} \text{mg}^{-1}_{\text{cat}}$ for $^{14}\text{NH}_4^+$ and $^{15}\text{NH}_4^+$). All these results were compared as shown in Figure 3A-13c and Table 3A-4 to validate the NH_3 yield and conclude that the detected NH_3 is produced from the Ag_3PO_4 (2h) catalysed NRR at 0 V (vs. RHE).

Table 3A-4: Validation of ammonia yield rates via different methods.

Detection method	$^{14}\text{NH}_3$ yield rate ($\mu\text{g h}^{-1} \text{mg}^{-1}_{\text{cat}}$)	$^{15}\text{NH}_3$ yield rate ($\mu\text{g h}^{-1} \text{mg}^{-1}_{\text{cat}}$)
Indophenol Blue	456.75	-
Nessler's reagent	435.80	-
^1H -NMR	460	410
LC-MS	479.38	455.08

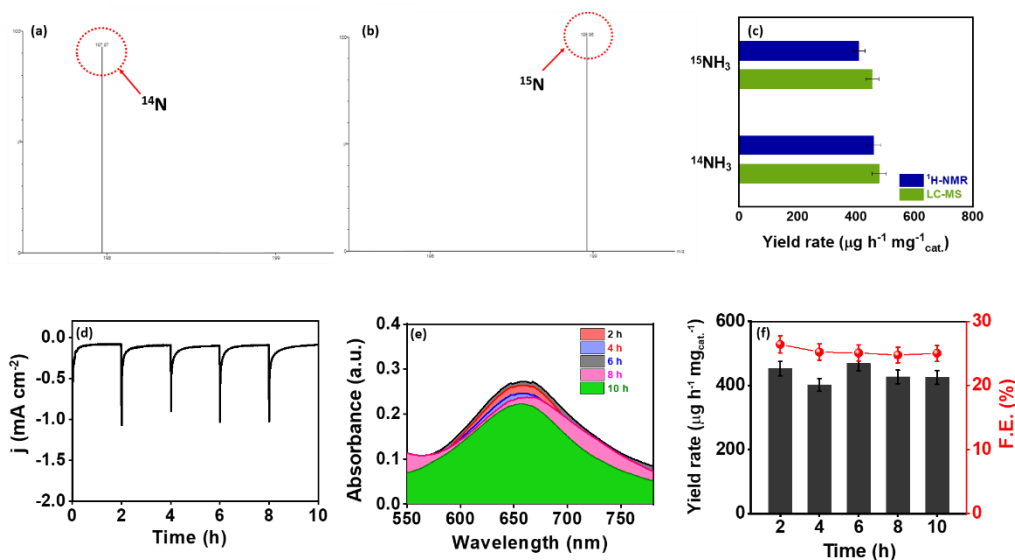


Figure 3A-13. Abundance of (a) ^{14}N and (b) ^{15}N Indophenol for the electrolyte samples obtained after NRR. (c) Comparison of the NH_3 yield calculated from LC-MS and ^1H -NMR methods. (d) Stability test of Ag_3PO_4 (2 h) at 0 V vs. RHE for 10 h in N_2 saturated 0.1 M KOH and (e) UV-Vis spectrum for electrolyte sample collected after the same. (f) F.E. and ammonia yield rates after NRR stability tests.

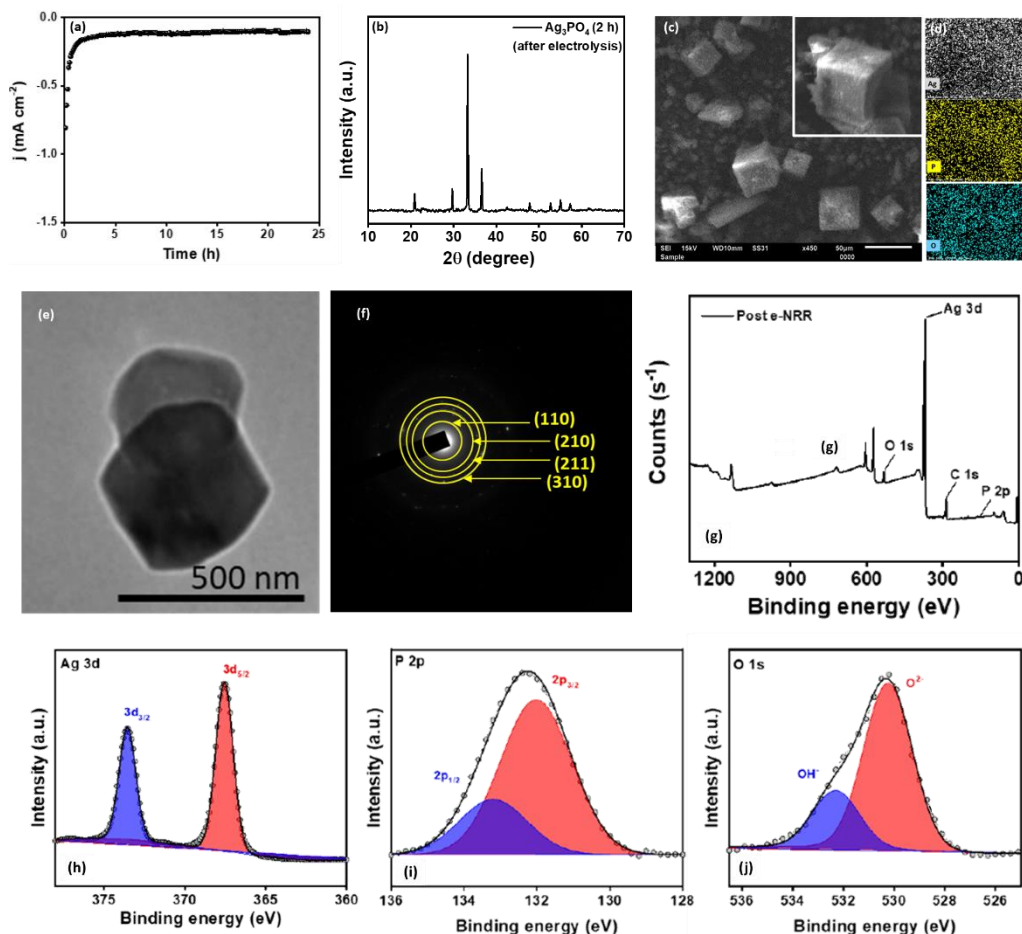


Figure 3A-14. (a) Chronoamperometry curve acquired after 24 h continuous NRR in N_2 -saturated 0.1 M KOH, (b) post-stability X-ray diffraction pattern for Ag_3PO_4 (2 h) after 10 h NRR, (c) SEM image, (d) EDS dot mapping for all respective elements in Ag_3PO_4 (2 h), (e) TEM image of Ag_3PO_4 (2 h) catalyst and (f) corresponding SAED pattern after NRR stability tests. Post-stability (g) survey spectrum and XP deconvoluted (h) Ag 3d, (i) P 2p and (j) O 1s spectra of Ag_3PO_4 (2 h).

3A-3.6 Stability measurements: In the end, the stability was assessed using CA at 0 V under N_2 -saturated electrolyte conditions which demonstrated the high stability with insignificant change in current response, F.E. and NH_3 yield rate after 10 h of NRR [Figures 3A-13(d-f)]. The stability of the Ag_3PO_4 (2 h) catalyst was even retained after 24 h of NRR operation under alkaline conditions (Figure 3A-14a). The morphological, structural and electronic attributes of the Ag_3PO_4 (2 h)

catalyst were studied after the stability measurements via a series of *ex-situ* characterizations. The P-XRD patterns in Figure 3A-14b represented no change in the structural phase and thus evidenced the robustness of catalyst, while the SEM, SAED, EDS and dot mapping analysis showed the retention of cuboidal morphology and planes associated with Ag_3PO_4 with no alteration in elemental composition (Table 3A-5) and uniform distribution over the scanned area respectively [Figures 3A-14c-f)]. The XPS analysis also didn't show any alteration in the electronic structure of the catalyst [Figures 3A-14(g-j)] and thus confirmed the feasibility of our approach to stabilize Ag by alloying it with an inorganic phosphate moiety. Henceforth, this study may open a floor for effective utilization of metallic phosphates to achieve high activity and stability during NH_3 production under ambient conditions.

Table 3A-5: Post EDS composition analysis of Ag_3PO_4 (2 h).

Before			After	
Element	Weight%	Atomic%	Weight%	Atomic%
O K	23.31	62.14	25.18	64.47
P K	7.69	10.58	7.54	9.98
Ag L	69.00	27.28	67.28	25.55

3A-4 Summary

In summary, a simple one-pot complexation methodology with reaction time variation was applied to synthesize a morphology controlled silver phosphate catalyst. Owing to its cuboidal morphology, Ag_3PO_4 (2 h) showed superior NRR activity than other two catalyst variants. A high F.E. of 26.67% was achieved at a positive potential of 0 V *vs.* RHE in alkaline media along with a high yield rate, emphasizing its competence to persuade highly selective, efficient and cost-effective ammonia synthesis under ambient conditions. Also, the F.E. and production yield rate showed negligible change after 10 h of stability test and retained the structural, morphological and electronic features of the catalyst. For that reason, adopting an inorganic variant of Ag *i.e.* Ag_3PO_4 may catch its broad

applicability in designing stable Ag based catalysts for N₂ conversion to NH₃.

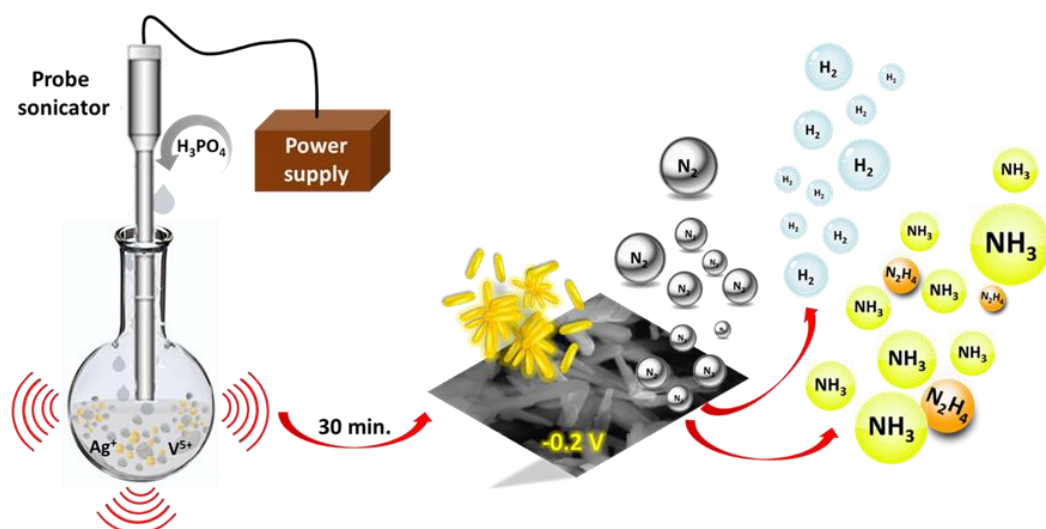
3A-5 References

1. V. Rosca, M. Duca, M. T. de Groot and M. T. Koper, *Chem. Rev.*, 2009, **109**, 2209-2244.
2. J. G. Chen, R. M. Crooks, L. C. Seefeldt, K. L. Bren, R. M. Bullock, M. Y. Darensbourg, P. L. Holland, B. Hoffman, M. J. Janik and A. K. Jones, *Science*, 2018, **360**, eaar6611.
3. J. Nørskov, J. Chen, R. Miranda, T. Fitzsimmons and R. Stack, *Sustainable Ammonia Synthesis—Exploring the scientific challenges associated with discovering alternative, sustainable processes for ammonia production*, US DOE Office of Science, 2016.
4. R. Cai and S. D. Minteer, *ACS Energy Lett.*, 2018, **3**, 2736-2742.
5. H.-P. Jia and E. A. Quadrelli, *Chem. Soc. Rev.*, 2014, **43**, 547-564.
6. S. Giddey, S. Badwal and A. Kulkarni, *Int. J. Hydrogen Energy*, 2013, **38**, 14576-14594.
7. D. Bao, Q. Zhang, F. L. Meng, H. X. Zhong, M. M. Shi, Y. Zhang, J. M. Yan, Q. Jiang and X. B. Zhang, *Adv. Mater.*, 2017, **29**, 1604799.
8. G. Qing, R. Ghazfar, S. T. Jackowski, F. Habibzadeh, M. M. Ashtiani, C.-P. Chen, M. R. Smith III and T. W. Hamann, *Chem. Rev.*, 2020, **120**, 5437-5516.
9. X. Wang, L. Li, Z. Fang, Y. Zhang, J. Ni, B. Lin, L. Zheng, C.-t. Au and L. Jiang, *ACS Catal.*, 2020, **10**, 9504-9514.
10. M. M. Shi, D. Bao, B. R. Wulan, Y. H. Li, Y. F. Zhang, J. M. Yan and Q. Jiang, *Adv. Mater.*, 2017, **29**, 1606550.
11. M. M. Shi, D. Bao, S. J. Li, B. R. Wulan, J. M. Yan and Q. Jiang, *Adv. Energy Mater.*, 2018, **8**, 1800124.
12. F. Pang, Z. Wang, K. Zhang, J. He, W. Zhang, C. Guo and Y. Ding, *Nano Energy*, 2019, **58**, 834-841.
13. J. Wang, L. Yu, L. Hu, G. Chen, H. Xin and X. Feng, *Nat. Commun.*, 2018, **9**, 1-7.
14. L. Yang, C. An, J. Zhang, J. Zhu and P. Chen, *J. Mater. Chem. A*, 2020, **8**, 25142-25147.
15. B. Yu, H. Li, J. White, S. Donne, J. Yi, S. Xi, Y. Fu, G. Henkelman, H. Yu and Z. Chen, *Adv. Funct. Mater.*, 2020, **30**, 1905665.
16. C. Yang, B. Huang, S. Bai, Y. Feng, Q. Shao and X. Huang, *Adv. Mater.*, 2020, 2001267.
17. C. Lv, C. Yan, G. Chen, Y. Ding, J. Sun, Y. Zhou and G. Yu, *Angew. Chem. Int. Ed.*, 2018, **57**, 6073-6076.
18. Y. Yao, S. Zhu, H. Wang, H. Li and M. Shao, *J. Am. Chem. Soc.*, 2018, **140**, 1496-1501.
19. T. C. Nagaiah, A. Maljusch, X. Chen, M. Bron and W. Schuhmann, *ChemPhysChem*, 2009, **10**, 2711-2718.
20. A. Tiwari and T. C. Nagaiah, *ChemCatChem*, 2016, **8**, 396-403.
21. D. Sun, X. Xu, Y. Qin, S. P. Jiang and Z. Shao, *ChemSusChem*, 2020, **13**, 39-58.
22. M. Ma, K. Liu, J. Shen, R. Kas and W. A. Smith, *ACS Energy Lett.*, 2018, **3**, 1301-1306.
23. R. Begum, Z. H. Farooqi, A. H. Aboo, E. Ahmed, A. Sharif and J. Xiao, *J. Hazard. Mater.*, 2019, **377**, 399-408.
24. E. J. Lim, S. M. Choi, M. H. Seo, Y. Kim, S. Lee and W. B. Kim, *Electrochem. Commun.*, 2013, **28**, 100-103.
25. X. Li, H. Xie and J. Mao, *J. Mater. Sci.*, 2020, **55**, 5203-5210.
26. J. S. Spendelov and A. Wieckowski, *Phys. Chem. Chem. Phys.*, 2007, **9**, 2654-2675.
27. J. Kahk, D. Sheridan, A. Kehoe, D. Scanlon, B. Morgan, G. Watson and D. Payne, *J. Mater. Chem. A*, 2014, **2**, 6092-6099.
28. J. Zhao, L. Sun, S. Canepa, H. Sun, M. N. Yesibolati, M. Sherburne, R. Xu, T. Sritharan, J. S. Loo and J. W. Ager III, *J. Mater. Chem. A*, 2017, **5**, 11905-11916.
29. Y. Seo, B.-E. Yeo, Y.-S. Cho, H. Park, C. Kwon and Y.-D. Huh, *Mater. Lett.*, 2017, **197**, 146-149.
30. R. Qu, W. Zhang, N. Liu, Q. Zhang, Y. Liu, X. Li, Y. Wei and L. Feng, *ACS Sustain. Chem. Eng.*, 2018, **6**, 8019-8028.
31. Y. Lu, Y. Wang and W. Chen, *J. Power Sources*, 2011, **196**, 3033-3038.

- 32. Y. Lu and W. Chen, *J. Power Sources*, 2012, **197**, 107-110.
- 33. M. Wang, S. Liu, T. Qian, J. Liu, J. Zhou, H. Ji, J. Xiong, J. Zhong and C. Yan, *Nat. Commun.*, 2019, **10**, 1-8.
- 34. M. R. Singh, Y. Kwon, Y. Lum, J. W. Ager III and A. T. Bell, *J. Am. Chem. Soc.*, 2016, **138**, 13006-13012.
- 35. Q. Liang, W. Ma, Y. Shi, Z. Li and X. Yang, *CrystEngComm*, 2012, **14**, 2966-2973.
- 36. W.-Y. Gao, Y.-C. Hao, X. Su, L.-W. Chen, T.-A. Bu, N. Zhang, Z.-L. Yu, Z. Zhu and A.-X. Yin, *Chem. Commun.*, 2019, **55**, 10705-10708.
- 37. Z. Yi, J. Ye, N. Kikugawa, T. Kako, S. Ouyang, H. Stuart-Williams, H. Yang, J. Cao, W. Luo and Z. Li, *Nat. Mater.*, 2010, **9**, 559-564.
- 38. J.-T. Ren, L. Chen, Y. Liu and Z.-Y. Yuan, *J. Mater. Chem. A*, 2021, **9**, 11370-11380.
- 39. U. B. Shahid, Y. Chen, S. Gu, W. Li and M. Shao, *Trends Chem.*, 2021, **4**, 142-156.
- 40. L. Li, C. Tang, D. Yao, Y. Zheng and S.-Z. Qiao, *ACS Energy Lett.*, 2019, **4**, 2111-2116.
- 41. J. Choi, H.-L. Du, C. K. Nguyen, B. H. Suryanto, A. N. Simonov and D. R. MacFarlane, *ACS Energy Lett.*, 2020, **5**, 2095-2097.
- 42. Y. Zhao, R. Shi, X. Bian, C. Zhou, Y. Zhao, S. Zhang, F. Wu, G. I. Waterhouse, L. Z. Wu and C. H. Tung, *Adv. Sci.*, 2019, **6**, 1802109.

Chapter 3B

Sustainable ammonia synthesis through electrochemical dinitrogen activation using $\text{Ag}_2\text{VO}_2\text{PO}_4$ catalyst



3B-1 Introduction

Fixation of abundant nitrogen to ammonia plays a critical role in the N_2 cycle where ammonia production by green and clean methodologies is even more significant.¹ Application of ammonia is widespread amongst which roughly 88% of domestic ammonia consumption is in fertilizer industry for synthesis of urea, ammonium nitrates, ammonium phosphates, and other nitrogen compounds.³ In addition to it, ammonia is a potential green H_2 carrier by virtue of its high hydrogen content (17.6% and $121 \text{ kg-}H_2 \text{ m}^{-3}$) and high volumetric energy density ($12.92\text{-}14.4 \text{ MJ L}^{-1}$).^{4, 5} And therefore the ammonia production is increasing drastically since 1946⁶ and will soon cross the \$100 billion global market.⁷ Haber-Bosch process, a thermochemical route for industrial NH_3 production leads to the consumption of approximately 1-2% of global energy and more than 2% of global CO_2 emissions.⁸ Further the involvement of steam methane reformation process (for H_2 production) is responsible of around 70% of the operational costs and global carbon emissions.⁹ Several efforts are being put forward in past six decades to improve the ammonia production technologies where the NH_3 production capacity is increased from 100 mt/day to 3300 mt/day accompanied by reduction in energy consumption from 60 GJ/mt of NH_3 to 40-50 GJ/mt and 30-40 GJ/mt in coke-based and natural gas based plants respectively.¹⁰ Despite of these efforts, the need of a green and efficient ammonia production process with low energy consumption and CO_2 emissions is anticipated, where in the electrocatalytic nitrogen reduction reaction in aqueous solutions is one of the most likely choice.^{11, 12} But there are certain drawbacks encountered during NRR such as activation of inert N_2 ($N\equiv N$) triple bond, competition with hydrogen evolution reaction, high susceptibility of contamination by N-labile impurities and false estimation of ammonia.^{13, 14, 15, 16} This obliges the design and development of an active and stable catalyst for NRR along with the rigorous analysis for true NH_3 estimation.

Ag based catalysts are shown to exhibit activity towards NRR due to their low sensitivity for hydrogen species¹⁷, for example, Ag nanosheets¹⁸, Ag nanotubes¹⁹,

Ag nanodots²⁰, B doped Ag²¹, Pd-Ag-S nanosponges²², sulfur modified Ag₂Te²³, Ag₃Cu²⁴, Ag₃PO₄²⁵, etc., but require further improvements to achieve high activity. In this context, the regulation of catalyst components can optimize the performance of electrocatalyst and thus to enhance the N₂ adsorption and activation over Ag metal based catalysts, alloying with other transition metals and non-metallic compounds is an effective strategy.²⁶ Alloying of Ag catalysts can also modify the electronic structure, tune the energy gap for NRR process²⁷, for example, in a report by Pang *et al.*²⁸, the alloying of Ag with Pd (Ag-Pd alloy) demonstrate improved NRR activity than Ag alone and reaction of Ag with inorganic phosphates (PO₄³⁻ polyanion) provide high activity and stability during NRR.^{25, 29} Besides, the addition of secondary metal into metal phosphate composites are known to enhance the conductivity over the monometallic counterparts and present better catalytic activity by virtue of altered geometric and electronic configurations.^{30, 31} By taking inspiration from the aforementioned statements, modification of Ag-phosphates with vanadium (V) as a secondary metal can be a generous approach due to the rich electrochemistry of vanadium metal with variable oxidation states (+2 to +5).³² In addition to it the tuning of morphology is equally important to determine the catalytic activity,^{33, 34} but the synthesis of bimetallic phosphate materials with well defined morphology rely on tedious and expensive approaches *viz.* dealloying route, templating route, galvanic replacement route, etc.³⁵ These synthetic approaches are very complicated, time consuming and yield toxic by-products and are not ideal from the practical point of view. Thus, in our work we propose the hypothesis to explore silver vanadium phosphorus oxide (Ag₂VO₂PO₄) as an electrocatalyst for electrochemical nitrogen fixation. Herein, Ag is alloyed with V as a secondary metal to enhance the conductivity, activity and N₂ adsorption in which the presence of vanadium metal can facilitate the electron transfer, the H⁺ adsorption can be reduced via presence of silver metal and phosphate moiety can provide the chemical stability to the catalyst during NRR. Notably, one-pot sonochemical synthesis is used to synthesise Ag₂VO₂PO₄ in an energy efficient and less time consuming manner to attain a well-defined rice-grain like morphology in

just few minutes. To deliberate the effect of synthesis approach towards the final morphology of catalyst and the role of morphology towards NRR, the catalyst is also synthesized by hydrothermal route. In this work, the $\text{Ag}_2\text{VO}_2\text{PO}_4$ catalyst synthesized via sonochemical route put forward a superior NRR performance with a high F.E. of 37.46% and NH_3 yield rate of $1.48 \text{ mg h}^{-1} \text{ mg}_{\text{cat.}}^{-1}$ at -0.2 V (vs. RHE) under alkaline conditions.

3B-2 Material synthesis

3B-2.1 Synthesis of $\text{Ag}_2\text{VO}_2\text{PO}_4$: The synthesis of $\text{Ag}_2\text{VO}_2\text{PO}_4$ catalyst was executed by means of sonochemical route under inert conditions. Initially, the AgNO_3 and NH_4VO_3 reactant precursors were dissolved in 35 mL of deionized water in a round bottomed flask to which an aqueous solution of H_3PO_4 was added dropwise. The addition of H_3PO_4 was accompanied by the probe sonication for a fixed interval of 1 min. and 15 seconds rest with a probe amplitude of 20 Hz for 30 minutes. After the reaction was complete, yellow precipitates of $\text{Ag}_2\text{VO}_2\text{PO}_4$ (s) were obtained which were washed with ethanol and KOH solutions to remove the NO_3 and NH_4 impurities and then dried in oven at 60°C overnight. To see the effect of synthetic route on morphology and thus activity towards NRR, identical material was synthesised using hydrothermal route in which AgNO_3 , NH_4VO_3 and H_3PO_4 were dissolved in deionized water and heated at 220°C for 24 h in an autoclave reactor. The light brown precipitates were obtained and designated as $\text{Ag}_2\text{VO}_2\text{PO}_4$ (h) which were filtered, washed and dried in a similar manner as done for $\text{Ag}_2\text{VO}_2\text{PO}_4$ (s).

3B-3 Results and discussion

3B-3.1 Physical characterization: The microstructure of the $\text{Ag}_2\text{VO}_2\text{PO}_4$ catalysts were investigated by means of P-XRD analysis. Figure 3B-1a depicted the synthesis of targeted material when matched with standard JCPDS data of $\text{Ag}_2\text{VO}_2\text{PO}_4$ (JCPDS no. 01-081-2149) crystallised in monoclinic lattice and C2/m space group with distorted VO_6 octahedra, PO_4 tetrahedra and Ag in +1 oxidation

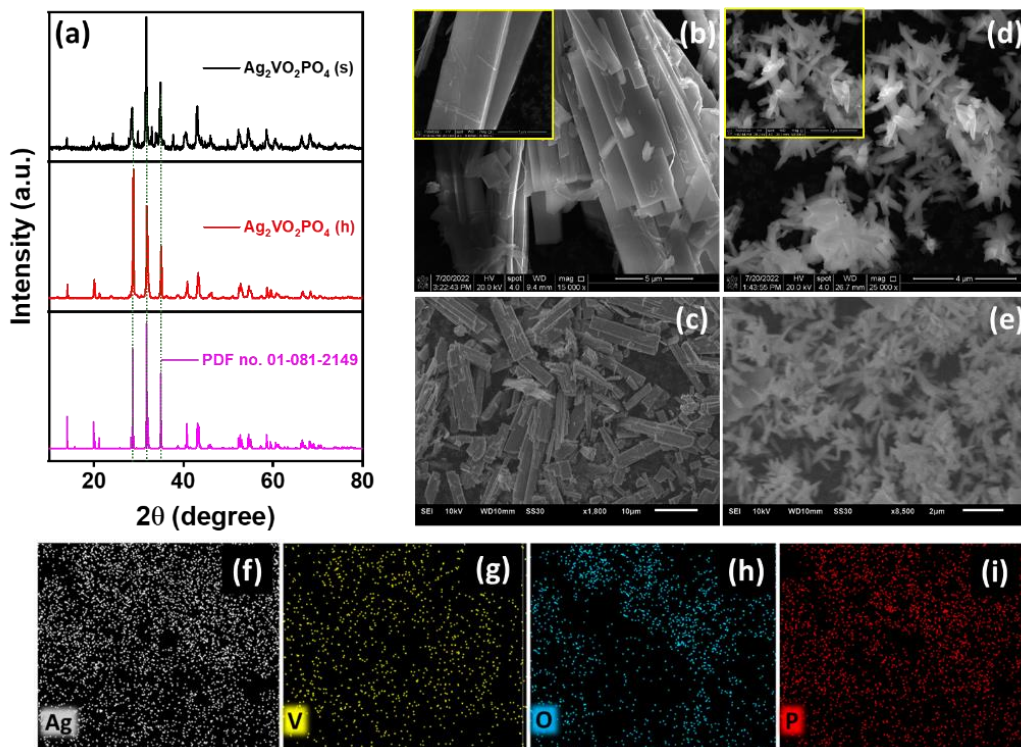


Figure 3B-1. (a) P-XRD pattern for as-synthesized $\text{Ag}_2\text{VO}_2\text{PO}_4$ catalysts via different synthetic routes and comparison with reference file. (b, d) FE-SEM and (c, e) SEM images of $\text{Ag}_2\text{VO}_2\text{PO}_4$ (h) and $\text{Ag}_2\text{VO}_2\text{PO}_4$ (s) catalysts respectively. (f-i) EDS dot mapping images showing homogeneous distribution of expected elements *i.e.* Ag, V, O and P over the scanned area.

state. The peaks obtained at 2θ value of 14.13° , 20.02° , 28.65° , 31.55° , 34.8° , 41° , 43.5° and 52.6° correspond to (110), (201), (311), (401), (221), (402), (421) and (403) planes respectively. Notably, although the synthesis route was varied, but the structural phase of the targeted material remained identical. Further, the crystallite size was calculated by using Scherrer's equation which ascertained the size of $\text{Ag}_2\text{VO}_2\text{PO}_4$ (s) and $\text{Ag}_2\text{VO}_2\text{PO}_4$ (h) to be 27.92 and 47.92 nm respectively based on the line width of highest intensity peak in relative diffraction patterns.

To further see the effect of synthesis method over the morphology of $\text{Ag}_2\text{VO}_2\text{PO}_4$ catalysts, SEM and FE-SEM analysis were carried out. A micro plate like morphology with a size and thickness of few micrometres was assimilated for

$\text{Ag}_2\text{VO}_2\text{PO}_4$ (h) catalyst from Figures 3B-1(b-c). While, a huge difference in the morphology was observed for $\text{Ag}_2\text{VO}_2\text{PO}_4$ (s) catalyst synthesized via sonochemical route where Figures 3B-1(d-e) demonstrated a typical rice-grain like morphology in nano range. This disparity in the morphology of material with same structural phase could be attributed to the decreased nucleation & growth rates and accelerated hydrolysis process under high power ultrasound waves to yield particles with narrower size distribution and high surface area at room temperatures. Further the presence and uniform distribution of expected elements *viz.* Ag, V, P and O in $\text{Ag}_2\text{VO}_2\text{PO}_4$ (s) were confirmed by EDS composition analysis (Table 3B-1) and dot mapping images shown in Figures 3B-1(f-i) respectively. Later to see the chemical state of the $\text{Ag}_2\text{VO}_2\text{PO}_4$ (s) catalyst, the XPS measurements were performed where in the survey spectrum affirmed the presence of Ag 3d, V 2p, P 2p and O 1s (Figure 3B-2a). Figure 3B-2b revealed the high-resolution deconvoluted XPS spectrum of Ag 3d with two peaks centered at a binding energy value of 374 and 368 eV, corresponding to the spin-orbit coupling of $3d_{5/2}$ and $3d_{3/2}$ states of Ag in +1 oxidation state. On the other hand, V 2p deconvoluted spectrum represented in Figure 3B-2c revealed two peaks at 516.6 ($2p_{3/2}$) and 524 eV ($2p_{1/2}$) related to +5 oxidation state of V. The P 2p deconvoluted XPS spectrum confirmed the presence of P in +5 oxidation state with major peaks at 133.2 and 132.1 eV while a broad peak appeared in O 1s XPS spectrum which upon deconvolution showed two peaks at 530.8 eV (high intensity peak due to O^{2-} of crystal lattice oxygen) and 531.9 eV (low intensity peak due to surface hydroxyl

Table 3B-1: Elemental composition analysis for $\text{Ag}_2\text{VO}_2\text{PO}_4$ (s) catalyst.

Element	Wt %	At %
O K	13.75	42.93
P K	8.64	13.93
Ag L	63.74	29.53
V K	13.88	13.61
Total	100.00	100.00

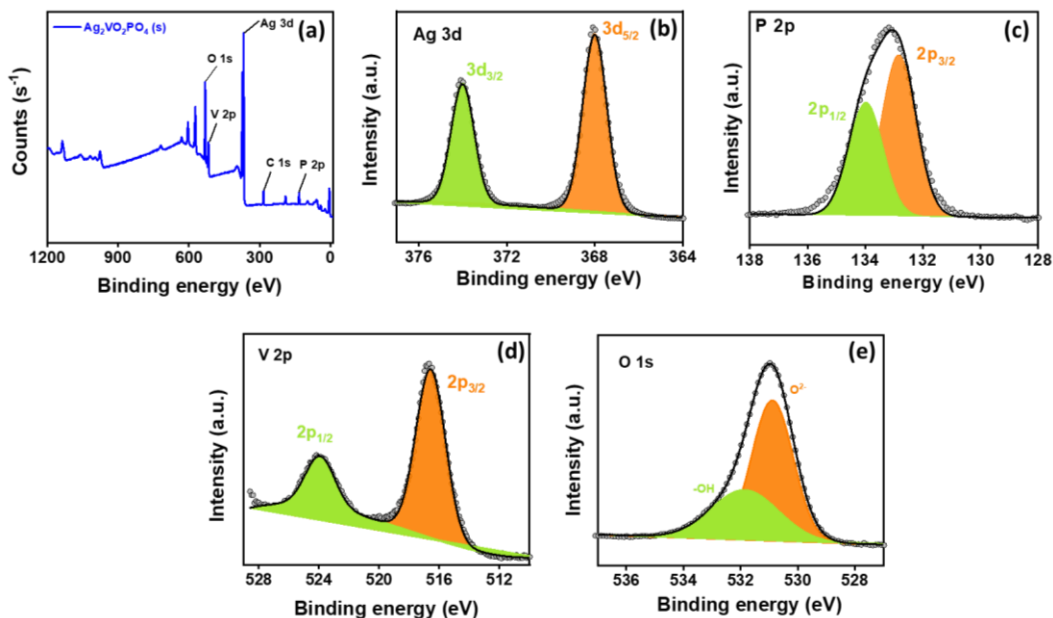


Figure 3B-2. (a) XP survey spectrum and deconvoluted XP spectrum of (b) Ag 3d, (c) P 2p, (d) V 2p, and (e) O 1s of $\text{Ag}_2\text{VO}_2\text{PO}_4$ (s) catalyst.

groups) respectively [Figures 3B-2(d-e)].

3B-3.2 Electrochemical dinitrogen reduction: After successful evaluation of physico-chemical properties of the as-synthesized catalysts, the electrocatalytic activity of the same were investigated via a series of electrochemical characterizations *c.a.* LSV, CV, CA, EIS, etc. Initially, the performance was studied in N_2 -saturated 0.1 M KOH electrolyte (pH=13) along with the control measurements in Ar-saturated electrolyte with a constant gas flow rate supply for 30 minutes before every NRR experiment. The LSV curve for $\text{Ag}_2\text{VO}_2\text{PO}_4$ catalysts presented in Figure 3B-3a were acquired in the potential range between 0 to -0.5 V vs. RHE which depicted the increase in reduction current density in absence of N_2 gas due to HER while a further increase in current density was observed under N_2 -saturated conditions due to NRR. The net current density change of 0.23 mA cm^{-2} and 0.16 mA cm^{-2} as well as more positive onset potential of -0.1 V and -0.25 V for $\text{Ag}_2\text{VO}_2\text{PO}_4$ (s) and $\text{Ag}_2\text{VO}_2\text{PO}_4$ (h) respectively in presence of N_2 in the electrolyte evidenced the possible NRR. It is noteworthy to mention that as expected, the $\text{Ag}_2\text{VO}_2\text{PO}_4$ (s) catalyst showed a high net current

density than that of $\text{Ag}_2\text{VO}_2\text{PO}_4$ (h) catalyst under identical experimental conditions entailing its superior NRR performance. Before performing NRR experiments, the gas supplies including N_2 ($^{14}\text{N}_2$ or $^{15}\text{N}_2$) and Ar were cleansed by passing through a home-made purification setup consisting of alkaline KMnO_4 solution (to trap NO_x impurities) and 0.1 N H_2SO_4 solution (to trap NH_4^+ impurities) to exclude the possibility of NH_3 overestimation. Thereafter, the assessment of electrocatalytic activity by catalysts were carried out by performing chronoamperometry (CA) at different applied potentials between -0.1 to -0.4 V for a fixed time duration of 2 h and at least three times using a three-electrode configuration in home built H-cell setup. Figures 3B-3(b-c) revealed the average current density normalized with geometric area of the electrode versus the time response at different applied potentials for $\text{Ag}_2\text{VO}_2\text{PO}_4$ catalysts, whose quantification was executed by

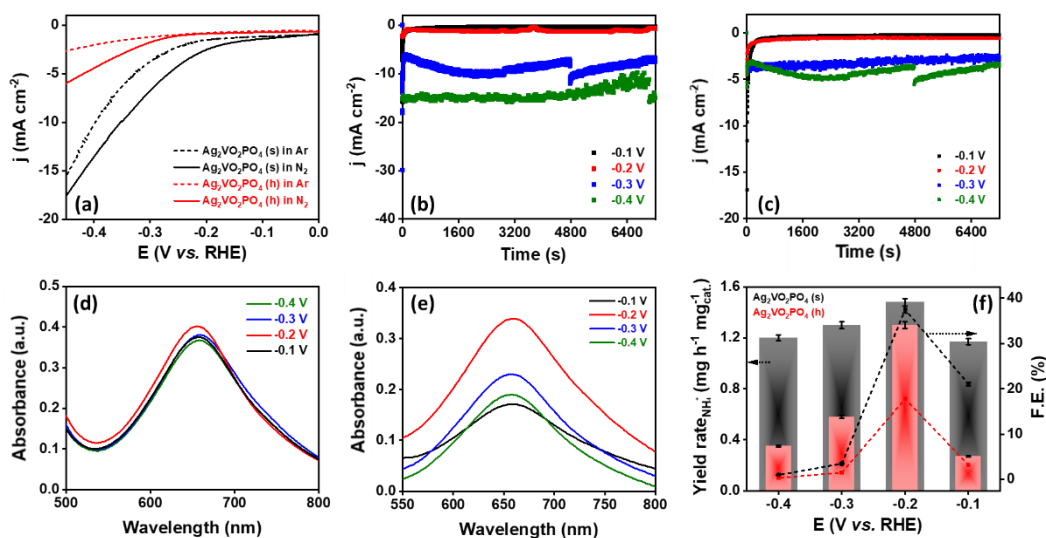


Figure 3B-3. (a) Linear sweep voltammograms for $\text{Ag}_2\text{VO}_2\text{PO}_4$ catalysts in Ar- and N_2 -saturated 0.1 M KOH electrolyte solution acquired at a scan rate of 25 mV s⁻¹, Chronoamperometric curves obtained after applying external potentials between -0.1 to -0.4 V vs. RHE for 2 h during NRR by (b) $\text{Ag}_2\text{VO}_2\text{PO}_4$ (s) and (c) $\text{Ag}_2\text{VO}_2\text{PO}_4$ (h) catalyst. UV-Vis. curve for electrolyte samples collected after quantification by Indophenol blue method upon NRR by (d) $\text{Ag}_2\text{VO}_2\text{PO}_4$ (s) and (e) $\text{Ag}_2\text{VO}_2\text{PO}_4$ (h) catalyst. (f) Comparison of NH_3 yield and F.E. of $\text{Ag}_2\text{VO}_2\text{PO}_4$ catalysts at different potentials.

Indophenol method and analysed by UV-Vis spectroscopy [Figures 3B-3(d-e)]. Figure 3B-3f evidenced the highest ammonia production yield rate and F.E. by $\text{Ag}_2\text{VO}_2\text{PO}_4$ (s) catalyst at -0.2 V (vs. RHE). The ammonia yield rate started to increase from -0.1 V to -0.2 V and achieved the highest production rate of $1.48 \text{ mg h}^{-1} \text{ mg}_{\text{cat.}}^{-1}$ at -0.2 V, however on further moving towards the negative potential region, the NH_3 production rate showed a decrease in the trend on account of the competing H_2 evolution reaction. The F.E. of the catalyst also demonstrated an analogous trend where initially it increased from 21.06% (-0.1 V) to 37.46% (-0.2 V) and subsequently decreased to 3.49% at -0.3 V respectively. The competition with HER was then affirmed by means of GC analysis which presented the expected trend in Figures 3B-4(a-c) *i.e.* the F.E. and H_2 production rate increased upon moving towards more negative potentials and exhibited yield rate of $0.0177 \text{ mmol h}^{-1} \text{ mg}^{-1}$ and selectivity of 57.59% at -0.2 V (vs. RHE). The maximum NH_3 yield rate produced by $\text{Ag}_2\text{VO}_2\text{PO}_4$ (s) catalyst was validated by Nessler's reagent test (Figure 3B-4d and Table 3B-2) which depicted the identical yield rate to that obtained from Indophenol blue method after NRR at -0.2 V. The quantification of another expected side product during NRR *viz.* N_2H_4 was carried out by Watt-Chrisp spectrophotometric method from which a N_2H_4 formation rate of $4.76 \times 10^{-6} \text{ mol cm}^{-2} \text{ h}^{-1}$ and F.E. of just 4% was attained (Figure 3B-4e). As projected, $\text{Ag}_2\text{VO}_2\text{PO}_4$ (s) catalyst revealed a superior NRR performance over $\text{Ag}_2\text{VO}_2\text{PO}_4$ (h) in terms of F.E. as well as NH_3 production yield rate (17.8% and $1.3 \text{ mg h}^{-1} \text{ mg}_{\text{cat.}}^{-1}$ @ -0.2 V. Despite of the similarities in the structural phase, elemental composition and chemical environments of the catalysts, a considerable variance is

Table 3B-2: Comparison of NH_3 yield rates obtained after 2 h of NRR by $\text{Ag}_2\text{VO}_2\text{PO}_4$ (2 h) at 0 V (vs. RHE).

S.No.	NH_3 detection method	NH_3 yield rate ($\text{mg h}^{-1} \text{ mg}_{\text{cat.}}^{-1}$)
1.	Indophenol Blue	1.48
2.	Nessler's reagent	1.49

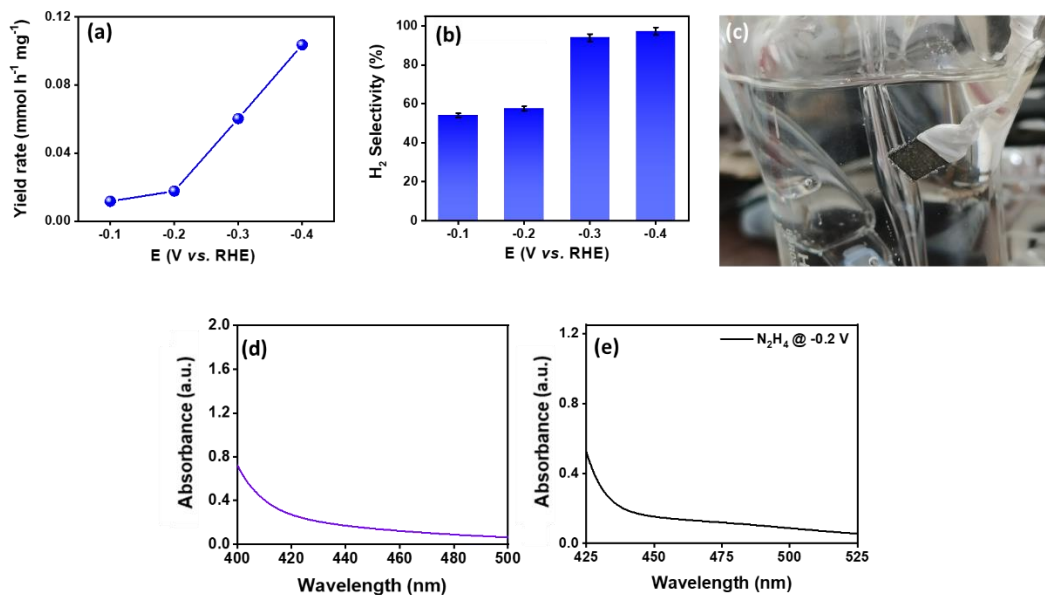


Figure 3B-4. (a) H₂ evolution yield rate and (b) H₂ selectivity (%) at different potentials calculated by GC for Ag₂VO₂PO₄ (s) catalyst. (c) Image showing the bubbles formation at electrode due to H₂ evolution in competition with NRR at -0.4 V. (d) UV-Vis. curve for electrolyte sample collected after quantification by Nessler's test upon NRR at -0.2 V by Ag₂VO₂PO₄ (s) catalyst for NH₃ detection and (e) N₂H₄ detection.

observed in NRR activity which could be endorsed to the dissimilarity in the particular morphology. The rice-grain like morphology in nano range for Ag₂VO₂PO₄ (s) could provide a comparatively higher surface area and exposed active centers for N₂ adsorption & activation along with the accelerated mass transport than that of the micro plate like morphology of Ag₂VO₂PO₄ (h). This could further be reinforced by electrochemical characterizations including ECSA, EIS and Tafel analysis. The superior activity of Ag₂VO₂PO₄ (s) was correlated with ECSA and double layer capacitance (C_{dl}) for which we performed the CV in non-faradaic region [Figures 3B-5(a-d)] for both catalysts and later extracted the linear plot of current vs. scan rate to calculate the resultant C_{dl} and ECSA values. Table 3B-3 revealed the high C_{dl} of 7.94 mF and ECSA of 19.85 cm² for Ag₂VO₂PO₄ (s) catalyst than Ag₂VO₂PO₄ (h), suggesting the augmented number of exposed active centers for N₂ adsorption.

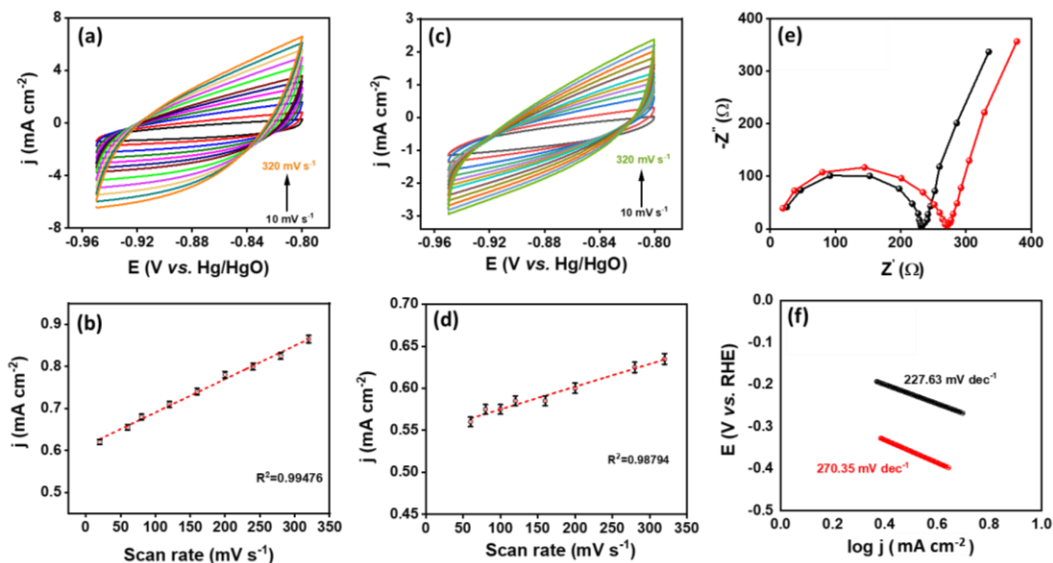


Figure 3B-5. (a, c) Cyclic voltammograms for $\text{Ag}_2\text{VO}_2\text{PO}_4$ (s), $\text{Ag}_2\text{VO}_2\text{PO}_4$ (h) catalyst at different scan rates and (b, d) corresponding current density vs. scan rate plots extracted from the CVs respectively. (e) Nyquist plots for both of the catalysts at -0.2 V (vs. RHE) and (f) Tafel plots extracted from Fig. 3a for evaluation of NRR+HER kinetics (color: red- $\text{Ag}_2\text{VO}_2\text{PO}_4$ (h); black- $\text{Ag}_2\text{VO}_2\text{PO}_4$ (s)).

The electron transfer kinetics at electrode-electrolyte interface were also scrutinized by EIS and Tafel analysis. EIS measurements were accomplished to calculate the charge transfer resistances (R_{ct}) at -0.2 V where the Nyquist plot shown in Figure 3B-5e revealed the semicircle in the lower frequency region related to the hybrid R_{ct} for HER and NRR. An increase in charge transfer resistance was observed from 209.30Ω to 251.89Ω for $\text{Ag}_2\text{VO}_2\text{PO}_4$ (s) and $\text{Ag}_2\text{VO}_2\text{PO}_4$ (h) respectively, illustrating the accelerated electron transfer kinetics at the interface

Table 3B-3: Electrochemical surface area (ECSA) determination from Figure 3B-5 for different catalysts.

S.No.	Electrocatalyst	C_{dl}^* (mF)	ECSA (cm^2)
1.	$\text{Ag}_2\text{VO}_2\text{PO}_4$ (s)	7.94	19.85
2.	$\text{Ag}_2\text{VO}_2\text{PO}_4$ (h)	2.698	6.745

in $\text{Ag}_2\text{VO}_2\text{PO}_4$ (s) owing to the formation of relatively thin diffusion layer (Table 3B-4). In the end, Tafel slopes were evaluated from which a lower Tafel slope value of $227.63 \text{ mV dec}^{-1}$ was achieved for the sonochemically synthesized $\text{Ag}_2\text{VO}_2\text{PO}_4$ catalyst (Figure 3B-5f). This lower Tafel slope value further reinforced the facilitated electron transfer at $\text{Ag}_2\text{VO}_2\text{PO}_4$ (s) surface by virtue of its enhanced surface area, exposed active sites, electron transfer ability of $[\text{PO}_4]^{3-}$ cluster and the synergistic effect between the metals centers (Ag & V), where in all the aforementioned factors contributed towards the improved intrinsic NRR activity for accelerated electron transfer and boosted N_2 adsorption.

Table 3B-4: Electrochemical Impedance analysis extracted from Figure 3B-5.

S. No.	Electrocatalyst	$R_s (\Omega)$	$R_p (\Omega)$	$R_{ct} (\Omega)$
1.	$\text{Ag}_2\text{VO}_2\text{PO}_4$ (s)	24.53	233.83	209.30
2.	$\text{Ag}_2\text{VO}_2\text{PO}_4$ (h)	20.06	271.95	251.89

3B-3.3 Identification/elimination of N-contamination during NRR: True estimation of NH_3 yield rate after N_2 reduction has become a challenging quest due to contribution of self-electrolysis of the electrode catalysts, environmental impurities and N-labile contaminations present in electrolyte solutions and gas-supplies. And therefore to avoid the false estimation of produced ammonia yield rate, the rigorous set of protocol were followed which involved the detection and elimination of the N-contaminations from; (i) the catalyst, since it involved NO_3^- and NH_4^+ based reactant precursors, (ii) the electrolytes used and (iii) gas-supplies viz. $^{14}\text{N}_2$, $^{15}\text{N}_2$ & Ar respectively. The $\text{Ag}_2\text{VO}_2\text{PO}_4$ catalysts were cleansed using alkaline KOH solution to remove any unreacted N-containing impurities³⁶ followed by the detection of NO_3^- and NO_2^- impurities in electrolyte used i.e. KOH.³⁷ The absence of nitrate and nitrite in the 0.1 M KOH electrolyte ruled out the likelihood of false NH_3 assessment from the electrolyte system [Figures 3B-6(a-b)]. Afterwards, the most crucial source of contamination i.e. gas supplies were

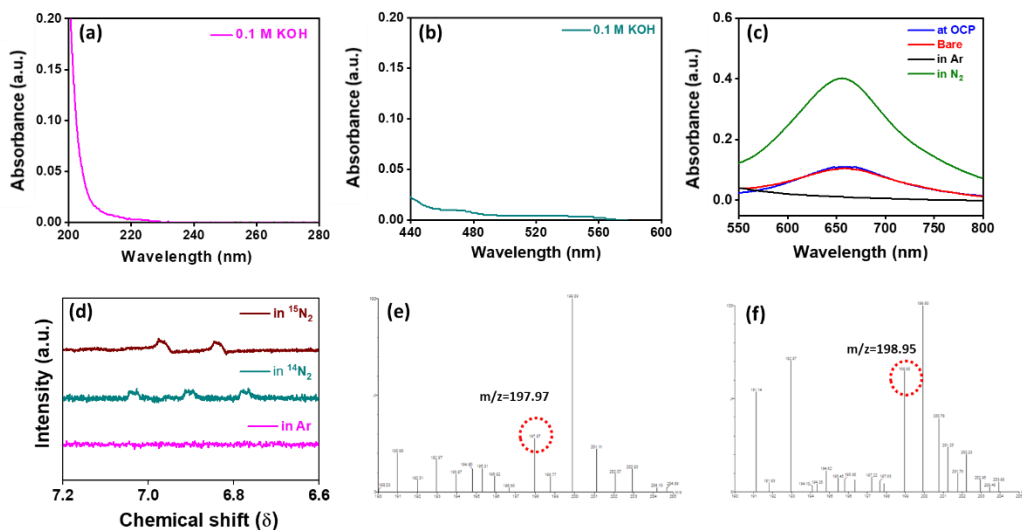


Figure 3B-6. UV-Vis. absorbance curves acquired for determination of (a) nitrate and (b) nitrite in electrolyte solutions by spectrophotometric methods. (c) UV-Vis. absorbance curves obtained after control NRR experiments over bare glassy carbon electrode and $\text{Ag}_2\text{VO}_2\text{PO}_4$ (s) coated glassy carbon electrode in N_2 -saturated, Ar-saturated electrolyte media at -0.2 V and in N_2 saturated conditions at open circuit voltage. (d) ^1H -NMR spectrum for electrolyte samples collected after isotope labelling NRR experiment in different gas-feed environments. (e-f) The mass spectrum for electrolyte samples collected after isotope labelling NRR experiments by $\text{Ag}_2\text{VO}_2\text{PO}_4$ (s) catalyst showing formation of ^{14}N -Indophenol and ^{15}N -indophenol red dye respectively.

analysed for $\text{NO}_x/\text{NH}_4^+$ impurities to eliminate the contribution towards NH_3 overestimation. The NO_x and NH_4^+ impurities in gas-supplies were quantified by means of spectrophotometric method³⁸ (for NO , NO_2 & NH_4^+) and GC-MS method (for N_2O)³⁹, which revealed a total of 0.6, 1.16 & 1.27 ppm of NO_x and 0.0, 0.09 & 0.08 ppm of NH_4^+ for Ar, $^{14}\text{N}_2$ and $^{15}\text{N}_2$ respectively.

These detected impurities in gas-supplies were effectually trapped after passing through the home-made purification setup described previously which was confirmed by again quantifying the expected impurities which didn't show any trace of the same (Table 3B-5). This analysis authorized that the NH_3 produced in this work was due to the N_2 gas fed into the electrolyte rather than any N-containing

impurity. In addition to it, other control experiments were also executed such as CA at -0.2 V by $\text{Ag}_2\text{VO}_2\text{PO}_4$ (s) in Ar-saturated 0.1 M KOH, over bare electrode and at OCP in N_2 -saturated 0.1 M. Upon quantification of NH_3 after control measurements by Indophenol blue method, a negligible NH_3 production yield was obtained indicating the NH_3 generation by N_2 reduction exclusively (Figure 3B-6c).

Table 3B-5: Detection and elimination of $\text{NO}_x/\text{NH}_4^+$ impurities from gas-supplies by colorimetric and GC-MS technique using purification setup.

S.No.	Gas supply	Conc. of contaminations before purification (ppm)			Conc. of contaminations after purification (ppm)		
		NO/NO ₂	N ₂ O	NH ₄ ⁺	NO/NO ₂	N ₂ O	NH ₄ ⁺
1.	Ar (99.99%, Sigma)	0.6	<0.01	-	-	-	-
2.	¹⁴ N ₂ (99.99% Sigma)	1.1	0.06	0.09	<0.01	<0.01	-
3.	¹⁵ N ₂ (98%, Sigma)	1.2	0.07	0.08	<0.01	<0.01	-

3B-3.4 Isotope labelling experiments: To offer an additional evidence for the ability of $\text{Ag}_2\text{VO}_2\text{PO}_4$ (s) catalyst towards genuine NH_3 production and contribution of N_2 as the only source for ammonia, isotope labelling experiments were conducted for qualitative as well as quantitative estimation of $^{14}\text{NH}_4^+$ & $^{15}\text{NH}_4^+$ species by ^1H -NMR spectroscopy and LC-MS.^{40, 41} The isotope labelling experiments were performed by means of CA at -0.2 V for 2 h by the catalyst in $^{15}\text{N}_2$ -saturated and $^{14}\text{N}_2$ -saturated 0.1 M KOH solutions under identical conditions after which the electrolyte aliquots were collected and tested for NH_3 production. A distinct triplet coupling for $^{14}\text{NH}_4^+$ was observed after NRR using $^{14}\text{N}_2$ gas supply, however a doublet coupling for $^{15}\text{NH}_4^+$ was witnessed when $^{15}\text{N}_2$ gas was fed into the electrolyte (Figure 3B-6d). In addition to it, the m/z value of 197.97

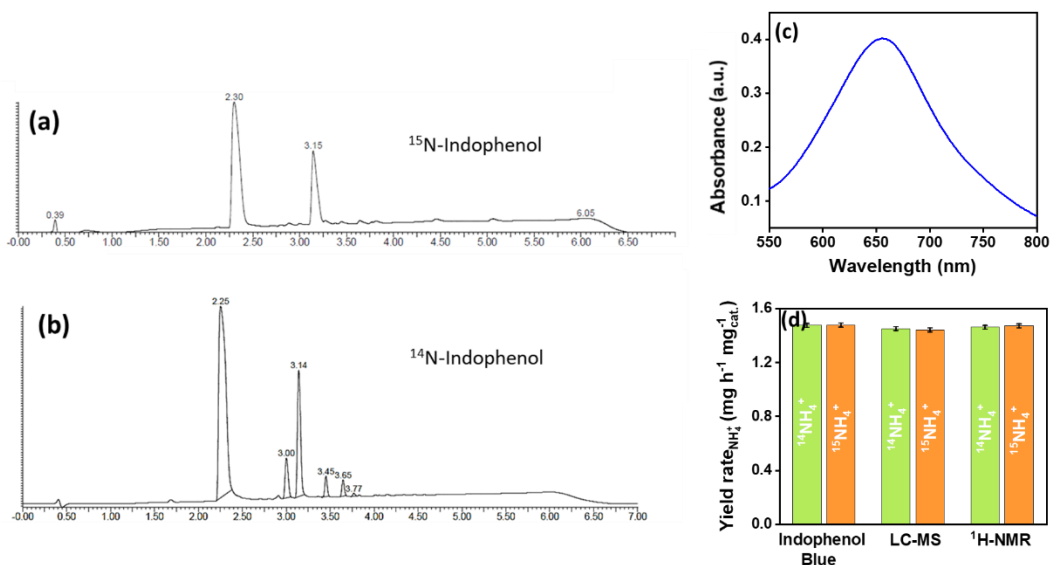


Figure 3B-7. (a-b) Liquid chromatograms obtained for electrolyte sample solutions collected after 2 hours of isotope labelling NRR experiments by $\text{Ag}_2\text{VO}_2\text{PO}_4$ (s) catalyst at -0.2 V (vs. RHE). (c) UV-Vis. absorbance curve obtained after isotope labelling NRR measurement at -0.2 V by $\text{Ag}_2\text{VO}_2\text{PO}_4$ (s) catalyst in $^{15}\text{N}_2$ -saturated 0.1 M KOH solution. (d) Comparison of $^{14}\text{NH}_4^+ / ^{15}\text{NH}_4^+$ yield rates quantified by different methods after NRR by $\text{Ag}_2\text{VO}_2\text{PO}_4$ (s) catalyst.

and 198.95 were observed for electrolyte samples collected after NRR in $^{14}\text{N}_2$ - and $^{15}\text{N}_2$ -saturated electrolyte corresponding to the formation of ^{14}N - and ^{15}N -Indophenol respectively [Figures 3B-6(e-f)]. Nevertheless, these results provided the qualitative assurance for N_2 as the exclusive source for NH_3 production and to further certify it, quantitative estimations were also performed. The NH_3 yield rates were calculated from the standard calibration curves extracted from NMR and LC-MS quantification methods which revealed an ammonia yield rate of 1.46 & 1.47 $\text{mg h}^{-1} \text{mg}_{\text{cat}}^{-1}$ and 1.45 & 1.44 $\text{mg h}^{-1} \text{mg}_{\text{cat}}^{-1}$ for $^{14}\text{NH}_4^+$ & $^{15}\text{NH}_4^+$ respectively from NMR and LC-MS [Figures 3B-7(a-b)]. The yield rates obtained after isotope labelling NRR were also quantified using Indophenol blue method (Figure 3B-7c) and demonstrated the similar values with $^{14}\text{NH}_4^+$ yield of 1.475 $\text{mg h}^{-1} \text{mg}_{\text{cat}}^{-1}$ and $^{15}\text{NH}_4^+$ yield of 1.476 $\text{mg h}^{-1} \text{mg}_{\text{cat}}^{-1}$. Figure 3B-7d showed the bar diagram

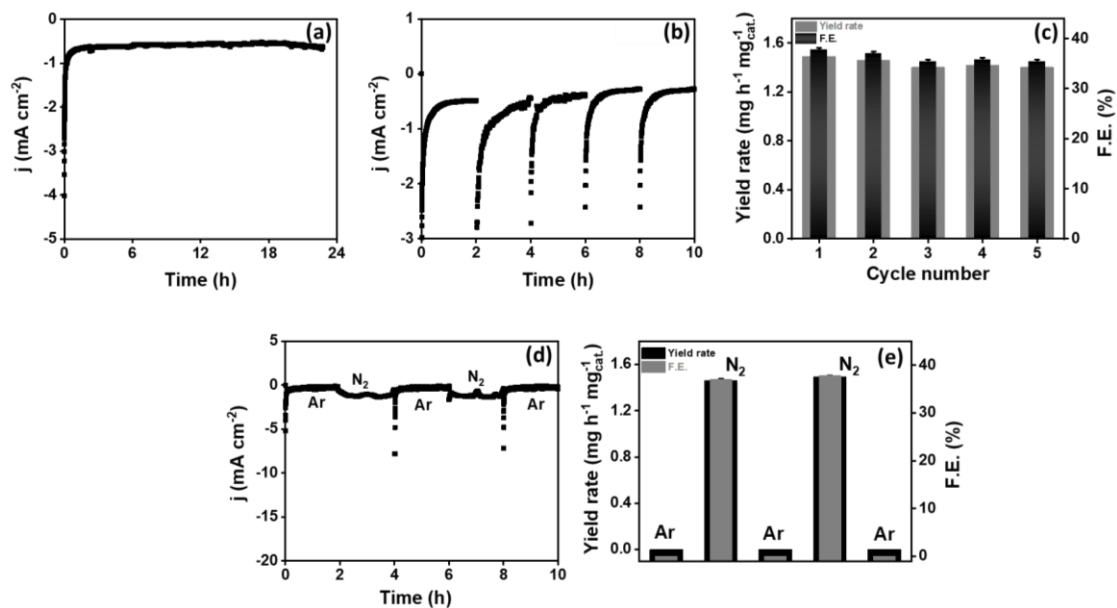


Figure 3B-8. (a) Chronoamperometry curve obtained after 24 hours of NRR at -0.2 V (vs. RHE) in N_2 -saturated 0.1 M KOH solution. (b) Chronoamperometry curves for NRR stability tests (5 consecutive cycles) in 0.1 M KOH solution by $\text{Ag}_2\text{VO}_2\text{PO}_4$ (s) catalyst at -0.2 V of applied potential. (c) Bar graph comparison of NH_3 yield rate and F.E. after NRR by $\text{Ag}_2\text{VO}_2\text{PO}_4$ (s) catalyst for 5 consecutive cycles at -0.2 V. (d) Switching chronoamperometry curves for $\text{Ag}_2\text{VO}_2\text{PO}_4$ (s) catalyst in different gas-feed environments (Ar and N_2) and (e) corresponding bar diagram for comparison of NH_3 yield rate and F.E.

comparison of NH_3 yield rates quantified by different methods after isotope labelling experiments and thus concluded the true and reliable ammonia production by $\text{Ag}_2\text{VO}_2\text{PO}_4$ (s) catalyst in 0.1 M KOH electrolyte.

3B-3.5 NRR Stability tests and post-stability material characterizations: In the end, the stability of the $\text{Ag}_2\text{VO}_2\text{PO}_4$ (s) catalyst was assessed. Chronoamperometric analysis was carried out for nonstop 10 h (5 cycles of 2 h each) at an applied potential of -0.2 V (vs. RHE) in N_2 -saturated 0.1 M KOH in which no attenuation in current density was witnessed for both 10 h and 24 h of NRR [Figures 3B-8(a-b)]. Remarkably, the F.E. and yield rate were also retained without any extensive decay after prolonged NRR *i.e.* from 37.75% & $1.49 \text{ mg h}^{-1} \text{ mg}_{\text{cat}}^{-1}$ to 35.42% & $1.4 \text{ mg h}^{-1} \text{ mg}_{\text{cat}}^{-1}$ (Figure 3B-8c). This ascertained the retention of around 94% of

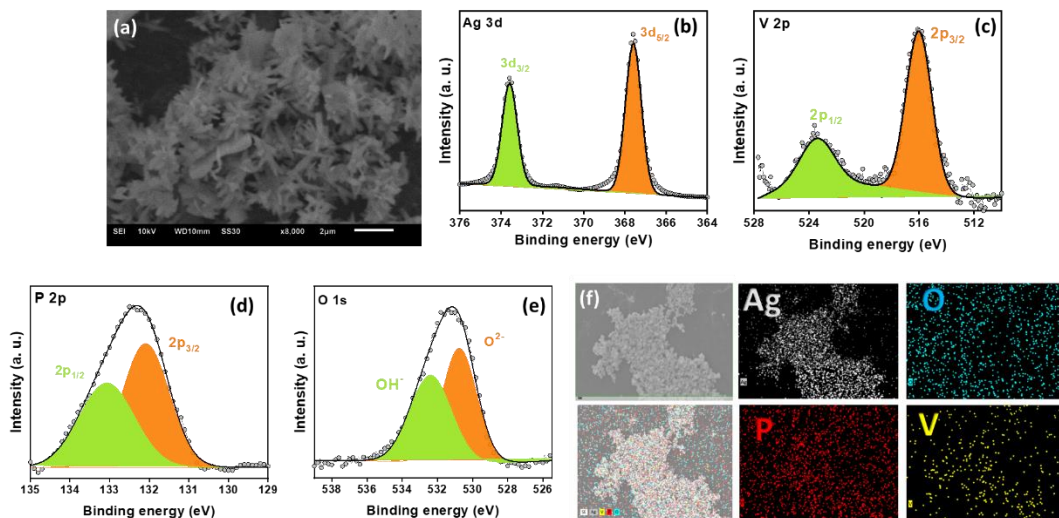


Figure 3B-9. (a) SEM image, XP deconvoluted spectrum of (b) Ag 3d, (c) V 2p, (d) P 2p, and (e) O 1s and (f) EDS dot mapping profiles for individual elements for $\text{Ag}_2\text{VO}_2\text{PO}_4$ (s) catalyst after NRR stability tests.

the initial NRR activity of catalyst after prolonged stability measurements. The catalyst stability was also studied under switching gas-supplies by similar CA measurements by simply switching the gas from Ar to N_2 and vice versa. The rapid change in current density on switching the gas-supply was depicted in Figure 3B-8d, imitating the high durability of $\text{Ag}_2\text{VO}_2\text{PO}_4$ (s) catalyst under different gaseous environments. In addition to it, no NH_3 production was perceived in presence of Ar but a high F.E. as well as NH_3 yield rate was beheld in presence of N_2 in the electrolyte solution (Figure 3B-8e).

The stability of morphological and elemental attributes of the catalyst were further analysed after prolonged NRR investigations. The SEM image shown in Figure 3B-9a revealed that the catalyst retained its rice-grain like morphology even after NRR. On the other hand, neither the chemical states [Figures 3B-9(b-e)], nor the elemental distribution (Figure 3B-9f) exposed any noticeable variation which was verified by XPS and EDS dot mapping analysis. All these outcomes asserted the robustness of $\text{Ag}_2\text{VO}_2\text{PO}_4$ (s) catalyst in due course of NRR for an extended time duration. As a future perspective, the bimetallic phosphates particularly Ag-based

phosphates doped with secondary transition metal could be utilised to improve the activity towards NRR and the amount of secondary metal doping could be tuned for enhanced activity.

3B-4 Summary

In conclusion, an energy efficient and less time consuming sonochemical route was presented for the synthesis of targeted bimetallic phosphate material ($\text{Ag}_2\text{VO}_2\text{PO}_4$) in comparison to the hydrothermal synthesis route. The effect of synthesis over morphology and thus NRR activity was evaluated. The as-synthesised $\text{Ag}_2\text{VO}_2\text{PO}_4$ (s) catalyst with rice-grain like morphology could achieve an ammonia yield rate as high as $1.48 \text{ mg h}^{-1} \text{ mg}_{\text{cat}}^{-1}$ along with a high F.E. of 37.46%, that too at an applied potential of just -0.2 V vs. RHE . The catalyst not only showed high activity but also a high durability for prolonged NRR with retention of current response, yield rate and F.E. as well. It is noteworthy to mention that the morphology, chemical states were not affected after the stability measurements. Moreover, the rigorous protocol utilized for identification and further elimination of the N-contaminants present in catalyst/electrolyte/electrode/cell-system/gas-supplies, allowed us to demonstrate the true and reliable NH_3 production in this work. Henceforth, the alloying of the silver based phosphate materials with a secondary metal with targeted morphology could be an interesting approach for improved activity and selectivity towards sustainable NH_3 synthesis in ambient conditions.

3B-5 References

1. J. N. Galloway, F. J. Dentener, D. G. Capone, E. W. Boyer, R. W. Howarth, S. P. Seitzinger, G. P. Asner, C. C. Cleveland, P. Green and E. A. Holland, *Biogeochemistry*, 2004, **70**, 153-226.
2. I. McPherson and J. Zhang, *Joule*, 2020, **4**, 12-14.
3. D. R. MacFarlane, P. V. Cherepanov, J. Choi, B. H. Suryanto, R. Y. Hodgetts, J. M. Bakker, F. M. F. Vallana and A. N. Simonov, *Joule*, 2020, **4**, 1186-1205.
4. A. Klerke, C. H. Christensen, J. K. Nørskov and T. Vegge, *J. Mater. Chem.*, 2008, **18**, 2304-2310.
5. J. Cha, Y. Park, B. Brigljević, B. Lee, D. Lim, T. Lee, H. Jeong, Y. Kim, H. Sohn and H. Mikulčić, *Renew. Sustain. Energy Rev.*, 2021, **152**, 111562.
6. J. W. Erisman, M. A. Sutton, J. Galloway, Z. Klimont and W. Winiwarter, *Nat. Geosci.*, 2008, **1**, 636-639.

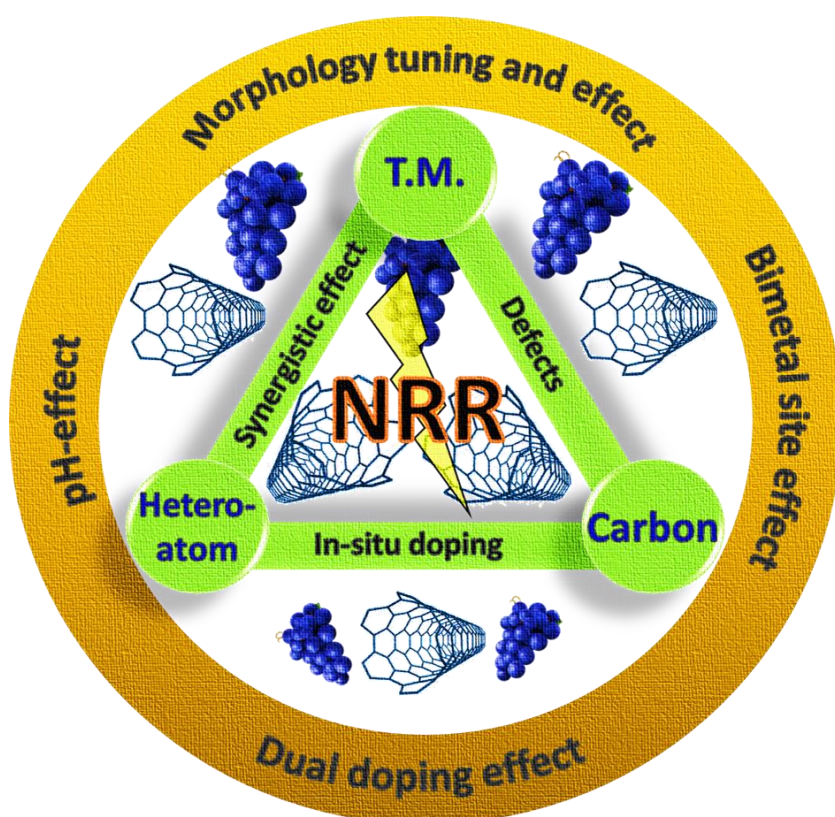
7. V. Pattabathula and J. Richardson, *Chem. Eng. Prog.*, 2016, **112**, 69-75.
8. T. Brown, *Journal*, 2016, **29**, 925-940.
9. R. Schlögl, *Angew. Chem. Int. Ed.*, 2003, **42**, 2004-2008.
10. S. Ghavam, M. Vahdati, I. Wilson and P. Styring, *Frontiers in Energy Research*, 2021, **9**, 34.
11. J. Baltrusaitis, *J. Climate*, 2017, **5**, 9527-9527.
12. F. Jiao and B. Xu, *Adv. Mater.*, 2019, **31**, 1805173.
13. H. Xu, K. Ithisuphalap, Y. Li, S. Mukherjee, J. Lattimer, G. Soloveichik and G. Wu, *Nano Energy*, 2020, **69**, 104469.
14. T. Wu, W. Fan, Y. Zhang and F. Zhang, *Mater. Today Phys.*, 2021, **16**, 100310.
15. J. Kibsgaard, J. K. Nørskov and I. Chorkendorff, *ACS Energy Lett.*, 2019, **4**, 2986-2988.
16. X. Zhao, G. Hu, G. F. Chen, H. Zhang, S. Zhang and H. Wang, *Adv. Mater.*, 2021, **33**, 2007650.
17. X. Liu, Y. Jiao, Y. Zheng, M. Jaroniec and S.-Z. Qiao, *J. Am. Chem. Soc.*, 2019, **141**, 9664-9672.
18. H. Huang, L. Xia, X. Shi, A. M. Asiri and X. Sun, *Chem. Commun.*, 2018, **54**, 11427-11430.
19. Q. Zhang, Y. Shen, Y. Hou, L. Yang, B. Chen, Z. Lei and W. Zhang, *Electrochim. Acta*, 2019, **321**, 134691.
20. W. Li, K. Li, Y. Ye, S. Zhang, Y. Liu, G. Wang, C. Liang, H. Zhang and H. Zhao, *Commun. Chem.*, 2021, **4**, 1-11.
21. Y. Li, H. Yu, Z. Wang, S. Liu, Y. Xu, X. Li, L. Wang and H. Wang, *Chem. Commun.*, 2019, **55**, 14745-14748.
22. H. Wang, S. Liu, H. Zhang, S. Yin, Y. Xu, X. Li, Z. Wang and L. Wang, *Nanoscale*, 2020, **12**, 13507-13512.
23. Z. Wang, W. Tian, Z. Dai, P. Wang, Y. Xu, X. Li, L. Wang and H. Wang, *Mater. Today Energy*, 2021, **21**, 100771.
24. H. Yu, Z. Wang, D. Yang, X. Qian, Y. Xu, X. Li, H. Wang and L. Wang, *J. Mater. Chem. A*, 2019, **7**, 12526-12531.
25. D. Gupta, A. Kafle, S. Kaur, P. Parimita Mohanty, T. Das, S. Chakraborty, R. Ahuja and T. C. Nagaiah, *J. Mater. Chem. A*, 2022, DOI: 10.1039/D2TA04155C.
26. R. Chen, D. Chen and Y. Xiao, *Mater. Today Energy*, 2021, **20**, 100684.
27. M. Nazemi, P. Ou, A. Alabbady, L. Soule, A. Liu, J. Song, T. A. Sulchek, M. Liu and M. A. El-Sayed, *ACS Catal.*, 2020, **10**, 10197-10206.
28. F. Pang, F. Wang, L. Yang, Z. Wang and W. Zhang, *Chem. Commun.*, 2019, **55**, 10108-10111.
29. J. Huang, A. C. Marschilok, E. S. Takeuchi and K. J. Takeuchi, *Chem. Mater.*, 2016, **28**, 2191-2199.
30. J. Wu, J. Zhang, Z. Peng, S. Yang, F. T. Wagner and H. Yang, *J. Am. Chem. Soc.*, 2010, **132**, 4984-4985.
31. T. Guo, L. Zhang, S. Yun, J. Zhang, L. Kang, Y. Li, H. Li and A. Huang, *Mater. Res. Bull.*, 2019, **114**, 80-84.
32. K. C. Kirshenbaum, D. C. Bock, A. B. Brady, A. C. Marschilok, K. J. Takeuchi and E. S. Takeuchi, *Phys. Chem. Chem. Phys.*, 2015, **17**, 11204-11210.
33. Y. Luo, L. Tang, U. Khan, Q. Yu, H.-M. Cheng, X. Zou and B. Liu, *Nature Commun.*, 2019, **10**, 1-9.
34. Y. Wan, J. Xu and R. Lv, *Mater. Today*, 2019, **27**, 69-90.
35. H. Zhao and Z. Y. Yuan, *ChemCatChem*, 2020, **12**, 3797-3810.
36. U. B. Shahid, Y. Chen, S. Gu, W. Li and M. Shao, *Trends Chem.*, 2022, **4**, 142-156.
37. L. Li, C. Tang, D. Yao, Y. Zheng and S.-Z. Qiao, *ACS Energy Lett.*, 2019, **4**, 2111-2116.
38. J. Choi, B. H. Suryanto, D. Wang, H.-L. Du, R. Y. Hodgetts, F. M. Ferrero Vallana, D. R. MacFarlane and A. N. Simonov, *Nat. Commun.*, 2020, **11**, 1-10.
39. D. Ekeberg, G. Ogner, M. Fongen, E. J. Joner and T. Wickstrøm, *J. Environ. Monit.*, 2004, **6**, 621-623.

Chapter 3B

40. S. Z. Andersen, V. Čolić, S. Yang, J. A. Schwalbe, A. C. Nielander, J. M. McEnaney, K. Enemark-Rasmussen, J. G. Baker, A. R. Singh and B. A. Rohr, *Nature*, 2019, **570**, 504-508.
41. S. E. Saji, H. Lu, Z. Lu, A. Carroll and Z. Yin, *Small Methods*, 2021, **5**, 2000694.

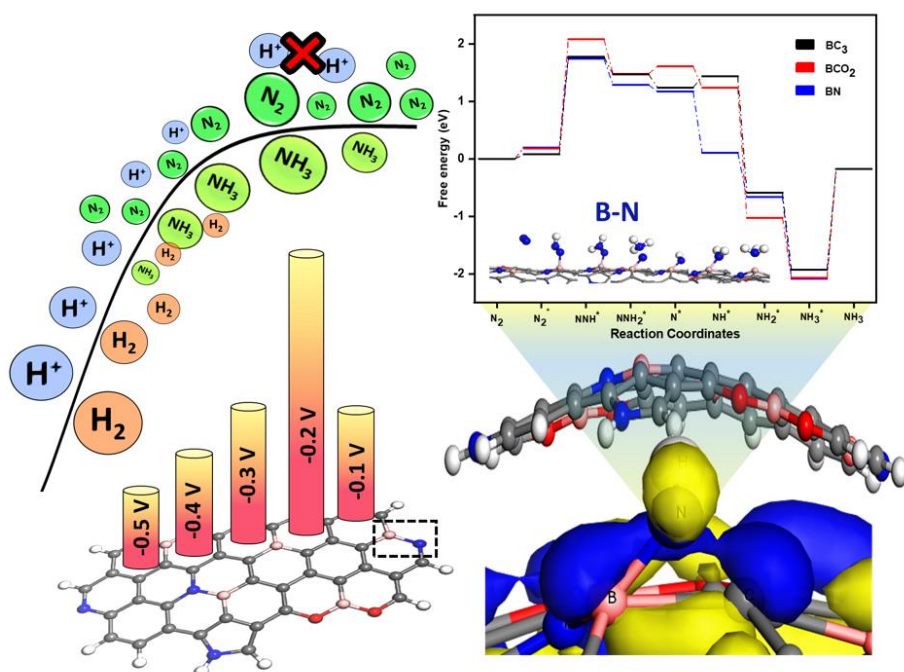
Chapter 4

Development of non-noble metal based catalysts for the electrochemical synthesis of NH_3



Chapter 4A

Selective electrochemical conversion of N_2 to NH_3 in neutral media using B, N containing carbon with nanotubular morphology



4A-1 Introduction

Ammonia (NH_3) plays a key role in fertilizer industry due to which its global production has increased to 172 million tons in 2017 and is estimated to reach upto 280.36 million tons in 2022.^{1,2,3} The energy intensive Haber Bosch process is responsible for NH_3 production at industrial scale⁴ but is associated with extensive energy requirement for $\text{N}\equiv\text{N}$ triple bond cleavage, dependence on steam reformation for H_2 production and harsh conditions of temperature and pressure. It accounts for more than 2% of world-wide energy consumption ($34 \text{ GJ ton}_{\text{NH}_3}^{-1}$) and heavy CO_2 emissions ($2 \text{ ton}_{\text{CO}_2} \text{ ton}_{\text{NH}_3}^{-1}$),⁵ and therefore obliges an alternative NH_3 production technology to accomplish long standing distribution of NH_3 for fertilizers and/or fuel technologies.⁶⁻⁸ N_2 conversion to NH_3 via electrochemical pathway is recognized to hold a great potential in terms of small scale and carbon-free ammonia synthesis under ambient conditions.^{9,10} But, it stresses over clogging of certain bottlenecks including $\text{N}\equiv\text{N}$ triple bond activation and adsorption, large HOMO-LUMO gap and competition with hydrogen evolution reaction (HER).^{11,12} This can be accomplished via designing and development of efficient heterogeneous catalysts, operational under ambient conditions for NRR.¹³ More specifically, the electrocatalyst must be able to reduce N_2 at lower overpotentials and suppress the competing HER in order to realize a high activity and selectivity towards NRR.¹⁴⁻¹⁶ To date many sophisticated electrocatalysts are reported in the literature, comprising transition metals based and metal-free carbon based. N-doped carbon materials are found to be very much attractive since they can modify the electronic properties of the carbon catalyst and facilitate selective N_2 adsorption. Plentiful of work is available for boosted NRR by N-doped carbons, however the poor Faradaic efficiency and yield rate hampers the practical implementation. To improve the activity of N-doped carbons, the addition of another heteroatoms viz. B, S and P can be a good strategy which results into more electrochemically active sites due to the synergistic effect and co-activation with adjacent carbon atom.¹⁷⁻¹⁹

We foresee a B, N containing carbon catalyst for selective electrochemical dinitrogen reduction in present study. This is based on the charge polarization between boron and adjacent carbon atoms which can aid the N₂ adsorption and activate it by donation of electron from partially occupied B-atom to the antibonding π^* orbital of N₂ via π -back bonding²⁰ and decrease N≡N bond order^{17,19}, similar to a pioneering work by Legare *et al.*²¹ for N₂ activation by borylene units. Besides, the Lewis acidic site^{22, 23} in B-doped carbon framework, presence of three valence electrons in boron and a vacant orbital equivalent to unoccupied *d*-orbital of transition metals (TM), makes it a better choice over other heteroatoms since it can bind with N₂ via π -back bonding.²⁰ More interestingly, Boron can also obstruct the H⁺ adsorption, suppress HER and hence promote NRR to imitate improved F.E. and NH₃ yield rate.^{24, 25} For example, Li *et al.*³⁴ reported electronically coupled BNQDs/C₃N₄ for NRR and achieved an ammonia yield rate of 72.3 $\mu\text{g h}^{-1} \text{mg}^{-1}$ (-0.3 V) and a F.E. of 19.5% (-0.2 V) where the BNQDs and C₃N₄ cooperatively adsorb N₂ and stabilize *N₂H intermediate for enhanced NRR. The synthesis of these heteroatom containing carbon catalysts is generally carried out by polymer pyrolysis or thermal doping of heteroatoms, which results into complex catalyst structure, deficient active sites, poor graphitization and low electrical conductivity of final composite.²⁶ In this regard, the simplified synthesis of heteroatom containing carbon with well-defined structure and morphology is critical. Very recently, P-doped carbon nanotubes (P-CNTs) were explored as NRR catalyst with a high NH₃ yield rate of 24.4 $\mu\text{g h}^{-1} \text{mg}_{\text{cat}}^{-1}$ due to P doping and highly conjugated CNTs.²⁷

Inspired from the abovementioned specifics, we hypothesize B & N containing carbon with nanotube morphology as an efficient catalyst for NRR, in which the e^- deficient B sites and B, N co-doping could activate the adjacent carbon and enhance the selective N₂ adsorption whereas the nanotube morphology can facilitate the electron as well as mass transfer. Also the development of exciting synthesis methods for heteroatom containing carbon materials is important to substitute the complex and costly practices such as arc discharge, laser ablation and chemical

vapor deposition.²⁸ In this context, metal-organic frameworks (MOF) are being explored to synthesize functional materials with porous structures and tailored compositions through morphology and pore control for energy related applications.²⁹ MOFs can also be used as precursors for the simplified synthesis of porous carbon/carbon nanotubes materials.³⁰ But then again, the low amount of dopants and/or low surface area obtained in heteroatom containing carbon materials impules for some solution. A recent literature report explains the application of ionic liquid (IL)-MOF composite as a precursor for synthesis of secondary heteroatom doped carbon to achieve a large surface area, narrow pore size distribution and increased amount of heteroatom doping.³¹

In this work we put forward an effective stratagem to synthesize B, N containing carbon by pyrolysing a MOF-IL composite at different temperatures and evaluate its performance towards NRR in neutral media (pH=7). The rupture of co-ordination bonds during thermal treatment of MOF-IL precursor (containing B, N heteroatoms) at an optimal temperature assist the development of B, N containing carbon with nanotubular morphology. The comprehensive experimental and theoretical analyses envisage the role of B-N bonds towards selective adsorption and activation of N₂ molecule to produce ammonia.

4A-2 Material synthesis

4A-2.1 Synthesis of [BMIM]⁺ Br⁻: A 1000 mL round-bottomed flask was taken to which a mixture of 1-methylimidazole (164.200 g, 2000.00 mmol) and n-butyl bromide (411.660 g, 3004.38 mmol) was added and the reaction mixture was stirred for 30 min. under N₂ atmosphere and room temperature. Above reaction mixture (60 mL) was then transferred to eight 100 mL Teflon microwave vials. The mixture was then heated to a temperature of 150 °C with a 2 min. ramp rate by a controlled temperature program under microwave irradiation and was held for 10 min. at 150 °C under a pressure and power limit of 18 bar and 900 W respectively. After the completion, the product analyses was performed using ¹H NMR (Figure 4A-1)

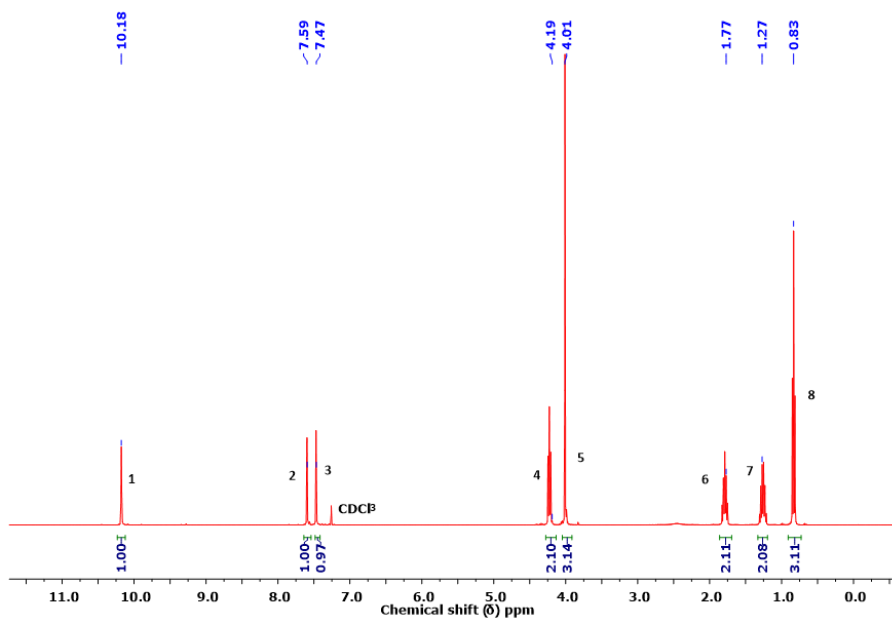


Figure 4A-1. ¹H NMR spectrum of compound [BMIM]⁺ Br⁻ in CDCl₃.

and TLC (80:20 dichloromethane: methanol in silica gel) and the excess n-butyl bromide was recovered (60.105 g, 438.66 mmol, 43.8% of 137.62 g excess of n-Butyl Bromide) by decanting from the reaction mixture. Afterwards, the evacuation of viscous ionic liquid residue was carried out under vacuum conditions (1×10^{-3} mbar) at 50 °C for 2 h and the rest n-butyl bromide (45.374 g, 331.15 mmol) was collected from the trap (total 77.0% of 137.62 g). Later the washing of as-obtained residue was executed using 100 mL of ethyl acetate for at least three times to remove any high-boiling organic impurities. The final product obtained was brown in color and was dried at 60 °C for 5 h under vacuum to get more than 98% of yield (433.35 g, 1977.68 mol, 98.9%) and the pure IL was finally solidified under ambient conditions of temperature.

FT-IR (ATR, cm⁻¹): 3402, 3140, 3078, 2955, 2870, 1628, 1566, 1458, 1381, 1335, 1165, 1111, 1026, 841, 756.

NMR (¹H, CDCl₃) δ ppm: 10.18 (s, 1H, NCHN), 7.59 (s, 1H, NCHCHCN), 7.47 (s, 1H, NCHCHCN), 4.19 (t, 2H), 4.01 (s, 3H), 1.77 (pent, 2H), 1.27 (sext, 2H), 0.83 (t, 3H).

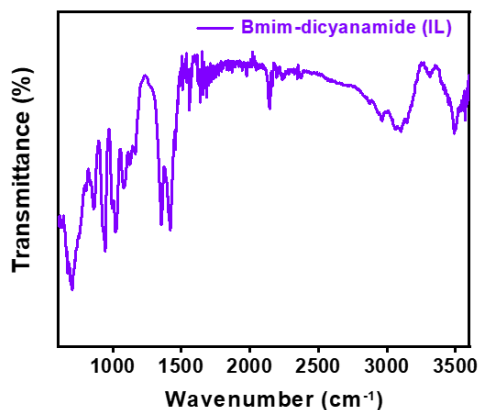


Figure 4A-2. FT-IR spectrum of compound IL.

4A-2.2 Synthesis of IL: 7.5 g (38.46 mmol) of compound (1) and 3.7 g (42.3 mmol) of sodium dicyanamide were dissolved in 10 mL DCM and transferred to a round-bottomed flask followed by 24 h of continuous stirring. The reaction mixture was filtered and extracted with distilled water and DCM atleast 4 times using 5 mL mixture of both and dried at 40 °C under vacuum to obtain 6.88 g (33.6 mmol) of IL with 87.4% yield. The anion exchange from Br⁻ to dicyanamide was confirmed with the help of ¹H NMR spectroscopy and the removal of Br⁻ was confirmed by performing silver nitrate test.

FT-IR (ATR, cm⁻¹): 3498, 3314, 3152, 3108, 3056, 2961, 2877, 2143, 1568, 1419, 1354, 1091, 1025, 953, 869, 708 (Figure 4A-2).

4A-2.3 Synthesis of ZIB-IL: After the successful synthesis of IL, the synthesis of precursor was started. Primarily, 0.55 g of boric acid was dissolved in 10 mL deionized water and mixed with aq. solution of 2-methylimidazole (1.012 g) under continuous stirring to completely dissolve the reactants. To the above reaction mixture, 25 wt% of Bmim-dicyanamide IL was added dropwise followed by the addition of aq. solution of Zinc nitrate hexahydrate (1.172 g). The mixture was then transferred to Teflon lined autoclave reactor and heated at 150 °C for 24 h to obtain ZIB-IL *i.e.* ionic liquid containing zinc imidazole borate. The ZIB-IL powder was filtered and washed several times by using 1:1 solution mixture of

ethanol and deionized water. ZIB precursor without IL was also synthesized in similar way by just not adding the IL during the synthesis, and denoted as ZIB.

4A-2.4 Synthesis of C-BN@T/ C-N@T and C-B@T: The as-synthesized ZIB-IL was pyrolyzed at different temperatures *viz.* 400 °C, 500 °C, and 600 °C respectively for 4 h under Ar atmosphere at a ramp rate of 5 °C min⁻¹ to obtain the heteroatom co-doped carbon (C-BN@T), where T designated the pyrolysis temperature. In order to remove the metal or metal oxides from the final catalyst after heat treatment, acid treatment was performed by washing the catalyst in 0.2 M H₂SO₄ solution for several times till the whole metal/metal oxides were removed. Further, the mono-heteroatom containing control catalysts were also synthesized to study the effect of dual-heteroatoms for which an identical synthetic route was followed and just addition of boric acid and 2-methylimidazole was eliminated to obtain boron-containing carbon and nitrogen-containing carbon composite. To be more specific, precursor for C-B@600 was synthesized using zinc nitrate and Boric acid only along with ionic liquid which was pyrolyzed at 600 °C under identical conditions. While, only zinc nitrate and 2-methylimidazole were taken along with ionic liquid to synthesize precursor for C-N@600 composite. The role of ionic liquid was also studied by pyrolysis of ZIB precursor without IL at 600 °C to get the final carbon composite of interest.

4A-3 Results and discussion

4A-3.1 Physical characterization: The synthesis procedure herein involved the pyrolysis of ZIB-IL, an IL containing MOF composite as a sacrificial template, at different temperatures between 400-600 °C for 4 h under Ar environment, followed by the removal of metal and/or metal oxide impurities by a simple acid treatment. ZIB-IL was synthesized by mixing an aq. solution of boric acid and 2-methylimidazole to which IL and zinc nitrate solution was added dropwise, followed by heating at 150 °C for 24 h by hydrothermal route. It is noteworthy to mention that the ZIB-IL contained both the heteroatoms in a single composite (B and N) which upon single-step pyrolysis yielded B, N containing carbon composite.

The synthesized precursor was initially screened to optimize the pyrolysis temperature by studying its thermal stability via TGA investigations. Figure 4A-3 displayed the TGA thermal degradation curves of ZIB-IL under inert conditions wherein a characteristic feature of MOF was witnessed. A little weight change with respect to the temperature could be observed which remained constant upto 150 °C while upon further increasing the temperature to 300 °C, reduction in weight was realized. This weight reduction of around 8% between 100 and 300 °C was attributed to the removal of guest molecules corks inside and adsorbed over the surface of ZIB-IL composite. On the other hand, a sharp decrease in the weight (~40%) was observed when temperature was increased from 300 to 600 °C, which evidenced the thermal decomposition, structure degradation and carbonization of ZIB-IL respectively. After the synthesis of C-BN@T catalyst, both precursor and final catalysts were thoroughly characterized by different techniques. At first, FT-IR spectroscopy analysis were implemented where the band observed at 1570 cm^{-1} and 1146 cm^{-1} in ZIB-IL were due to the C=N stretching and aromatic C-N stretching vibration respectively (Figure 4A-4a). Other peaks were also observed at 992 and 760 cm^{-1} which corresponded to the C-N and C-H bending modes. In addition to it, the presence of Zn-N stretching vibration band at 426 cm^{-1} evidenced the presence of Zn ions co-ordinated with N atoms of 2-methylimidazole to form

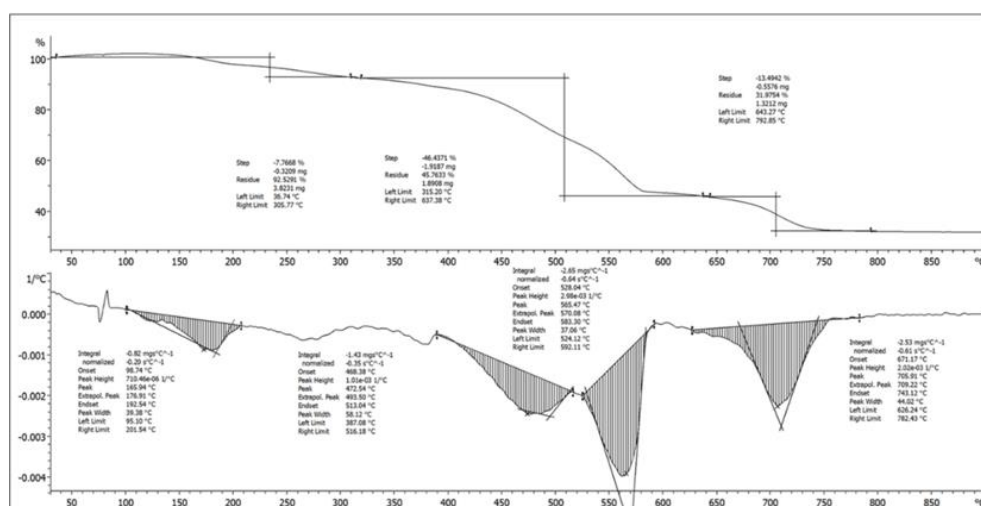


Figure 4A-3. TGA and first derivative TGA curve of ZIB-IL composite.

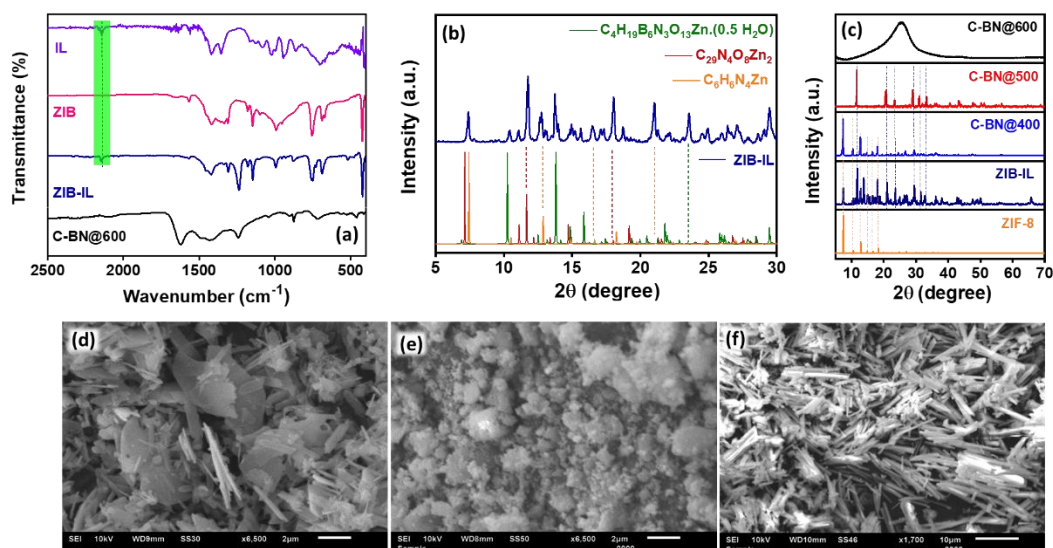


Figure 4A-4. (a) FT-IR spectrum of IL, ZIB, ZIB-IL and C- 600@B/N, (b) P-XRD pattern of ZIB-IL and matching phases extracted from reference CIF files and (c) C-BN@T composites in comparison with ZIB-IL. (d-f) SEM images for (a) ZIB-IL, (b) C-BN@400 and (c) C-BN@500.

imidazolate whilst the strong band observed at 953 cm^{-1} confirmed the formation of borate. The presence of IL in ZIB-IL was then confirmed by a peak which appeared at 2143 cm^{-1} ($\nu_{\text{N-C-N}}$) which was found to be absent in ZIB alone (without IL). Abovementioned outcomes revealed the successful formation of zinc-imidazole borate composite with ionic liquid incorporated in its matrix. On the other hand, peaks corresponding to in-plane stretching of the B–N group (1414 cm^{-1}) and stretching modes of B–C bond were witnessed (1233 cm^{-1} and 1030 cm^{-1}) along with the presence of C–N, C=C/C=O, C–O–C and O–B–O bonds (1610 , 880 , 820 and 711 cm^{-1}).

Further, the PXRD pattern for ZIB-IL in Figure 4A-4b embodied the high intensity peaks related to the indexing patterns of three previously reported compounds including ZIF-8³², $\text{C}_{29}\text{N}_4\text{O}_8\text{Zn}_2$ ³³ and $\text{C}_4\text{H}_{19}\text{B}_6\text{N}_3\text{O}_{13}\text{Zn} \cdot (0.5 \text{ H}_2\text{O})$ ³⁴. The high intensity peak observed at 11.6° was designated to (201) plane of $\text{C}_{29}\text{N}_4\text{O}_8\text{Zn}_2$, while other sharp peaks observed at 7.4° , 10.5° , 12.6° , 16.4° and 21.02° could be assigned to (110), (200), (211), (310) and (400) planes of ZIF-8. In addition to it

two more peaks were observed at 2θ values of 13.6° and 23.5° which were attributed to the presence of (400) and (022) plane in $\text{C}_4\text{H}_{19}\text{B}_6\text{N}_3\text{O}_{13}\text{Zn} (0.5 \text{ H}_2\text{O})$ respectively. Figure 4A-4c showed the diffraction patterns for C-BN@T catalysts, in which the peaks related to ZIF-8 became more intense in C-BN@400 whilst the same were found to be disappeared in C-BN@500 catalyst with appearance of high intensity peaks related to ZIB-IL. This could be attributed to the partial carbonization or elimination of crystallinity accompanied with the incremental loss of long-range order in the composite upon increasing the temperature from 400 to 500 °C. Interestingly, all the sharp and high intensity peaks were disappeared at a pyrolysis temperature of 600 °C while two additional peaks were observed at 25.5° and 44.5° related with (100) and (002) plane of graphitic carbon in C-BN@600. This indicated the complete carbonization and absence of metal/metal oxide in resultant C-BN@600 composite. Thereafter, SEM analysis were acquired as shown in Figures 4A-4(d-f) which depicted an irregular flake like morphology for ZIB-IL which upon pyrolysis at 400 °C presented a distorted morphology. Upon further increasing the temperature to 500 °C formation of micro-rods was witnessed. Remarkably, when ZIB-IL was pyrolyzed at a temperature of 600 °C, nanotubular morphology was perceived by means of FESEM (Figure 4A-5a), which could be due to the spatial confinement effect and energy released upon breakage of coordination bonds in MOF with ionic liquid acting as a structure directing agent, in which carbon atoms condense to form nanotubes and use of heteroatom containing carbon source aids formation of heteroatom-containing carbon with nanotubular morphology.³⁵ The role of ionic liquid is verified to be parallel to that of a structure directing agent and a contributor towards high surface area and narrow pore size distribution in C-BN@600. The SEM image in Figure 4A-5b for the catalyst obtained after pyrolysis of ZIB presented a distorted morphology rather than a nanotubular one, and further suggested the structure directing ability of ionic liquid in the precursor. Further, N_2 physisorption studies were carried out where Figures 4A-5(c-d) depicted the N_2 adsorption/desorption isotherms for ZIB and ZIB-IL derived carbon.

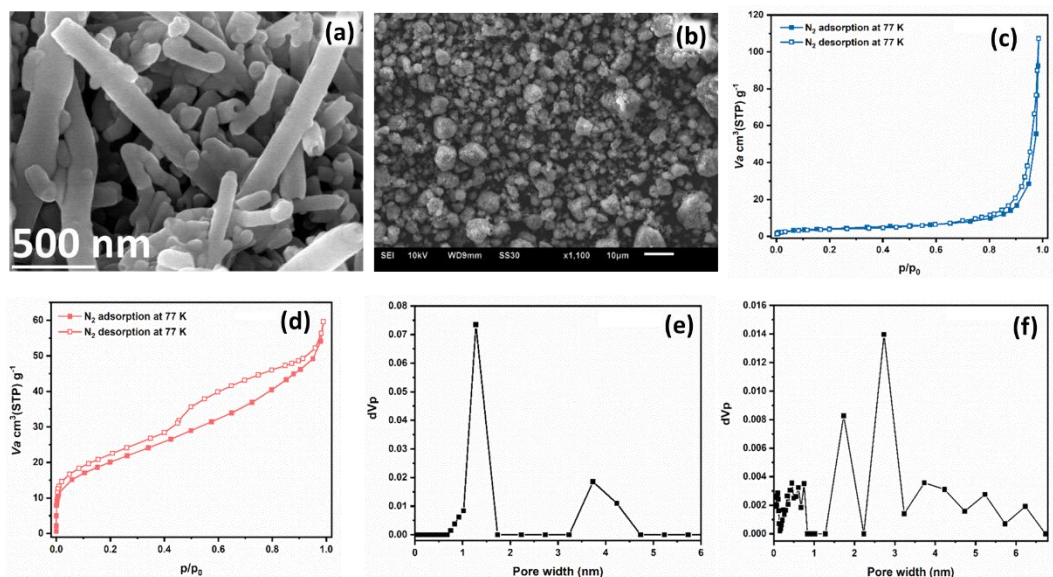


Figure 4A-5. (a) FE-SEM image of C-BN@600, (b) SEM image showing distorted morphology for dual-heteroatom doped carbon composite obtained after pyrolysis of ZIB. (c), (d) BET analysis for N₂-adsorption/desorption isotherms on ZIB derived C-BN@600, ZIB-IL derived C-BN@600 and (e), (f) pore size distribution for ZIB and ZIB-IL derived C-BN@600 catalysts respectively.

A hysteresis loop with a sharp increase in amount of N₂ adsorbed over ZIB derived carbon was observed at high relative pressures ($P/P_0 > 0.8$), which suggested a behaviour similar to type IV isotherm possessing large pores consisting of both meso as well as macropores. However, C-BN@600 *i.e.* ZIB-IL derived carbon, revealed a type IV isotherm, characteristic of a cylindrical and channel-like mesoporous structure which showed a steep N₂ uptake at low pressure and progressive increase in the same at high pressures which could be due to co-existence of both micro and mesopores. This was further complemented with an expansion of hysteresis loop which suggested the decreased number of macropores while increased mesopores in the final composite. The effect of ionic liquid over the pore size distribution and surface area was also investigated [Figures 4A-5(e-f)]. The capillary cohesion of ZIB derived carbon was detected at higher pressure ($P/P_0 > 0.8$) while at lower pressures ($P/P_0 > 0.5$) for ZIB-IL derived carbon. This evidenced the large average pore size (33.2 nm) for ZIB derived carbon as

compared to the ZIB-IL derived carbon (8.4 nm) whereas a smaller surface area ($14.8 \text{ m}^2 \text{ g}^{-1}$) and pore volume ($0.123 \text{ cm}^3 \text{ g}^{-1}$) is observed for ZIB derived carbon than ZIB-IL derived carbon with a surface area of $71.2 \text{ m}^2 \text{ g}^{-1}$ and a pore volume of $0.15 \text{ cm}^3 \text{ g}^{-1}$. All these results indicated the low porosity of the carbon derived from ZIB and a narrow pore size distribution of ZIB-IL derived carbon due to a capillary condensation step at low pressures of $0.5 < P/P_0 < 0.8$ (Table 4A-1).

Table 4A-1. BET calculations for carbon catalysts derived from ZIB and ZIB-IL precursors after pyrolysis at 600°C .

Catalyst	BET surface area	Pore volume	Average pore size
ZIB derived carbon	$14.8 \text{ m}^2 \text{ g}^{-1}$	$0.123 \text{ cm}^3 \text{ g}^{-1}$	33.2 nm
ZIB-IL derived carbon	$71.2 \text{ m}^2 \text{ g}^{-1}$	$0.15 \text{ cm}^3 \text{ g}^{-1}$	8.4 nm

The nanotubular morphology of C-BN@600 was confirmed by means of HRTEM [Figures 4A-6(a-b)] which displayed the nanotubes with an average inner and outer diameter of 70-100 nm and 120-150 nm respectively. The lattice fringes observed at edges of the tubes correspond to (002) plane of BN while the EDS dot mapping analysis revealed the homogeneous distribution of C, B and N over the scanned area (Figure 4A-6c). In the end, the electronic structure of ZIB-IL and C-BN@600 was determined by using XPS analyses. The presence of Zn, B, C, N and O elements in ZIB-IL was witnessed from the respective survey spectrum but the C-BN@600 showed only peaks related to C, N, O and B, which could be due to the

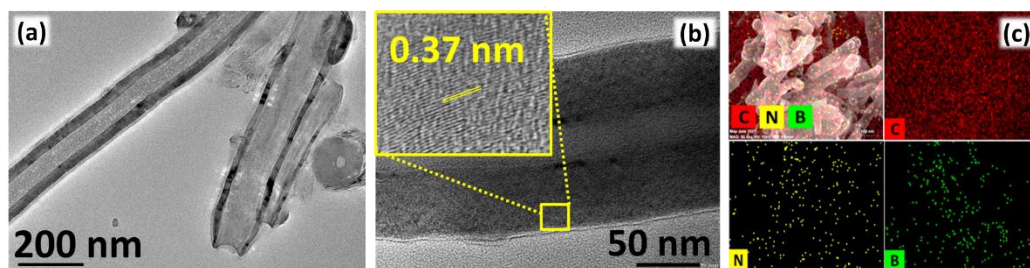


Figure 4A-6. (a-b) HR-TEM images of C-BN@600 [inset of (b): lattice fringes for B-N]. (c) EDS dot mapping showing C, B and N elements over the scanned area.

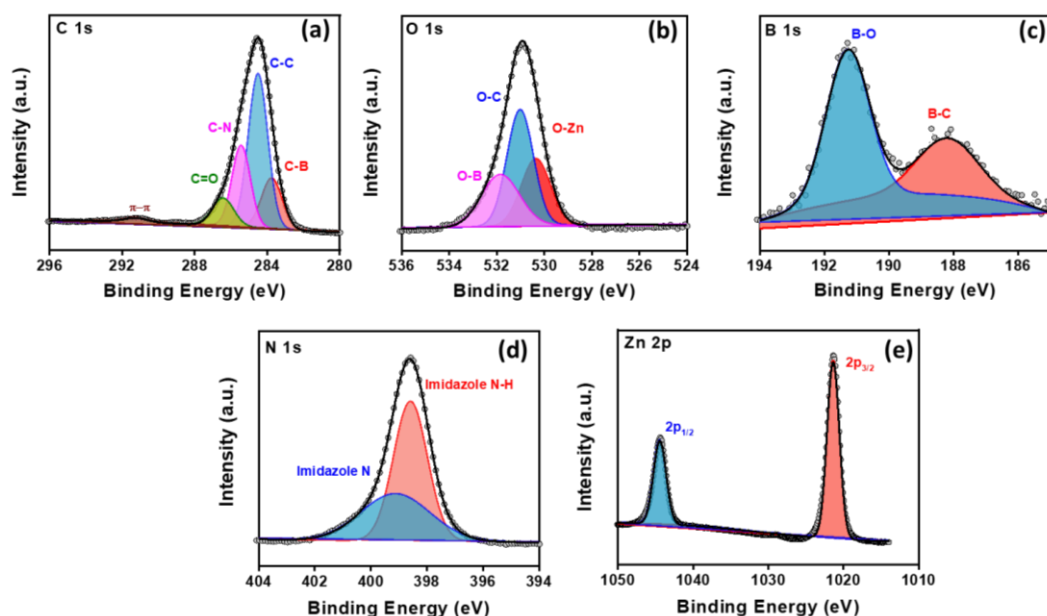


Figure 4A-7. XPS deconvoluted spectrum (a) C 1s, (b) O 1s, (c) B 1s, (d) N 1s and (e) Zn 2p of ZIB-IL composite.

metal-free nature of catalyst after pyrolysis and acid treatment. Figure 4A-7 exposed the deconvoluted XP spectrum for ZIB-IL where the peaks, corresponding to Zn $2p_{1/2}$ and Zn $2p_{3/2}$ were observed at B.E. values of 1044.5 and 1021.3 eV. The C 1s spectra exhibited peaks at 283.7, 284.5, 285.4, 286.5, 291.2 eV labelled as C-B, C-C, C-N, C=O and π - π transition respectively. On the other hand, peaks for O-C, O-Zn and O-B were also perceived at 531, 530.3 and 531.8 eV. The peaks at 398.5 and 399.2 eV in N 1s deconvoluted XP spectra of ZIB-IL were equivalent to imidazole N-H and imidazole N in ZIF-8. To sum up, the borate linkage was confirmed by a peak present at 191.3 eV whilst peak at 188.2 eV ascertained the formation of B-C bond in B 1s deconvoluted XP spectra. In contrast, when the C 1s spectra of C-BN@600 was deconvoluted, it displayed five peaks centered at 283.5, 287.5, 285.7, 284.6 and 289.1 eV where in the first two peaks could be related to the incorporation of B and N into the carbon matrix while the later three peaks could be assigned to C-O, C-C and C=O respectively (Figure 4A-8a). Figures 4A-8(b-c) confirmed the presence of different N-functionalities and well as N-B in

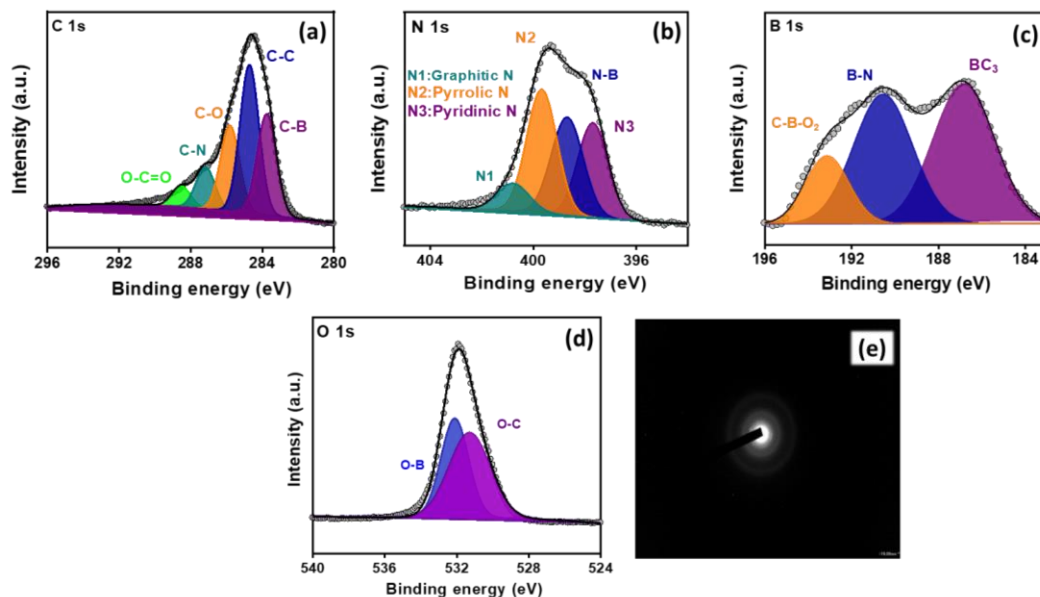


Figure 4A-8. Deconvoluted XP spectra of (a) C 1s, (b) N 1s, (c) B 1s and (d) O 1s in C-BN@600. (e) SAED pattern for C-BN@600 showing amorphous nature.

N 1s deconvoluted XP spectrum and B 1s XPS spectra revealed the B-N, BC₃ and BCO₂ functionalities in C-BN@600, which would be effective sites towards NRR.³⁶ Further the complete graphitization and amorphous nature of C-BN@600 was additionally confirmed with the help of CHNS analysis and SAED pattern for the same (Table 4A-2 and Figure 4A-8e).

Table 4A-2. CHNS analysis of C-BN@600.

Catalyst	Carbon (%)	Nitrogen (%)	Hydrogen (%)	Sulfur (%)
C-BN@600	75.902	2.630	2.893	-

4A-3.2 Electrocatalytic activity towards NRR: The well-defined nanotubular morphology, secondary heteroatom doping and finely distributed B and N over carbon matrix in C-BN@600 predicted it to be a better catalyst amongst other variants. To evaluate its activity, we then tested its performance towards NRR in 0.1 M Na₂SO₄ electrolyte using a two compartment H-cell separated by a

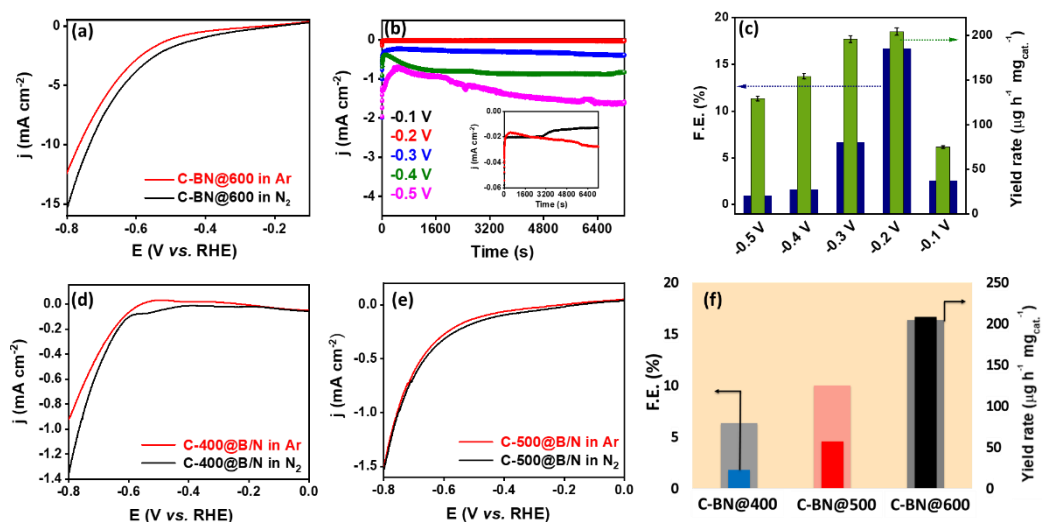


Figure 4A-9. (a) Linear sweep voltammetry curves and (b) Chronoamperometric curves obtained at different potentials after 2 h for C-BN@600 in N₂-saturated electrolyte. (c) Faradaic efficiencies and NH₃ yield rates of C-BN@600 at different potentials. LSV curves for (d) C-BN@400, (e) C-BN@500 in Ar and N₂ saturated 0.1 M Na₂SO₄. (f) Bar diagram comparison of NRR activity of C-BN@T composites.

Nafion-117 proton exchange membrane with a three-electrode configuration. The chances of false or overestimation of the ammonia produced during NRR due to contamination in feeding gases, were excluded by passing the gases through KMnO₄ and acid trap prior to every NRR experiment. Initially, LSV measurements were conducted in an applied potential range between 0 to -0.8 V vs. RHE in Ar- and N₂-saturated electrolyte. Figure 4A-9a depicts the LSV curve of C-BN@600 where the reduction current density showed an increase at around -0.3 V in presence of Ar while the reduction process was witnessed earlier (at -0.2 V) when the electrolyte was saturated with N₂. This inferred the N₂ fixation to NH₃ by C-BN@600 catalyst and so further product analyses was carried out by means of chronoamperometry (CA) tests at different applied potentials for a fixed time duration of 2 h (Figure 4A-9b). Upon quantification by Indophenol blue method, a maximum NH₃ yield rate and F.E. was observed at -0.2 V with values of 204 $\mu\text{g h}^{-1}\text{mg}_{\text{cat}}^{-1}$ and 16.7% respectively along with a high turnover frequency (TOF) of

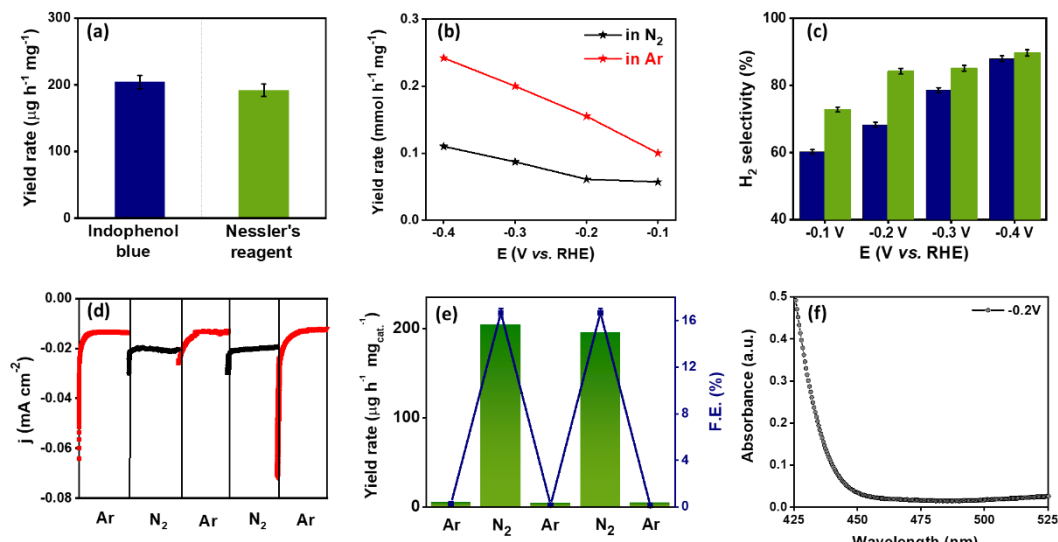


Figure 4A-10. (a) NH₃ yield rate for C-BN@600 at -0.2 V (vs. RHE) by different quantification methods, (b) H₂ production yield rate and (c) H₂ selectivity at different applied potentials on C-BN@600 in presence of Ar and N₂ saturated electrolyte (in Ar: green; in N₂: navy). (d) Switching chronoamperometry measurements performed under Ar and N₂ saturated environments at -0.2 V (vs. RHE) and (e) corresponding F.E. and yield rate obtained after the same. (f) UV-Vis spectrum of electrolyte sample collected after 2 h chronoamperometry by C-BN@600 at -0.2 V vs. RHE for hydrazine detection.

0.2 h⁻¹, as displayed in Figure 4A-9c. As predicted, a superior performance of C-BN@600 was witnessed over other catalyst variants in terms of higher current density, lower overpotential as well as high NRR activity [Figures 4A-9(d-f)]. Moreover, the quantified ammonia yield rate was validated by means of Nessler's reagent method (192 μg h⁻¹ mg_{cat}⁻¹), which were found out to be in close agreement with each other (Figure 4A-10a). The decremental behaviour of F.E. upon moving towards negative potentials was justified by quantification of H₂ by GC analysis. Figures 4A-10(b-c) revealed the increased HER selectivity from 72.8 to 89.7% in Ar-saturated electrolyte under applied potentials, while in the presence of N₂ in the electrolyte, the HER selectivity trend varied from 60.3 to 68.3% from -0.1 to -0.2 V which further increased on more negative potentials, describing the effectual HER suppression by C-BN@600 under N₂-saturated conditions. To further provision the suppressed HER, CA analysis (Figure 4A-10d) was executed under

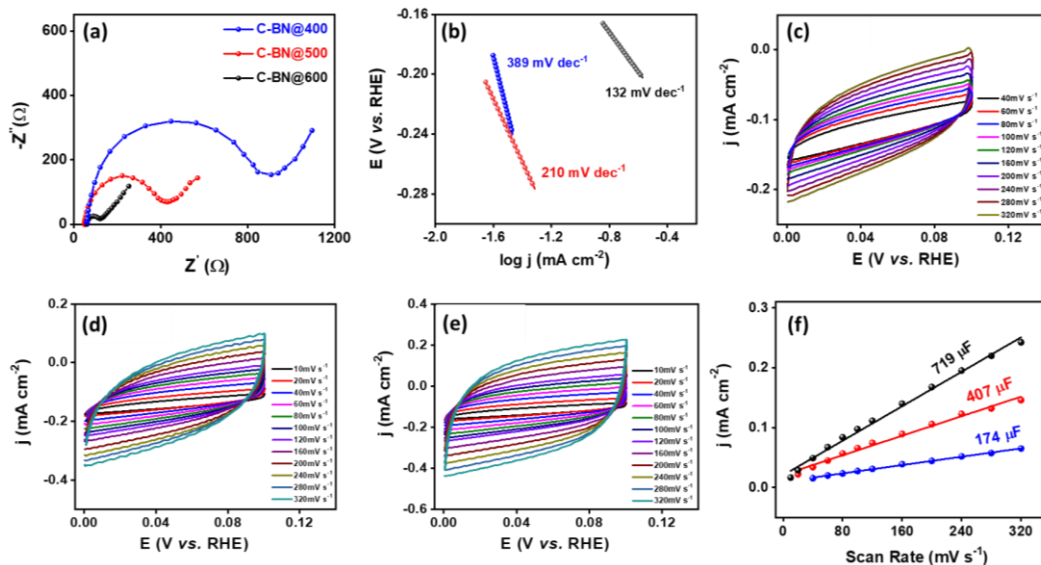


Figure 4A-11. (a) Nyquist plots acquired for different catalysts, (b) Tafel plots extracted for different catalysts. CV curves under non-faradaic region for (c) C-BN@400, (d) C-BN@500 and (e) C-BN@600 catalysts and (f) scan rate vs. current density curve representing C_{dl} value for C-BN@T catalysts (Blue: C-BN@400; Red: C-BN@500; Black: C-BN@600).

switching gas feed environments, which depicted an immediate change in current response with a lower current density in presence of Ar (0.2 mA cm^{-2}) while an increased current density was observed (0.3 mA cm^{-2}) in presence of N_2 . Moreover, no ammonia production in absence of N_2 was revealed after quantification of the same as shown in Figure 4A-10e. Notably, the selective NH_3 production was confirmed by absence of by-product N_2H_4 (Figure 4A-10f)

The superior catalytic performance of C-BN@600 catalyst over C-BN@400 and C-BN@500 catalyst was accomplished by performing different electrochemical characterizations. Primarily, the charge transfer resistance (R_{ct}) for the catalysts were evaluated by means of EIS, where the lowest R_{ct} value of 71.09Ω for C-BN@600 pointed towards the faster kinetics at electrode-electrolyte interface (Figure 4A-11a and Table 4A-3). This could be attributed to the nano-tubular channels and BN bonds which could effectively improve the mass and charge transfer during NRR.³⁷⁻⁴⁰ This was further supported by the lowest Tafel slope value of 132 mV dec^{-1} for C-BN@600 (Figure 4A-11b). Later, the electrochemical

surface area (ECSA) of electrocatalysts were evaluated since they unveil a strong correlation with the electrocatalytic activity based on the double layer capacitance (C_{dl}). As anticipated, the ECSA value of 18 cm² was obtained for C-BN@600 catalyst which was higher than other catalyst variants, and thus supported the availability of increased number of electroactive sites for NRR [Figures 4A-11(c-f) and Table 4A-4].

Table 4A-3. Electrochemical Impedance analysis extracted from Figure 4A-11a.

Sample	R_s (Ω)	R_p (Ω)	R_{ct} (Ω)
C-BN@400	53.9	898	844.6
C-BN@500	37.2	413	376
C-BN@600	47.9	119	71

Table 4A-4. Charge double layer (C_{dl}) and ECSA determination.

Catalyst	C_{dl} (μF)	ECSA (cm ²)
C-BN@400	174	4.3
C-BN@500	407	10.2
C-BN@600	719	18

As a matter of interest, the role of dual-heteroatoms for NRR over single heteroatom was scrutinized by means of physical and electrochemical characterization of control catalysts *i.e.* catalyst containing a single heteroatom either B or N, denoted as C-N@600 and C-B@600. The diffraction patterns presented in Figure 4A-12a for C-N@600, C-B@600 and C-BN@600 revealed the similar peaks related to that of graphitic carbon, while a discrete incongruence in morphology was witnessed moving from aggregated fibrous network to micro tubes formation and finally to the formation of nanotubes for N-, B- and BN-containing carbon catalyst respectively [Figures 4A-12(b-c)]. The lower activity was perceived for C-B@600 and C-N@600 based on the inferior net current density difference in LSV curves [Figures 4A-12(d-e)], thus accentuated the role of dual-heteroatom doping into the carbon matrix. The dual-heteroatom containing

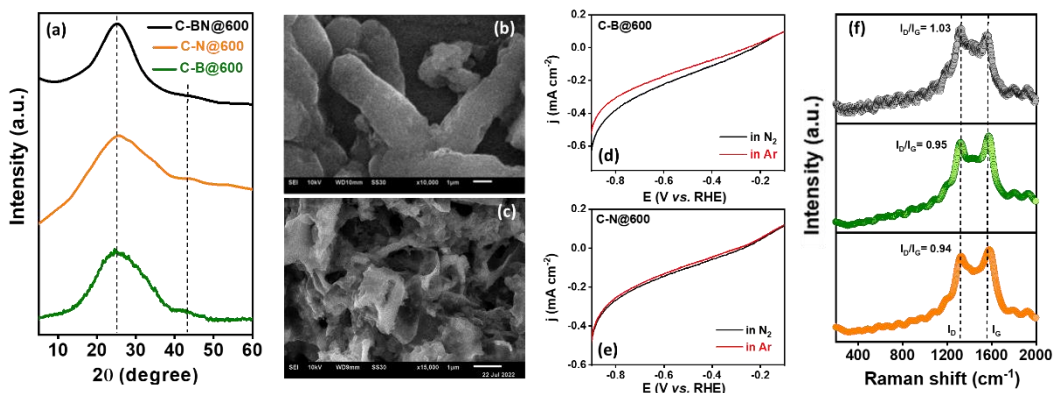


Figure 4A-12. (a) P-XRD patterns of C-N@600, C-B@600 and C-BN@600 catalysts. SEM images of (b) C-B@600 and (c) C-N@600 catalysts. Linear sweep voltammograms for (d) C-B@600 and (e) C-N@600 catalysts in Ar- and N₂-saturated electrolyte solutions. (f) Raman spectrum for C-BN@600 (black), C-B@600 (green) and C-N@600 (orange) catalysts with respective D and G bands.

carbon could induce increased surface defects than that of the mono-heteroatom containing carbon and was inspected by means of Raman spectroscopy. A characteristic feature of carbon materials *c.a.* two bands designated as D- and G-band were beheld for mono- as well as dual-heteroatom containing carbon at around 1328 cm⁻¹ (in-plane A_{1g} vibration) and 1572 cm⁻¹ (in-plane E_{2g} vibration) subsequently (Figure 4A-12f). The degree of disorder were estimated by peak area ratio of D and G bands (I_D/I_G) where a higher I_D/I_G ratio of 1.03 was attained for C-BN@600 than C-B@600 and C-N@600 with I_D/I_G ratio of 0.95 and 0.94 correspondingly, and so exposed an increased degree of disorder and density of defects in dual-heteroatom containing carbon. These interpretations labelled the benefit of dual-heteroatoms above a single heteroatom in carbon matrix for enhanced NRR activity.

4A-3.3 True estimation of NH₃ yield: The true estimation of NH₃ yield rate and the authentic NH₃ production source is just as essential as the NRR activity examination. It is very significant in order to circumvent the untrue and overestimated ammonia yield caused by the occurrence of N-contaminants in catalyst, electrolyte and gas-supplies. The gas supplies *viz.* ¹⁴N₂, Ar, ¹⁵N₂ were

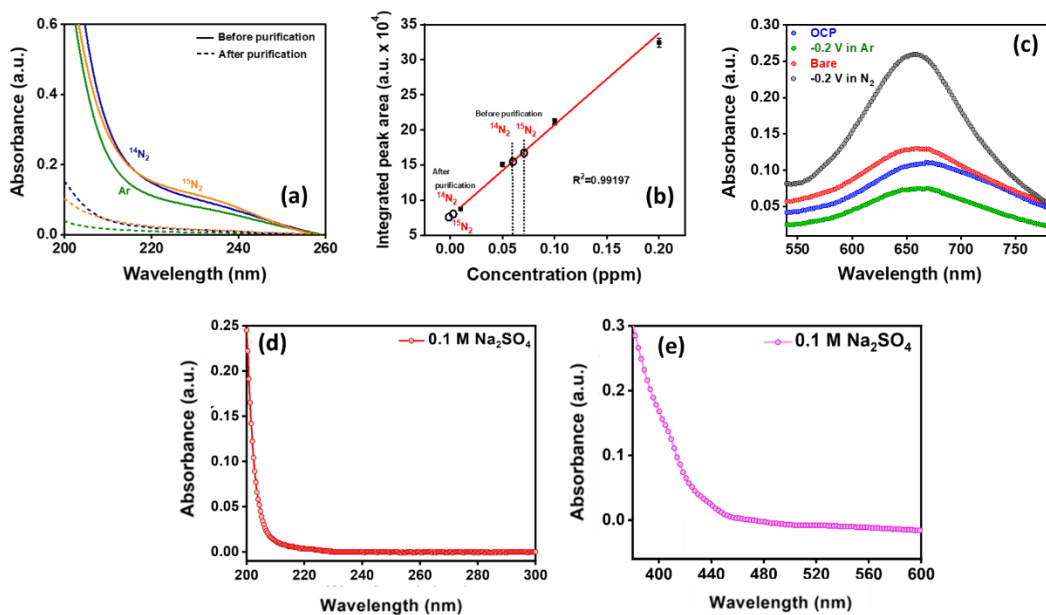


Figure 4A-13. (a) UV-Vis curves for NO_x in gas supplies before and after purification and (b) standard calibration curve extracted from chromatograms obtained after quantification of standard N₂O gaseous samples via GC-MS with labelled concentration of N₂O in gas supply before and after purification. (c) UV-Vis spectrum of C-BN@600 at OCP in N₂ saturated 0.1 M Na₂SO₄, at -0.2 V vs. RHE in N₂/Ar saturated electrolyte, and UV-vis spectrum of bare GC at -0.2 V vs. RHE in N₂ saturated 0.1 M Na₂SO₄. Detection of amount of (d) NO₃⁻ and (e) NO₂⁻ in electrolyte solution.

therefore cleansed by following the reported procedures in advance of NRR examinations. This involved the effective trapping of NO_x with an alkaline KMnO₄ solution ensued by the capturing of NH₄⁺ impurities via acidic solution. The trapped impurities were quantified before and after cleansing by GC-MS and colorimetric methods [Figures 4A-13(a-b)]. Thereafter, other control experiments including NRR at bare GC electrode, at OCP and under Ar-saturated conditions were implemented which authorized the insignificant ammonia production and thus waived off the possibility of contamination in gas-supply (Figure 4A-13c). In addition to it, the electrolyte solutions were also assessed for NO₂⁻/NO₃⁻ contaminations and didn't point out the presence of same [Figures 4A-13(d-e)]. As a matter of concern, if the catalyst itself contains N-atom which could contribute towards ammonia production and therefore necessitated the quantitative isotope

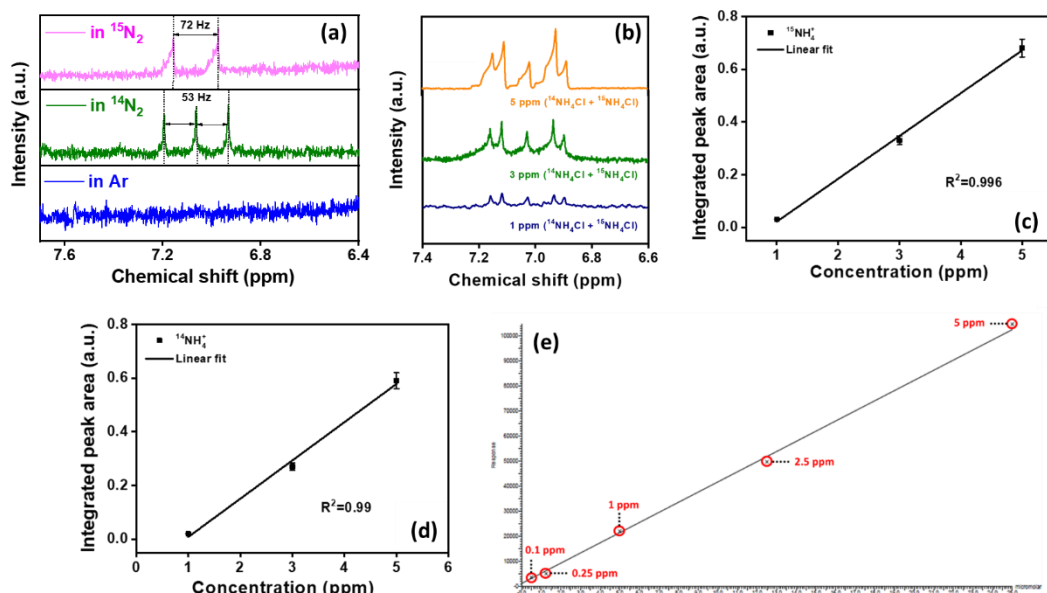


Figure 4A-14. (a) ^1H -NMR spectrum obtained after NRR by C-BN@600 in Ar-, $^{14}\text{N}_2$ - & $^{15}\text{N}_2$ -saturated 0.1 M Na_2SO_4 electrolyte solution. (b) ^1H NMR spectra of standard equimolar mixture of $^{14}\text{NH}_4\text{Cl}$ and $^{15}\text{NH}_4\text{Cl}$ solutions with different concentrations ranging between 1 ppm to 5 ppm and (c-d) calibration curves for different $^{15}\text{NH}_4^+ / ^{14}\text{NH}_4^+$ concentrations extracted from the same. (e) Liquid chromatograms obtained for standard ^{14}N -indophenol samples at different concentrations.

labelling measurements. The CA was carried out for 2 h by C-BN@600 catalyst in $^{15}\text{N}_2$ -, $^{15}\text{N}_2$ - and Ar-saturated 0.1 M Na_2SO_4 electrolyte and examined by means of colorimetric, ^1H NMR and LC-MS techniques. The occurrence of doublet coupling in ^1H NMR spectra revealed the formation of $^{15}\text{NH}_4^+$ after $^{15}\text{N}_2$ isotopic labelling NRR experiment. Contrastingly, the appearance of triplet coupling due to $^{14}\text{NH}_4^+$ and absence of any peak related to NH coupling in NH_4^+ after NRR in $^{14}\text{N}_2$ and Ar-saturated conditions confirmed the externally purged gas as the only source of produced ammonia and not the N-contamination in the catalyst (Figure 4A-14a). Upon quantification of ammonia after isotope labelling experiments using the standard calibration curves for NMR and LC-MS in Figures 4A-14(b-e), the analogous yield rates were witnessed which validated the yield (Figure 4A-15a).

4A-3.4 Stability studies: In addition to promising NRR activity, the durability of

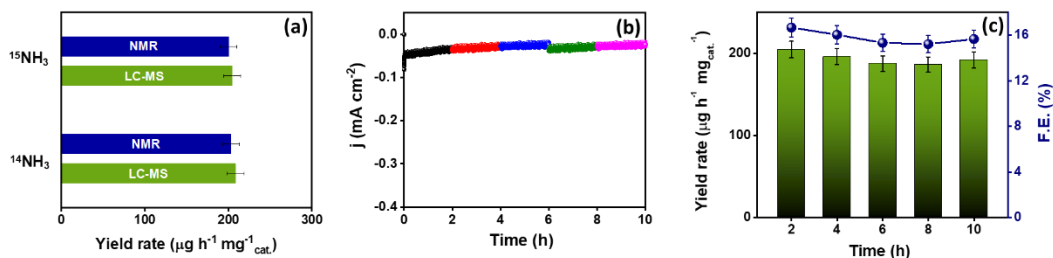
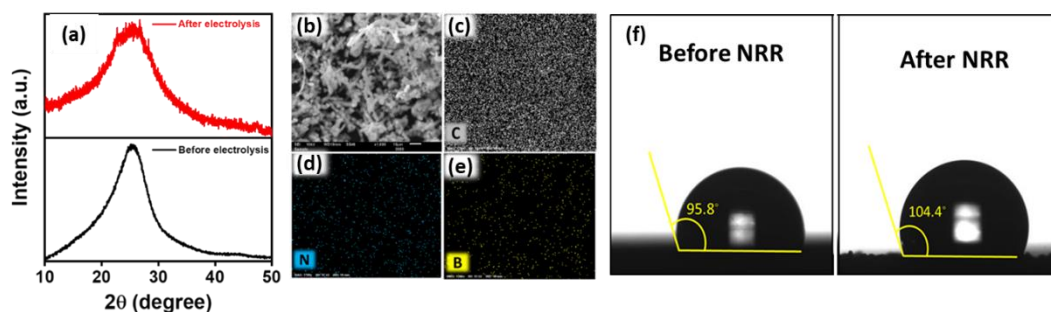


Figure 4A-15. (a) Comparison of $^{14}\text{NH}_3/^{15}\text{NH}_3$ yield rates obtained after isotope labelling NRR experiments via different quantification methods. (b) Chronoamperometry performed for 10 h at -0.2 V vs. RHE with C-BN@600 under continuous N_2 purging. (c) Bar diagram representation of F.E. & NH_3 yield rate obtained after 10 h of NRR stability tests under N_2 -saturated electrolyte.

catalyst during long-term electrolysis is critical too. In this regard, we performed the NRR stability tests by utilizing CA technique at -0.2 V (vs. RHE) which revealed a stable current response (Figure 4A-15b) and reproducible NH_3 yield and F.E. as demonstrated by the bar diagram in Figure 4A-15c. Further, a set of ex-situ characterizations including P-XRD, XPS, contact angle measurements, SEM, EDS and dot mapping were also accomplished to see the effect on the structural and morphological attributes of the catalyst after stability tests. The structural phase as well as the nanotubular morphology was found to be well retained along with the presence and homogeneous distribution of all the elements from respective P-XRD pattern, SEM image and EDS dot mapping images, and thus evidenced the



4A-16. (a) P-XRD pattern, (b) SEM image and EDX dot mapping for C-BN@600 after stability test showing uniform distribution of (c) Carbon, (d) Nitrogen and (e) Boron over scanned area. (f) Water contact angle images showing hydrophobic character of catalyst after NRR.

robustness of C-BN@600 catalyst in due course of NRR [Figures 4A-16(a-e)]. Later, the increased water contact angle for C-BN@600 (104.4°) after NRR illustrated the increased hydrophobicity of catalyst which could suppress the adsorption of H atoms and thus accelerate the N_2 adsorption (Figure 4A-16f).⁴¹ This augmentation in hydrophobicity of catalyst was ascribed to the exposure of hydrophobic B-N bonds (as per Wenzel and Cassie-Baxter model for homogeneous and heterogeneous wetting regimes) after NRR.⁴⁸ The exposure of B-N bonds was further reinforced by the increased intensity of peak allied with BN in B 1s deconvoluted XP-spectrum of C-BN@600 shown in Figures 4A-17(a-d), which might be due to likely rearrangement of atoms upon NRR, as confirmed from variation in relative atomic concentrations of different species [Figures 4A-17(e-g)]. These outcomes experimentally clinched the B-N to be an active site which was sustained by the theoretical model as well.⁴⁹⁻⁵⁰

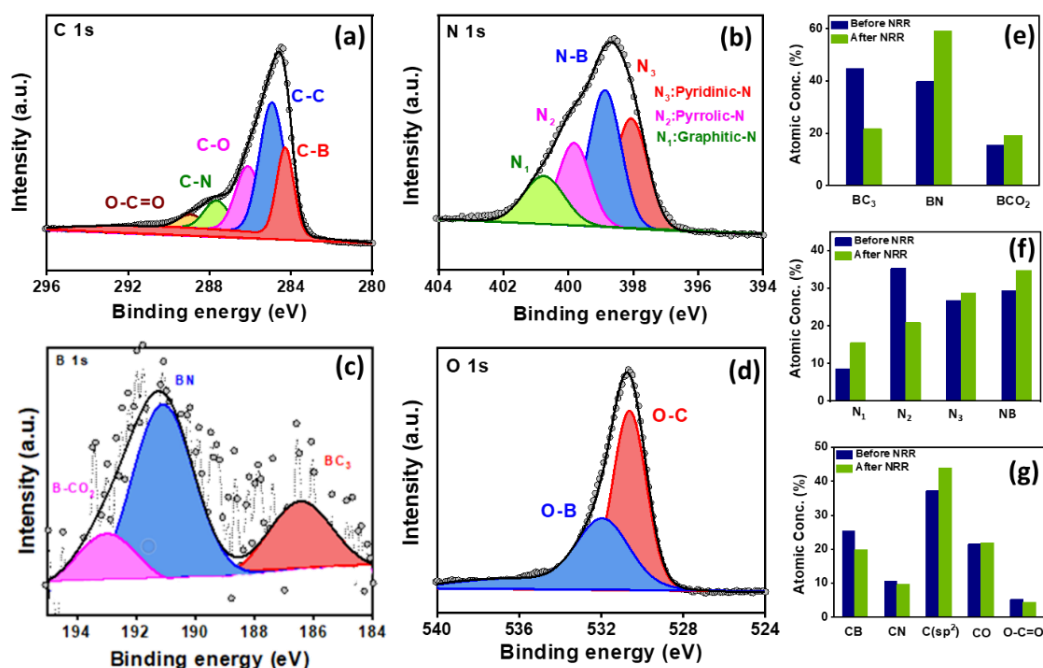


Figure 4A-17. Deconvoluted (a) C 1s, (b) N 1s, (c) B 1s and (d) O 1s XP spectra for C-600@B/N after NRR and (e-g) corresponding bar diagram representing relative atomic concentration of various N, B and C species in XPS of C-BN@600 before and after NRR.

4A-3.5 Theoretical investigations: Density functional theory (DFT) calculations were successively commenced to recognize the NRR performance and active site determination of C-BN@600 catalyst [Figures 4A-20(a-b)]. Since, the hydrazine formation was not perceived as a N_2 reduction product, so amongst different NRR pathways, the associative distal pathway was deliberated as the possible NRR mechanism pathway in which N atom could undergo preferential protonation to produce ammonia. Initially, the free energy calculation were conducted for three probable active sites such as BN, BCO_2 and BC_3 [Figures 4A-20(c-e)] which depicted the weak N_2 adsorption with an adsorption energy of -0.24 eV at BN and BCO_2 and -0.27 eV at BC_3 .

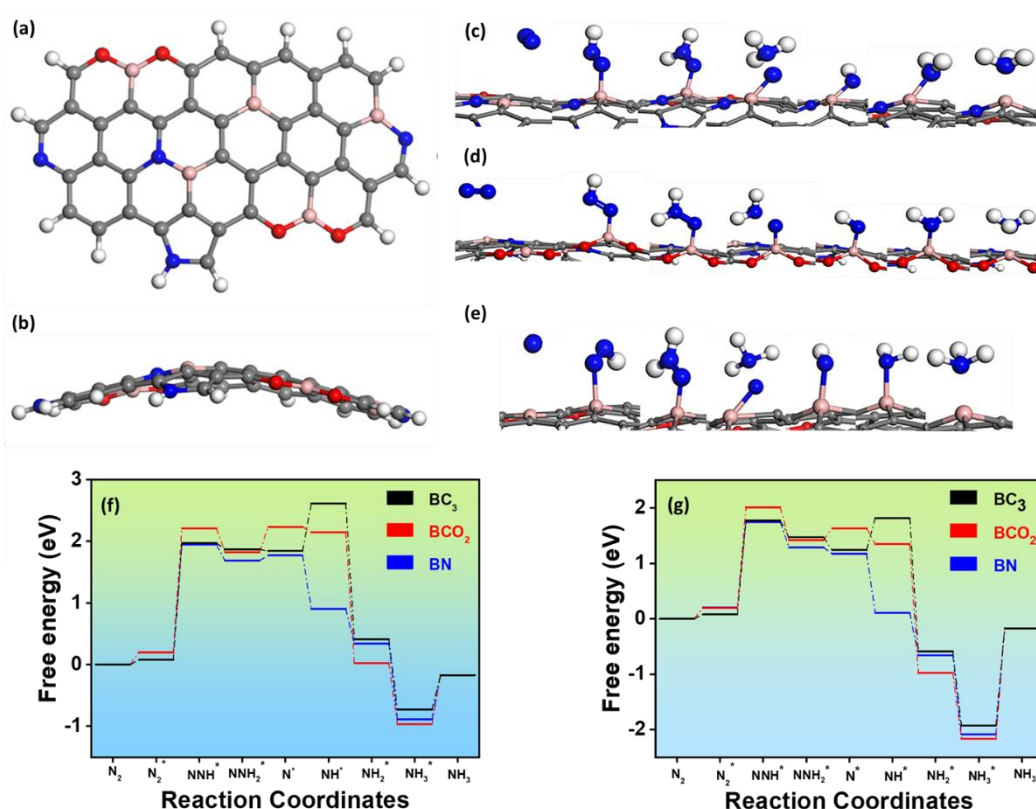


Figure 4A-20. (a) Top, (b) side view of C-BN@600 catalyst predicted by theoretical calculations (color codes:- H: white; B: pink; C: grey; N: blue; O: red). Optimized structures of different intermediate configuration of C-BN@600 during NRR at (c) BN, (d) BCO_2 and (e) BC_3 site. Free energy diagram of NRR at (f) $U=0$ V vs. RHE, (g) $U=-0.2$ V vs. RHE.

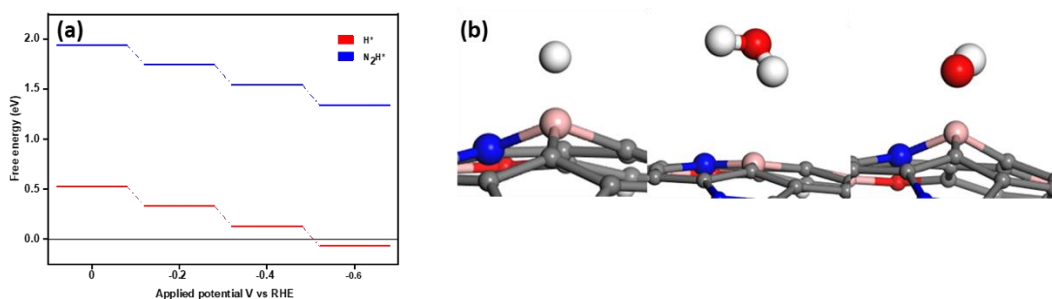


Figure 4A-21. (a) Free energy diagram of effect of applied potential on N_2H^* and H^* configuration. (b) Adsorption configuration of H^* , H_2O^* and OH^* on the catalyst surface (Color code: Blue, N; Pink, B; Grey, C; Red, O; White, H).

Nonetheless, a substantial loss of entropy attributable to gas phase N_2 binding led to the increased adsorption free energy of 0.2, 0.18 and 0.08 eV at BN, BCO_2 and BC_3 respectively. After which the adsorbed N_2 (N_2^*) could interact with the H^+/e^- pair to form the first reduced intermediate NNH^* . The rate limiting first protonation step *i.e.* $\text{N}_2^* \rightarrow \text{NNH}^*$ showed the Gibbs free energy changes of 1.74, 1.94 and 2.01 eV for BN, BC_3 and BCO_2 , where the additional uphill barrier of 0.77 eV at fourth protonation step of BC_3 put forward an energetically less favorable site for NRR (Figure 4A-20f). For this reason, BN was exclusively considered as the most favorable active site for NRR by virtue of its low energy barrier at first reduction step and sequential stabilization of B-N bond by adjacent carbon atom. Figure 4A-20g demonstrated the free energy change for the first protonation step which was reduced to 1.54 eV on applied potential of -0.2 V vs. RHE while rest of the steps became exergonic and feasible for further reduction process. The influence of applied potential on the free energy of NRR and HER processes was conclusive of the dominance of HER over NRR at higher cathodic potentials, where the free energy for HER turned out to be more negative with increase in cathodic potential (Figure 4A-21a). The selectivity of NRR over HER on BN active site were also premeditated by DFT calculation, which described that the deterioration of NRR activity ascended because of coverage of active sites by H^+ , H_2O and OH^- species over C-BN@600 (Figure 4A-21b) with adsorption energies of 0.012, 0.001 and -

0.008 eV respectively. All the adsorptions were found out to be weaker than N_2^* (-0.238 eV) and therefore confirmed the primary N_2^* adsorption over BN sites as the dominant process even in presence of other species.

4A-4 Summary

In summary, B, N containing carbon catalyst was fabricated via one step pyrolysis of MOF-IL composite to achieve a high F.E. (16.7%), TOF (0.2 h^{-1}) and NH_3 yield rate ($204 \mu\text{g h}^{-1} \text{ mg}_{\text{cat}}^{-1}$) at a reasonably lower overpotential than majority of reported catalysts under neutral electrolytic conditions. This high NRR activity benefited from the nanotubular morphology plus the existence of BN bond in C-BN@600 catalyst. Additionally, the theoretical understandings offered supplementary proof for the experimental conclusions, entitling the role of BN bond for N_2 adsorption and HER suppression. For this reason, advance assessment of B & N containing carbon with well defined morphology could bid colossal enhancement in forthcoming years for application in electrochemical ammonia synthesis.

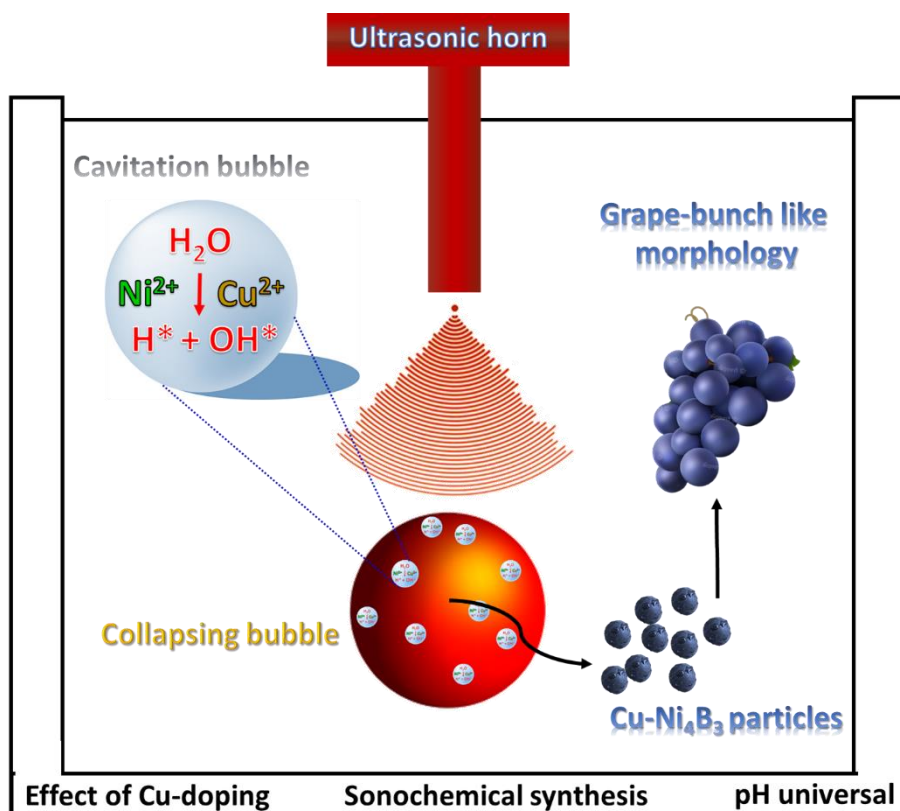
4A-5 References

1. V. Smil, *Nature*, 1999, **400**, 415-415.
2. J. A. Turner, *Science*, 1999, **285**, 687-689.
3. J. G. Chen, R. M. Crooks, L. C. Seefeldt, K. L. Bren, R. M. Bullock, M. Y. Darensbourg, P. L. Holland, B. Hoffman, M. J. Janik, A. K. Jones, M. G. Kanatzidis, P. King, K. M. Lancaster, S. V. Lyman, P. Pfromm, W. F. Schneider and R. R. Schrock, *Science (New York, N.Y.)*, 2018, **360**, 1419.
4. G. Leigh, in *Catalysts for nitrogen fixation*, Springer, 2004, pp. 33-54.
5. G. Soloveichik, *Nat. Catal.*, 2019, **2**, 377-380.
6. S. Ghavam, M. Vahdati, I. Wilson and P. Styring, *Front. Energy Res.*, 2021, **9**, 34.
7. R. Lan, J. T. Irvine and S. Tao, *Int. J. Hydrogen Energy*, 2012, **37**, 1482-1494.
8. A. Afif, N. Radenahmad, Q. Cheok, S. Shams, J. H. Kim and A. K. Azad, *Renew. Sustain. Energy Rev.*, 2016, **60**, 822-835.
9. A. Liu, Y. Yang, X. Ren, Q. Zhao, M. Gao, W. Guan, F. Meng, L. Gao, Q. Yang and T. Ma, *ChemSusChem*, 2020, **13**, 3766-3788.
10. R. Cai and S. D. Minteer, *ACS Energy Lett.*, 2018, **3**, 2736-2742.
11. H. Xu, K. Ithisuphalap, Y. Li, S. Mukherjee, J. Lattimer, G. Soloveichik and G. Wu, *Nano Energy*, 2020, **69**, 104469.
12. C. J. Van der Ham, M. T. Koper and D. G. Hettterscheid, *Chem. Soc. Rev.*, 2014, **43**, 5183-5191.
13. B. Yang, W. Ding, H. Zhang and S. Zhang, *Energy Environ. Sci.*, 2021, **14**, 672-687.
14. X. Cui, C. Tang and Q. Zhang, *Adv. Energy Mater.*, 2018, **8**, 1800369.

15. D. Liu, M. Chen, X. Du, H. Ai, K. H. Lo, S. Wang, S. Chen, G. Xing, X. Wang and H. Pan, *Adv. Funct. Mater.*, 2021, **31**, 2008983.
16. Y. Zhao, L. Yan and X. Zhao, *ChemElectroChem*, 2022, **9**, e202101126.
17. J.-T. Ren, C.-Y. Wan, T.-Y. Pei, X.-W. Lv and Z.-Y. Yuan, *Appl. Catal. B Environ.*, 2020, **266**, 118633.
18. X. Xue, R. Chen, C. Yan, P. Zhao, Y. Hu, W. Zhang, S. Yang and Z. Jin, *Nano Res.*, 2019, **12**, 1-21.
19. C. Liu, Q. Li, C. Wu, J. Zhang, Y. Jin, D. R. MacFarlane and C. Sun, *J. Am. Chem. Soc.*, 2019, **141**, 2884-2888.
20. C. Hering-Junghans, *Angew. Chem. Int. Ed.*, 2018, **57**, 6738-6740.
21. M.-A. L  gar  , G. B  langer-Chabot, R. D. Dewhurst, E. Welz, I. Krummenacher, B. Engels and H. Braunschweig, *Science*, 2018, **359**, 896-900.
22. X. Yu, P. Han, Z. Wei, L. Huang, Z. Gu, S. Peng, J. Ma and G. Zheng, *Joule*, 2018, **2**, 1610-1622.
23. W. Ouyang, Q. Zhi, L. Gong, H. Sun, M. Liu, J. Zhang, X. Han, Z. Xia and L. Zhang, *J. Mater. Chem. A*, 2021, **9**, 24590-24599.
24. S. Zhou, X. Yang, X. Xu, S. X. Dou, Y. Du and J. Zhao, *J. Am. Chem. Soc.*, 2019, **142**, 308-317.
25. B. You, X. Liu, G. Hu, S. Gul, J. Yano, D.-e. Jiang and Y. Sun, *J. Am. Chem. Soc.*, 2017, **139**, 12283-12290.
26. S. Oh, J. R. Gallagher, J. T. Miller and Y. Surendranath, *J. Am. Chem. Soc.*, 2016, **138**, 1820-1823.
27. L.-P. Yuan, Z.-Y. Wu, W.-J. Jiang, T. Tang, S. Niu and J.-S. Hu, *Nano Res.*, 2020, **13**, 1-7.
28. Y. Segawa, H. Ito and K. Itami, *Nat. Rev. Mater.*, 2016, **1**, 1-14.
29. F. Marpaung, M. Kim, J. H. Khan, K. Konstantinov, Y. Yamauchi, M. S. A. Hossain, J. Na and J. Kim, *Chem. Asian J.*, 2019, **14**, 1331-1343.
30. S. Mukherjee, D. A. Cullen, S. Karakalos, K. Liu, H. Zhang, S. Zhao, H. Xu, K. L. More, G. Wang and G. Wu, *Nano Energy*, 2018, **48**, 217-226.
31. A. Aijaz, T. Akita, H. Yang and Q. Xu, *Chem. Commun.*, 2014, **50**, 6498-6501.
32. O. Karagiari, M. B. Lalonde, W. Bury, A. A. Sarjeant, O. K. Farha and J. T. Hupp, *J. Am. Chem. Soc.*, 2012, **134**, 18790-18796.
33. K. O. Kongshaug and H. Fjellv  g, *Inorg. Chem.*, 2006, **45**, 2424-2429.
34. M. A. Altahan, M. A. Beckett, S. J. Coles and P. N. Horton, *Inorganics*, 2019, **7**, 44.
35. X. Wang, A. Dong, Y. Hu, J. Qian and S. Huang, *Chem. Commun.*, 2020, **56**, 10809-10823.
36. C. Chen, D. Yan, Y. Wang, Y. Zhou, Y. Zou, Y. Li and S. Wang, *Small*, 2019, **15**, 1805029.
37. T. C. Nagaiah, D. Gupta, S. D. Adhikary, A. Kafle and D. Mandal, *J. Mater. Chem. A*, 2021, **9**, 9228-9237.
38. D. Gupta, S. Chakraborty, R. G. Amorim, R. Ahuja and T. C. Nagaiah, *J. Mater. Chem. A*, 2021, **9**, 21291-21301.
39. J. Cao, N. Li and X. Zeng, *New J. Chem.*, 2021, **45**, 6327-6335.
40. V. V. Ivanovskaya, A. Zobelli, O. St  phan, P. R. Briddon and C. Colliex, *J. Phys. Chem. C*, 2009, **113**, 16603-16609.
41. J. Zhang, B. Zhao, W. Liang, G. Zhou, Z. Liang, Y. Wang, J. Qu, Y. Sun and L. Jiang, *Adv. Sci.*, 2020, **7**, 2002630.

Chapter 4B

Modification of Ni_4B_3 composite with copper for enhanced electrochemical N_2 reduction to NH_3



4B-1 Introduction

The rational design and development of competent electrocatalysts exhibiting high activity, selectivity and stability towards NRR under the wide pH range is critical and meaningful for applied electrochemical NH_3 synthesis.¹⁻³ Earth-abundant non-precious transition metal (TM) based materials comprising metallic oxides, sulphides, nitrides, and carbides have been widely studied for NRR.⁴⁻⁷ Transition metal borides (TMBs) have also riveted plentiful of consideration⁸, mainly owing to their rich reserves, environment affability, and electron-deficient nature as well as reverse electron transfer property of boron, but they are still at infancy in the field of NRR.^{9, 10} TMBs are already well explored for water electrolysis, CO_2 reduction reaction, etc. because the incorporation of boron into TMs can tune the *d*-band centers and optimize the Gibbs free energies of different chemical reactions.¹¹⁻¹³ In addition to it, the strong covalent character of M-B and B-B bond can possibly enhance the electron transmission and the hybridization between *d*-orbital of TM and *p*-orbital of B to stabilize the final TMB composite against oxidation.¹⁰ A few theoretical reports^{9, 14} have been published for different TMBs to provide an idea about the optimal choice of TM with better NRR activity prior to experimental analysis, however, only limited experimental studies are known in the literature showing activity of TMBs towards NRR. For instance, a report from Fu *et al.* presents the molybdenum aluminium boride (MoAlB) single crystals for NRR to give a F.E. of 30.1% and NH_3 production yield rate of $9.2 \mu\text{g h}^{-1} \text{cm}^{-2} \text{mg}^{-1}_{\text{cat}}$ at -0.05 V (vs. RHE) in 0.1 M KOH electrolyte.¹⁵ Another report by Chu *et al.*¹⁶ reports FeB_2 porous nanosheets to realize a F.E. of 16.7% at -0.2 V and NH_3 yield rate of $39.8 \mu\text{g h}^{-1} \text{mg}^{-1}$ at -0.3 V respectively in 0.5 M LiClO_4 solution. Li *et al.* used TiB_2 for NRR which gave a F.E. of 11.37% and an NH_3 yield rate of $1.75 \times 10^{-10} \text{mol s}^{-1} \text{cm}^{-2}$ at -0.3 V in acidic 0.1 M HCl solution.¹⁷ And very recently, ZrB_2 is reported for NRR with an attractive performance in which 18.2% of F.E. and $37.7 \mu\text{g h}^{-1} \text{mg}^{-1}$ of yield rate is obtained at -0.3 V.¹⁸ Even though TMBs have been scrutinized to a certain level towards NRR, but still there's a lot

of room to increase the F.E. and dissatisfactory NH_3 yield rates. Amid numerous classes of TMBs, nickel (Ni) boride composites reflect versatile catalyst properties due to high electron density over Ni caused by the reverse electron transfer from more electronegative boron thereby preventing oxidation and provides high stability under a wide pH range and high temperatures.¹⁹⁻²¹ Besides, the modification of nickel borides by addition of other transition metal acts as one of the most efficient route to enhance the performance towards electrocatalytic applications and selective hydrogenation reactions.²²⁻²⁷ For instance, the economical and copious transition metal *viz.* copper (Cu) can be a potential dopant into the nickel boride catalyst since it possesses a high density of *d*-electrons that can form a *d-d* band with another TM (Ni) and alter its e^- density and in turn influence the reaction kinetics.²⁸ Moreover, the high conductivity of Cu can expedite the charge transfer and augment the catalytic activity and the d^{10} electronic structure of Cu metal makes it tough to adsorb hydrogen and thus can end up in poor HER activity.²⁹ In the symbiotic N_2 fixation process via nitrogenase enzyme³⁰, Cu work as active centers and a necessary cofactor which has the ability to inhibit hydrogen evolution.³¹ In recent times, Cu-based catalysts³²⁻³⁵ have been investigated as NRR catalysts for the reason that it is capable of synergistically accepting the electrons from N_2 and again donating them (π -feedback behaviour) back.³⁶ This leads to the weakening and thus activation of the strong $\text{N}\equiv\text{N}$ bond as well as strengthening of the metal-N bond and in turn increase the adsorption of N_2 molecule.³⁷⁻³⁹ Nonetheless, to the best of our knowledge, Cu-doped nickel boride composites as NRR catalysts are not explored and can flourish the green ammonia synthesis sector with high ammonia production rate and improved Faradaic efficiency.⁴⁰

In the present study, Cu is introduced to modify the surface of nickel boride composite with the intention of illuminating the NRR activity through the modification of electronic structures of metal borides. On the whole, copper-nickel boride ($\text{Cu-Ni}_4\text{B}_3$) composite with grape bunch-like morphology composed of

nanospheres were prepared by a simplified sonochemical approach in a single step and is shown to unveil enhanced activity and durability during NRR than the equivalent monometallic counterpart *viz.* Ni_4B_3 . The electrocatalytic performance towards NRR was probed in acidic, alkaline plus neutral electrolytes. The Cu- Ni_4B_3 (1:2) catalyst reveal the maximum F.E. of 43.42% and NH_3 yield rate of $684 \mu\text{g}_{\text{NH}_3} \text{h}^{-1} \text{mg}_{\text{cat}}^{-1}$ in 0.1 M H_2SO_4 electrolyte at -0.3 V (*vs.* RHE).

4B-2 Material synthesis

4B-2.1 Synthesis of Cu- Ni_4B_3 : Cu- Ni_4B_3 catalyst in this work was synthesized via one-step sonochemical reduction method in which initially the 2 mmol of nickel nitrate ($\text{Ni}(\text{NO}_3)_2 \cdot 6\text{H}_2\text{O}$) and 1 mmol of copper nitrate ($\text{Cu}(\text{NO}_3)_2 \cdot 6\text{H}_2\text{O}$) solution in 10 mL deionized water were added to a three neck round bottom flask and kept in ice-bath till the completion of the reaction. After which, 10 mL of reducing agent *i.e.* aqueous solution containing 6 mmol sodium borohydride (NaBH_4) was added to the reaction mixture containing metal salts. The addition of the reducing agent was carried out in a dropwise manner along with the probe sonication at a fixed probe amplitude of 20 Hz for every 1 min. followed by rest for 2 min. consequently. The black precipitates of Cu- Ni_xB_y were obtained after the reaction completion (bubble generation ceased) and collected by filtration followed by washing with deionized water and ethanol and were later washed with KOH solution to remove any NO_3^- contamination from the precursors. The precipitates were then dried in a binder oven overnight and labelled as Cu- Ni_4B_3 (1:2). Copper-nickel borides with different mole ratios of Cu and Ni metal (2:1 and 1:1), and monometallic nickel boride (Ni_4B_3) were also synthesized to optimize the best catalytic performance towards NRR and study the role of Cu addition in Ni_4B_3 composite.

4B-3 Results and discussion

4B-3.1 Physical characterization: To examine the physicochemical properties of as-synthesized catalysts, a series of material characterizations were performed including P-XRD, SEM, FESEM, EDS, HR-TEM and XPS. The X-ray diffraction

patterns of the catalysts could be seen in Figures 4B-1(a-b). The diffraction peaks present at 2θ value of 36.42° , 43.2° , 62.2° and 43.2° , 50.5° , 74.1° match well with the $(1\bar{1}2)$, $(\bar{1}04)$, (200) and (111) , (200) , (220) planes of Ni_4B_3 (ICSD: 24307) and Cu (JCPDS no. 04-0836) respectively for $\text{Cu-Ni}_4\text{B}_3$ (1:2/1:1/2:1) catalysts. A slight shift in peaks related to metallic Cu towards lower 2θ values point to the lattice expansion of the same. The structural phase of Ni_4B_3 in absence of Cu as an additional metal persisted to be the same even after changing the bimetallic composition and thus could not be assigned as a descriptor of activity towards NRR. Subsequently, the morphology of the catalyst was analyzed by means of field-emission scanning electron microscopy (FE-SEM). As, shown in Figure 4B-1c, the FE-SEM image showed a typical grape-bunch-like morphology of the

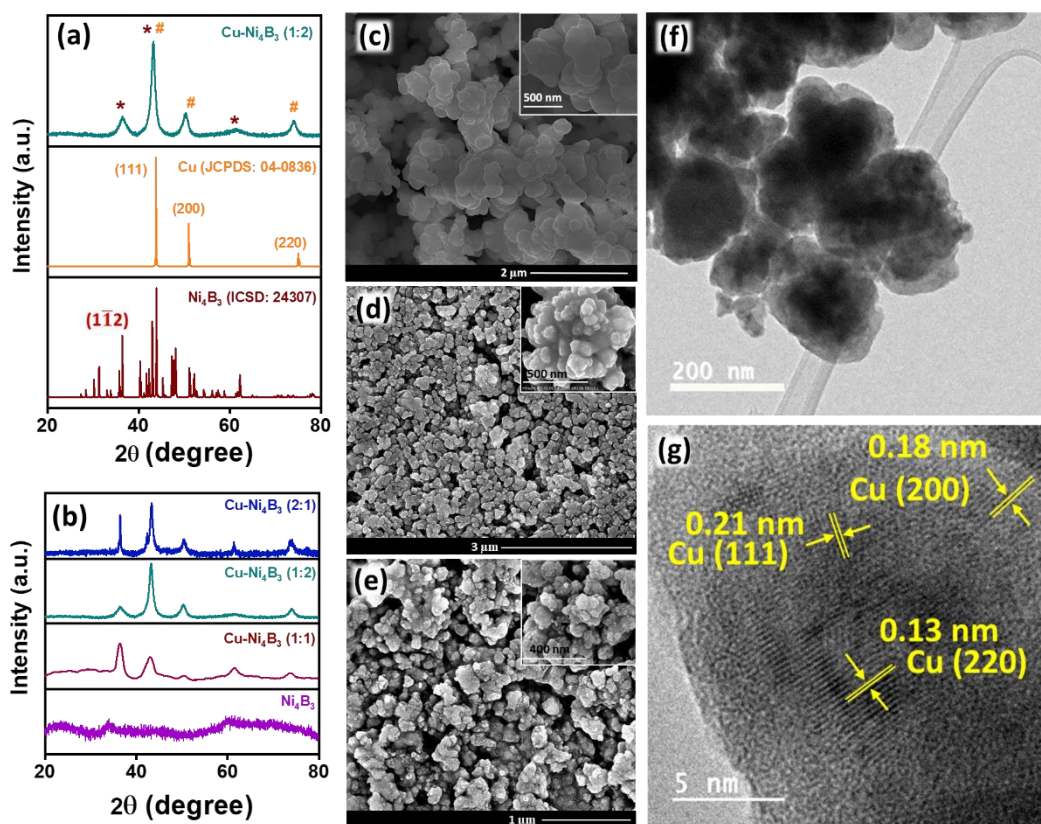


Figure 4B-1. (a-b) P-XRD patterns for Ni_4B_3 and $\text{Cu-Ni}_4\text{B}_3$ catalysts, FE-SEM images of (c) $\text{Cu-Ni}_4\text{B}_3$ (1:2), (d) $\text{Cu-Ni}_4\text{B}_3$ (1:1) and (e) $\text{Cu-Ni}_4\text{B}_3$ (2:1) respectively. (f) TEM and (g) HR-TEM images for $\text{Cu-Ni}_4\text{B}_3$ (1:2) catalyst.

Cu-Ni₄B₃ (1:2) composed of nanospheres with average diameter between 200-250 nm. In contrast, the respective FE-SEM images of Cu-Ni₄B₃ (1:1) and Cu-Ni₄B₃ (2:1) catalysts showed a clustered and aggregated morphology which is different from the Cu-Ni₄B₃ (1:2) catalyst and thus could be one of the deciding factor towards NRR [Figures 4B-1(d-e)]. The grape bunch-like morphology of Cu-Ni₄B₃ was later identified by the transmission electron microscopy (TEM) image shown in Figure 4B-1f. Instead, the HR-TEM image displayed in Figure 4B-1g, exposed the presence of Cu in metallic form with lattice fringe of ≈ 0.13 , 0.18 and 0.21 nm corresponding to the (220), (200) and (111) plane of metallic Cu respectively while no fringes related to Ni₄B₃ phase were detected designating the formation of an amorphous layer over the catalyst particles as observed in the HRTEM image as well. Further, the elemental dot mapping images (Figure 4B-2) revealed the presence and uniform distribution of Cu, Ni, B and O elements over scanned area for Cu-Ni₄B₃ (1:2) composite. Later, the XPS analyses identified the oxidation states of the expected elements in Cu-Ni₄B₃ (1:2) upon deconvolution. In Cu 2p XPS deconvoluted spectra, two major peaks for Cu 2p_{3/2} and Cu 2p_{1/2} were observed due to spin-orbit coupling.

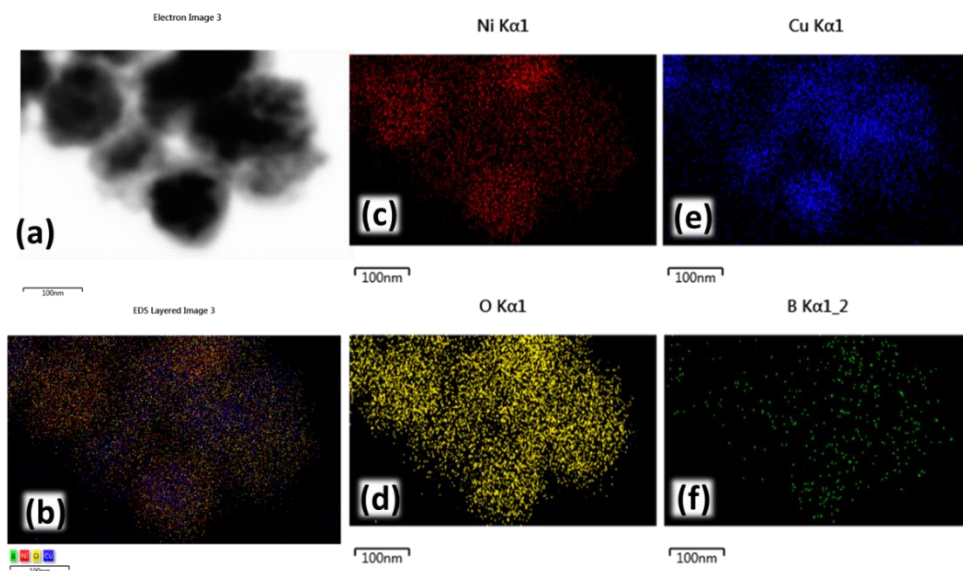


Figure 4B-2. EDS dot mapping images for Cu-Ni₄B₃ (1:2) catalyst showing the homogeneous distribution of elements.

Upon deconvolution, it publicized the formation of Cu in metallic form along with the trace CuO (Figure 4B-3a). The peaks at 932.7 and 934 eV were ascribed to $2p_{3/2}$ orbital of Cu^0 and $2p_{3/2}$ orbital of Cu (II) while the peaks at 952.6 and 954 eV belonged to $2p_{1/2}$ orbital of Cu^0 and Cu (II) respectively. The high-resolution Ni 2p deconvoluted spectra revealed two major peaks related to Ni $2p_{3/2}$ and Ni $2p_{1/2}$ along with the satellite peaks (Figure 4B-3b). Upon deconvolution, the peaks at 852.7 and 868.7 eV confirmed the binding of Ni with B in addition to the presence of Ni in +2 oxidation state (856.3 and 874.2 eV). Besides, the peaks at 188.7 and 192 eV observed in deconvoluted B 1s XP spectrum deep-rooted the presence of M-B accompanied with BO_x species due to oxidation of the catalyst (Figure 4B-3c).

4B-3.2 Catalytic activity towards NRR: To test the ability of Cu-modified nickel boride catalysts with different mole ratios and the monometallic Ni_4B_3 towards

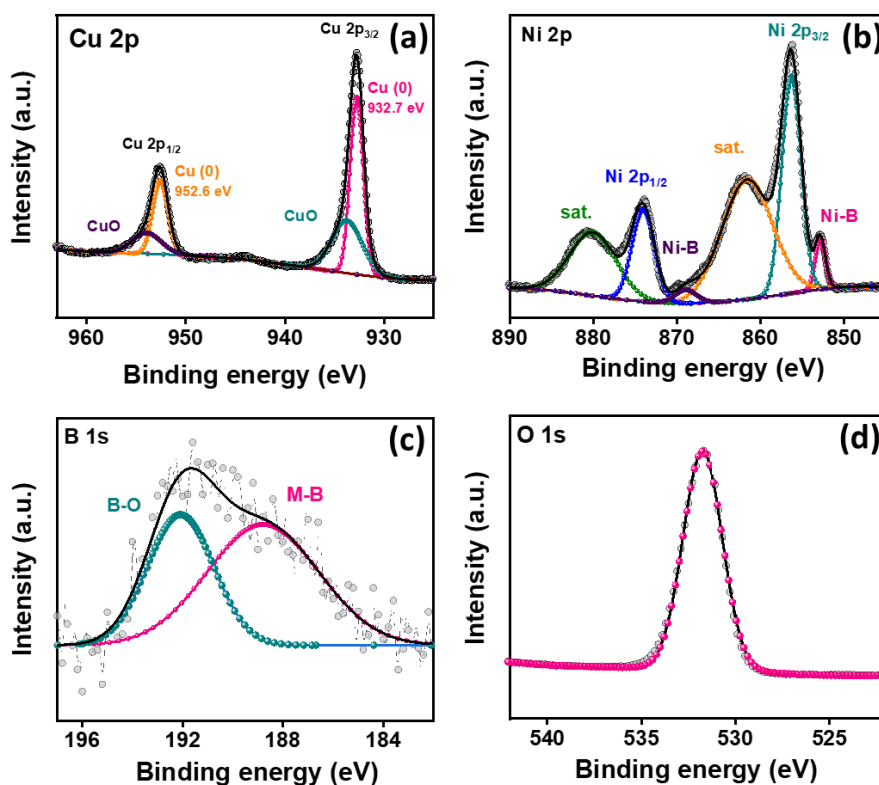


Figure 4B-3. XP deconvoluted (a) Cu 2p, (b) Ni 2p, (c) B 1s and (d) O 1s spectrum for Cu- Ni_4B_3 (1:2) catalyst respectively.

NRR, the linear sweep voltammetry was performed initially in N₂- and Ar-saturated electrolyte solution (0.1 M H₂SO₄). As shown in Figures 4B-4(a-d), the high net current density of Cu-Ni₄B₃ with Cu and Ni in a 1:2 ratio than other parallel composites and Ni₄B₃ alone pointed that Cu-Ni₄B₃ (1:2) exhibited the superior catalytic activity towards NRR. Moreover, an apparent current density gap observed in the LSV curves for Cu-Ni₄B₃ (1:2) catalyst in N₂- and Ar-saturated 0.1 M H₂SO₄ indicated that the N₂ reduction has occurred on the application of external potential. This set forth the optimized configuration of Cu-Ni₄B₃ (1:2) composite on the road to N₂ reduction to NH₃ and the role of addition of Cu into Ni₄B₃ catalyst and so was mainly concentrated during NRR examinations.

The cell setup, electrolyte solution, electrode surface and gas-supplies were purified during the course of the experiments by the rigorous purification procedures mentioned in previous chapters. Successively, chronoamperometric experiments (CA) were executed for Cu-Ni₄B₃ (1:2) at different applied potentials between -0.25 to -0.45 V (*vs.* RHE) for a time period of 2 h considering the qualitative and quantitative estimation of reduction product (Figures 4B-4e). When -0.3 V of external potential was applied then a prominent NRR activity was acquired with a NH₃ yield rate of 684 $\mu\text{g}_{\text{NH}_3} \text{h}^{-1} \text{mg}_{\text{cat}}^{-1}$ and the F.E. reached a peak value of 43.42% respectively (Figure 4B-4f). We witnessed a diminution in the NRR activity upon increasing the negative applied potentials as a consequence of competing H₂ evolution. The F.E. of NH₃ and H₂ could be compared from Figure 4B-4e, which clearly suggested the most impressive NRR selectivity at -0.3 V (*vs.* RHE) by Cu-Ni₄B₃ (1:2). The high selectivity towards NRR was further sustained by absence of N₂H₄ as a by-product during NRR at -0.3 V (Figure 4B-4f). As projected, Ni₄B₃, Cu-Ni₄B₃ (1:1) and Cu-Ni₄B₃ (2:1) catalysts demonstrated activity towards NRR as well but with an inferior NH₃ yield rate of 603.4, 160.91 & 268.18 $\mu\text{g}_{\text{NH}_3} \text{h}^{-1} \text{mg}_{\text{cat}}^{-1}$ and an F.E. of 11.35, 4.54 & 12.38% respectively than Cu-Ni₄B₃ (1:2) at -0.3 V (*vs.* RHE) in 0.1 M H₂SO₄ electrolyte (Figure 4B-5a). This fortifies the role of Cu in nickel boride catalyst and the improved performance of Cu-Ni₄B₃ catalyst with Cu:Ni mole ratio of 1:2 respectively which could be

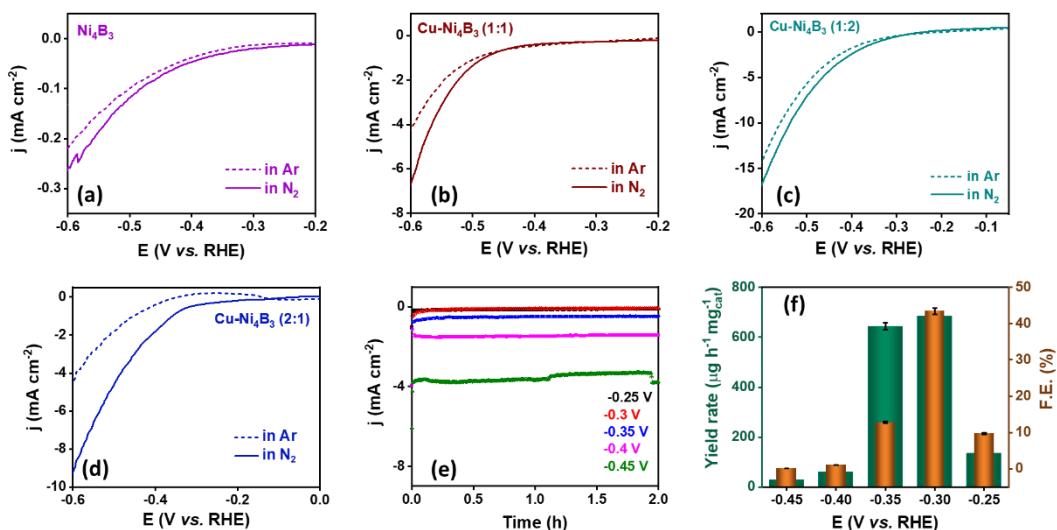


Figure 4B-4. LSV curves for (a) Ni_4B_3 (b) $\text{Cu-Ni}_4\text{B}_3$ (1:1), (c) $\text{Cu-Ni}_4\text{B}_3$ (1:2) and (d) $\text{Cu-Ni}_4\text{B}_3$ (2:1) in Ar- and N_2 -saturated 0.1 M H_2SO_4 electrolyte. (e) CA curves acquired at different potentials after NRR by $\text{Cu-Ni}_4\text{B}_3$ (1:2) catalyst and (f) comparison of NH_3 yield rate and F.E. obtained after NRR by $\text{Cu-Ni}_4\text{B}_3$ (1:2) catalyst.

attributed to the well-defined grape-bunch like morphology of the same. We also corroborated the NRR catalytic activity of $\text{Cu-Ni}_4\text{B}_3$ (1:2) under neutral (0.1 M Na_2SO_4) and alkaline (0.1 M KOH) electrolyte conditions (Figures 4B-5(b-c)). It was understood that the catalyst could still produce ammonia but at a mediocre rate than that produced under acidic conditions, and therefore established the capability of $\text{Cu-Ni}_4\text{B}_3$ to reduce N_2 over a wide range of pH. The NH_3 yield rates are 201.14 (at -0.4 V) and 268.18 $\mu\text{g}_{\text{NH}_3} \text{h}^{-1} \text{mg}_{\text{cat}}^{-1}$ (at -0.25 V) while the F.E. is 5.1 (at -0.4 V) and 2.86% (at -0.25 V) in neutral and alkaline conditions respectively (Figures 4B-5(d-e)). These values disclosed that $\text{Cu-Ni}_4\text{B}_3$ (1:2) reveal superior NRR activity in 0.1 M H_2SO_4 electrolyte compared with other electrolyte solutions. The superior activity was then scrutinized by means of different electrochemical characterizations discussed later in the chapter.

4B-3.3 Role of Cu-modification and optimal metal to precursor ratio on electrochemical NRR performance: Besides the structural and morphological

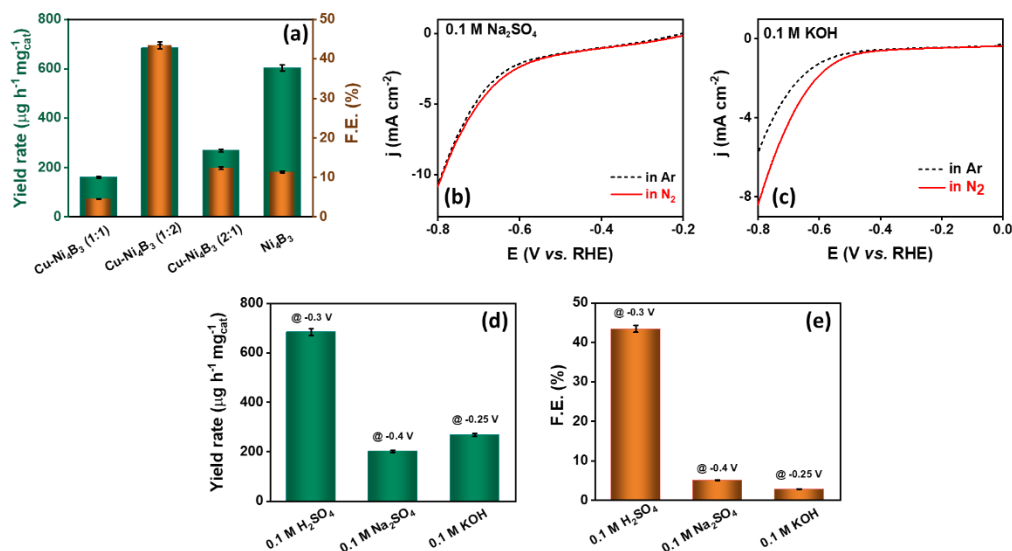


Figure 4B-5. (a) Bar diagram comparison of ammonia yield rate and F.E. after NRR by different catalysts. LSV curves for Cu-Ni₄B₃ (1:2) in (b) 0.1 M Na₂SO₄ and (c) 0.1 M KOH electrolyte under Ar- and N₂-saturated conditions. (d) NH₃ yield rate and (e) F.E. comparison after NRR by Cu-Ni₄B₃ (1:2) catalyst in different electrolytes.

features, the electrochemical features during NRR are also necessary to be determined for the comparison of the activity of catalysts among each other. For this purpose, we looked after certain electrochemical characterizations including Tafel analysis, EIS and electrochemical surface area (ECSA) analysis. Figure 4B-6a displayed the Tafel slope of Cu-Ni₄B₃ (1:2) which was found to be 63 mV dec⁻¹ which was lower than those of Cu-Ni₄B₃ (1:1), Cu-Ni₄B₃ (2:1) and Ni₄B₃ with Tafel slope values of 172, 148 and 248 mV dec⁻¹ respectively. The lowest Tafel slope value of Cu-Ni₄B₃ (1:2) catalyst pointed towards the accelerated kinetics during NRR and was further supported by means of EIS. The Nyquist plots for all catalysts revealed one semicircle and as anticipated, the smallest semi-circular domain was observed for Cu-Ni₄B₃ (1:2) with the lowest R_{ct} value of 66.86 Ω (Figure 4B-6b and Table 4B-1) and suggested the higher charge-transfer rate at the interface of solid electrode and liquid electrolyte. This implied that the modification of Ni₄B₃ with an optimal ratio of metallic Cu can significantly decrease the charge-transfer resistance (R_{ct}) by virtue of good conductivity and

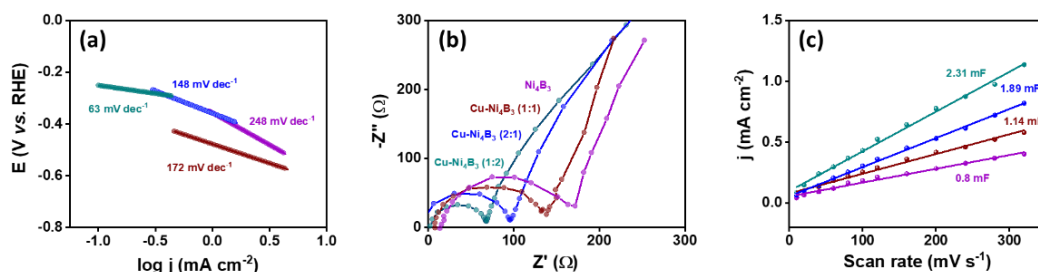


Figure 4B-6. (a) Tafel plots extracted from LSV curves for different catalysts in N_2 saturated electrolyte, (b) Nyquist plots for all catalytic variants and (c) scan rate vs. current density plots for C_{dl} calculation (color code: cyan- $\text{Cu-Ni}_4\text{B}_3$ (1:2), blue- $\text{Cu-Ni}_4\text{B}_3$ (2:1), maroon- $\text{Cu-Ni}_4\text{B}_3$ (1:1), purple- Ni_4B_3).

well-defined morphology. In the end, the double-layer capacitance (C_{dl}) and ECSA of designed catalysts were estimated and found out to be 2.31 mF and 5.775 cm^2 for $\text{Cu-Ni}_4\text{B}_3$ (1:2) catalyst which was higher than those of other control catalysts under identical potential range (Figures 4B-6c and Table 4B-2). All these inferences concluded the superior activity of $\text{Cu-Ni}_4\text{B}_3$ (1:2) catalyst over other variants and Ni_4B_3 alone owing to the synergetic effect between Cu and Ni_4B_3 and nanospherical morphology assembled into a grape bunch, which improved the overall kinetics as well as mass transport.

Table 4B-1. EIS analysis of $\text{Cu-Ni}_4\text{B}_3$ catalysts.

S. No.	Electrocatalyst	$R_s (\Omega)$	$R_p (\Omega)$	$R_{ct} (\Omega)$
1.	Ni_4B_3	14	169.71	155.71
2.	$\text{Cu-Ni}_4\text{B}_3$ (1:1)	7.38	137.93	130.55
3.	$\text{Cu-Ni}_4\text{B}_3$ (1:2)	1.84	68.7	66.86
4.	$\text{Cu-Ni}_4\text{B}_3$ (2:1)	6.22	97.93	91.71

Table 4B-2. ECSA determination for $\text{Cu-Ni}_4\text{B}_3$ catalysts.

S.No.	Electrocatalyst	$C_{dl}^* (\text{mF})$	ECSA (cm^2)
1.	Ni_4B_3	0.8	2
2.	$\text{Cu-Ni}_4\text{B}_3$ (1:1)	1.14	2.85
3.	$\text{Cu-Ni}_4\text{B}_3$ (1:2)	2.31	5.775
4.	$\text{Cu-Ni}_4\text{B}_3$ (2:1)	1.89	4.725

4B-3.4 Detection/Elimination of false positives in NRR: Several control experiments were conducted in this work to confirm the actual origin of the produced ammonia. Since we had used nickel nitrate and copper nitrate salts as reactant precursors for the synthesis of Cu-Ni₄B₃, therefore we cleansed the catalyst with an alkaline KOH solution to remove any trace nitrate impurities prior to NRR investigations. Also, the impact of impurities from electrolytes and feeding gas (*i.e.* Ar, ¹⁴N₂, ¹⁵N₂) was not excluded and control measures were taken. The electrolyte solution under study was evaluated for the presence of any nitrite or nitrate species by spectrophotometric methods which confirm the purity of electrolyte solution (described in previous chapters) and its negligible contribution towards NH₃ production. The purity of the feeding gases purged during the NRR experiments was assured by spectrophotometric and chromatography methods and by passing them through the scrubbing solution (detailed in previous chapters) prior every NRR measurement. These findings were further reinforced by performing other control tests such as 2 h electrolysis by purging Ar gas at -0.3 V (*vs.* RHE) for Cu-Ni₄B₃ (1:2) coated GCE, NRR over bare GCE and also under open circuit potential (OCP) with a N₂-saturated electrolyte. According to Figure 4B-7a, no NH₃ production was spotted in all control measurements and thus designated that the NH₃ is produced exclusively from reduction of purged N₂ and didn't originate from the NO_x/NH₄⁺ contaminations. The true source for ammonia production was also assessed by ¹H-NMR spectroscopy. Figure 4B-7b displayed a distinct triplet for ¹⁴NH₄⁺ in ¹H-NMR spectra acquired after NRR using ¹⁴N₂ as a feeding gas. In contrast, a doublet was witnessed when ¹⁵N₂ was used as a feeding gas during isotope labelling experiments under identical experimental conditions. This unambiguously labelled that the NH₃ production ascended from the N₂ reduction rather than any N-contaminants.

4B-3.5 Validation of NH₃ yield rate by isotope labelling experiments: When the origin of NH₃ produced during NRR was efficaciously tracked, the validation of the same was implemented by carrying out ¹⁵N₂-isotope labelling experiments and

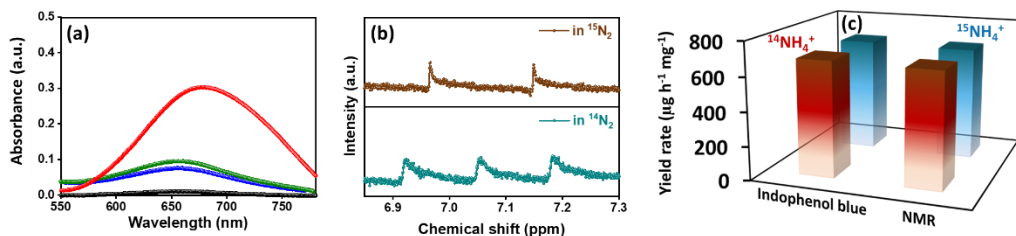


Figure 4B-7. (a) UV-Vis absorbance curves after NRR over bare electrode surface, at OCP and under Ar-saturated conditions (N_2 : red, Ar: black, OCP: green, Bare: blue), (b) ^1H -NMR spectrum acquired after NRR by $\text{Cu-Ni}_4\text{B}_3$ (1:2) catalyst in both $^{14}\text{N}_2$ - and $^{15}\text{N}_2$ -saturated electrolyte. (c) Bar diagram comparison for ammonia yield rates after isotope labelling experiments using different quantification methods.

quantification of produced $^{14}\text{NH}_4^+$ and $^{15}\text{NH}_4^+$ yield rates by different methods including spectrophotometric as well as NMR. The NH_3 yield rates were calculated to be $677 \mu\text{g}_{\text{NH}_3} \text{h}^{-1} \text{mg}_{\text{cat}}^{-1}$ ($^{14}\text{NH}_4^+$) and $670 \mu\text{g}_{\text{NH}_3} \text{h}^{-1} \text{mg}_{\text{cat}}^{-1}$ ($^{15}\text{NH}_4^+$) by NMR which are consistent with those obtained via Indophehnol blue method ($^{14}\text{NH}_4^+$: $684 \mu\text{g}_{\text{NH}_3} \text{h}^{-1} \text{mg}_{\text{cat}}^{-1}$, $^{15}\text{NH}_4^+$: $680 \mu\text{g}_{\text{NH}_3} \text{h}^{-1} \text{mg}_{\text{cat}}^{-1}$) respectively. For a better comparison, the NH_3 yield rates after isotope labelling experiments were presented in a bar graph in Figure 4B-7c, which validate the estimated NH_3 yield rate in this work.

4B-3.6 Catalyst stability: The stability of the electrocatalyst is deliberated to be an imperious measure to gauge the catalytic durability in addition to the activity. The stability of $\text{Cu-Ni}_4\text{B}_3$ (1:2) during NRR was tested by measuring the NRR

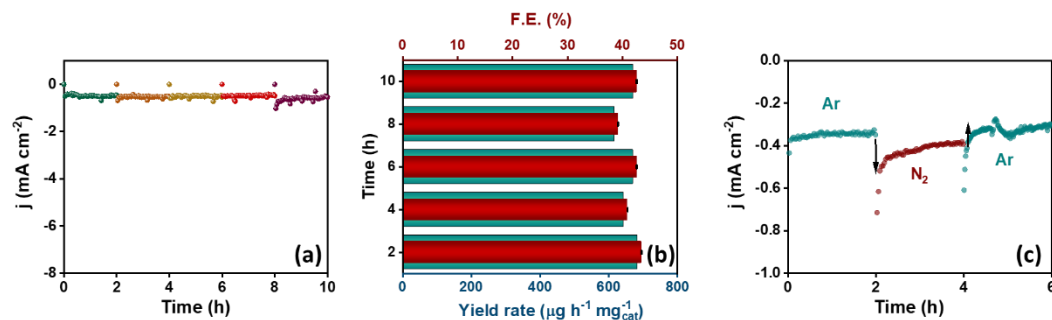


Figure 4B-8. (a) CA curves measured for 10 h for NRR at -0.3 V by $\text{Cu-Ni}_4\text{B}_3$ (1:2) catalyst in N_2 -saturated $0.1 \text{ M H}_2\text{SO}_4$ solution and (b) corresponding ammonia yield rate and F.E. obtained. (c) CA analysis under switching gas feed environments.

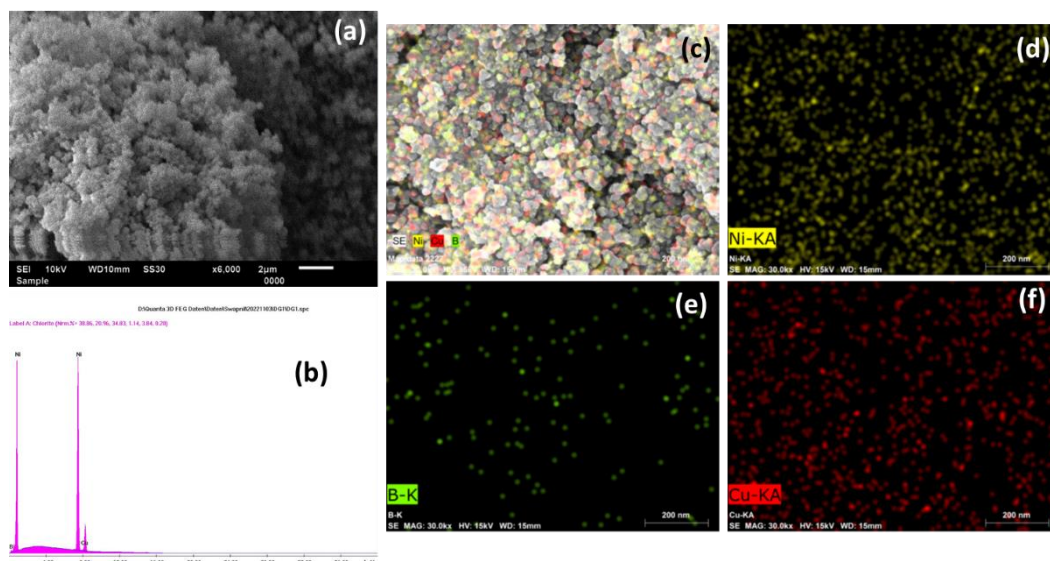


Figure 4B-9. (a) SEM image of Cu-Ni₄B₃ after NRR, (b) EDS spectrum showing presence of Cu, Ni and B and (c) the EDS dot mapping images for post NRR Cu-Ni₄B₃.

activity over a prolonged time duration of 10 h at a constant applied potential of -0.3 V (vs. RHE). Meanwhile, Cu-Ni₄B₃ (1:2) exhibited the high stability as the CA curves (Figure 4B-8a) disclosed negligible change in current density in N₂-saturated 0.1 M H₂SO₄ for 10 h. The ammonia production yield rate and F.E. measured after each CA cycle was equivalent (Figure 4B-8b) and hence stimulated that no degradation happened during NRR. Additionally, the CA measurements were performed under switching feeding gas (Ar and N₂) environments employing Cu-Ni₄B₃ (1:2) catalyst at -0.3 V (Figure 4B-8c). These results proposed the high stability of the catalyst even under switching feeding gas environments. The *ex-situ* material characterizations attained after stability measurements evidenced the morphology retention and unaltered elemental dot mapping surface distribution of Cu and Ni (Figure 4B-9).

4B-4 Summary

In this work, we have carried out the surface modification of Ni₄B₃ by the addition of metallic Cu via a green and energy efficient sonochemical reduction method

which revealed high activity towards N_2 reduction and formation of ammonia as a liquid product (F.E.: 43.42%, NH_3 yield rate: $684 \mu\text{g}_{\text{NH}_3} \text{h}^{-1} \text{mg}_{\text{cat.}}^{-1}$ @ -0.3 V vs. RHE). The role of Cu towards NRR activity was also ascertained by testing the control catalysts without Cu *i.e.* Ni_4B_3 which provided a lesser F.E. as well as lesser yield for ammonia at the identical applied potential. Cu- Ni_4B_3 catalyst variant with Cu-Ni mole ratio of 1:2 was found to be the optimal one with maximum activity in 0.1 M H_2SO_4 electrolyte. The activity of Cu- Ni_4B_3 (1:2) catalyst could be attributed to the grape-bunch-like morphology composed of nanospheres and the synergetic effect between Cu and metallic boride which resulted in the accelerated kinetics and rapid mass transfer of reactant. The catalyst also demonstrated a pH universal NRR activity over a wide pH range between 1-13, underlining its ability to activate and reduce N_2 molecules to ammonia in different electrolytes. Henceforth, this work could be further explored for the study of the effect of Cu towards the activity and selectivity of metal borides towards NH_3 production under ambient conditions.

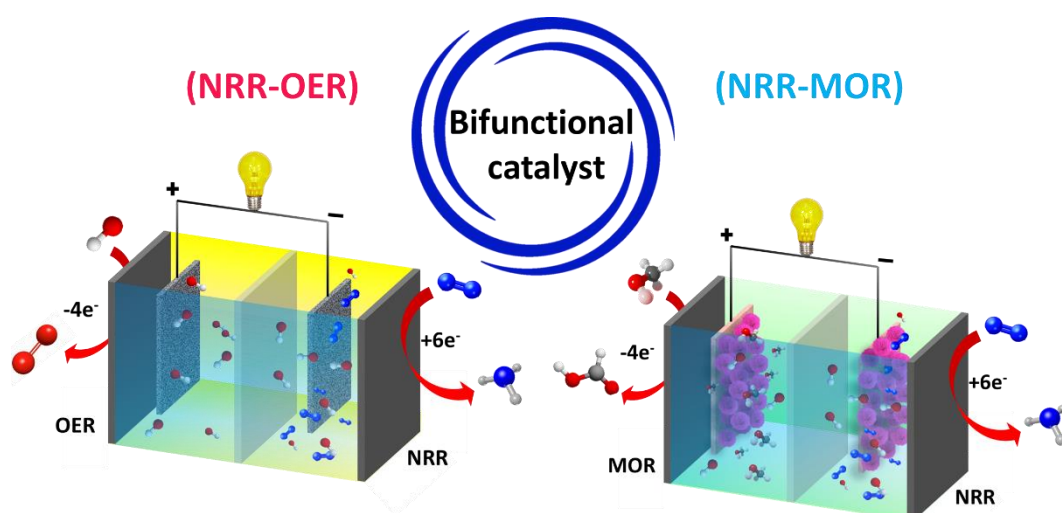
4B-5 References

1. C. J. Van der Ham, M. T. Koper and D. G. Hetterscheid, *Chem. Soc. Rev.*, 2014, **43**, 5183-5191.
2. A. J. Martín, T. Shinagawa and J. Pérez-Ramírez, *Chem*, 2019, **5**, 263-283.
3. X. Guo, H. Du, F. Qu and J. Li, *J. Mater. Chem. A*, 2019, **7**, 3531-3543.
4. X. Yang, B. Xu, J. G. Chen and X. Yang, *ChemSusChem*, 2023, **16**, e202201715.
5. K. N. Dinh, Q. Liang, C.-F. Du, J. Zhao, A. I. Y. Tok, H. Mao and Q. Yan, *Nano Today*, 2019, **25**, 99-121.
6. Y. H. Moon, N. Y. Kim, S. M. Kim and Y. J. Jang, *Catalysts*, 2022, **12**, 1015.
7. Z. J. Huba, M. D. Donakowski and A. Epshteyn, *Chem. Mater.*, 2017, **29**, 1467-1471.
8. Y. Kang, Y. Tang, L. Zhu, B. Jiang, X. Xu, O. Guselnikova, H. Li, T. Asahi and Y. Yamauchi, *ACS Catal.*, 2022, **12**, 14773-14793.
9. S. Qi, Y. Fan, L. Zhao, W. Li and M. Zhao, *Appl. Surf. Sci.*, 2021, **536**, 147742.
10. Z. Pu, T. Liu, G. Zhang, X. Liu, M. A. Gauthier, Z. Chen and S. Sun, *Small Methods*, 2021, **5**, 2100699.
11. S. H. Mir, V. K. Yadav and J. K. Singh, *ACS Appl. Mater. Interfaces*, 2022, **14**, 29703-29710.
12. L. Shi, P. Wang, Q. Wang, X. Ren, F. Ichihara, W. Zhou, H. Zhang, Y. Izumi, B. Cao and S. Wang, *J. Mater. Chem. A*, 2020, **8**, 21833-21841.
13. Z. Guo, J. Zhou and Z. Sun, *J. Mater. Chem. A*, 2017, **5**, 23530-23535.
14. Y. Xiao, C. Shen and T. Long, *Chem. Mater.*, 2021.
15. Y. Fu, P. Richardson, K. Li, H. Yu, B. Yu, S. Donne, E. Kisi and T. Ma, *Nano-Micro Lett.*, 2020, **12**, 1-13.
16. K. Chu, W. Gu, Q. Li, Y. Liu, Y. Tian and W. Liu, *J. Energy Chem.*, 2021, **53**, 82-89.

17. S. Li, Y. Wang, J. Liang, T. Xu, D. Ma, Q. Liu, T. Li, S. Xu, G. Chen and A. M. Asiri, *Mater. Today Phys.*, 2021, **18**, 100396.
18. Q. Li, Y. Cheng, X. Li, Y. Guo and K. Chu, *Chem. Commun.*, 2020, **56**, 13009-13012.
19. J. Masa, C. Andronesco, H. Antoni, I. Sinev, S. Seisel, K. Elumeeva, S. Barwe, S. Marti-Sanchez, J. Arbiol and B. Roldan Cuenya, *ChemElectroChem*, 2019, **6**, 235-240.
20. J. Wu, M. Hou, Z. Chen, W. Hao, X. Pan, H. Yang, W. Cen, Y. Liu, H. Huang and P. W. Menezes, *Adv. Mater.*, 2022, **34**, 2202995.
21. J. Hong, S. Mutalik, M. Miola, D. Gerlach, R. Mehrabi K, M. Ahmadi, B. J. Kooi, G. Portale, P. Rudolf and P. P. Pescarmona, *Chem. Mater.*, 2023, **35**, 1710-1722.
22. D. Acosta, N. Ramírez, E. Erdmann, H. Destéfani and E. Gonzo, *Catal. Today*, 2008, **133**, 49-55.
23. J. Zhang, X. Li, Y. Liu, Z. Zeng, X. Cheng, Y. Wang, W. Tu and M. Pan, *Nanoscale*, 2018, **10**, 11997-12002.
24. H. Chen and X. Zou, *Inorg. Chem. Front.*, 2020, **7**, 2248-2264.
25. O. Gudaev and V. Malinovskii, *Phys. Solid State*, 2002, **44**, 837-842.
26. N. Xu, G. Cao, Z. Chen, Q. Kang, H. Dai and P. Wang, *J. Mater. Chem. A*, 2017, **5**, 12379-12384.
27. H. Liu, R. Zhang, L. Chen, L. Wang, Y. Guo and Y. Yang, *Adv. Sustain. Syst.*, 2021, **5**, 2000184.
28. K. Xiao, X. Qi, Z. Bao, X. Wang, L. Zhong, K. Fang, M. Lin and Y. Sun, *Catal. Sci. Technol.*, 2013, **3**, 1591-1602.
29. L. Zhang, H. Shoushuang, J. Bao, L. Liu, T. Ye, X. Cong, K. Uvdal and Z. Hu, *J. Alloys Compd.*, 2022, **910**, 164759.
30. H. V. Leland and J. L. Carter, *Freshwater biology*, 1985, **15**, 155-173.
31. W. Weisany, Y. Raei and K. H. Allahverdiipoor, *Bulletin of Environment, Pharmacology and Life Sciences*, 2013, **2**, 77-84.
32. J. Kong, M.-S. Kim, R. Akbar, H. Y. Park, J. H. Jang, H. Kim, K. Hur and H. S. Park, *ACS Appl. Mater. Interfaces*, 2021, **13**, 24593-24603.
33. Y.-X. Lin, S.-N. Zhang, Z.-H. Xue, J.-J. Zhang, H. Su, T.-J. Zhao, G.-Y. Zhai, X.-H. Li, M. Antonietti and J.-S. Chen, *Nat. Commun.*, 2019, **10**, 4380.
34. C. Dong and X. Han, *Mater. Today Energy*, 2022, **30**, 101181.
35. Y. Qu, T. Dai, Y. Cui, Y. Zhang, Z. Wang and Q. Jiang, *Chem. Eng. J.*, 2022, **433**, 133752.
36. H. S. Kim, H. Jin, S.-H. Kim, J. Choi, D. W. Lee, H. C. Ham, S. J. Yoo and H. S. Park, *ACS Catal.*, 2022, **12**, 5684-5697.
37. X. Wang, S. Qiu, J. Feng, Y. Tong, F. Zhou, Q. Li, L. Song, S. Chen, K. H. Wu and P. Su, *Adv. Mater.*, 2020, **32**, 2004382.
38. K. Li, L. Ding, Z. Xie, G. Yang, S. Yu, W. Wang, D. A. Cullen, H. M. Meyer III, G. Hu and P. Ganesh, *ACS Appl. Mater. Interfaces*, 2023, **15**, 11703-11712.
39. J. M. V. Nsanzimana, Y. Peng, Y. Y. Xu, L. Thia, C. Wang, B. Y. Xia and X. Wang, *Adv. Energy Mater.*, 2018, **8**, 1701475.
40. M. Wei, D. Zhang, J. Deng, X. Xiao, L. Wang, X. Wang, M. Song, S. Wang, X. Zheng and X. Liu, *Ind. Eng. Chem. Res.*, 2022, **61**, 7777-7786.

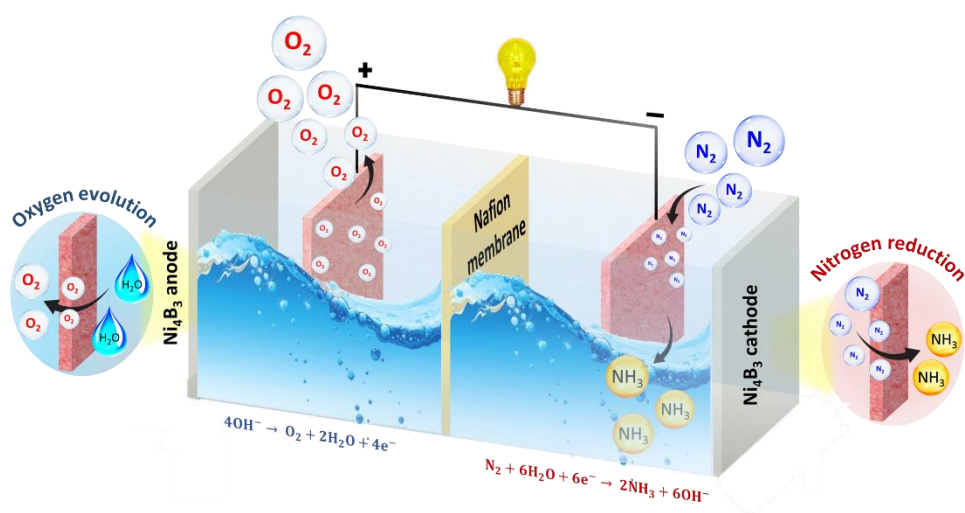
Chapter 5

Designing of high performance bifunctional catalysts for overall ammonia synthesis



Chapter 5A

Bifunctional electrocatalysis towards N_2 reduction and O_2 evolution via Ni_xB_y catalyst for overall NH_3 synthesis



5A-1 Introduction

Ammonia is a dominant constituent (~ 80%) for large-scale production of fertilizers in industries which is responsible for ~2% of the world's fossil fuel energy consumption and about 1% of global greenhouse gas (GHG) emissions.¹ Application of renewable energy sources for H₂ generation as well as driving the reduction of nitrogen for ammonia synthesis is conspicuous², where electrochemical ammonia synthesis is one of the most promising candidates. It involves NH₃ production at the cathode from N₂ and H₂O under ambient conditions³ and the generation of O₂ at the anode. The overall cell potential depends on anodic and cathodic reactions occurring in the cell during operation *i.e.* sum of anodic and cathodic potential. Hence, for efficient synthesis of ammonia, the development of active catalysts for electrochemical nitrogen reduction (NRR) and oxygen evolution reaction (OER) are important to reduce the overpotential associated with both the processes taking place. The cathodic NRR process is associated with certain challenges such as the activation of N≡N triple bond due to its high first-bond cleavage energy (410 kJ mol⁻¹) and high HOMO-LUMO energy gap (22.9 eV)⁴. Additionally the competing hydrogen evolution reaction (HER) at the cathode accounts for the poor selectivity and hence the poor Faradaic efficiency during NRR.⁵ On the other hand, the OER at the anode exhibit sluggish kinetics due to four electron transfer, requiring a high overpotential. Therefore, the sluggish kinetics of both NRR and OER results in the higher overall voltage in full cell conditions and thus the poor efficiency of overall device.⁶

At present the precious RuO₂ based catalysts⁷ are employed as benchmark catalysts for OER but show a poor activity towards NRR. On the other hand, noble metal catalysts like Au^{8,9,10}, Ru^{11,12,13}, Rh¹⁴, Pt^{15,16} and Pd^{17,18} have been extensively explored towards NRR. But, their scarcity and high cost may also increase the overall cost of the reactor if applied. Due to which the research has been shifted towards the development of non-noble metal based¹⁹, carbonaceous materials²⁰, and MOF/MOF-derived catalysts.²¹ Due to the difference in fundamental

mechanism of the two different processes involved during overall ammonia synthesis, generally two different catalysts are employed on either sides of the NRR-OER full cell device. This ultimately leads to the increased complexity and material processing costs of the system and demands the designing of a cost-effective non-noble metal-based bifunctional catalyst for OER and NRR. The performance of NRR-OER coupled overall ammonia synthesis device is completely reliant on the activity and robust phase stability of bifunctional NRR-OER catalysts engaged at the cathode and anode which is rarely considered. The development of a bifunctional catalyst can simplify the cell setup and reduce the cost of the overall cell with maximum utilization of electrocatalyst.^{22, 23}

To design a bifunctional catalyst for OER and NRR, it is important to consider the mechanism of both reactions. Electrocatalytic dinitrogen reduction²⁴ and water electrolysis²⁵ both involve different mechanisms and hence different catalysts are employed to achieve better activity and performance.²⁶⁻²⁸ Despite the extreme efforts being made for the development of a suitable NRR catalyst for cathode and OER catalyst for anode separately, the development of an appropriate catalyst targeting the robust and efficient couplings between OER and NRR for application in a full-cell configuration is of huge significance but challenging.²⁹ The major challenge is to facilitate or accelerate the kinetically sluggish 4e⁻ OER and 6e⁻ NRR which affect the efficiency of the cell system due to which very few reports in this area have been reported so far. Ren *et al.* has reported cobalt phosphates for NRR-OER bifunctional activity at Zn-N₂ battery cathode with a power density of 0.49 mW cm⁻² as well as a high NH₃ F.E. of 24.42%.²⁹ Li *et al.* employed 2D bimetal-MOFs (Co_xFe-MOF) nanosheets for NH₃ synthesis in alkaline media with an overpotential of 280 mV at a current density of 10 mA cm⁻² and a small Tafel slope of 38 mV dec⁻¹ in 1.0 M KOH electrolyte. At the cathode, it is capable of producing NH₃ with a F.E. up to 25.64% and NH₃ yield rate of 8.79 µg h⁻¹ mg_{cat}⁻¹ at -0.2 V (vs. RHE) in 0.1 M KOH electrolyte.³⁰ Sun *et al.* has developed a bifunctional nickel, iron-nanomesh array electrocatalyst demonstrating an excellent NRR

activity with an ammonia yield of $16.89 \mu\text{g h}^{-1} \text{mg}_{\text{cat}}^{-1}$ and a F.E. of 12.50% at -350 mV (vs. RHE), in addition to OER activity with a small overpotential of 191 mV to achieve 10 mA cm^{-2} .³¹ A remarkable ammonia production performance is also revealed under full-cell conditions with an ammonia yield of $2.07 \mu\text{g h}^{-1} \text{mg}_{\text{cat}}^{-1}$ at 1.9 V, and FE of 9.87% at 1.6 V, and good durability for 30 h. Wang *et al.* reported Ni foam (NF) supported sisal-like porous MoO_2 nanosheet array (MoO_2/NF) to achieve an NH_3 yield rate of $9.56 \mu\text{g h}^{-1} \text{cm}^{-2}$ and a Faradaic efficiency of 5.14% in 0.1 M KOH along with a good performance for the OER in 0.1 M KOH, exhibiting a small overpotential of 340 mV to realize a current density of 10 mA cm^{-2} . In the full-cell configuration, a remarkable ammonia yield of $5.73 \mu\text{g h}^{-1} \text{cm}^{-2}$, and FE of 15.8% is achieved with a 24 h of stability.³²

Transition metal borides (TMBs) including cobalt and nickel have been broadly used in electrocatalysis because of their enhanced electrical conductivity, stability and hardness.^{33,34} TMBs, especially Ni-based borides, exhibit superior oxygen evolution reaction (OER) performance in alkaline media compared with noble metal catalysts, metal oxides, and metal alloy counterparts.³⁵⁻³⁹ And so, in this work we have synthesized the nickel boride composite and explored towards its bifunctional activity for NRR and OER under alkaline conditions. Here, we propose a simple one-step sonochemical reduction approach to synthesize a Ni_xB_y catalyst which can simultaneously meet the requirement of both NRR and OER. Ni_xB_y can offer a low overpotential of 300 mV to achieve 10 mA cm^{-2} and a small Tafel slope of 74 mV dec^{-1} , which outperforms the benchmark RuO_2 catalytic performance as well as the Ni_xB_y catalyst synthesized via simple chemical reduction method. A similar trend is observed during NRR analysis, where sonochemically synthesized Ni_xB_y is able to achieve a high F.E. and ammonia production yield rate of 47.9% and $1.55 \text{ mg h}^{-1} \text{mg}_{\text{cat}}^{-1}$ at -0.2 V vs. RHE in 0.1 M KOH electrolyte which is definitely superior to the Ni_4B_3 catalyst (maximum activity at -0.4 V with $0.88 \text{ mg h}^{-1} \text{mg}_{\text{cat}}^{-1}$ of NH_3 yield rate and 17.9% of F.E.) synthesized via chemical reduction method. Furthermore, the NRR-OER full cell

assembly employing Ni_xB_y as a bifunctional catalyst is capable of initiating NH₃ production at just 1.9 V to produce 1.08 mg h⁻¹ mg_{cat}⁻¹ of ammonia while O₂ evolution on the other side is witnessed with a yield rate of 0.81 mg h⁻¹ mg_{cat}⁻¹ respectively. These outcomes indicate that the TMB catalysts provide a pathway for the design of high-performance bi-functional electrocatalysts coupling OER and NRR in a full-cell configuration.

5A-2 Material synthesis

5A-2.1 Synthesis of Ni_xB_y: The synthesis of Ni_xB_y catalyst was carried out via a sonochemical reduction method using NiCl₂ as a metal precursor and NaBH₄ as a reducing agent. Briefly, 4.5 mmol of NiCl₂ (0.576 g in 10 mL deionized water) was taken in a three-necked round-bottomed flask kept in an ice bath and sealed properly with continuous purging of Ar gas-feed to maintain the inert conditions during synthesis. After creating an inert atmosphere for around half an hour, the 4.85 mmol solution of NaBH₄ (0.183 g in 10 mL deionized water) was added dropwise to the metal precursor solution over a time duration of 30 min. under probe sonication (1 min. sonication and 5 min. rest and applied frequency of 20 Hz) till the completion of the reaction and ceasing of bubbles due to H₂ evolution. The black precipitates were obtained which were centrifuged, washed and then filtered using a Whatman filter paper followed by drying at 60 °C in a Binder oven to form B(OH)₃ which can be filtered off through filter paper leaving the pure Ni_xB_y particles behind. The catalyst was denoted as Ni_xB_y (SR) in this study. To see the effect of the synthetic route over morphology and thus the activity of the catalyst, Ni_xB_y was also synthesized via the chemical reduction method which had all the steps similar but no ultrasonication was provided during the synthesis, and the obtained catalyst was denoted as Ni_xB_y (CR).

5A-3 Results and discussion

5A-3.1 Physical characterization: We have synthesized Ni_xB_y catalyst via two approaches *i.e.* one involved a simple chemical reduction of Ni metal precursor

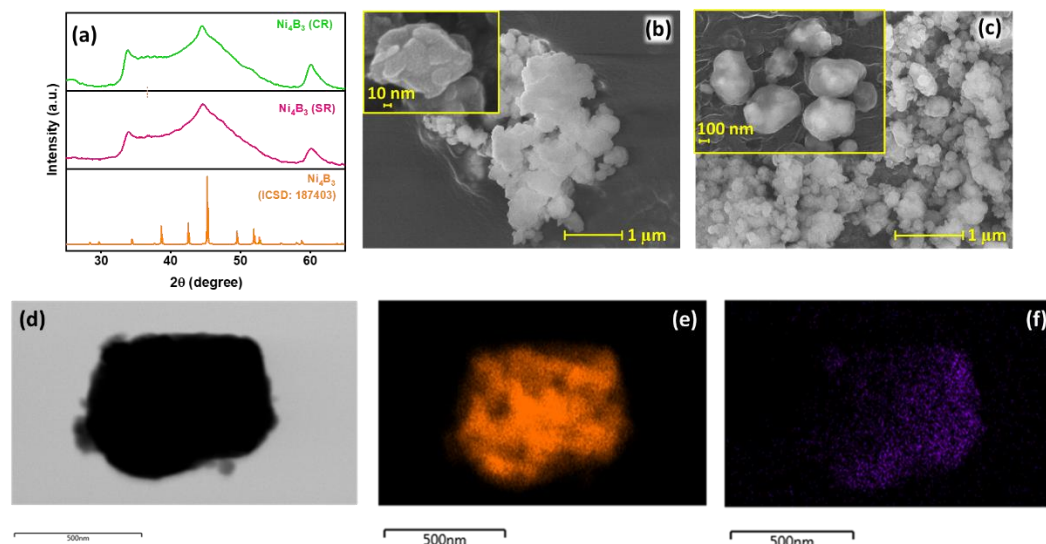


Figure 5A-1. (a) P-XRD patterns for as-synthesized Ni_4B_3 catalysts and the matching reference pattern, FE-SEM images of (b) Ni_4B_3 (CR) and (c) Ni_4B_3 (SR) catalysts. (d-f) TEM-EDS dot mapping images showing the homogeneous distribution of Ni (orange) and B (blue) over the scanned area.

under inert conditions using NaBH_4 as a reducing agent while the other was based upon a facile, less time consuming, energy efficient sonochemical reduction method using the same reactants under identical synthesis conditions. The structural phase of as-synthesized Ni_xB_y catalysts were primarily examined by powder X-ray diffraction. The diffraction patterns shown in Figure 5A-1a verified that the Ni_xB_y synthesized by different methods exhibited presence of a major peak at around 44.26° which could be attributed to the presence of Ni_4B_3 phase (ICSD: 187403) crystallized in the monoclinic C2/c space. On the other hand, the two additional peaks observed at 34.5° and 60.2° revealed the presence of NiO phase due to surface oxidation during filtering and washing. From the P-XRD measurements, Ni_4B_3 was identified as a dominant product with traces of NiO .

Thereafter, the morphology of Ni_xB_y catalysts were discerned well by FE-SEM images. The FE-SEM image in Figures 5A-1(b-c) indicated an aggregated cluster like morphology for Ni_xB_y catalyst synthesized via chemical reduction route, on the other hand, the Ni_xB_y (SR) catalyst revealed a foamy cotton-like morphology.

The elemental composition and distribution of Ni_xB_y (SR) were further examined by TEM-EDS and dot mapping analysis [Table 5A-1 and Figures 5A-1(d-f)] which revealed the composition of Ni and B to be approximately Ni₄B₃. The TEM images of Ni_xB_y (SR) in Figure 5A-2a clearly evidenced the cotton-like morphology while the HR-TEM image further supported the presence of Ni₄B₃ spherical nanoparticles

Table 5A-1: Elemental composition analysis for Ni_xB_y (SR).

Element	Weight%	σ (Standard deviation)
Ni K	32.5	0.7
B K	6.8	0.9
O K	18.6	0.5
C	42.1	0.8

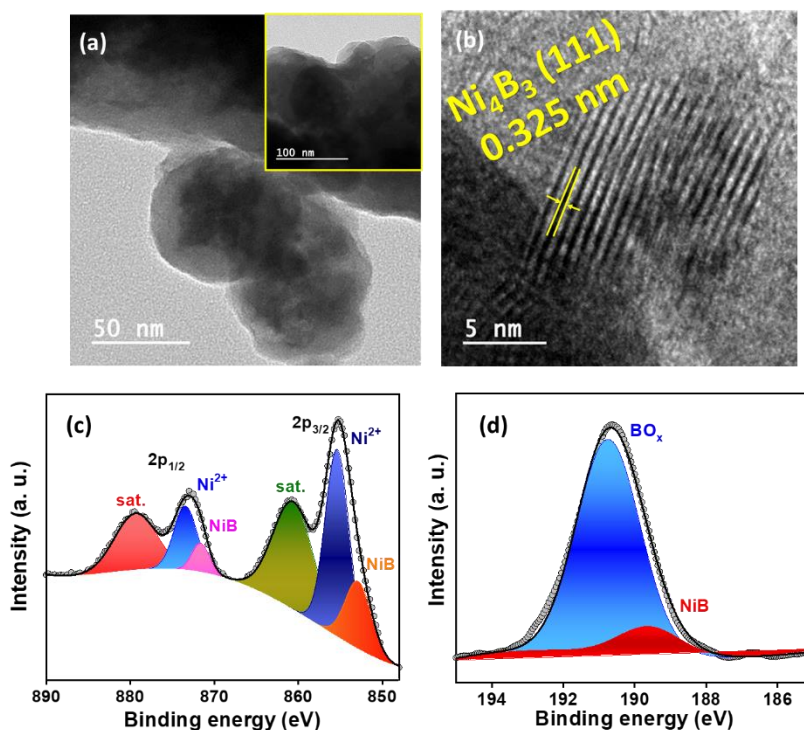


Figure 5A-2. (a) TEM and (b) HR-TEM image of Ni_xB_y (SR) catalyst. The deconvoluted (c) Ni 2p XP spectrum and (d) B 1s spectrum for Ni_xB_y (SR) catalyst.

diffused inside the thin cotton-like amorphous layer with the lattice fringes of 0.325 nm attributed to the (111) plane of Ni_4B_3 (Figure 5A-2b). The chemical and electronic states of the Ni_xB_y (SR) catalyst were then determined by means of XPS spectrum. The Ni 2p spectra of Ni_xB_y (SR) showed in Figure 5A-2c demonstrated two main peaks of Ni 2p_{3/2} and Ni 2p_{1/2} at 855.1 and 873.1 eV, respectively. Upon deconvolution, the characteristic peaks at 852.8 and 871.8 eV were witnessed and assigned to Ni-B (Ni in 0 oxidation state) while the peaks at 855.5 and 873.5 eV were identified as Ni in +2 oxidation state. On the other hand, the B 1s spectrum displayed the two major peaks corresponding to the M-B bond and B-O bond (due to surface oxidation) at 189.4 and 191 eV of binding energies respectively (Figure 5A-2d).

5A-3.2 Electrocatalytic NRR activity: Ni_xB_y catalysts synthesized in this work were employed as electrocatalysts to estimate the resultant electrochemical NRR performance under ambient conditions in 0.1 M KOH under a three-electrode configuration at first. The NRR ability was preliminarily probed by means of linear

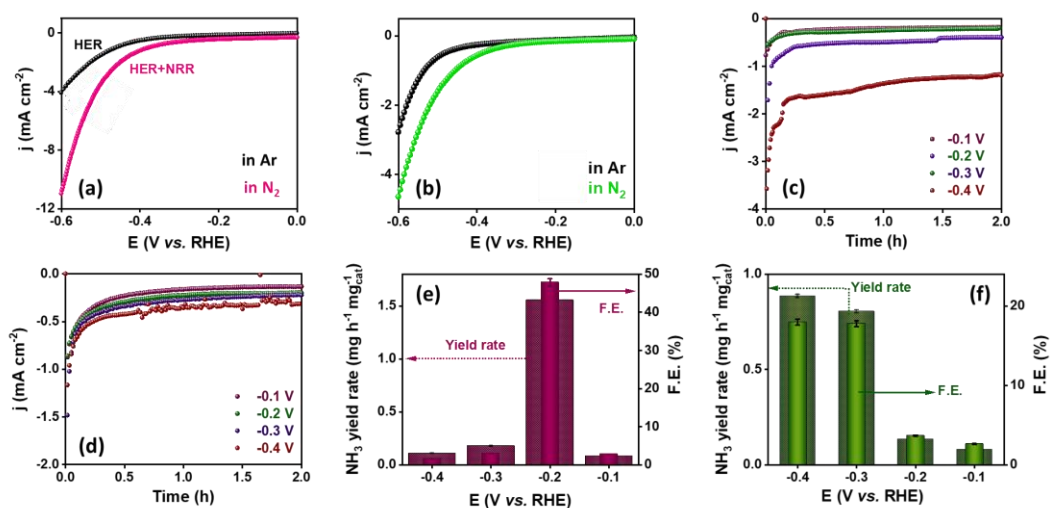


Figure 5A-3. Linear sweep voltammograms acquired for (a) Ni_xB_y (SR) and (b) Ni_xB_y (CR) in Ar- and N_2 -saturated 0.1 M KOH electrolyte. CA curves recorded at different applied potentials for NRR by (c) Ni_xB_y (SR) and (d) Ni_xB_y (CR) catalysts. Bar diagram showing the F.E. and ammonia yield rates obtained after NRR at different potentials by (e) Ni_xB_y (SR) and (f) Ni_xB_y (CR) catalysts respectively.

sweep voltammetry under identical experimental conditions for both Ni_xB_y (CR) and Ni_xB_y (SR). The LSV curves in Figures 5A-3(a-b) acquired in 0.1 M KOH electrolyte with Ar and N₂ feeding gas was measured for both catalysts variants respectively, where both the catalyst could describe the enhanced current density in presence of N₂ than in Ar. The net current density ($j_{N_2}-j_{Ar}$) of Ni_xB_y (CR) was found to be only -2 mA cm⁻² at -0.6 V (*vs.* RHE) under N₂-saturation, while Ni_xB_y (SR) catalyst could achieve a net current density of -6.87 mA cm⁻² at identical applied potential and conditions. These outcomes were sufficient enough to prove the activity of Ni_xB_y catalysts towards NRR and the superior activity of Ni_xB_y (SR) with a cotton-like morphology under applied potentials. Further potentiostatic experiments *viz.* chronoamperometry (CA) at different potentials were accomplished to understand and better reflect the NRR ability of electrocatalysts followed by the calculation of NH₃ yield rate and F.E. using the standard quantification method. Figures 5A-3(c-d) presented the CA curves of Ni_xB_y catalysts for 2 h electrolysis under N₂-saturated 0.1 M KOH electrolyte at different applied potentials *ca.* from -0.1 V to -0.4 V consequently. No degradation in the current densities could be observed with change in time and thus confirmed the stability of Ni_xB_y catalysts in due course of NRR. On the other hand, the best activity towards NRR was achieved by Ni_xB_y (SR) catalyst which reached 1.56 mg h⁻¹ mg_{cat}⁻¹ (NH₃ yield rate) and 47.9% (F.E.) respectively at -0.2V *vs.* RHE. These values were far superior to that obtained for Ni_xB_y (CR) under similar potentials (0.14 mg h⁻¹ mg_{cat}⁻¹ NH₃ yield rate and 3.68% F.E.) and even the maximum NRR activity was obtained at -0.4 V with 0.88 mg h⁻¹ mg_{cat}⁻¹ (NH₃ yield rate) and 17.9% (F.E.) is inferior to the that of sonochemically synthesized catalyst. And thus these outcomes reflect the role of morphology towards NRR activity [Figures 5A-3(e-f)]. Further, the sharp decrement observed in F.E. and ammonia yield rate at larger negative potentials could be ascribed to the predominance of HER which resulted in the competitive kinetics of HER over NRR. The superior activity of Ni_xB_y (SR) was correlated with its lower Tafel slope, lower charge transfer resistance (R_{ct}) and higher ECSA value over Ni_xB_y (CR) by executing EIS and CV in the non-faradaic

region at different scan rates consecutively (Table 5A-2). A typical semicircular behaviour was observed in the Nyquist plots shown in Figure 5A-4a with a less diameter for Ni_xB_y (SR) which depicted the lower R_{ct} value ($83.5\ \Omega$) and thus the accelerated charge-transfer process during NRR at the electrode-electrolyte interface due to the formation of a comparatively thin-diffusion layer.

Table 5A-2: EIS and ECSA for Ni_xB_y catalysts.

Electrocatalyst	EIS analysis			ECSA analysis	
	R_s	R_p	R_{ct}	C_{dl}	ECSA
Ni_xB_y (SR)	$2.12\ \Omega$	$85.63\ \Omega$	$83.5\ \Omega$	$2.6\ \text{mF}$	$6.5\ \text{cm}^2$
Ni_xB_y (CR)	$10.8\ \Omega$	$111.8\ \Omega$	$101\ \Omega$	$2.18\ \text{mF}$	$5.4\ \text{cm}^2$

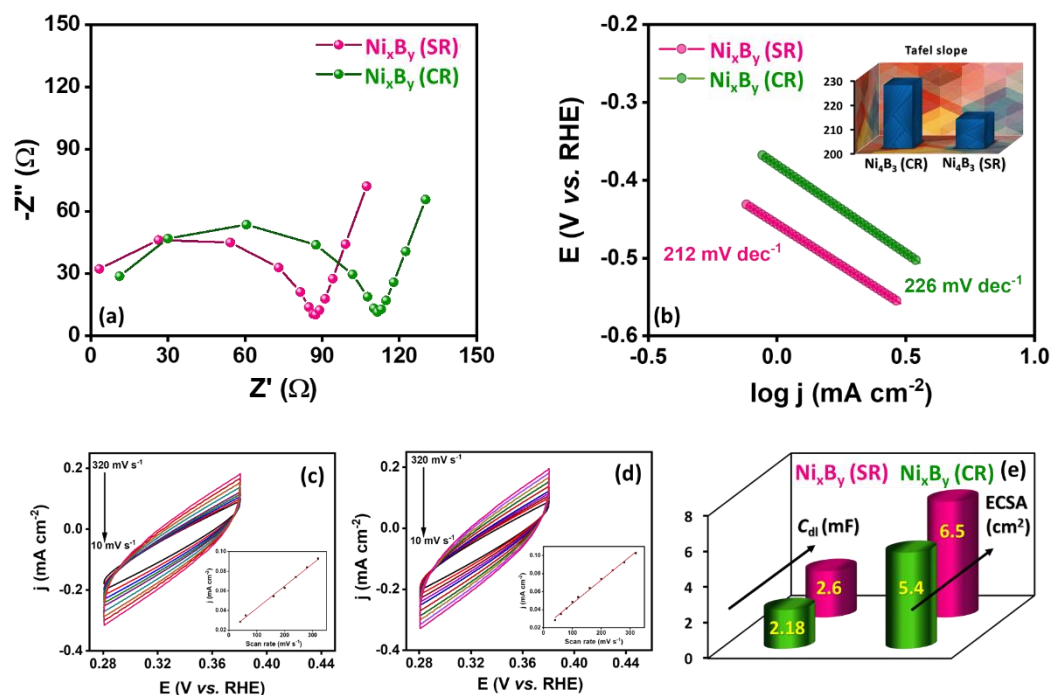


Figure 5A-4. (a) Nyquist plots and (b) Tafel plots of Ni_xB_y catalysts. (c) Cyclic voltammograms recorded under non-faradaic region at different scan rates and respective scan rate vs. current density plots in inset for (c) Ni_xB_y (CR) and (d) Ni_xB_y (SR). (e) Bar graph comparison of Ni_xB_y catalysts for charge double-layer capacitance and electrochemically active surface area extracted from Figures 5A-4(c-d).

This was in accordance with the lower Tafel slope value of 212 mV dec⁻¹ for Ni_xB_y (SR), as revealed in Figure 5A-4b. Moreover, the high ECSA value of 6.5 cm² was perceived for the Ni_xB_y catalyst synthesized via the sonochemical reduction method and thus affirmed the availability of the increased number of active sites for N₂ adsorption, activation and simultaneous reduction to ammonia [Figures 5A-4(c-e)]. Thereafter, the practicability of Ni_xB_y (SR) was evaluated by conducting recycling tests for 8 h at -0.2 V, where the maximum NRR activity was achieved. Figure 5A-5a displayed that the ammonia production yield rates remained stable during the 5 consecutive NRR cycles (2 h each) while maintaining the F.E. more or less constant. Moreover, there was no significant alteration in the current density even after the long-term NRR operation (Figure 5A-5b). Additionally, the Ni₄B₃ (SR) catalyst was characterized after NRR test by P-XRD, SEM, EDS and dot mapping analysis. The retention of analogous cotton-like morphology even after stability tests in corresponding FE-SEM image (Figure 5A-5c) and the uniform distribution in dot mapping images [Figures 5A-5(d-f)] evidenced the structural,

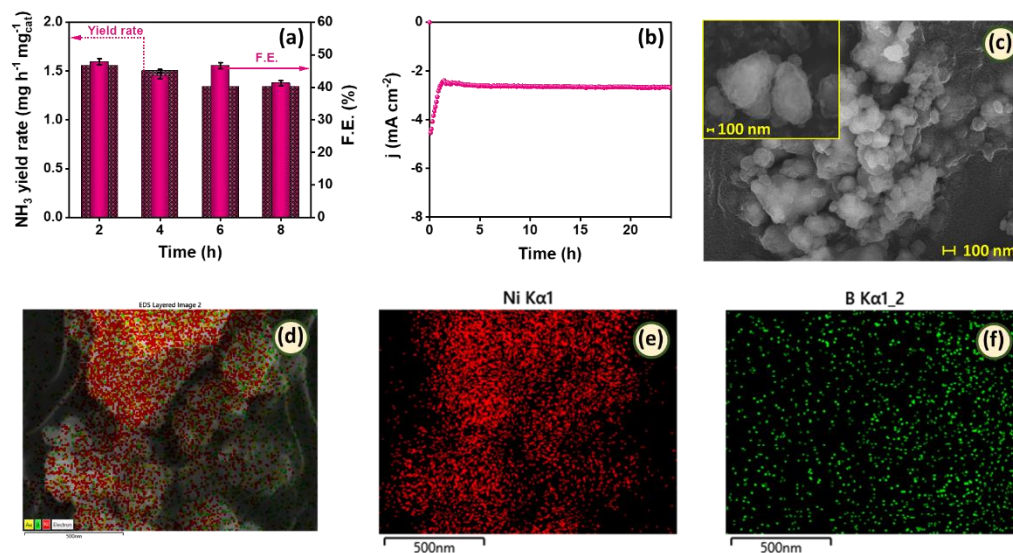


Figure 5A-5. (a) Bar graph representing the F.E. and NH₃ yield rate obtained at -0.2 V (vs. RHE) after NRR stability tests for 8 h and (b) CA curve showing stable current response for over 24 h of NRR in N₂-saturated 0.1 M KOH electrolyte. (c) FE-SEM and (d-f) EDS dot mapping images for Ni₄B₃ (SR) catalyst collected after NRR stability tests by Ni_xB_y (SR).

morphological and elemental robustness of the catalyst after NRR. To further confirm the reliability of the reported ammonia yield rate by the Indophenol blue method, the Nessler's reagent test was also performed after NRR by Ni_xB_y (SR) at -0.2 V, which gave a yield rate value of $1.54 \text{ mg h}^{-1} \text{ mg}_{\text{cat}}^{-1}$ *i.e.* almost similar to that obtained from Indophenol blue method (Table 5A-3). This verified the accuracy of NRR measurements in this work, where particular care was taken to detect and eliminate the presence of NO_x or NH_4^+ impurities in electrode setup, electrolyte solution and even gas-feed streams via well-established cleansing procedures. Furthermore, the ammonia yield rate was also compared in an Ar-saturated 0.1 M KOH electrolyte, over bare GCE and under OCP conditions, where no obvious peak related to NH_4^+ could be detected in the UV-Vis absorbance curve after Indophehnol blue method (Figure 5A-6a). This demonstrated that the ammonia produced in this study involved externally purged N_2 as the only source rather than any other contaminations. Followed by this, an isotope labelling experiment was performed using $^{15}\text{N}_2$ as the gas supply for 2 h at an applied potential of -0.2 V. The ^1H -NMR spectrum of the electrolyte sample collected after NRR in the $^{15}\text{N}_2$ environment revealed a typical doublet peak corresponding to $^{15}\text{NH}_4^+$ signal with a coupling constant of approx. 73 Hz while a triplet peak was observed when NRR was performed under $^{14}\text{N}_2$ saturated conditions. This confirmed that the produced ammonia was generated due to NRR process only.

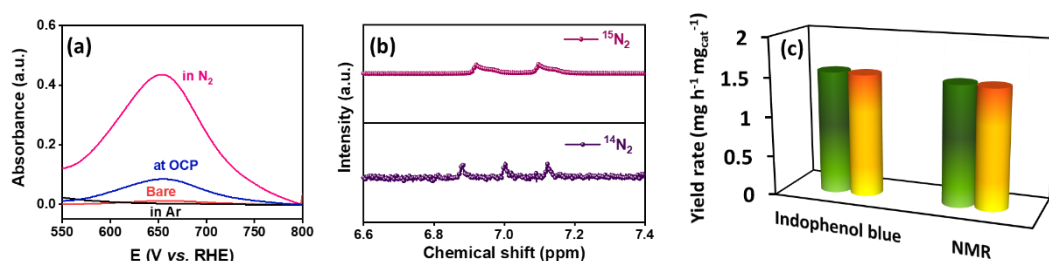


Figure 5A-6. (a) UV-Vis absorbance curves for electrolyte sample collected after NRR by Ni_xB_y (SR) at -0.2 V under Ar- and N_2 -saturated conditions, over bare electrode and also at open circuit potential, (b) ^1H -NMR spectrum for electrolyte samples obtained after isotope labelling NRR experiments and (c) comparison of ammonia yield rates obtained after isotope labelling experiments via different quantification methods (green: $^{14}\text{NH}_4^+$ and orange: $^{15}\text{NH}_4^+$).

The $^{14}\text{NH}_4^+$ and $^{15}\text{NH}_4^+$ yield rates were then quantified from the Indophenol method as well as from the NMR spectrum acquired after isotope labelling measurements which put forward almost identical yield rates and thus uphold the reliability of the reported data [Figures 5A-6(b-c) and Table 5A-3]. Overall, the above illustrations demonstrated that Ni_xB_y (SR) could be an effectual and competent catalyst towards NRR.

Table 5A-3: Validation of ammonia yield rates via different methods.

Detection method	$^{14}\text{NH}_3$ yield rate ($\text{mg h}^{-1} \text{mg}_{\text{cat.}}^{-1}$)	$^{15}\text{NH}_3$ yield rate ($\text{mg h}^{-1} \text{mg}_{\text{cat.}}^{-1}$)
Indophenol Blue	1.55	1.53
Nessler's reagent	1.54	-
$^1\text{H-NMR}$	1.51	1.5

5A-3.3 Electrocatalytic OER activity: The electrocatalytic OER activity of designed catalysts was then evaluated by performing LSV in 0.1 M KOH electrolyte under an applied potential range between 1 to 1.95 V (*vs.* RHE). For comparison, the benchmark RuO_2 catalyst was also studied under similar loading and experimental conditions. Figure 5A-7a depicted the OER polarization curved obtained after LSV measurements scanned at a rate of 5 mV s^{-1} with *iR*-correction. As expected, the Ni_xB_y (SR) catalytic variant with cotton-like morphology exhibited superior OER performance with a low overpotential (η) of 300 mV to acquire a current density of 10 mA cm^{-2} . Although the overpotential required to generate the same current density was similar for Ni_xB_y (CR) and RuO_2 catalysts respectively but the current density acquired at 1.8 V was way too higher (174 mA cm^{-2}) than Ni_xB_y (CR) which achieved just 31 mA cm^{-2} at the similar potential. The current density was even superior to that of the benchmark RuO_2 catalyst (150 mA cm^{-2}). More interestingly, the Ni_xB_y (SR) also had a lower Tafel slope (74 mV dec^{-1}) than Ni_xB_y (CR) (Figure 5A-7b) and therefore suggested a more favourable and facilitated reaction kinetics during OER. As shown in Figure 5A-7c, the Ni_xB_y (SR) demonstrated remarkable stability at a constant current density (10 mA cm^{-2}) even

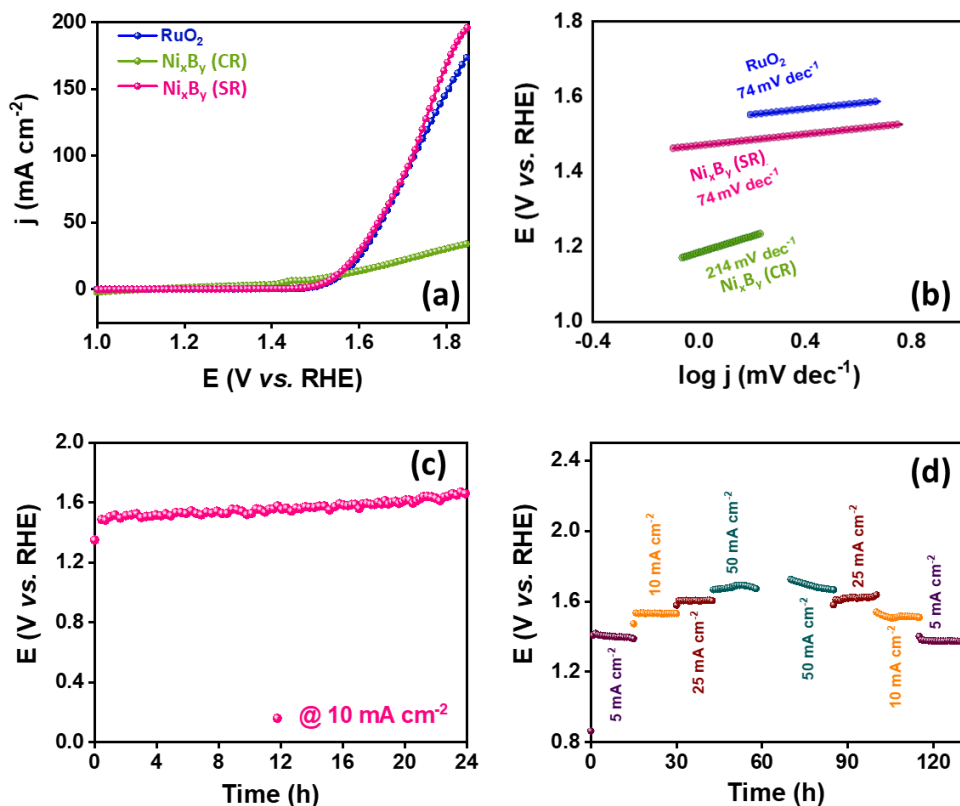


Figure 5A-7. (a) LSV curves for OER by Ni_xB_y catalysts and comparison with benchmark RuO₂ catalyst and (b) corresponding Tafel plots extracted from Figure 5A-7a. (c) CP curve for 24 h by Ni_xB_y (SR) catalyst at 10 mA cm⁻² of current density and (d) CP at different current densities for catalyst stability measurements.

after 24 h as well as when we increased the current density from 10 to 50 mA cm⁻² and again to 10 mA cm⁻² where the potential response was restored back as shown in Figure 5A-7(d) consequently. Based on the above-mentioned findings, the Ni_xB_y catalyst with well-defined morphology was able to improve the overall OER activity of the catalyst more than that of the Ni_xB_y catalyst with the same structural phase but aggregated morphology. This could be due to the presence of exposed active sites which might have provided a better mass and charge transport channel and thus benefited the catalytic activity towards OER.

5A-3.4 Overall ammonia synthesis: Since, the Ni_xB_y (SR) catalyst was shown to have a superior OER and NRR electrocatalytic activities in an alkaline medium, we

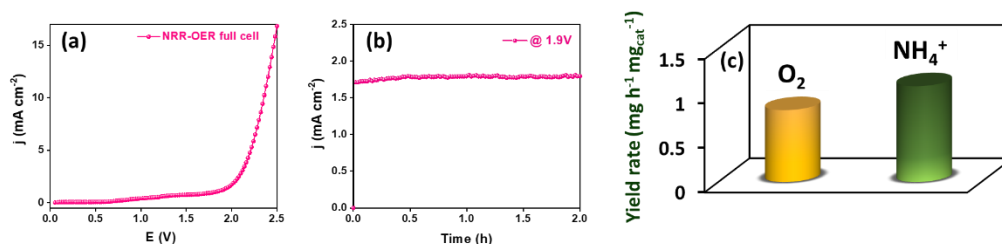


Figure 5A-8. (a) LSV curves for NRR-OER full cell device equipped with Ni_xB_y (SR) as a bifunctional catalyst, (b) CA carried out at 1.9 V to produce ammonia at cathode and oxygen at anode for 2 h. (c) Corresponding production yield rate for O_2 and NH_3 quantified via GC and Indophenol Blue methods under full cell conditions in 2 h.

have realized the solicitation of the designed catalyst for full cell NH_3 production. We assembled the OER-NRR full-cell device using a home-built H-cell setup separated with a proton exchange membrane. Ni_xB_y (SR) was employed as a bifunctional electrocatalyst on either sides of the device *i.e* at anode (to carry out OER) and cathode (to carry out NRR) and 0.1 M KOH was taken as electrolyte. LSV was acquired under full cell conditions in a potential range between 0 to 2.5 V (Figure 5A-8a) from where a sharp increase in current density could be observed at 1.7 V, which signified the ammonia synthesis. Later, the N_2 was purged into the cathodic chamber while the anodic chamber was kept as such, and the onset potential was applied to carry out electrolysis for 2 h (Figure 5A-8b). Ammonia production was scrutinized by collecting the electrolyte sample after electrolysis via Indophenol blue method. A total ammonia production yield rate of $1.08 \text{ mg h}^{-1} \text{ mg}_{\text{cat}}^{-1}$ was witnessed after NRR under full cell conditions. In contrast, the GC analysis was carried out to quantify the oxygen production yield rate as well during overall ammonia synthesis. The O_2 production rate of $0.81 \text{ mg h}^{-1} \text{ mg}_{\text{cat}}^{-1}$ was attained after 2 h of electrolysis (Figure 5A-8d). Henceforth, this study has provided a less complex, simplified and facile ammonia production under ambient conditions at just 1.7 V of potential wherein the TMBs synthesized via an energy-efficient sonochemical reduction method could provide a well-defined morphology over the conventional chemical reduction method in lesser time duration.

5A-4 Summary

In summary, we have presented an efficient electroreduction of N_2 to NH_3 on Ni_xB_y catalyst at 1.7 V under full cell conditions. The Ni_xB_y (SR) catalyst synthesized via the sonochemical reduction route revealed a well-defined cotton-like morphology rather than the aggregated clusters for the Ni_xB_y (CR) obtained via the chemical reduction method. Ni_xB_y (SR) catalyst exhibited high activity and selectivity for NRR half-cell in 0.1 M KOH electrolyte, achieving an NH_3 yield rate of about $1.55 \text{ mg h}^{-1} \text{ mg}_{\text{cat}}^{-1}$ and a F.E. of 47.9% at -0.2V vs. RHE. The catalyst also demonstrated a bifunctional activity towards OER with an overpotential of 300 mV to attain 10 mA cm^{-2} . The bifunctional catalyst was employed at both anode and cathode to carry out overall ammonia production and could execute the same at 1.7 V and high efficiency at 1.9 V with an overall ammonia yield rate of $1.08 \text{ mg h}^{-1} \text{ mg}_{\text{cat}}^{-1}$ while the O_2 production rate was found out to be $0.81 \text{ mg h}^{-1} \text{ mg}_{\text{cat}}^{-1}$ respectively. Our findings open up an avenue to develop efficient bifunctional electrocatalysts based on TMBs with a well-defined morphology via a sonochemical approach for overall ammonia synthesis under full-cell configuration so that they could be realized in practice.

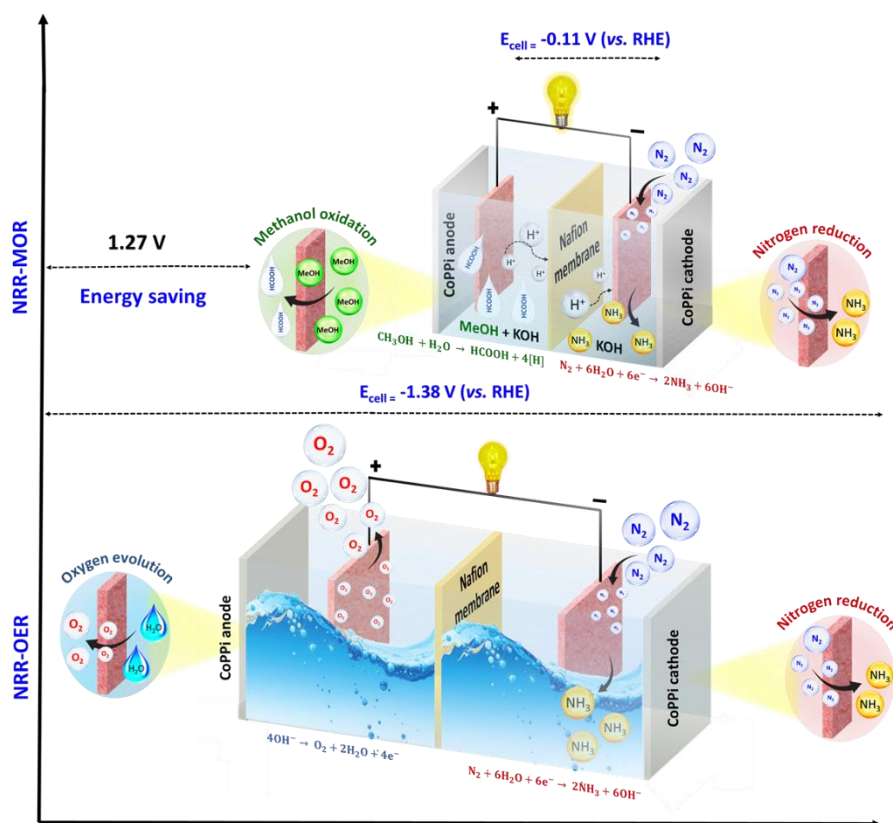
5A-5 References

1. M. A. Shipman and M. D. Symes, *Catal. Today*, 2017, **286**, 57-68.
2. A. Liu, Y. Yang, X. Ren, Q. Zhao, M. Gao, W. Guan, F. Meng, L. Gao, Q. Yang and T. Ma, *ChemSusChem*, 2020, **13**, 3766.
3. K. Kugler, B. Ohs, M. Scholz and M. Wessling, *Phys. Chem. Chem. Phys.*, 2014, **16**, 6129-6138.
4. C. Tang and S.-Z. Qiao, *Chem. Soc. Rev.*, 2019, **48**, 3166-3180.
5. H. Wang, L. Wang, Q. Wang, S. Ye, W. Sun, Y. Shao, Z. Jiang, Q. Qiao, Y. Zhu and P. Song, *Angew. Chem. Int. Ed.*, 2018, **57**, 12360-12364.
6. I. J. McPherson, T. Sudmeier, J. Fellowes and S. C. E. Tsang, *Dalton Trans.*, 2019, **48**, 1562-1568.
7. M. G. Chourashiya and A. Urakawa, *J. Mater. Chem. A*, 2017, **5**, 4774-4778.
8. M. Nazemi, S. R. Panikkanvalappil and M. A. El-Sayed, *Nano Energy*, 2018, **49**, 316-323.
9. Y. Yao, S. Zhu, H. Wang, H. Li and M. Shao, *J. Am. Chem. Soc.*, 2018, **140**, 1496-1501.
10. Z. Wang, Y. Li, H. Yu, Y. Xu, H. Xue, X. Li, H. Wang and L. Wang, *ChemSusChem*, 2018, **11**, 3480-3485.
11. K. Kugler, M. Luhn, J. A. Schramm, K. Rahimi and M. Wessling, *Phys. Chem. Chem. Phys.*, 2015, **17**, 3768-3782.

12. H. Tao, C. Choi, L.-X. Ding, Z. Jiang, Z. Han, M. Jia, Q. Fan, Y. Gao, H. Wang and A. W. Robertson, *Chem*, 2019, **5**, 204-214.
13. Y. Yao, H. Wang, X.-Z. Yuan, H. Li and M. Shao, *ACS Energy Lett.*, 2019.
14. H.-M. Liu, S.-H. Han, Y. Zhao, Y.-Y. Zhu, X.-L. Tian, J.-H. Zeng, J.-X. Jiang, B. Y. Xia and Y. Chen, *J. Mater. Chem. A*, 2018, **6**, 3211-3217.
15. R. Lan, J. T. Irvine and S. Tao, *Sci. Rep.*, 2013, **3**, 1-7.
16. R. Manjunatha and A. Schechter, *Electrochem. Commun.*, 2018, **90**, 96-100.
17. J. Wang, L. Yu, L. Hu, G. Chen, H. Xin and X. Feng, *Nat. Commun.*, 2018, **9**, 1-7.
18. F. Pang, Z. Wang, K. Zhang, J. He, W. Zhang, C. Guo and Y. Ding, *Nano Energy*, 2019, **58**, 834-841.
19. G.-F. Chen, X. Cao, S. Wu, X. Zeng, L.-X. Ding, M. Zhu and H. Wang, *J. Am. Chem. Soc.*, 2017, **139**, 9771-9774.
20. V. Singh, A. Tiwari and T. C. Nagaiah, *J. Mater. Chem. A*, 2018, **6**, 22545-22554.
21. Z. Jiang, W. Lu, Z. Li, K. H. Ho, X. Li, X. Jiao and D. Chen, *J. Mater. Chem. A*, 2014, **2**, 8603-8606.
22. D. Farrusseng and A. Tuel, *Encapsulated Catalysts*, 2017, 335-386.
23. P. Fornasiero and M. Cargnello, *Morphological, Compositional, and Shape Control of Materials for Catalysis*, Elsevier, 2017.
24. S. Zhao, X. Lu, L. Wang, J. Gale and R. Amal, *Adv. Mater.*, 2019, **31**, 1805367.
25. Z. Jin, S. Hou, Z. Luo, R. Ma, Y. Li, Y. Wang, J. Ge, C. Liu and W. Xing, *Electrochemical Water Electrolysis: Fundamentals and Technologies*, 2020, 69.
26. J. H. Montoya, C. Tsai, A. Vojvodic and J. K. Nørskov, *ChemSusChem*, 2015, **8**, 2180-2186.
27. Z.-F. Huang, S. Xi, J. Song, S. Dou, X. Li, Y. Du, C. Diao, Z. J. Xu and X. Wang, *Nat. Commun.*, 2021, **12**, 3992.
28. J. Liu, X. Liu, H. Shi, J. Luo, L. Wang, J. Liang, S. Li, L.-M. Yang, T. Wang and Y. Huang, *Appl. Catal. B Environ.*, 2022, **302**, 120862.
29. J.-T. Ren, L. Chen, Y. Liu and Z.-Y. Yuan, *J. Mater. Chem. A*, 2021, **9**, 11370-11380.
30. W. Li, W. Fang, C. Wu, K. N. Dinh, H. Ren, L. Zhao, C. Liu and Q. Yan, *J. Mater. Chem. A*, 2020, **8**, 3658-3666.
31. Y. Sun, T. Jiang, J. Duan, L. Jiang, X. Hu, H. Zhao, J. Zhu, S. Chen and X. Wang, *ACS Catal.*, 2020, **10**, 11371-11379.
32. H.-Y. Wang, J.-T. Ren, C.-C. Weng, X.-W. Lv and Z.-Y. Yuan, *Chem. Eng. J.*, 2021, **426**, 130761.
33. X. Ma, K. Zhao, Y. Sun, Y. Wang, F. Yan, X. Zhang and Y. Chen, *Catal. Sci. Technol.*, 2020, **10**, 2165-2172.
34. N. Xu, G. Cao, Z. Chen, Q. Kang, H. Dai and P. Wang, *J. Mater. Chem. A*, 2017, **5**, 12379-12384.
35. S. Gupta, M. K. Patel, A. Miotello and N. Patel, *Adv. Funct. Mater.*, 2020, **30**, 1906481.
36. C. Wang, P. Zhai, M. Xia, Y. Wu, B. Zhang, Z. Li, L. Ran, J. Gao, X. Zhang and Z. Fan, *Angew. Chem. Int. Ed.*, 2021, **60**, 27126-27134.
37. J. M. V. Nsanzimana, Y. Peng, Y. Y. Xu, L. Thia, C. Wang, B. Y. Xia and X. Wang, *Adv. Energy Mater.*, 2018, **8**, 1701475.
38. J. Masa, C. Andronesco, H. Antoni, I. Sinev, S. Seisel, K. Elumeeva, S. Barwe, S. Marti-Sanchez, J. Arbiol and B. Roldan Cuenya, *ChemElectroChem*, 2019, **6**, 235-240.
39. J. Hong, S. Mutalik, M. Miola, D. Gerlach, R. Mehrabi K, M. Ahmadi, B. J. Kooi, G. Portale, P. Rudolf and P. P. Pescarmona, *Chem. Mater.*, 2023, **35**, 1710-1722.

Chapter 5B

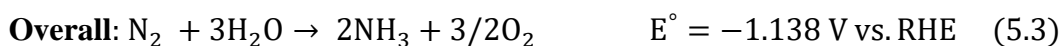
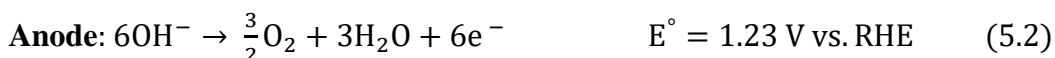
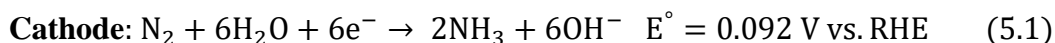
Dinitrogen reduction coupled with methanol oxidation for low overpotential electrochemical NH_3 synthesis over cobalt pyrophosphate as bifunctional catalyst



5B-1 Introduction

Electrochemical nitrogen fixation to green ammonia is gaining immense consideration due to its extensive applications, especially for fertilizer production and as an alternative fuel and non- dangerous H₂ carrier.^{1,2} Quite a lot of advantages are offered by electrochemical nitrogen reduction reaction (NRR) including operation under mild conditions of temperature and pressure, zero carbon emission, utilization of electricity generated by renewable sources, and use of earth abundant water as H₂ source.^{3, 4} The overall ammonia synthesis process pairs nitrogen reduction at cathode (Equation 5.1) and oxygen evolution reaction (OER) at anode (Equation 5.2).⁵

On the other hand, the poor kinetics of OER on account of four electron transfer requires high energy input and ultimately the energy efficiency of NH₃ electrolyzers is deprived as a result of large cell voltages (Equation 5.3).⁶⁻⁸



In order to overcome this drawback, OER at anode can be replaced with an alternative anode reaction which exhibits faster kinetics, is thermodynamically more feasible and can yield a value-added product at anode as well.^{9, 10} Alcohol oxidation reaction (AOR), especially methanol oxidation reaction (MOR) can be a potential alternative since it requires comparatively lesser activation energy than other alcohols (e.g., ethanol) reason being the absence of strong C-C bond.^{11, 12} About 1.1 V of energy can be saved by replacing OER with MOR as it holds an electrode potential of 0.103 V (vs. RHE) which is very low than OER (1.23 V) plus the formation of important industrial intermediates/products such as formic acid or formate ion can be projected.^{13, 14} And therefore, we propose to couple NRR with

MOR to witness the ammonia production at reduced cell voltage with high energy efficiency.

Anodic MOR: $\text{CH}_3\text{OH} + \text{H}_2\text{O} \rightarrow \text{HCOOH} + 4[\text{H}] \quad E^\circ = 0.103 \text{ V vs. RHE} \quad (5.4)$

Although, the replacement of OER with MOR can tackle with the energy consumption and efficiency related issues, but still both NRR and MOR hold certain defies which prerequisites to be addressed. NRR suffers from difficult adsorption and activation of $\text{N}\equiv\text{N}$ bond, its further hydrogenation and competition with HER. While catalyst poisoning, adverse effects on environment due to CO_2 release and poor methanol tolerance of catalyst are the major drawbacks of MOR.¹⁵⁻

¹⁷ Besides, the use of precious metal based catalysts (e.g., Pt-Ru/C for MOR) limit the practical applicability. While the unsatisfactory F.E. and NH_3 yield rates because of unavailability of efficient NRR catalyst obliges the development of extremely active, durable and cost-effective catalysts by greener approach.¹⁸⁻²⁰ Furthermore, employing two different catalysts for NRR and MOR can inevitably upsurge the material and processing costs and is in responsible for complex cell configuration.²¹ Till date only one literature report is available based on the coupling of NRR with MOR for low overpotential NH_3 synthesis but with different catalysts at anode and cathode.²²

For that reason, the design and development of a competent and economical bifunctional electrocatalyst active towards both NRR and MOR to carry out NH_3 synthesis is of huge interest however challenging. The major challenge is attributable to the involvement of two reactions with entirely different fundamental mechanisms and reaction intermediates. In the midst of existing developments, the transition metal (TM) based catalysts are extensively explored for NRR owing to the presence of vacant *d*-orbital which can ease the N_2 chemisorption.^{23, 24} While the outer *s*-orbital accepts lone pair of electrons from N_2 and downshift the N_2 antibonding orbital in which the metal *d*-orbital back transfer the electrons to antibonding N_2 orbital and thus activates the N_2 triple bond.²⁵⁻²⁸ Amongst these

TMs, cobalt catalysts demonstrate exciting NRR activity and phosphate-based cobalt composites are clutching attention by virtue of their optical, electrical and magnetic properties.²⁸⁻³¹ For instance, cobalt phosphate nanocrystals-loaded heteroatoms-doped carbon nanosheets have been realized as NRR catalyst in Zn-N₂ battery and the same group extended the application of cobalt phosphate microspheres to enhance the NRR performance and achieved a high NH₃ yield rate of 16.48 $\mu\text{g h}^{-1} \text{mg}_{\text{cat.}}^{-1}$ with a faradaic efficiency of 4.46% at -0.2 V *vs.* RHE.^{32, 33} Metal phosphates are also well explored for MOR owing to easy generation of adsorbed OH species and tolerance towards poisoning intermediates.³⁴ More interestingly, cobalt pyrophosphates (CoPPi) have gained massive attention reason being their unique geometry, structure rigidity, improved electrical properties and flexible co-ordination of pyrophosphate groups which can modify the local positions and stabilize intermediate state of transition metals to dodge structural distortions throughout electrocatalysis.³⁵⁻³⁸ A number of routes have been exploited for the synthesis of CoPPi like high temperature annealing, hydrothermal, sol-gel, however development of a more facile and proficient route with one-step and benign synthesis of CoPPi is a prerequisite for its scalable production.^{39, 40}

In this chapter, we present the synthesis of cobalt pyrophosphate (CoPPi) micro flowers assembled by uniform nanosheets thru surfactant assisted-sonochemical reduction method under ambient conditions. The as-synthesized CoPPi catalyst is scrutinized as a bifunctional catalyst for N₂ reduction to NH₃ at cathode and methanol oxidation at anode during electrolysis. The uniform nanosheets can effectively render plentiful of active sites and expedite the electron and mass transfer. The flexible pyrophosphate groups can impede the catalyst deformation and preserve the stability during electrocatalysis. This is the first report to present CoPPi as a bifunctional electrocatalyst for MOR-NRR coupled ammonia synthesis and can possibly lead to improvement in rate of overall electrochemical NH₃ synthesis at lower overpotentials with an benefit of producing value-added chemicals at both anode and cathode.

5B-2 Material synthesis

5B-2.1 Synthesis of CoPPi: A sonochemical synthesis method was utilized to synthesize CoPPi catalyst under ice cold conditions. The reaction was carried out between $\text{CoCl}_2 \cdot 6\text{H}_2\text{O}$ and $\text{NaH}_2\text{PO}_4 \cdot 2\text{H}_2\text{O}$ in presence and absence of Triton X-100 surfactant. Briefly, 2 mL of surfactant was dissolved in 20 mL aq. solution of $\text{CoCl}_2 \cdot 6\text{H}_2\text{O}$ (2.38 g) to which an aq. solution of $\text{NaH}_2\text{PO}_4 \cdot 2\text{H}_2\text{O}$ (1.78 g in 20 mL deionized water (pH adjusted to 9 with 0.1 M NaOH) was added dropwise for 15 minutes. The reaction was carried out under periodic probe sonication at a constant horn frequency of 20 Hz where the reaction mixture was sonicated for 1 min. and kept at rest for 1 min. till the reaction completion. The as-prepared purple colored precipitates were then collected, filtered and washed several times with 1:1 mixture of ethanol:water followed by complete drying overnight at 60 °C in hot air oven. To study the role of surfactant, CoPPi was also synthesized in an analogous manner but without the addition of Triton X-100 initially and denoted as *SF*-CoPPi, where *SF* designated surfactant free.

5B-3 Results and discussion

5B-3.1 Physical characterization: The CoPPi micro-flowers assembled from uniform nanosheets were synthesized using a green, energy efficient and less time consuming sonochemical route as described previously. The synthesis involved a surfactant assisted approach to tune the morphology of the final catalyst i.e. by use of Triton X-100, a non-ionic surfactant, which acted as a template to control the nucleation rate during particle growth and the reaction between metal precursor and sodium hypophosphite resulted into CoPPi production within 15 minutes. After the successful synthesis of targeted catalyst, its microstructure was probed through P-XRD analysis and the relative diffraction pattern is shown in Figure 5B-1a. High intensity and sharp diffraction peaks were witnessed at 2θ of 26.1°, 26.98°, 29.2°, 30.4°, 33.7°, 35.1°, 44.7°, and 55.34° and were attributed to the presence of (11 $\bar{1}$), (021), (111), (12 $\bar{1}$), (031), (210), (022), and (320) planes of $\text{Co}_2\text{P}_2\text{O}_7$ (PDF Card no.: 01-087-0457) respectively. This evidenced the formation of $\text{Co}_2\text{P}_2\text{O}_7$ in a

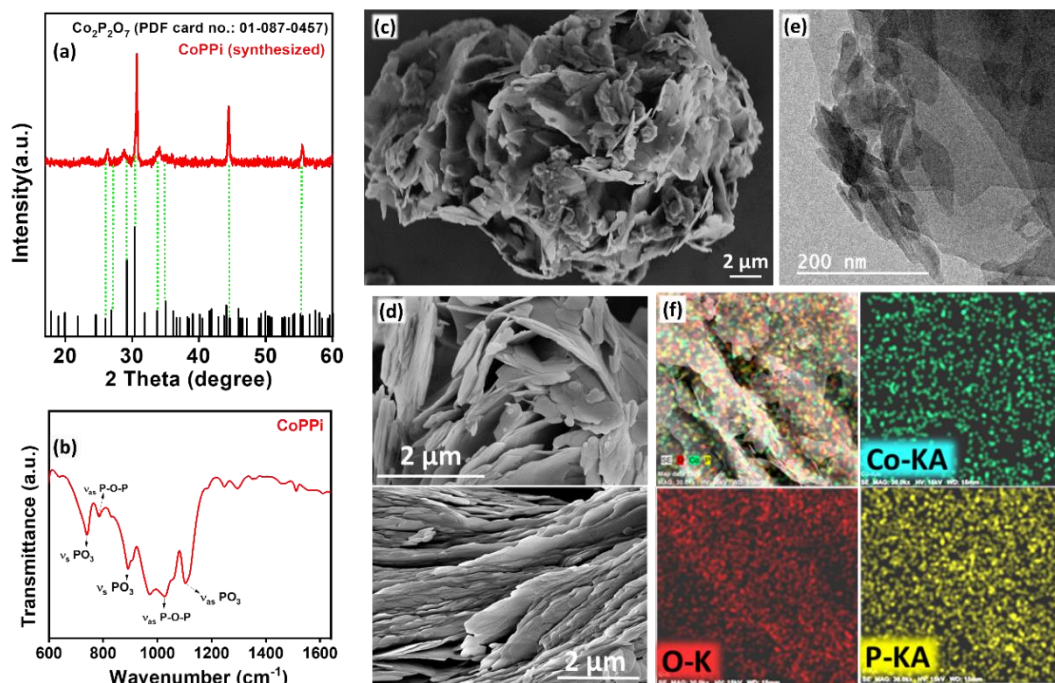


Figure 5B-1. a) P-XRD pattern for as-synthesized CoPPi and reference $\text{Co}_2\text{P}_2\text{O}_7$ file. b) FT-IR spectrum, c-d) FE-SEM images and e) TEM image of CoPPi. f) Elemental dot mapping showing homogeneous distribution of Co, O, and P elements over scanned area of CoPPi respectively.

monoclinic crystal system with unit cell parameters of $a = 5.3390 \text{ \AA}$, $b = 9.9230 \text{ \AA}$, $c = 4.4880 \text{ \AA}$ and $\text{Vol} = 235.762 \text{ \AA}^3$. Further the FT-IR spectrum shown in Figure 5B-1b displayed characteristic bands related to pyrophosphate ($\text{P}_2\text{O}_7^{4-}$) groups due to asymmetric and symmetric stretching vibrations by P-O-P bridging bond at 892 and 740 cm^{-1} respectively. In addition to it, the presence of $(\text{PO}_3)^{2-}$ groups was affirmed by the vibration bands amidst 975 to 1300 cm^{-1} while rocking/deformation modes of PO_3 groups could be assigned to the bands present between 400 - 700 cm^{-1} . These PO_3 groups revealed the bent configuration of P_2O_7 (pyrophosphate) moiety in the CoPPi catalyst. The morphological attributes of the catalyst were then premeditated using FE-SEM analysis where the respective images of CoPPi portrayed a micro-flower like morphology composed of uniform and layered nanosheets with thickness of the order of 100 - 125 nm [Figures 5B-1(c-d)]. Such an

assembly of nanosheets to yield micro-flowers could exclusively offer plentiful pores and active sites to accelerate the mass and charge transport during electrocatalysis.⁴¹ The TEM further revealed the clear stacks of nanosheets and EDS elemental profile and dot mapping analysis illustrated the presence and uniform distribution of Co, P and O [Figures 5B-1(e-f) and Table 5B-1]. Atomic force microscopy (AFM) was also accomplished to support the formation of layered nanosheets by the resultant phase image showed in Figure 5B-2a. Later, XPS analyses was implemented to understand the electronic structure and chemical binding state of CoPPi catalyst. Upon deconvolution of Co 2p XP spectra (Figure 5B-2b), a doublet was witnessed at 798.03 and 782.09 eV of binding energy which could be accredited to the Co 2p_{1/2} and Co 2p_{3/2} due to spin-orbit coupling between Co²⁺ and Co³⁺ states respectively along with two satellite peaks at 803.25 and 785.6 eV respectively. Whereas, the deconvoluted P 2p spectrum of CoPPi showed in Figure 5B-2c revealed two peaks corresponding to P 2p_{3/2} (133.2 eV) and P 2p_{1/2} (134.3 eV) of phosphate group. Figure 5B-2d illustrated the peak related with P=O group in O 1s deconvoluted spectrum at a lower binding energy value of 531.4 eV while the presence of chemisorbed hydroxyl groups (OH) was asserted by the peak observed at 532.5 eV respectively.⁴²

Table 5B-1. EDS (%) composition analysis for different elements in CoPPi.

S.No.	Element	Mass normalized (%)	Atomic (%)
1.	Cobalt	38.06	16.02
2.	Phosphorus	16.08	12.87
3.	Oxygen	45.87	71.11
	Total	100.00	100.00

5B-3.2 Electrochemical N₂ reduction: The electrocatalytic ability of CoPPi catalyst towards NRR was evaluated in aqueous 0.1 M KOH electrolyte for effectual HER suppression, since release of protons is difficult at higher pH due to increased dissociation energy for H₂O and K⁺ ions can enhance N₂ adsorption over

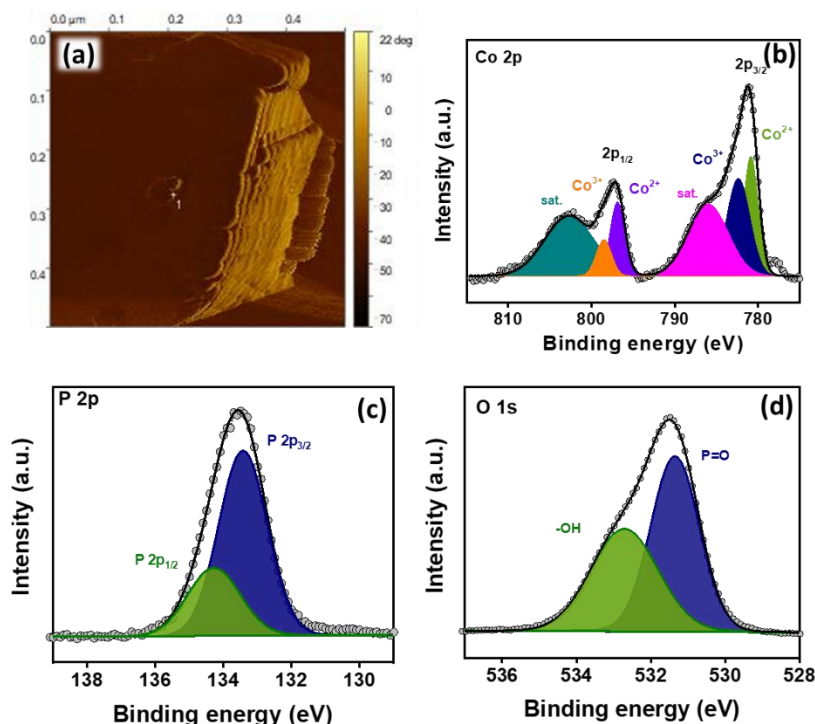


Figure 5B-2. (a) AFM phase image for CoPPi catalyst. (b) The deconvoluted XP spectrum showing Co 2p, (c) P 2p and (d) O 1s of CoPPi catalyst respectively.

the catalyst surface due to boosted electric field in Stern layer.⁴³ Figure 5B-3a described the sharp increase in reduction current density of CoPPi catalyst in LSV curve acquired under Ar-saturated electrolyte due to HER. A distinct competition of HER and NRR was illustrated by increased current density in N₂-saturated electrolyte even before HER, and further suggested the ability of CoPPi catalyst to reduce N₂ under applied potentials. Thereafter, chronoamperometry (CA) was performed for 2 h at different potentials in N₂-saturated conditions which defined a stable current response during the NRR (Figure 5B-3b). The electrolyte samples were then collected from the cathode compartment of H-cell and quantified for possible products formed during NRR *viz.* NH₃ and N₂H₄. Ammonia formation could be vindicated from the absorbance band observed at 660 nm in UV-Vis spectrum of electrolyte samples collected after NRR (Figure 5B-3c). The highest NH₃ yield rate and F.E. were realized in Figure 5B-3d at -0.2 V (*vs.* RHE) with the

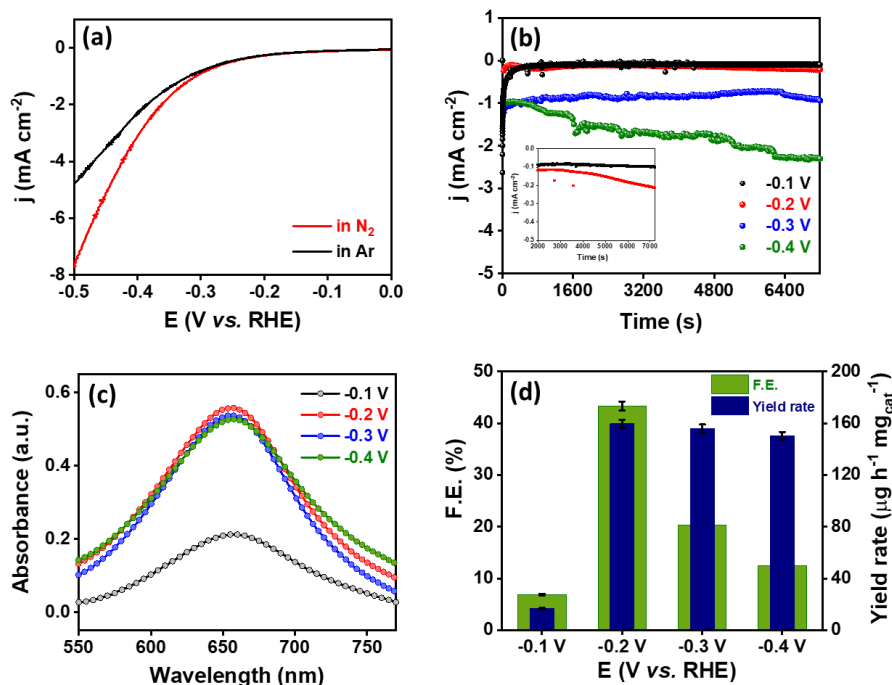


Figure 5B-3. (a) Linear sweep voltammogram for CoPPi under Ar- and N₂-saturated 0.1 M KOH electrolyte at 25 mV s⁻¹ of scan rate. (b) Chronoamperometric curves obtained after NRR (2 h) by CoPPi at different applied potentials in N₂-saturated 0.1 M KOH electrolyte. (c) UV-Vis absorbance curves obtained after Indophenol blue test for samples obtained after NRR (2 h chronoamperometry) at different potentials varying from -0.1 V to -0.4 V vs. RHE. (d) Bar diagram representing the F.E. and NH₃ yield rate achieved by CoPPi catalyst.

values of 159.6 μg h⁻¹ mg_{cat}⁻¹ and F.E. of 43.37% respectively, which showed a deterioration upon application of more negative potentials, reason being HER. On the other hand, no hydrazine could be detected as a N₂ reduction product after NRR at -0.2 V, and thus warranted the selective ammonia production by CoPPi catalyst. This remarkable performance of CoPPi towards NRR must be endorsed to the effective HER suppression and was corroborated by means of CA measurements under switching gas supply (Ar/N₂) environments. Figure 5B-4a evidenced the abrupt change in current density with switching gas supplies and further emphasized the HER suppression and high durability of CoPPi. Likewise, no NH₃ production was witnessed in presence of Ar, while in presence of N₂ the NRR

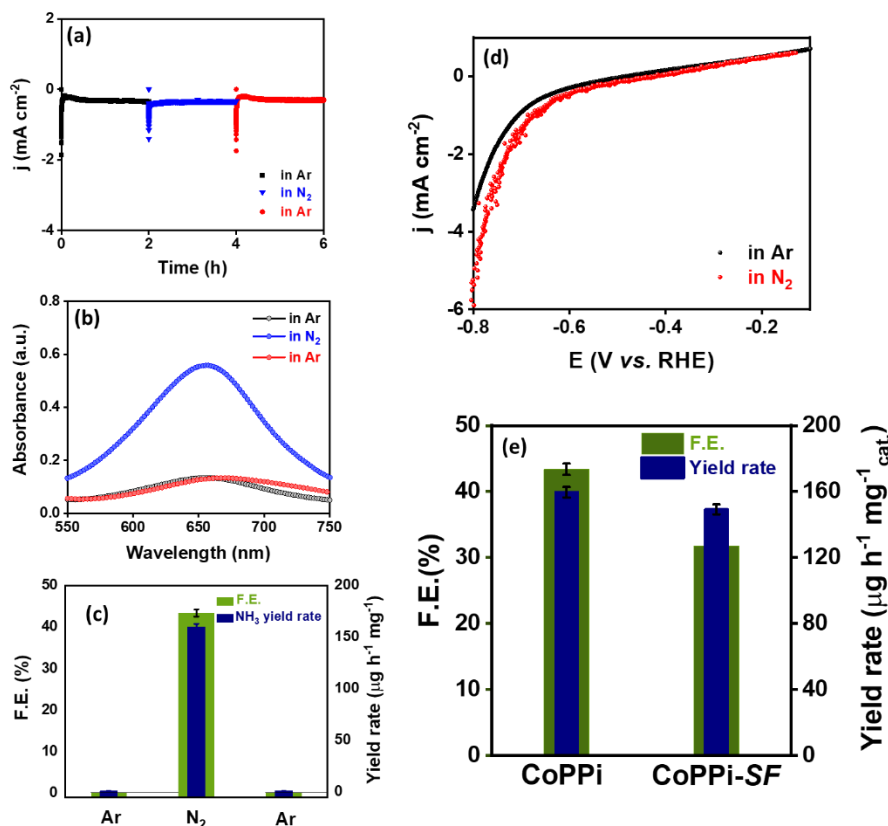


Figure 5B-4. (a) Chronoamperometric curves recorded for CoPPi catalyst under switching gas-feed environments (Ar/N₂) to substantiate HER suppression and (b) UV-Vis absorbance curves for samples collected after CA under switching gas-supplies. (c) Bar diagram representing the F.E. and NH₃ yield rate obtained after switching chronoamperometry experiment @ -0.2 V (vs. RHE) in Ar-/N₂-saturated 0.1 M KOH electrolyte. (d) Linear sweep voltammogram for CoPPi-SF catalyst in 0.1 M KOH solution. (e) Comparison of F.E. and NH₃ yield rate of CoPPi and CoPPi-SF after NRR at -0.2 V vs. RHE under identical experimental conditions.

activity of catalyst could be recovered [Figures 5B-4(b-c)]. To substantiate the choice of electrolyte *i.e.* KOH towards HER suppression, the LSV were performed for CoPPi in 0.1 M H₂SO₄ (acidic) electrolyte as well (Figure 5B-4d), which revealed an inferior performance in terms of net current density (-0.12 mA cm⁻²) as well as the NRR activity (F.E.: 29%, yield rate: 68.13 μg h⁻¹ mg_{cat.}⁻¹) at same applied potential (Figure 5B-4e). Afterwards, the role of morphology intended for N₂ adsorption, activation and reduction was understood by the synthesis of a

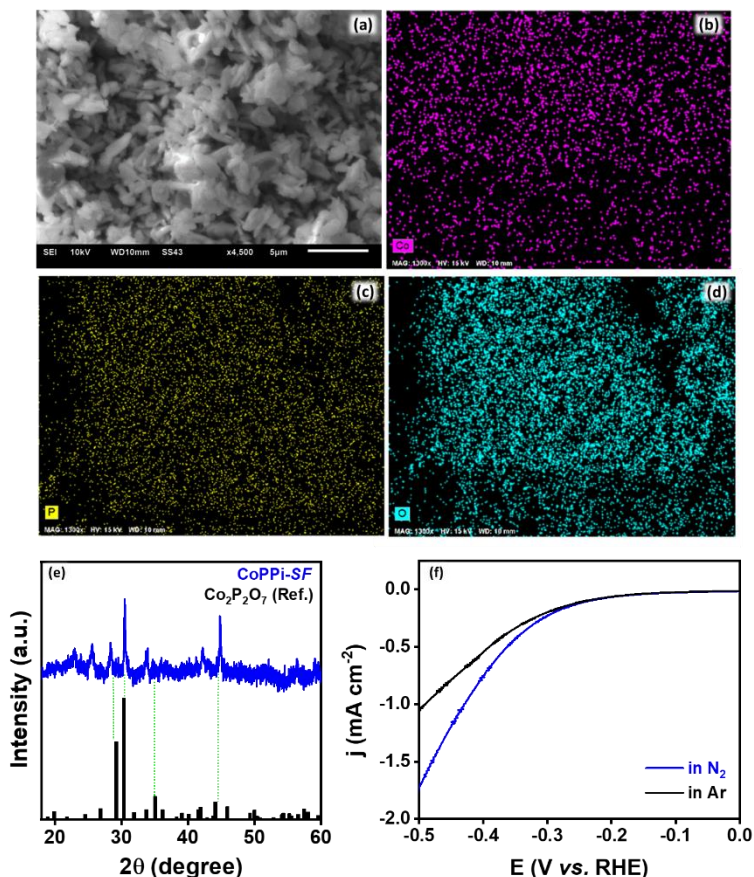


Figure 5B-5. (a) SEM image of CoPPi-SF catalyst. (b-d) EDS dot mapping images showing presence and homogeneous distribution of Co, P and O in CoPPi-SF over the scanned area. (e) P-XRD pattern for CoPPi-SF catalyst compared with reference $\text{Co}_2\text{P}_2\text{O}_7$ file (PDF card no.: 01-087-0457).

control catalyst, *SF*- CoPPi (surfactant free-cobalt pyrophosphate) without surfactant. The catalyst synthesized without surfactant didn't reveal a micro-flower assembled via nanosheets morphology, instead, it exposed the formation of irregular and aggregated leaf-like structure (Figure 5B-5a) with presence and uniform distribution of all the respective elements in EDS dot mapping images [Figures 5B-5(b-d)]. Even though the diffraction patterns of both CoPPi and *SF*-CoPPi revealed a parallel structural phase (Figure 5B-5e), but a huge inconsistency in morphology and thus electrochemical NRR performance could be perceived. Figure 5B-5f defined the lower current density in LSV curve of *SF*-CoPPi than

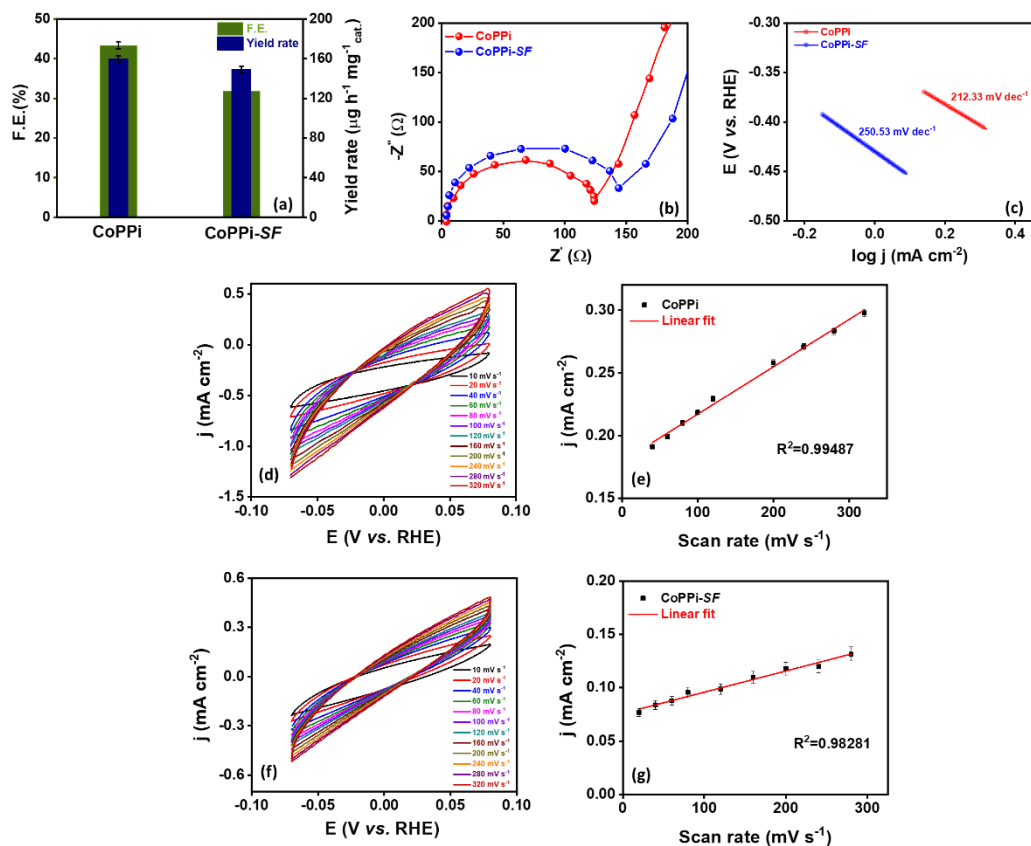


Figure 5B-6. (a) Comparison of F.E. and NH₃ yield rate of CoPPi and CoPPi-SF after NRR at -0.2 V vs. RHE under identical experimental conditions. (b) Nyquist plots for CoPPi and CoPPi-SF catalyst at -0.2 V vs. RHE. (c) Tafel plots for CoPPi catalysts. (d) Cyclic voltammetry for CoPPi in non-faradaic region. (e) Scan rate vs. current density plots. (f) Cyclic voltammetry for CoPPi-SF in non-faradaic region and (g) corresponding scan rate vs. current density plots.

CoPPi and point towards the low NRR activity. This was supported by the reduced NH₃ yield rate ($149.3 \mu\text{g h}^{-1} \text{mg}_{\text{cat.}}^{-1}$) and F.E. (31.8%) obtained after NRR at -0.2 V by SF-CoPPi in 0.1 M KOH (Figure 5B-6a). From the above stated findings, we speculated the role of morphology as a contributor towards NRR activity by virtue of exposed metal active sites and uniform layered nanosheets which could facilitate the electron and mass transfer during NRR. This superior activity of CoPPi was then reinforced by diverse electrochemical investigations such as EIS, ECSA and

Tafel analysis. The decreased diameter of semicircle in the Nyquist plot of CoPPi was witnessed in Figure 5B-6b with a low R_{ct} value of 122.87 Ω as compared to that of *SF*-CoPPi with the R_{ct} value of 141.29 Ω (Table 5B-2), which demonstrated the improved reaction kinetics. The same trend was observed for Tafel analysis where a lower Tafel slope (212.33 mV dec⁻¹) was obtained for CoPPi over *SF*-CoPPi with a slope value of 250.53 mV dec⁻¹, as showed in Figure 5B-6c. Further, the higher C_{dl} and ECSA value of 377 μ F and 9.425 cm² respectively were found for CoPPi than *SF*-CoPPi [Figures 5B-6(d-g) and Table 5B-3] and hence imitated the superior performance of CoPPi catalyst with well-defined morphology. Followed by which, the actual active sites involved during NRR were determined by addition of SCN⁻ in the electrolyte during NRR, since it can poison the Co species in metal

Table 5B-2. EIS calculations obtained from Nyquist plots.

S.No.	Catalyst	R_s (Ω)	R_p (Ω)	R_{ct} (Ω)
1.	CoPPi	3.64	123.66	120.02
2.	CoPPi- <i>SF</i>	3.64	144.32	140.68

Table 5B-3. ECSA calculations.

S.No.	Catalyst	C_{dl} (μ F)	ECSA (cm ²)
1.	CoPPi	377	9.425
2.	CoPPi- <i>SF</i>	198	4.95

composites via strong coordination between Co and CN⁻. Figure 5B-7a depicted the CA curves for CoPPi catalyst during NRR in presence of SCN⁻ which displayed a decay in current response and could be attributed to the role of Co as an active site. This was further justified by the decrement in ammonia yield (65.33 μ g h⁻¹ mg_{cat.}⁻¹) and F.E. (8.78%) observed in Figure 5B-7b after addition of SCN⁻. Later, the durability of CoPPi was tested during long-term NRR upto 10 h by performing CA measurements at -0.2 V (where the maximum NRR activity was achieved).

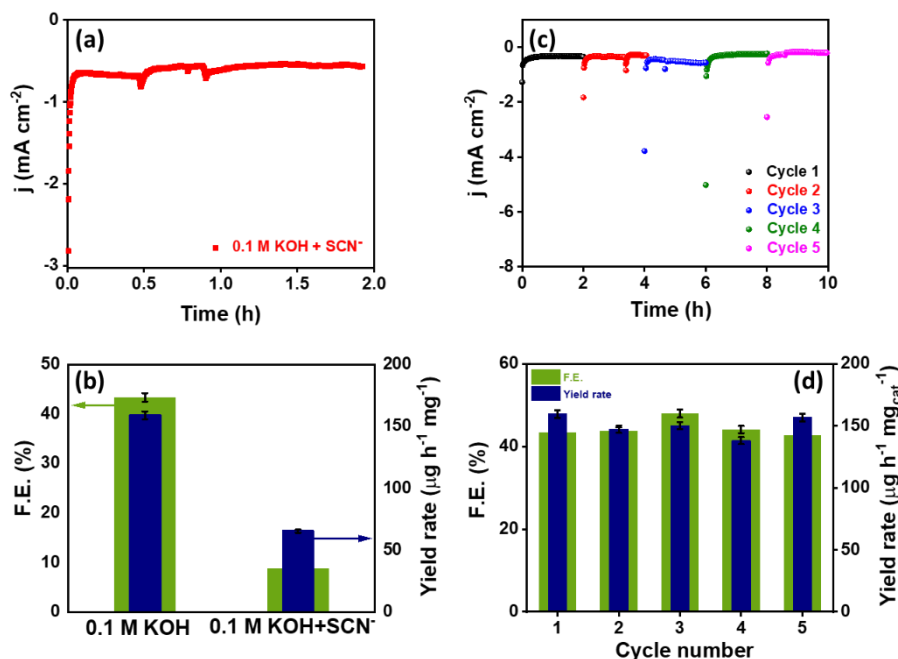


Figure 5B-7. (a) Chronoamperometry performed for 2 h under N₂-saturated 0.1 M KOH in presence of SCN⁻ ions, (b) Comparison of F.E. and NH₃ yield rate obtained in absence and presence of SCN⁻ ions in 0.1 M KOH solution. (c) Chronoamperometric measurements obtained for continuous 10 h of NRR by CoPPi at a potential of -0.2 V (vs. RHE). (d) Comparison of ¹⁴NH₄⁺ yield rate obtained after NRR by CoPPi catalyst by different quantification methods viz. Indophenol blue method, Nessler's reagent method and LC-MS method respectively.

The current response, ammonia production rate as well as the F.E. were well maintained even after the stability tests [Figures 5B-7(c-d)] and thus manifested good durability of prepared catalyst. This could be attributed to the unique geometry and the structural rigidity of pyrophosphate composites. Besides, the morphology and elemental composition of CoPPi were retained even after prolonged NRR measurements when characterized with *ex-situ* techniques comprising SEM, TEM, EDS [Figures 5B-8(a-c) and Table 5B-4]. Moreover, similar oxidation states of respective elements in CoPPi were witnessed from post-stability XPS analyses [Figures 5B-8(d-f)]. After appraising the stability of catalyst, the reported ammonia yield by Indophenol blue quantification method

Table 5B-4. EDS (%) composition analysis for in CoPPi after NRR stability test.

S.No.	Element	Mass normalized (%)	Atomic (%)
1.	Cobalt	34.667	14.049
2.	Phosphorus	16.036	12.365
3.	Oxygen	49.297	73.586
	Total	100.00	100.00

was validated by two other methods *c.a.* Nessler's reagent test and LC-MS in turn. The ammonia yield rate calculated after Nessler's test for the electrolyte sample collected after NRR by CoPPi at -0.2 V (vs. RHE) was found out to be $163.3 \mu\text{g h}^{-1} \text{mg}_{\text{cat}}^{-1}$ while it came out to be $161.18 \mu\text{g h}^{-1} \text{mg}_{\text{cat}}^{-1}$ when calculated using LC-MS [Figures 5B-9(a-b)]. Figure 5B-9c represent the bar diagram comparison of $^{14}\text{NH}_4^+$ yields acquired after NRR by CoPPi catalyst using different quantification

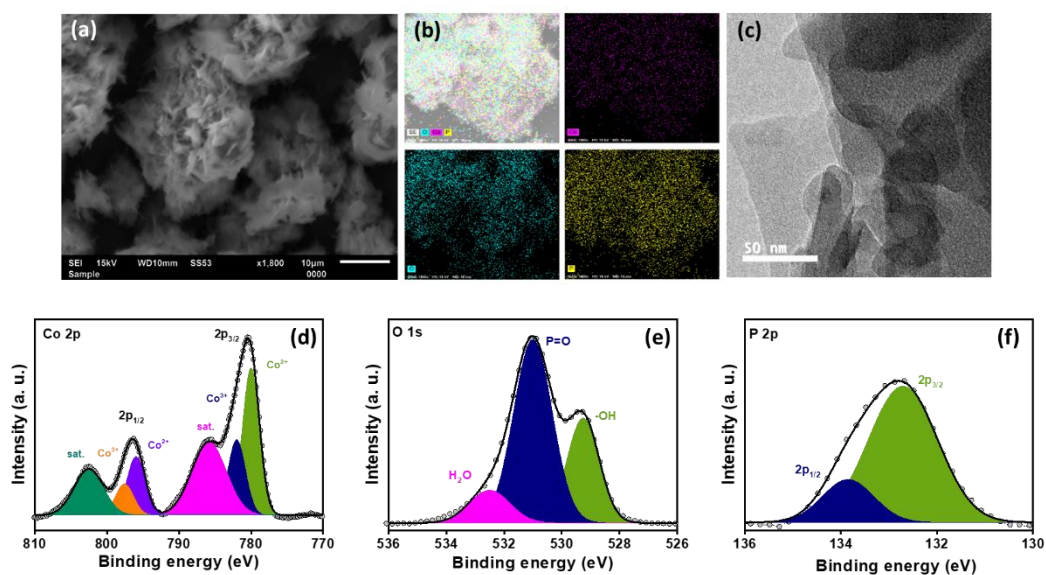


Figure 5B-8. (a) SEM image showing morphology of CoPPi after NRR stability test. (b) EDS dot mapping for CoPPi showing homogeneous distribution of all the respective elements over the scanned area after NRR stability test. (c) TEM image, deconvoluted XP spectrum for (d) Co 2p, (e) O 1s and (f) P 2p for CoPPi catalyst after NRR stability test.

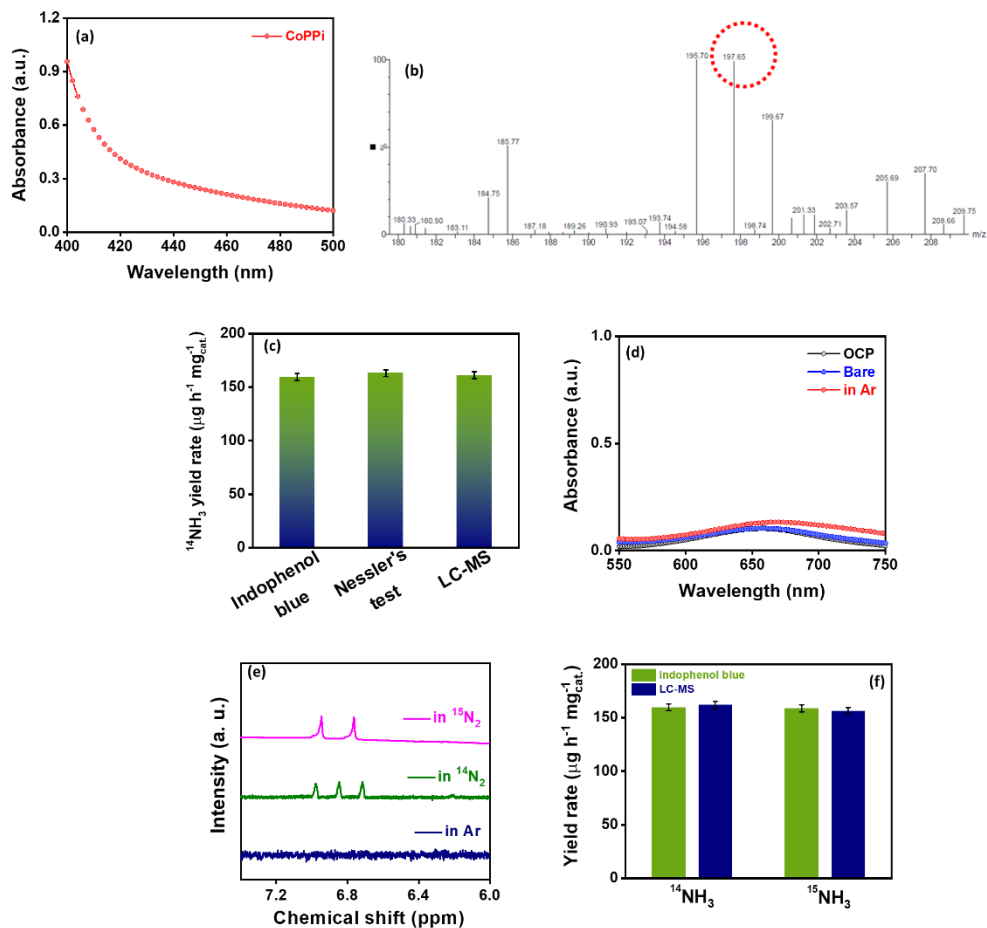


Figure 5B-9. (a) UV-Vis absorbance curve obtained after Nessler's reagent test for electrolyte sample collected after NRR by CoPPi @ -0.2 V. (b) Mass spectrum obtained for ^{14}N -Indophenol in electrolyte sample collected after NRR by CoPPi @ -0.2 V showing formation of $^{14}\text{NH}_4^+$ ($m/z = 197.65 \sim 198$). (c) Comparison of $^{14}\text{NH}_4^+$ yield rate obtained after NRR by CoPPi catalyst by different quantification methods *viz.* Indophenol blue method, Nessler's reagent method and LC-MS method respectively. (d) UV-Vis absorbance curves obtained after NRR control experiments in Ar-saturated electrolyte, over bare electrode and at open circuit potential respectively. (e) ^1H -NMR spectrum obtained after isotope labelling experiment in $^{14}\text{N}_2$ - and $^{15}\text{N}_2$ -saturated 0.1 M KOH electrolyte. (f) Comparison of $^{14}\text{NH}_4^+$ & $^{15}\text{NH}_4^+$ yield rates obtained after isotope labelling NRR experiment via LC-MS and Indophenol blue quantification method.

methods, which depicted the analogous yield rates and thus validated the reported ammonia yields. Further to substantiate the exact source of NH_3 after NRR the

rigorous control procedures were followed. Initially, the catalyst, electrolyte and gas-supplies were checked for any N-labile contaminations which could lead to overestimation of ammonia yield rates. The CoPPi catalyst synthesis was synthesized using NO_3^- free precursor and thus couldn't contribute towards ammonia production. On the other hand, the electrolyte solution also didn't contain any nitrate or nitrite species. In the end, the gas-supplies were cleansed in a similar fashion as described previously. All these results validated the true NH_3 estimation in this work. Subsequently, other control measurements *viz.* chronoamperometry on bare glassy carbon electrode (GCE) without catalyst at -0.2 V in presence of N_2 , at open circuit potential and in presence of Ar at -0.2 V with catalyst were also performed (Figure 5B-9d). We couldn't observe any ammonia production after the same and so the isotope labelling experiments were also performed to ascertain the exclusive source of produced NH_3 . Figure 5B-9e presented the ^1H -NMR spectrum acquired after isotope labelling NRR by CoPPi with different gas-supplies where the doublet corresponding to $^{15}\text{N-H}$ in $^{15}\text{NH}_4^+$ and triplet related to $^{14}\text{N-H}$ in $^{14}\text{NH}_4^+$ could be seen. This ensured the purged N_2 gas as the true and only source for NH_3 production rather than any N-labile contaminants. Further upon quantification by LC-MS, the $^{14}\text{NH}_4^+$ and $^{15}\text{NH}_4^+$ yield rate came out to be 161.18 and 156.33 $\mu\text{g h}^{-1} \text{mg}_{\text{cat}}^{-1}$ respectively *i.e.* matching with the yield obtained from Indophenol blue method (Figure 5B-9f). This arduous and inclusive scrutiny of reliable and accurate NH_3 production during NRR upholds the budding ability of CoPPi catalyst to run through NRR at commercial level.

5B-3.3 Methanol electro-oxidation: After the evaluation of NRR activity of the catalyst, its ability to catalyse MOR was studied by performing LSV using 1M KOH in absence and presence of 1M MeOH at 10 mV s^{-1} of scan rate. Before LSV measurements, the catalyst was activated by performing CV at different scan rates between 10-100 mV s^{-1} in just KOH to expose the active Co-OOH phase of catalyst for MOR (Figure 5B-10a). A comparatively low onset potential for MOR is achieved (1.29 V) for CoPPi than OER which could achieve 100 mA cm^{-2} of current

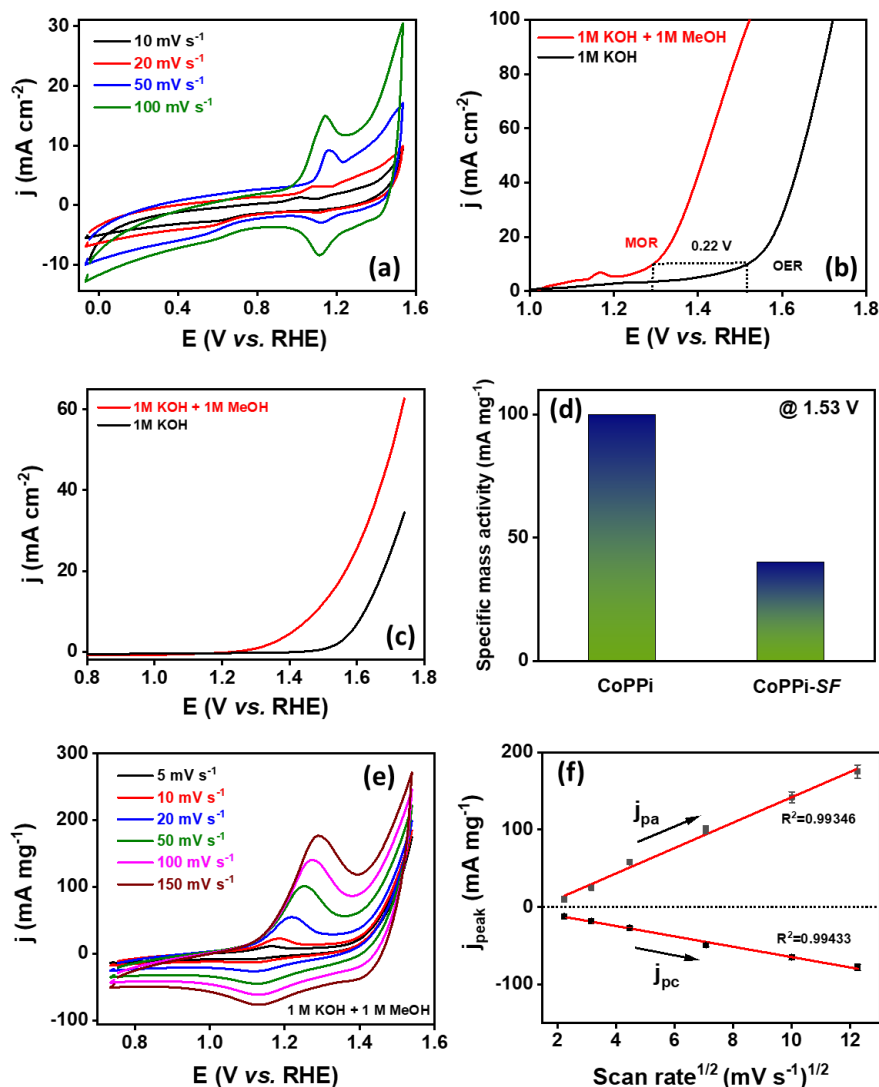


Figure 5B-10. (a) Cyclic voltammetry performed at different scan rates for activation of CoPPi catalyst before MOR in 1 M KOH electrolyte. Linear sweep voltammograms acquired for comparison of activity of (b) CoPPi and (c) SF-CoPPi catalyst towards MeOH oxidation and oxygen evolution in presence and absence of 1M MeOH in 1 M KOH electrolyte respectively at a scan rate of 10 mV s⁻¹. (d) Specific mass activity of CoPPi and CoPPi-SF catalyst extracted from their respective linear sweep voltammograms at 1.53 V (vs. RHE). (e) Cyclic voltammograms obtained after MOR by CoPPi catalyst at different scan rates in 1M KOH electrolyte after addition of 1M MeOH. (f) Square root of scan rate vs. anodic/cathodic peak current density plots.

density at just 1.52 V *vs.* RHE. On the other hand, *SF*-CoPPi was able to initiate MOR with a negative shift in onset potential at 1.34 V and could achieve just 21 mA cm⁻² of current density at 1.52 V respectively [Figures 5B-10(b-c)]. The enhanced or superior MOR activity of CoPPi was also supported by its high mass current density of 100 mA mg⁻¹ at 1.53 V *vs.* RHE (Figure 5B-10d). Our strategy to replace sluggish OER with MOR at anode during ammonia synthesis was justified from the reduced energy requirements (around 0.2 V @ 10 mA cm⁻²) to carry out MOR by CoPPi catalyst, as shown in LSV curves acquired in absence and presence of methanol as well as the increased anodic current density. This could be consigned to the layered nanosheets with micro-flower like assembly, which afford immense active sites with even channels for electrolyte

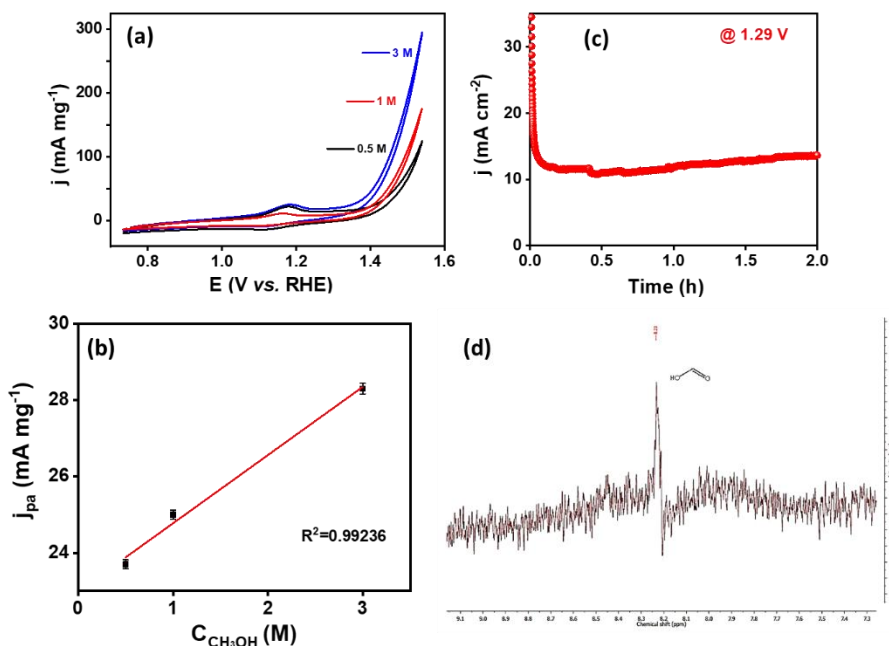


Figure 5B-11. (a) Cyclic voltammetry performed at different with different MeOH concentrations in 1M KOH solution and (b) corresponding linear plot between peak current density and MeOH concentration extracted (c) Chronoamperometric curves obtained for CoPPi catalyst during MOR stability test at corresponding onset potential for 2 h of time duration. (d) ¹H-NMR spectrum obtained after 2 h of MOR by CoPPi catalyst in 1M KOH+1M MeOH electrolyte.

transfer and the electronegative pyrophosphate which could accept e^- from Co metal and enhance H^+ adsorption due to negative charge during MOR. To get deep insights into the mechanism of CoPPi during MOR, CV was executed in a potential window of 0.75 to 1.55 V (vs. RHE) which revealed well-defined redox peaks related to Co^{2+}/Co^{3+} oxidation in anodic scan and Co^{3+}/Co^{2+} in cathodic scan respectively (Figure 5B-10e). Notably, a linear relationship between scan rate and current density was observed from the plots of j_{pa} vs. $v^{1/2}$ and j_{pc} vs. $v^{1/2}$ pointing towards the diffusion controlled process over catalyst surface during methanol electro-oxidation rather than surface controlled process (Figure 5B-10f). A linear enhancement trend was also attained when peak current densities were plotted against MeOH concentration from 0.5 M to 3 M, evidencing the tolerance of

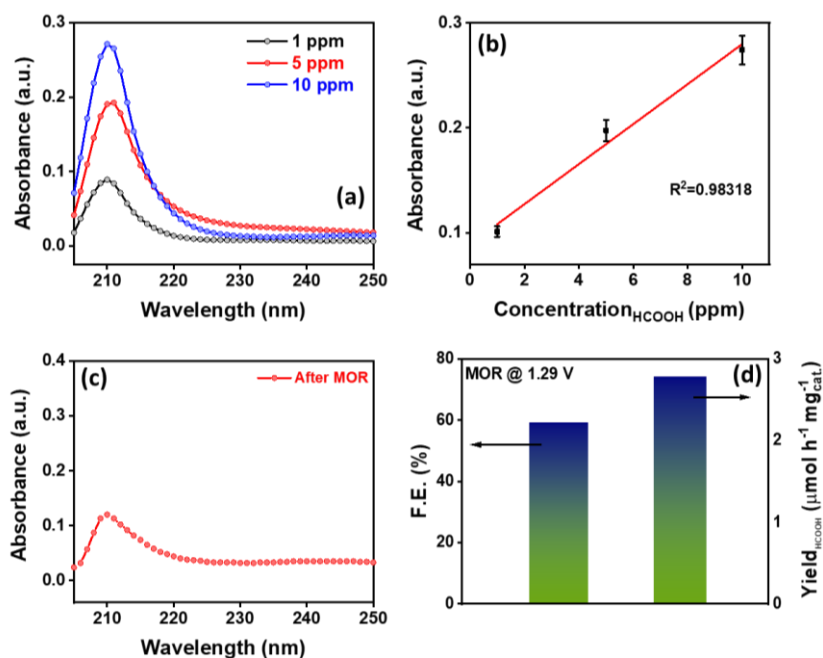


Figure 5B-12. (a) UV-Vis absorbance curves for standard HCOOH solution of varying concentrations between 1 to 10 ppm and b) corresponding standard calibration curve. (c) UV-Vis absorbance curve acquired from the sample collected after 2 h MOR@1.29 V (vs. RHE) by CoPPi catalyst. (d) Bar diagram representing the F.E. and HCOOH yield rate obtained after 2 h of MOR at 1.29 V (vs. RHE).

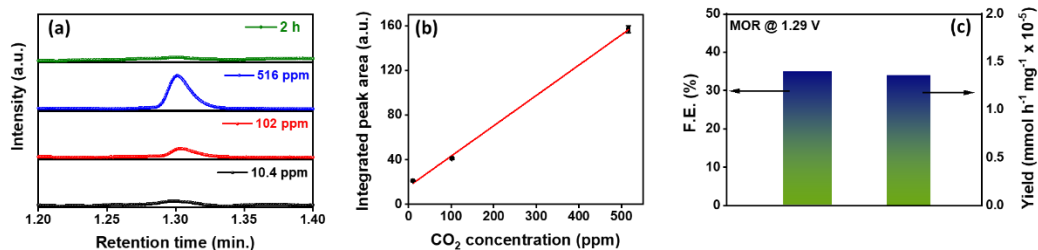


Figure 5B-13. (a) Gas-chromatograms for different concentrations of CO₂ gas and for the gas collected after MOR at 1.29 V in 0.1 M KOH electrolyte and (b) standard calibration curve extracted from (a) for quantification of CO₂ formed. (c) Bar graph representing the FE and yield rate for CO₂ produced after MOR by CoPPi catalyst.

catalyst towards high methanol concentrations [Figures 5B-11(a-b)]. Later the stability of catalyst during MOR was inspected by means of CA measurements at 1.29 V *vs.* RHE, as showed in Figure 5B-11c. The catalyst was able to provide a stable current response for 2 hours and the production of formic acid was alleged as a partial oxidation product. The formic acid production was affirmed by the presence of peak at a chemical shift of 8.23 ppm in ¹H-NMR spectrum of electrolyte taken after the MeOH electro-oxidation (Figure 5B-11d). The produced HCOOH was then quantified via UV-Vis spectroscopy [Figures 5B-12(a-d)] which gave a total yield of 2.78 μmol h⁻¹ mg_{cat.}⁻¹ and a F.E. of 59.2%. Since, the complete oxidation of MeOH could lead to the formation of CO₂ and so it was also quantified using GC, which furnished a F.E. of 35% for CO₂ at identical potential [Figures 5B-13(a-c)]. In the end, the catalyst stability was assessed by physical characterizations like SEM and P-XRD measurements which revealed the robustness in terms of elemental distribution and morphology [Figures 5B-14(a-b)]. While the O 1s deconvoluted XP spectrum for CoPPi after MOR propose the surface oxidation of catalyst with presence of peak associated with Co-OOH (O²⁻ at 531 eV) species [Figures 5B-14(c-e)]. The aforesaid outcomes divulged the high activity and stability of CoPPi catalyst for methanol electro-oxidation in alkaline media to possibly substitute the sluggish anodic OER in NH₃ synthesis.

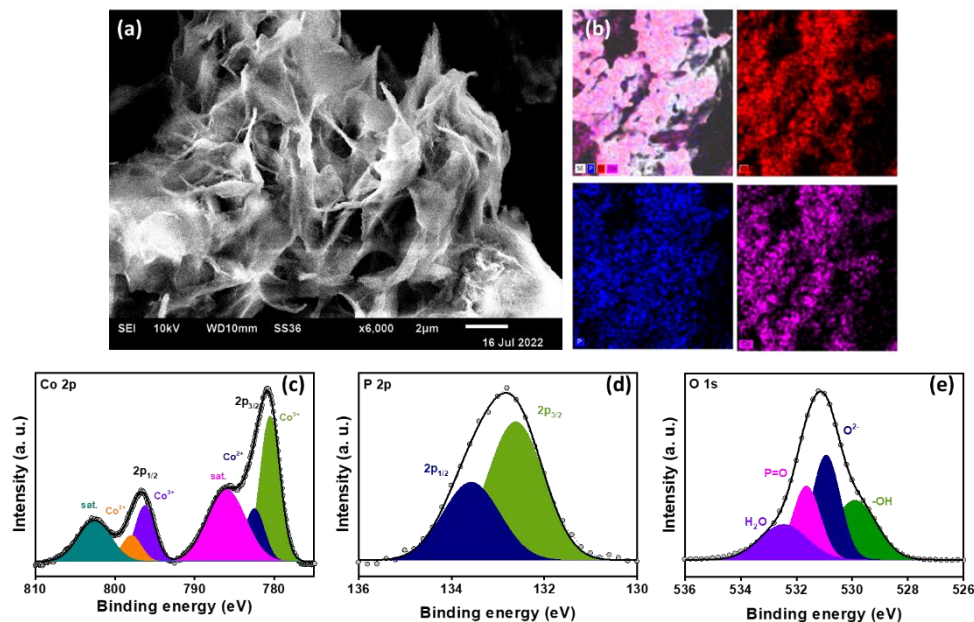


Figure 5B-14. (a) SEM image showing morphology and (b) EDS dot mapping for showing homogeneous distribution of all the respective elements over the scanned area of CoPPi after MOR stability test. Deconvoluted XP spectrum for (c) Co 2p, (d) P 2p and (e) O 1s for CoPPi catalyst after MOR stability test.

5B-3.4 Overall NH₃ synthesis: The designed bifunctional catalyst was applied for overall ammonia synthesis under full-cell conditions after determining their activity concerning half-cell reactions. A membrane separated H-cell configuration was employed to carry out ammonia synthesis with CoPPi as anode and cathode (Figure 5B-15a), where in the anolyte was taken as 1M MeOH+1M KOH and N₂-saturated 0.1 M KOH was taken as catholyte. The LSV curve was acquired for full-cell setup (Figure 5B-15b) which represented a steep increase in current density at 1.6 V evidencing the ammonia production. The CA was then performed for 2 h at onset potential to obtain a NH₃ yield of 95.2 μg h⁻¹ mg_{cat}⁻¹ and HCOOH formation rate of 2.53 μmol h⁻¹ mg⁻¹ (Figure 5B-15c). The hypothesis of substituting OER with MOR to reduce the cell voltage was authorized by assembling another full-cell which comprised of OER (1 M KOH anolyte) at anode and NRR at cathode. The LSV curve assimilated for NRR-OER required 1.8 V (i.e. 0.2 V higher than NRR-MOR full cell) to commence ammonia production. Also, NRR-OER full cell required 2.13 and 2.43 V to achieve a

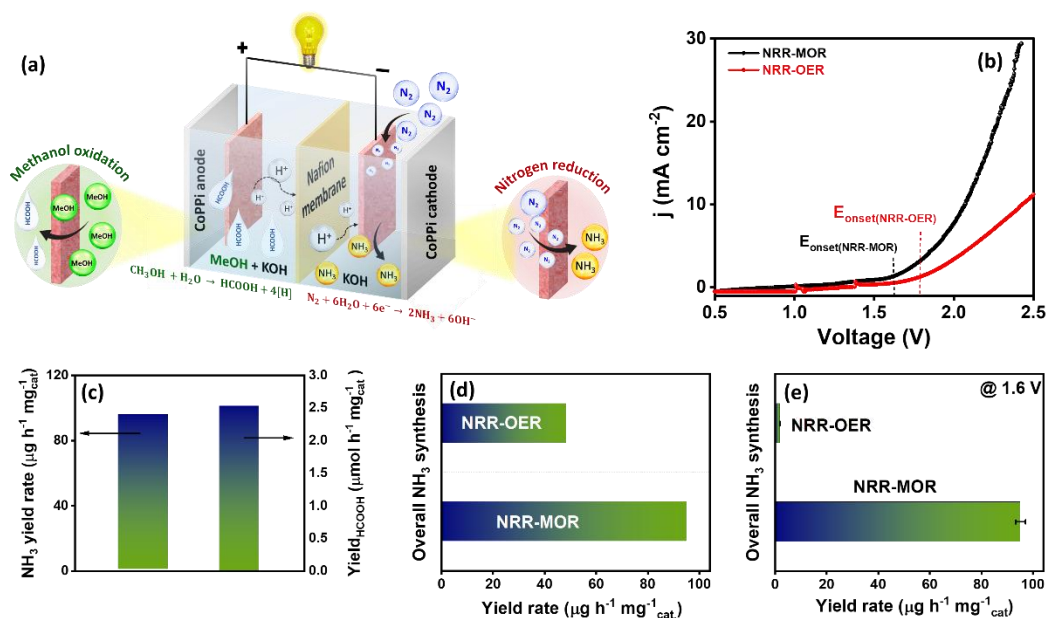


Figure 5B-15. (a) Schematic representation of cell-setup acquired for overall NH_3 synthesis in an H-cell separated by a membrane showing NRR at cathode and MOR at anode equipped with a bifunctional CoPpi catalyst. (b) Comparison of NRR-MOR and NRR-OER full-cell NH_3 synthesis via linear sweep voltammetry by CoPpi as an electrocatalyst. (c) Bar graph representing the obtained NH_3 and HCOOH yield rate after full-cell NH_3 synthesis in NRR-MOR cell setup, (d) the obtained NH_3 yield rate after full-cell NH_3 synthesis in NRR-MOR and NRR-OER cell setup at respective onset potentials and (e) comparison of NH_3 yield rate obtained after electrolysis in NRR-MOR and NRR-OER full-cell at similar potential of 1.6 V.

current density of 5 and 10 mA cm^{-2} respectively while just 1.88 and 2 V were essential to realize the same current density when OER was substituted with MOR. In addition, the low NH_3 yield was observed ($48.53 \mu\text{g h}^{-1} \text{mg}_{\text{cat}}^{-1}$) after electrolysis at respective onset potential in NRR-OER configuration (Figure 5B-15d) strengthening the prominence of our conceptualization. Besides, the concept of anodic reaction replacement was authenticated by performing the electrolysis for 2 h at onset potential of NRR-MOR configuration (1.6 V) in NRR-OER full cell. A negligible NH_3 yield was attained with a value of $95.2 \mu\text{g h}^{-1} \text{mg}_{\text{cat}}^{-1}$ (Figure 5B-15e), and proposed the necessity of extra energy to produce ammonia in NRR-OER full cell configuration. As a consequence, this study would

crack the enactment of metal pyrophosphates for overall NH_3 synthesis at reduced cell voltages with replacement of anodic OER with MOR to be put into practice.

5B-4 Summary

An environmentally generous and time saving sonochemical method was realized for synthesis of $\text{Co}_2\text{P}_2\text{O}_7$ micro-flowers assembled by uniform layered nanosheets. The described structure could bid the higher electrolyte and charge transfer in the course of NH_3 synthesis with a decent stability attributable to the presence of pyrophosphate groups. In addition, the cationic charge distribution over metal species could be accountable for high N_2 adsorption and anionic $\text{P}_2\text{O}_7^{4-}$ groups might promote the hydrogenation of adsorbed N species to produce NH_3 molecule. The present study astounded the limitation of sluggish OER kinetics by replacement with MOR at anode to produce NH_3 at reduced cell voltage along with the production of value-added formic acid at anode. That's why, this work may possibly seek out courtesy for the assessment of metal-based pyrophosphates on the road to electrochemical NH_3 synthesis with enriched activity and durability.

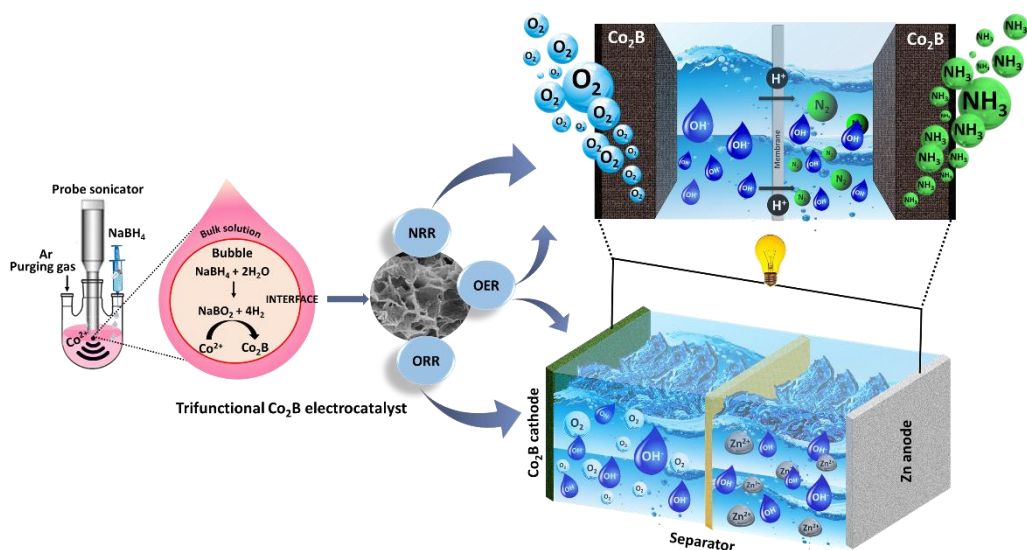
5B-5 References

1. F. Jiao and B. Xu, *Adv. Mater.*, 2019, **31**, 1805173.
2. G. Soloveichik, *Nat. Catal.*, 2019, **2**, 377-380.
3. F. B. Juangsa, A. R. Irhamna and M. Aziz, *Int. J. Hydrogen Energy*, 2021, **46**, 14455.
4. A. Chen and B. Y. Xia, *J. Mater. Chem. A*, 2019, **7**, 23416-23431.
5. W. Li, W. Fang, C. Wu, K. N. Dinh, H. Ren, L. Zhao, C. Liu and Q. Yan, *J. Mater. Chem. A*, 2020, **8**, 3658-3666.
6. S. Li, X. Hao, A. Abudula and G. Guan, *J. Mater. Chem. A*, 2019, **7**, 18674-18707.
7. J. Li, W. Huang, M. Wang, S. Xi, J. Meng, K. Zhao, J. Jin, W. Xu, Z. Wang and X. Liu, *ACS Energy Lett.*, 2018, **4**, 285-292.
8. S. Giddey, S. Badwal and A. Kulkarni, *Int. J. Hydrogen Energy*, 2013, **38**, 14576-14594.
9. Q. Qin, T. Heil, J. Schmidt, M. Schmallegger, G. Gescheidt, M. Antonietti and M. Oschatz, *ACS Appl. Energy Mater.*, 2019, **2**, 8359-8365.
10. L. Wang, X. Zhang, L. Yang, C. Wang and H. Wang, *Catal. Sci. Technol.*, 2015, **5**, 4800-4805.
11. M. T. Bender, X. Yuan and K.-S. Choi, *Nat. Commun.*, 2020, **11**, 1-4.
12. A. Santasalo-Aarnio, Y. Kwon, E. Ahlberg, K. Kontturi, T. Kallio and M. T. Koper, *Electrochem. Commun.*, 2011, **13**, 466-469.
13. X. Wei, Y. Li, L. Chen and J. Shi, *Angew. Chem. Int. Ed.*, 2021, **60**, 3148-3155.
14. H. Zhong, M. Iguchi, M. Chatterjee, Y. Himeda, Q. Xu and H. Kawanami, *Adv. Sustain. Syst.*, 2018, **2**, 1700161.

15. M. Kolen, D. Ripepi, W. A. Smith, T. Burdyny and F. M. Mulder, *ACS Catal.*, 2022, **12**, 5726-5735.
16. Y. Tong, X. Yan, J. Liang and S. X. Dou, *Small*, 2021, **17**, 1904126.
17. A. Yuda, A. Ashok and A. Kumar, *Catal. Rev.*, 2022, **64**, 126-228.
18. D. Gupta, S. Chakraborty, R. G. Amorim, R. Ahuja and T. C. Nagaiah, *J. Mater. Chem. A*, 2021, **9**, 21291-21301.
19. X. L. Tian, L. Wang, P. Deng, Y. Chen and B. Y. Xia, *J. Energy Chem.*, 2017, **26**, 1067-1076.
20. J. Wang, S. Chen, Z. Li, G. Li and X. Liu, *ChemElectroChem*, 2020, **7**, 1067-1079.
21. G.-R. Xu, M. Batmunkh, S. Donne, H. Jin, J.-X. Jiang, Y. Chen and T. Ma, *J. Mater. Chem. A*, 2019, **7**, 25433-25440.
22. Z. Chang, F. Kong, M. Wang, S. Han, X. Cui, H. Tian, Y. Chen, G. Meng, C. Chen and Y. Liu, *Chem. Catal.*, 2022, **2**, 358-371.
23. V. S. Marakatti and E. M. Gaigneaux, *ChemCatChem*, 2020, **12**, 5838-5857.
24. L. Li, T. Zhang, Y. Zhou, X. Wang, C.-t. Au and L. Jiang, *J. Rare Earths*, 2022, **40**, 1-10.
25. C. Huang, L. Shang, P. Han, Z. Gu, A. M. Al-Enizi, T. M. Almutairi, N. Cao and G. Zheng, *J. Colloid Interface Sci.*, 2019, **552**, 312-318.
26. D. Gupta, A. Kafle, S. Kaur, P. P. Mohanty, T. Das, S. Chakraborty, R. Ahuja and T. C. Nagaiah, *J. Mater. Chem. A*, 2022.
27. K. Chu, Y.-p. Liu, Y.-b. Li, H. Zhang and Y. Tian, *J. Mater. Chem. A*, 2019, **7**, 4389-4394.
28. W. Guo, Z. Liang, J. Zhao, B. Zhu, K. Cai, R. Zou and Q. Xu, *Small Methods*, 2018, **2**, 1800204.
29. C. Li, R. Xu, S. Ma, Y. Xie, K. Qu, H. Bao, W. Cai and Z. Yang, *Chem. Eng. J.*, 2021, **415**, 129018.
30. X. Peng, H. Cai, Y. Zhou, J. Ni, X. Wang, B. Lin, J. Lin, L. Zheng, C.-t. Au and L. Jiang, *ACS Sustain. Chem. Eng.*, 2022, **10**, 1951-1960.
31. T.-N. Ye, S.-W. Park, Y. Lu, J. Li, J. Wu, M. Sasase, M. Kitano and H. Hosono, *J. Am. Chem. Soc.*, 2021, **143**, 12857-12866.
32. J.-T. Ren, L. Chen, H.-Y. Wang and Z.-Y. Yuan, *ACS Appl. Mater. Interfaces*, 2021, **13**, 12106-12117.
33. J.-T. Ren, L. Chen, Y. Liu and Z.-Y. Yuan, *J. Mater. Chem. A*, 2021, **9**, 11370-11380.
34. S. Chen, X. Yang, X. Tong, F. Zhang, H. Zou, Y. Qiao, M. Dong, J. Wang and W. Fan, *ACS Appl. Mater. Interfaces*, 2020, **12**, 34971-34979.
35. H. Pang, Z. Yan, Y. Ma, G. Li, J. Chen, J. Zhang, W. Du and S. Li, *J. Solid State Electrochem.*, 2013, **17**, 1383-1391.
36. Y. Zhang, X. Wu, G. Fu, F. Si, X.-Z. Fu and J.-L. Luo, *Int. J. Hydrogen Energy*, 2022, **47**, 17150-17160.
37. L.-J. Gao, C.-C. Weng, Y.-S. Wang, X.-W. Lv, J.-T. Ren and Z.-Y. Yuan, *J. Colloid Interface Sci.*, 2022, **606**, 544-555.
38. B. Li, R. Zhu, H. Xue, Q. Xu and H. Pang, *J. Colloid Interface Sci.*, 2020, **563**, 328-335.
39. L. Xiao, Y. Liang, Z. Li, S. Wu, S. Zhu, S. Luo, C. Chang and Z. Cui, *ACS Sustain. Chem. Eng.*, 2020, **8**, 19072-19083.
40. A. Padhy, A. K. Samantara and J. Behera, *Sustain. Energy Fuels*, 2021, **5**, 3729-3736.
41. X. Liu, S. Deng, D. Xiao, M. Gong, J. Liang, T. Zhao, T. Shen and D. Wang, *ACS Appl. Mater. Interfaces*, 2019, **11**, 42233-42242.
42. J. Zhang, P. Liu, R. Bu, H. Zhang, Q. Zhang, K. Liu, Y. Liu, Z. Xiao and L. Wang, *New J. Chem.*, 2020, **44**, 12514-12521.
43. M. Wang, S. Liu, T. Qian, J. Liu, J. Zhou, H. Ji, J. Xiong, J. Zhong and C. Yan, *Nat. Commun.*, 2019, **10**, 1-8.

Chapter 6

Trifunctional Co₂B catalyst enables high power density Zn-air batteries to drive the electrochemical NH₃ synthesis



6-1 Introduction

The electrochemical N_2 fixation to ammonia is one of the potential alternative to conventional Haber-Bosch process^{1,2,3} by virtue of its simplified operation under ambient conditions, involvement of water as a green H_2 source and use of power supply generated from renewable energy sources without carbon emissions.^{4,5} In addition to it, application of high-power density rechargeable metal-air batteries *viz.* Zn-air batteries (ZAB) for electrochemical ammonia synthesis would be a game changing strategy.⁶ Since the reliance over the renewable energy sources like solar energy and wind energy to power the electrochemical device impose disadvantages like dependency on the weather which have led to the development of clean and renewable energy alternatives like integrated energy systems (IES) such as combined solar cell and lithium storage unit, water splitting powered by solar cells/metal-air batteries.⁷ In this context, Zn-air batteries have demonstrated their potential as the power source due to earth abundant, economical and environment friendly metal anode and its high theoretical energy density (1353 Wh kg^{-1}), which is three times higher than Li-ion batteries ($100\text{-}265 \text{ Wh kg}^{-1}$).⁸ And therefore, elimination of the use of any external power supply to power ammonia synthesis by using an energy storage device such as Zn-air battery could be interesting. Integration of ZAB in electrochemical NH_3 production will also provide cumulative efficiency compared to its individual device. Nevertheless, so far merely two reports are available in which ZABs have been used to power the electrochemical NH_3 synthesis. Although this strategy would be interesting but challenging, due to several disadvantages such as drying out of the electrolyte, inadequate performance of air electrodes, water flooding and CO_2 contamination of electrolyte which leads to the deterioration of the battery.⁹

To bring about these provisions, the major assignment is to design and develop highly efficient and robust catalysts active towards nitrogen reduction reaction and oxygen electrocatalysis *viz.* oxygen reduction reaction (ORR) and oxygen evolution reaction (OER) for ZAB.¹⁰ Degradation of air cathodes during cycling in

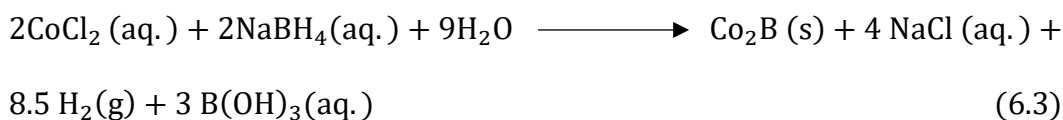
Zn-O₂ battery due to sluggish multielectron process of OER and ORR are the main drawbacks during its operation.⁹ On the contrary, adsorption and activation of strong N≡N triple bond, negative e⁻ affinity, high ionization potential, high HOMO-LUMO gap and permanent dipole, are the major struggles confronted during synthesis of NH₃.¹¹ At present the precious Pt/C is the benchmark ORR catalyst but is not competent towards OER/NRR. On the other hand IrO₂/RuO₂ are the benchmark OER catalysts but are not efficient for ORR/NRR.¹²⁻¹⁴ Further, the costly and limited geographical distribution of precious metal based benchmark catalysts along with their sluggish kinetics inhibit the concurrent application of the same.¹⁵ This restraint stresses the development of a cost-effective non-noble metal-based catalyst for OER, ORR and NRR, which embraces ability to compete or even beat the activity of precious benchmark catalysts.^{16,17} Without a doubt, the designing of such a catalyst^{11,18,19,20} which own abundant active sites and robustness towards three different reactions^{21,22,23} with utterly diverse fundamental mechanisms is so far problematic but the need of the hour.^{24,25,26,27}

Transition metal borides (TMBs) give the impression of an imperative inorganic class of materials with prevalent applications in different fields, for instance, energy storage & conversion, superconductivity, thermoelectricity, etc.^{28,29,30,31} Cobalt and nickel based TMBs are recurrently used in electrocatalysis for the reason that they possess enhanced electrical conductivity, stability and hardness.^{32,33} TMBs reveal higher OER activity in alkaline media than benchmark catalysts.³⁴ For instance, Co₂B had been recently reported by Jose *et al.*³⁵ for ORR in alkaline media which outperformed the activity of Pt/C. Moreover, a few theoretical investigations are reported screening the ability of TMBs towards NRR as well.^{36,37,38,39,40} Consequently, in the present work we have divulged a cost-effective, energy efficient, less time consuming and facile sonochemical method for the synthesis of TMBs.^{41,42} This approach holds an added advantage of obstructing the particle agglomeration under chemical environments owing to the ultrasound waves generated during sonochemical synthesis.⁴³ At this juncture, we

report the synthesis of amorphous cobalt boride with porous nanosheet morphology as a trifunctional catalyst for NRR, ORR and OER via sonochemical method. The optimized cobalt boride was equipped in Zn-air battery as air cathode and successfully powered a self-driven NH_3 synthesis. To the best of our knowledge, this is the first report to explore metal borides as a trifunctional catalyst for battery driven NH_3 synthesis under ambient conditions. The catalyst showed good activity towards electrochemical NH_3 synthesis with F.E. of 20.45 % in alkaline media at -0.3 V vs. RHE. When Co_2B was employed as air-cathode catalyst for Zn-air battery, a remarkable electrocatalytic activity was witnessed with an open circuit potential of 1.45 V, a high power density of 500 mW cm^{-2} & an energy density of 1078 W h kg^{-1} which could carry out NH_3 generation with an overall NH_3 production yield rate of $1.048 \text{ mg h}^{-1} \text{ mg}_{\text{cat}}^{-1}$.

6-2 Material synthesis

6-2.1 Synthesis of Co_2B : The synthesis of Co_2B (1:8) was carried out by a simple and environment friendly sonochemical method using cheap reactant precursors. The reaction was carried out in a round bottom flask (RBF) under ice cold and inert atmospheric conditions. An aq. solution of $\text{CoCl}_2 \cdot 6\text{H}_2\text{O}$ (476 mg, 1 mmol, in 40 mL deionized water) was added to the RBF, to which 8 mmol of NaBH_4 solution was added (302 mg in 10 mL deionized water) in a dropwise manner. The bath sonication was continued till completion of the reaction and the probe sonication was employed during the reaction at regular intervals *i.e.* 15 second sonication and 30 second rest) with a horn frequency of 20 Hz. Once the reducing agent was completely added into the metal precursor solution, the reaction mixture was kept undisturbed for reaction completion (confirmed from disappearance of bubble evolution). Reactions which might have taken place during the synthesis could be described as follows:



At last, the precipitates were collected via centrifugation for atleast 5 minutes and washed 3-4 times with a 1:1 mixture of ethanol and water by volume and dried overnight at 60 °C to obtain Co₂B catalyst (Metal : Boron). The Metal: Boron ratio were varied as 1:4/1:8/1:12 mmol in this study for optimization of trifunctional activity towards NRR, OER and ORR.

6-3 Results and discussion

6-3.1 Physical characterization: The difference in physico-chemical properties of the catalysts with only difference in metal: boron ratio during synthesis was inspected by carrying out a sequence of *ex-situ* characterizations. The P-XRD pattern of Co₂B (1:8) in Figure 6-1a exposed the formation of Co₂B with a distinct peak at $2\theta=45^\circ$ with no other peaks, specifying the pure amorphous Co₂B phase. While the presence of additional peaks at 26° and 36.8° related to B₂O₃ (PDF card: 06-0297) and elemental B (PDF card: 12-0377) imply the amorphous boron-oxide

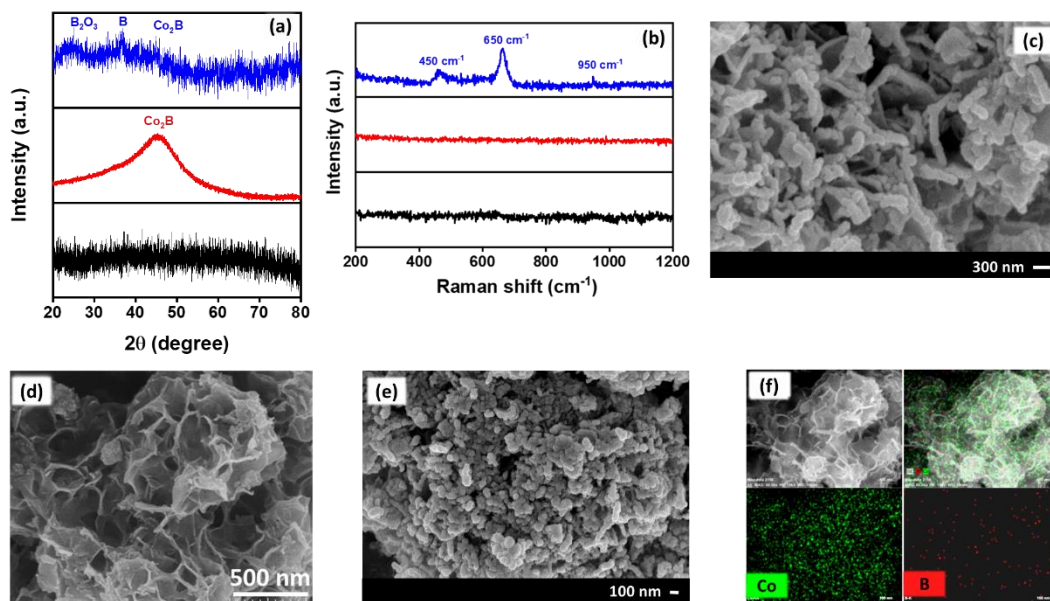


Figure 6-1. (a) Powder X-ray diffraction patterns of Co₂B [black: Co₂B (1:4); red: Co₂B (1:8); blue: Co₂B (1:12)] and (b) Raman spectrum for Co₂B catalysts. FE-SEM images of (c) Co₂B (1:4) (d) Co₂B (1:8) and (e) Co₂B (1:12) at different magnifications. (f) Elemental dot mapping images for Co₂B (1:8) showing uniform distribution of Co and B elements over the scanned area.

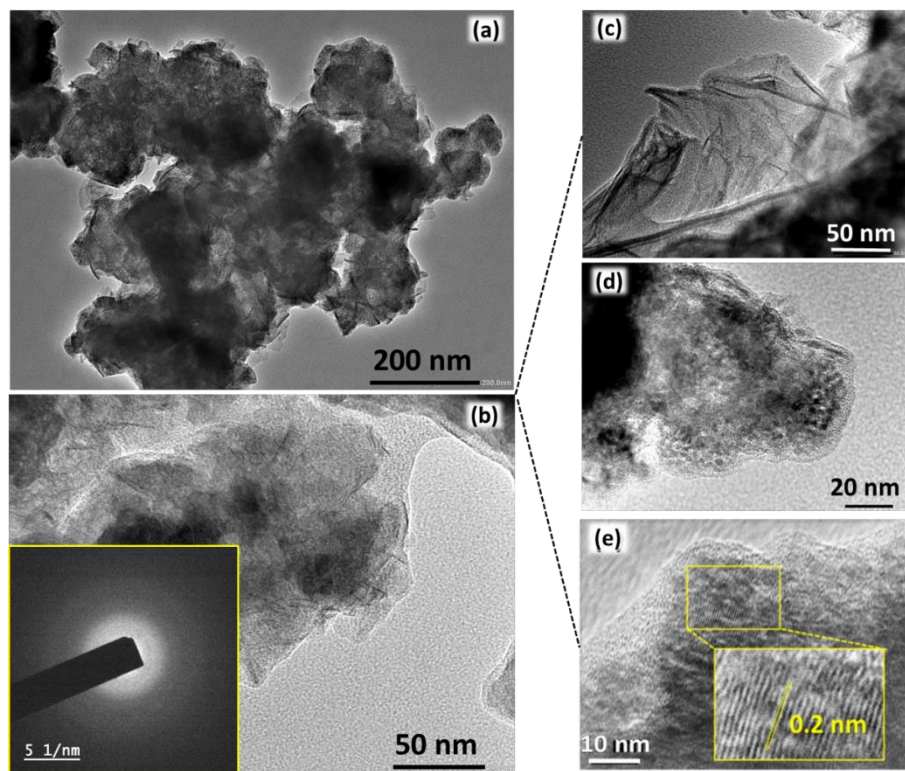


Figure 6-2. (a-e) HR-TEM images of Co_2B (1:8) at different magnifications (inset of (b) shows SAED pattern for Co_2B (1:8) revealing an amorphous nature and inset of (e) shows d-spacing corresponding to Co_2B with short range atomic arrangement at few locations).

layer over the catalyst surface in Co_2B (1:12). But then again, the peaks corresponding to other possible impurities *i.e.* metallic cobalt and $\text{Co}(\text{OH})_2$ in the diffraction pattern of amorphous Co_2B with low signal-to-noise ratio might not be observed as they could have risen above the background noise. And therefore, Raman spectroscopy analysis was implemented to check the purity of the Co_2B catalyst. Figure 6-1b revealed the Raman spectrum of Co_2B catalysts, where no peaks related with metallic cobalt or $\text{Co}(\text{OH})_2$ phase were witnessed in Co_2B (1:4) and Co_2B (1:8). On the other hand, three bands were observed at $650, 950 \text{ cm}^{-1}$ for B_2O_3 and at 465 cm^{-1} corresponding to O-Co-O bond in $\text{Co}(\text{OH})_2$ respectively. These results evidenced that the bulk phase in Co_2B (1:8) catalyst is Co_2B only whilst upon increasing the boron ratio other phases such as B_2O_3 and $\text{Co}(\text{OH})_2$ also appeared but Co_2B remained as the major phase. Further, FE-SEM analysis was

carried out which showed the variation in morphological attributes from stacks of assembled nano-particles in Co₂B (1:4) to surface nanostructuring to form porous nanosheets in Co₂B (1:8). Upon further increment in boron content, the spherical nanoparticles were observed [Figures 6-1(c-e)]. The Co₂B (1:8) porous nanosheets demonstrated the homogeneous distribution of Co and B in the EDS dot mapping image showed in Figure 6-1f. The porous nanosheet like morphology was also confirmed by means of TEM analysis [Figures 6-2(a-b)]. The HRTEM images shown in Figure 6-2c depicted the edge site of entangled nanosheets without any clear lattice fringes but a very short-range ordered atomic arrangement at few locations with an interlayer *d*-spacing of 0.2 nm which could be attributed to the (210) plane of Co₂B. The observed crystalline plane could be embedded within the diffused amorphous phase as confirmed with the P-XRD pattern which showed the presence of amorphous Co₂B [Figures 6-2(d-e)]. The ratio of Co:B in Co₂B (1:8) was then estimated from the EDS analysis tabulated in Table 6-1, which came out to be 1.83:1 with around 26.07 at.% of boron and 47.76 at.% of cobalt with rest oxygen. XPS was also utilized to find the Co:B ratio which presented the final composition to be Co_{2.3}B_{1.0} \approx Co₂B. MP-AES analysis further deep rooted the formation of Co₂B phase by giving a 79.1% cobalt and 10.5% of boron in the catalyst which described the existence of Co₂B as a major phase in Co₂B (1:8) catalyst with minimal trace impurities.

Table 6-1. EDS Composition analysis (at.%) for Co₂B (1:8).

Catalyst	Cobalt	Boron	Oxygen
Co ₂ B (1:8)	47.76	26.07	26.17

Thereafter, the BET surface area investigations were accomplished for all the catalysts in this study which represented a type IV curve in N₂ adsorption-desorption isotherm with a hysteresis loop which confirmed the presence of mesopores in the synthesized catalysts. A high surface area of 103 m² g⁻¹ was obtained for Co₂B (1:8) which was higher than other variants i.e. 73.2 m² g⁻¹ for Co₂B (1:4)

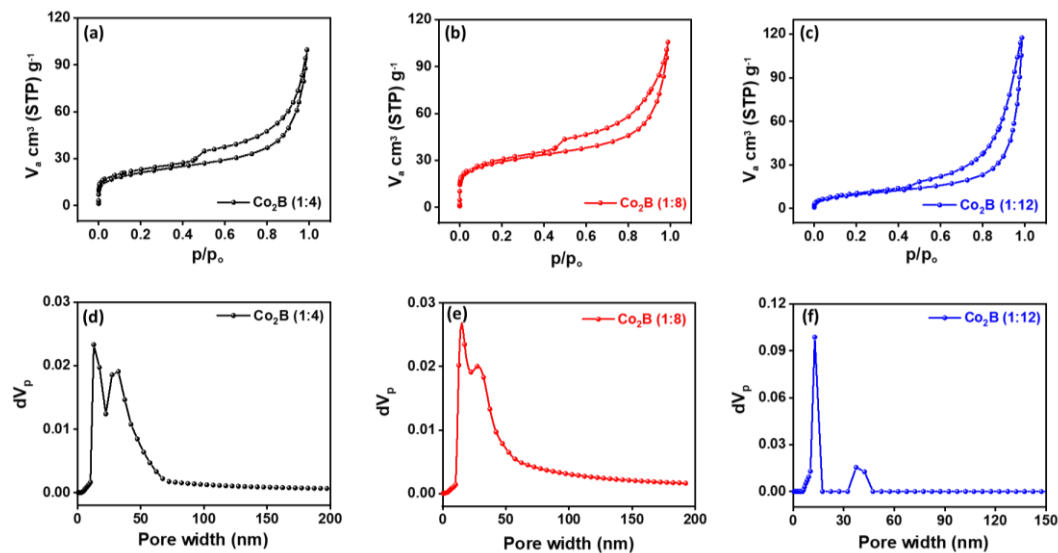


Figure 6-3. (a)-(c) N₂ adsorption/desorption isotherms and (d)-(f) Pore size distribution for Co₂B catalysts respectively.

and 34.1 m² g⁻¹ for Co₂B (1:12) and hence would provide active sites for reactant adsorption during NRR (Figure 6-3). To further understand the chemical state of Co and B in Co₂B (1:8) catalyst, XPS analysis was performed where the Co 2p deconvoluted XP spectrum showed two distinct peaks at 779.07 and 795.4 eV with additional satellite peaks at 785.1 eV and 801.7 eV corresponding to Co 2p_{3/2} and Co 2p_{1/2} respectively (Figure 6-4a). The peaks displayed at 778.5 and 795 eV were ascribed to the formation of metal-boride. The interaction of boron with cobalt was ascertained by the peak observed at 188.6 eV in B 1s deconvoluted XP spectrum of Co₂B (1:8) catalyst (Figure 6-4b), which was found to be shifted towards the higher binding energy by 1.6 eV than elementary boron (187 eV). This positive shift could be allocated to the electron transfer from B atom to vacant *d*-orbital of Co metal. The presence of another peak at 191.5 eV was witnessed due to existence of boron-oxo (B-O) species as a characteristic of amorphous metal-borides when exposed to atmosphere. These outcomes revealed the oxidation of boron species and indicated the oxidation of Co₂B nanoparticles to a certain degree with Co₂B as the bulk phase. The formation of boron oxide was quite expected as the work-up

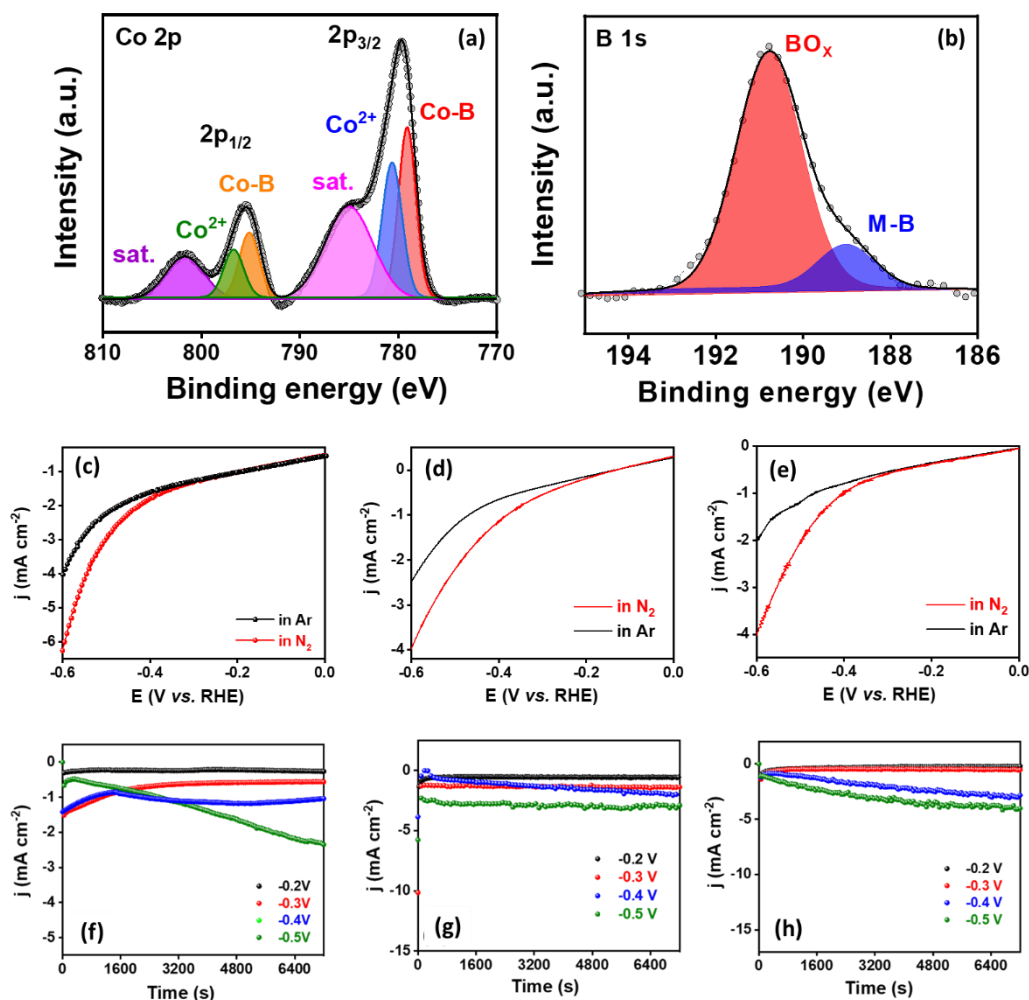


Figure 6-4. XPS deconvoluted (a) Co 2p and (b) B 1s spectrum for Co₂B (1:8) catalyst. Linear sweep voltammograms for (c) Co₂B (1:8), (d) Co₂B (1:4) and (e) Co₂B (1:12) in Ar- and N₂-saturated 0.1 M KOH. Chronoamperometric curves recorded at different potentials for (f) Co₂B (1:4), (g) Co₂B (1:8) and (h) Co₂B (1:12) during NRR.

(filtering and washing) of prepared catalyst was performed under atmospheric conditions. This BO₂⁻ species might have been appeared due to the self-hydrolysis of the non-stabilized NaBH₄. The commercial bulk Co_xB sample also showed the peaks related to boride as well as borate/oxidized boron.

6-3.2 Electrochemical dinitrogen reduction (NRR): To comprehend the electrocatalytic ability of the designed catalysts concerning NRR, linear sweep

voltammetry was acquired preliminarily in Ar and N₂-saturated 0.1 M KOH electrolyte. The gas-supplies were cleansed as explained previously prior any NRR measurement. A sharp increase in reduction current density in presence of N₂ in the electrolyte than in Ar-saturated conditions, affirmed the activity of all Co₂B catalysts towards NRR [Figures 6-4(c-e)]. The higher current density suggested the superior activity of Co₂B (1:8) catalyst to reduce N₂ to NH₃ over other catalytic variants. The chronoamperometry (CA) analyses were acquired for 2 h at different potentials for Co₂B catalysts followed by quantification of the electrolyte samples collected from the cathodic chamber [Figures 6-4(f-h)]. As displayed in Figure 6-5a, the highest F.E. of 20.45% and NH₃ yield rate of 2.9 mg h⁻¹ mg_{cat.}⁻¹ was realized for Co₂B(1:8) after 2 h of electrolysis at -0.3 V vs. RHE respectively with a high TOF value of 0.74 h⁻¹. The formation of NH₃ was further evidenced by presence of peak at 1455 cm⁻¹ in FT-IR spectrum of the electrolyte sample acquired after NRR

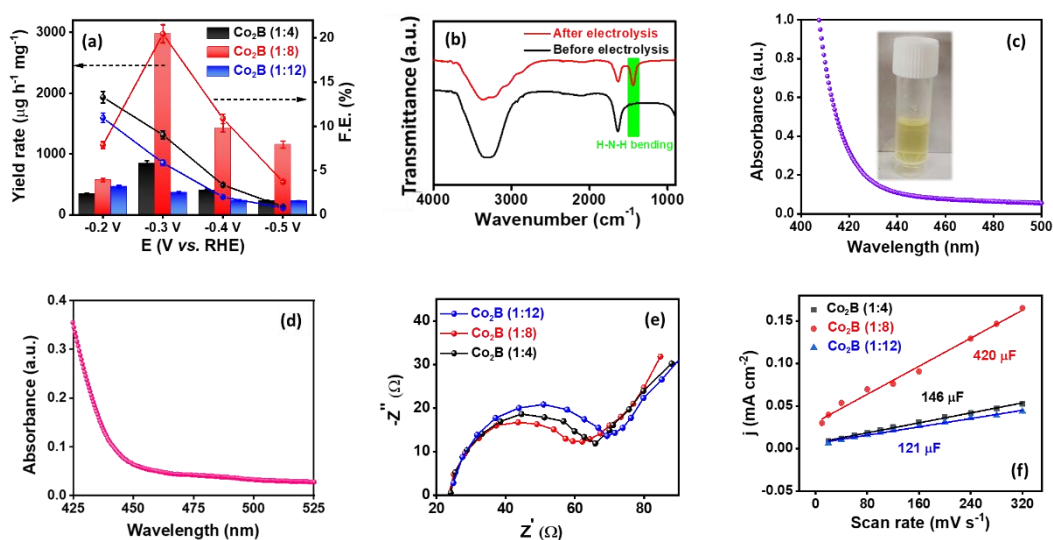


Figure 6-5. (a) Comparison of yield rates and F.E. of Co₂B catalysts at different applied potentials, (b) FT-IR spectra comparison of electrolyte samples obtained before and after NRR by Co₂B (1:8). (c) UV Vis. absorbance curve for solution collected after 2 h electrolysis by Co₂B (1:8) in N₂-saturated 0.1 M KOH during Nessler's test. (d) UV-Vis curve for electrolyte sample collected after NRR by Co₂B (1:8) at -0.3 V upon quantification with Watt-Chrisp method. (e) Nyquist plots acquired for Co₂B catalysts. (f) Scan rate vs. current density plots showing C_{dl} values of Co₂B catalysts.

by Co₂B (1:8) which correspond to the NH stretching. The same was found to be absent before NRR (Figure 6-5b). The NH₃ yield rate calculated from Indophenol blue method was also validated by quantifying the electrolyte sample with Nessler's reagent test (Figure 6-5c), in which almost similar yield rates were observed (2.98 and 2.35 mg h⁻¹ mg_{cat}⁻¹ via Indophenol blue and Nessler's test respectively). Other possible N₂ reduction product namely N₂H₄ was found to be absent after 2 h of NRR, and pointed towards the selective ammonia production (Figure 6-5d). As expected, an inferior NRR activity was attained for Co₂B (1:4) and Co₂B (1:12) catalysts with a F.E. and yield rate of 9.03 & 5.86% and 844.78 & 363.72 µg h⁻¹ mg_{cat}⁻¹ respectively. The superior performance of Co₂B (1:8) was allied with the accelerated interfacial charge transfer process at electrode-electrolyte interface which could be due to the presence of strong M-B bond and exposure of higher electrochemically active sites. The Nyquist plots acquired after EIS measurements (Figure 6-5e) revealed the semicircular behavior of all Co₂B catalysts, with the lowest charge transfer resistance (R_{ct}) of 35.85 Ω for Co₂B (1:8) catalyst than Co₂B (1:4) and Co₂B (1:12) with R_{ct} of 42.27 and 44.81 respectively. On the other hand, the high C_{dl} and ECSA value of 420 µF and 10.5 cm² obtained for Co₂B (1:8) as compared to other variants indicated the increased number of exposed active sites for NRR. This could be related with the high surface area of Co₂B (1:8) catalyst originated due to the inter-sheet space and intra-sheet holes leading to a slit-shaped porosity (Figure 6-5f and Table 6-2).

The synthesized porous Co₂B (1:8) nanosheets were extremely hydrophobic when compared with other variants owing to the 'Lotus effect' caused by the surface nanostructuring which influenced the electrocatalytic activity of the catalyst

Table 6-2. Values of C_{dl} , ECSA and roughness factor for Co₂B catalysts

Catalyst	C_{dl} (µF)	ECSA (cm ²)	Roughness factor (a.u.)
Co ₂ B (1:4)	146	3.65	116.24
Co ₂ B (1:8)	420	10.5	334.39
Co ₂ B (1:12)	121	3.025	96.33

towards NRR. The water contact angle images showed in Figures 6-6(a-c) revealed a contact angle of 115° for Co_2B (1:8) which was way too higher than contact angle of 105° and 96.5° for Co_2B (1:4) and Co_2B (1:12) respectively, and subsequently the increased surface hydrophobicity of Co_2B (1:8). This increased hydrophobicity could effectually reduce the accessibility for H_2O molecules (H^+ donor) and thus suppress HER while preferentially adsorbing N_2 molecule. This was further substantiated by performing CA under switching gas-supplies (Ar and N_2) which displayed a rapid increase in current density in presence of N_2 and immediate decrease in current density in presence of Ar (Figure 6-6d). Besides, the negligible NH_3 production in Ar-saturated conditions indicated the inactivity towards NRR which could be retained after saturating the electrolyte with N_2 gas(Figure 6-6e). Other control measurements viz. at OCP, in Ar and over bare electrode at -0.3 V further revealed that the NH_3 produced after NRR was exclusively due to the N_2 purged into the solution (Figure 6-6f). The high

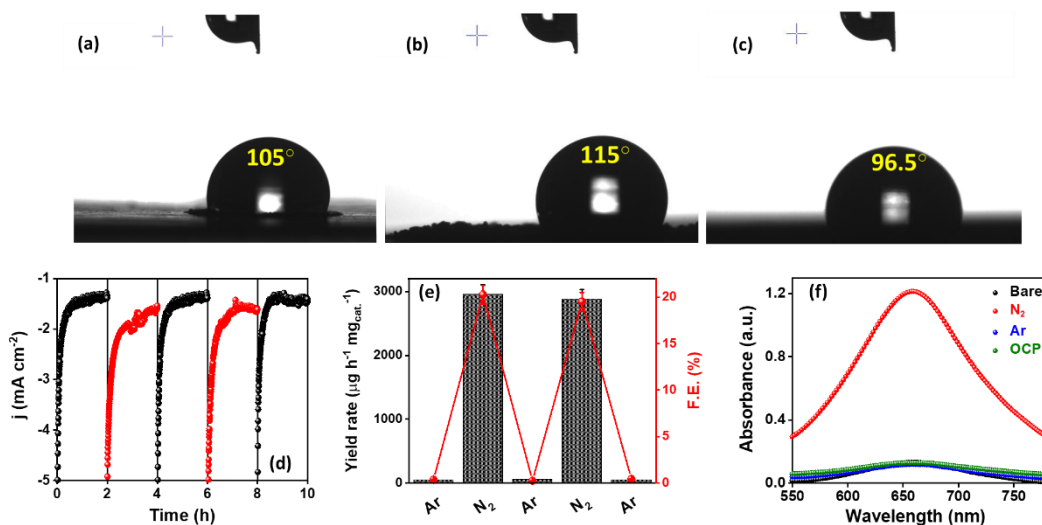


Figure 6-6. Water contact angle images of (a) Co_2B (1:4), (b) Co_2B (1:8) and (c) Co_2B (1:12) respectively. (d) Chronoamperometric curves obtained for Co_2B (1:8) at -0.3 V vs. RHE in switching gas feed environments. (e) F.E. and yield rates obtained during NRR under switching gas-feed (Ar/ N_2) environments (Ar: black, N_2 : red). (f) Absorbance curves obtained for Co_2B (1:8) after quantification during control experiments in Ar-saturated electrolyte, bare electrode and at open circuit potential.

ammonia yield rate obtained after NRR by Co₂B (1:8) catalyst prompted us to conduct ¹⁵N₂ isotopic labelling experiments by executing CA at -0.3 V for 2 h (where max. ammonia production was witnessed) followed by the quantification of ¹⁵NH₄⁺/¹⁴NH₄⁺ yield rates by NMR spectroscopy, colorimetry and LC-MS techniques. The ¹H-NMR spectrum represented in Figure 6-7a matched well with the standard NH couplings and thus confirmed that the ammonia production was due to reduction of N₂ purged into the electrolyte solution and not from the N-labile impurities. The ammonia yield rates were also quantified during isotope labelling measurements at different time intervals and were found out to be 1.87 (1 h) & 2.94 mg h⁻¹ mg_{cat.}⁻¹ (2 h) for ¹⁴NH₄⁺ while 1.8 (1 h) & 2.93 mg h⁻¹ mg_{cat.}⁻¹ (2 h) for ¹⁵NH₄⁺ in that order [Figures 6-7(b-c)]. These yield rates were in accordance with those obtained from Indophenol blue as well as LC-MS methods and thus validated the reported NH₃ yield rate by Co₂B (1:8) catalyst (Figure 6-7d and Table 6-3). In addition, the stability of the Co₂B (1:8) was also assessed after long-term NRR experiments by conducting CA at -0.3 V (*vs.* RHE) for continuous 10 h. An insignificant change in current density was perceived even after 10 h of NRR (Figure 6-7e) along with the retention NRR performance in terms of F.E. as well as ammonia production yield rate (Figure 6-7f). These results assisted the high durability of Co₂B in due course of NRR.

Table 6-3. Comparison of NH₃ yield rates obtained after NRR isotope labelling experiments by Co₂B (1:8) catalyst via different quantification methods.

Quantification method	¹⁴ NH ₄ ⁺ yield rate (mg h ⁻¹ mg _{cat.} ⁻¹)	¹⁵ NH ₄ ⁺ yield rate (mg h ⁻¹ mg _{cat.} ⁻¹)
Indophenol blue	2.94	2.93
¹ H-NMR spectroscopy	2.94	2.93
Liquid chromatography-mass spectroscopy	2.98	2.95

Later the structural stability of catalyst was also studied by utilizing *ex-situ* techniques like FE-SEM and EDS dot mapping. The porous nanosheet like morphology was reserved even after 10 h of NRR with well-distributed boron and

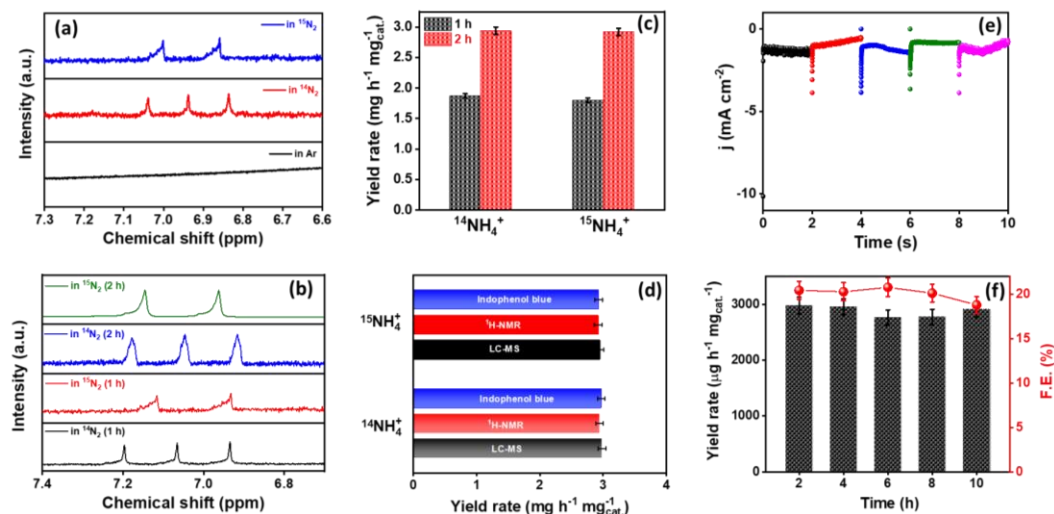


Figure 6-7. ¹H-NMR spectrum acquired after 2 h isotope labelling NRR experiment by Co₂B (1:8) under different gas-supply (Ar/¹⁴N₂/¹⁵N₂) saturated electrolyte solutions, (b) for different time intervals and (c) corresponding yield rate calculated from the same. (d) Bar diagram comparison of ¹⁴NH₄⁺ & ¹⁵NH₄⁺ yield rates obtained by different quantification methods. (e) Chronoamperometric curves obtained for Co₂B (1:8) at -0.3 V vs. RHE for 10 h and (f) F.E. and NH₃ yield obtained after chronoamperometry tests performed for 10 h under N₂-saturated 0.1 M KOH for Co₂B (1:8).

cobalt over the entire scanned area in EDS dot mapping analysis as showed in Figures 6-8(a-e). These outcomes were evident of the remarkable NRR activity of the catalyst.

6-3.3 Theoretical investigations for NRR: The major contributor towards NRR activity was scrutinized by performing systematic electronic structure calculations along with the framework of density functional theory (DFT) formalism. As a matter of interest, we didn't come across the formation of N₂H₄ during NRR, due to which the the associative distal pathway was considered as a probable NRR pathway by Co₂B. The adsorption free energies for seven intermediates (N₂^{*}, N₂H^{*}, N₂H₂^{*}, N^{*}, NH^{*}, NH₂^{*}, and NH₃^{*}) corresponding to both Co (Fig. 6-9a) and B site(Figure 6-9b) of the catalytic Co₂B surface were determined. The free energy diagrams of N₂ reduction over Co and B individually predicted Co to be more favorable site for NRR than B in Co₂B, which could be due to the greater electron

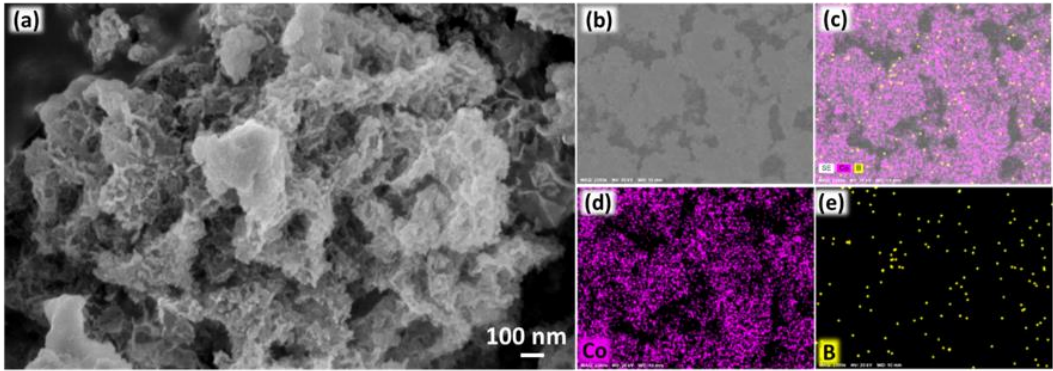


Figure 6-8 (a) FE-SEM image and (b-e) EDS dot mapping showing presence of both Co and B for Co₂B (1:8) after stability test for NRR.

affinity of Co than B. The Gibbs adsorption free energy (ΔG) were generated at different electrode potentials (0V and -0.3 V) as tabulated in Tables 6-4 and 5 where the adsorption energy could be given as:

$$E_{ad} = E_{sub+ads} - E_{sub} - E_{ads} \quad (6.4)$$

Here in, $E_{sub+ads}$ is the total energy of the optimized structure, E_{sub} is the energy of the catalyst, and E_{ads} is the energy of the adsorbate. Gibbs free energy could further be determined as:

$$\Delta G = E_{ad} + \Delta ZPE - T\Delta S + \Delta G_U \quad (6.5)$$

Where E_{ad} is the adsorption energy of intermediates, ΔZPE is the difference in the zero point energy between adsorbed state and gas phase, $T\Delta S$ gives entropic

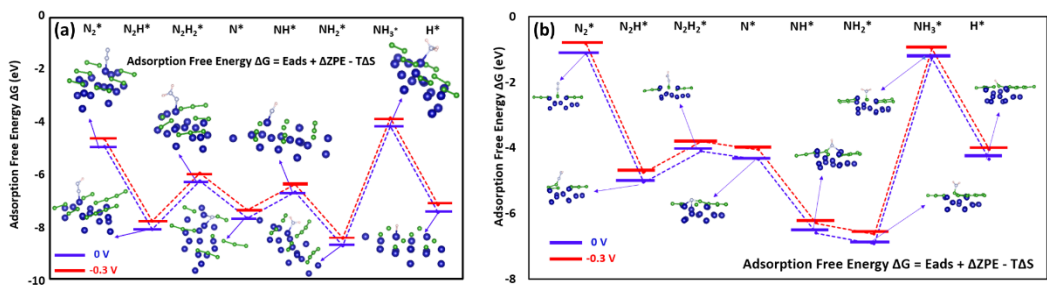


Figure 6-9. (a) Free energy diagrams of NRR distal pathway on Co₂B surface (Co active site) at applied potentials of 0 and -0.3 V and H⁺ adsorption at identical potentials and (b) Reaction coordinate corresponding to N₂ reduction to NH₃ on B site of Co₂B catalyst surface.

contribution, ΔG_U is the free energy contribution related to applied external potential. Figure 6-9a demonstrated the free energy plot for NRR at Co active site of Co₂B surface at different applied potentials of 0 and -0.3 V vs. RHE. Under thermoneutral conditions ($\Delta G \sim 0.0$ eV), the catalyst with an adsorption free energy value close to zero must deliver facilitated reaction rate due to lowered activation barrier. The $\Delta G_{N_2^*}$ value over Co₂B surface was found out to be -4.93 eV at 0 V which braced the high activity of catalyst at -0.3 V with a lower $\Delta G_{N_2^*}$ value of -4.63 eV. Further the free energy diagram depicted the NRR mechanism to proceed via end-on adsorption of N₂ molecule over Co active site as a first step with an adsorption energy of -4.63 eV at -0.3 V. Subsequently, the adsorbed N₂^{*} underwent first hydrogenation step (H⁺/e⁻) to form N₂H^{*} with a downhill in the corresponding free energy profile by -7.74 eV. In the second hydrogenation step, *i.e.* the N₂H^{*} intermediate captured another H⁺+e⁻ pair to form N₂H₂^{*} with an uphill Gibbs free energy change of 1.81 eV (rate limiting step). Then the third hydrogenation step continued with the formation of N^{*} + NH₃ to release first NH₃ molecule following an exothermic pathway with a free energy change of -1.39 eV.

Successful hydrogenation of remaining adsorbed N^{*} took place with corresponding free energy changes of 0.98, -2.03 and 4.51 eV to form NH^{*}, NH₂^{*} and NH₃^{*}

Table 6-4. Adsorption free energy values calculated from DFT model for NRR over “Co” in Co₂B (1:8) catalyst.

Structure	E _{surface + adsorbate} (eV)	E _{Surface} (eV)	E _{adsorbate} (eV)	E _{adsorption energy} (eV)	ΔG Free energy (eV) @ 0 V	ΔG Free energy (eV) @ -0.3 V
N ₂ [*] on Co	-166.206473	-145.05757	-16.657685	-4.4912184	-4.9322184	-4.6322184
N ₂ H [*] on Co	-171.4847209	-145.05757	-18.017425	-8.4097255	-8.0487255	-7.7487255
N ₂ H ₂ [*] on Co	-172.6671155	-145.05757	-21.084547	-6.5249982	-6.2349982	-5.9349982
N [*] on Co	-160.8272799	-145.05757	-8.3288429	-7.4408675	-7.6218675	-7.3218675
NH [*] on Co	-159.9010614	-145.05757	-8.1026962	-6.7407957	-6.64779574	-6.34779574
NH ₂ [*] on Co	-167.6530729	-145.05757	-13.525779	-9.0697238	-8.67172382	-8.37172382
NH ₃ [*] on Co	-169.5893949	-145.05757	-19.533373	-4.99845196	-4.16145196	-3.86145196
H [*] on Co	-156.1036094	-145.05757	-3.3852118	-7.660828035	-7.42082803	-7.12082803

Table 6-5. Adsorption free energy values calculated from DFT model for NRR over “B” in Co₂B (1:8) catalyst.

Structure	E _{surface + adsorbate} (eV)	E _{Surface} (eV)	E _{adsorbate} (eV)	E _{adsorption} energy (eV)	ΔG _{Free energy} (eV) at 0 V	ΔG _{Free energy} (eV) at -0.3 V
N ₂ [*] on B	-162.410528	-145.05757	-16.657685	-0.6952734	-1.1362734	-0.8362734
N ₂ H [*] on B	-168.495766	-145.05757	-18.017425	-5.4207707	-5.0597707	-4.7597707
N ₂ H ₂ [*] on B	-170.536490	-145.05757	-21.084547	-4.3943734	-4.1043734	-3.8043734
N [*] on B	-157.563482	-145.05757	-8.3288429	-4.1770703	-4.3580703	-4.0580703
NH [*] on B	-159.854048	-145.05757	-8.1026962	-6.6937823	-6.6007823	-6.3007823
NH ₂ [*] on B	-165.919044	-145.05757	-13.525779	-7.3356955	-6.9376955	-6.6376955
NH ₃ [*] on B	-166.713559	-145.05757	-19.533373	-2.1226165	-1.2856165	-0.9856165
H ⁺ on B	-153.040994	-145.05757	-3.3852118	-4.5982128	-4.3582128	-4.0582128

respectively followed by the release of second NH₃ molecule. Besides, the adsorption free energy of hydrogen (H^{*}) was also calculated to get deep insights into hydrogen evolution over Co₂B surface. Under thermoneutral conditions, the optimal catalysts should not attain an adsorption free energy close to zero for H⁺ adsorption. The adsorption free energy corresponding to N₂ was -4.63 eV at -0.3

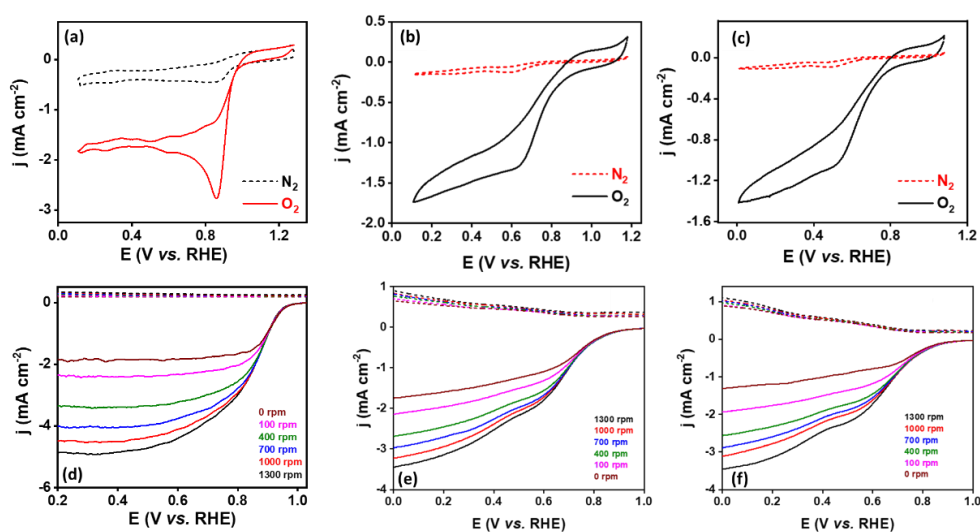


Figure 6-10. Cyclic voltammograms of (a) Co₂B (1:8), (b) Co₂B (1:4) and (c) Co₂B (1:12) for oxygen reduction activity in 0.1 M KOH at 25 mV s⁻¹. RRDE polarization curves of (d) Co₂B (1:8), (e) Co₂B (1:4) and (f) Co₂B (1:12) in presence of O₂ at varying rotation rates and at a scan rate of 5 mV s⁻¹.

V, whilst it turned out to be -7.12 eV for H^+ adsorption. This stimulated the availability of optimal active sites for NRR than HER over Co_2B catalyst surface under similar applied potential.

6-3.4 Oxygen bifunctional activity: After evaluating the NRR activity of catalysts, the oxygen bifunctional activity of Co_2B catalysts were also examined to recognize its capability to oblige as air-cathode in Zn-air battery. The ORR activity was analysed by means of CV in O_2 - and N_2 -saturated 0.1 M KOH electrolyte. The voltammograms showed in Figures 6-10(a-c) revealed the most positive reduction peak potential for Co_2B (1:8) at 0.97 V vs. RHE in presence of O_2 in the electrolyte. Afterwards, the reaction kinetics was gauged by performing RRDE experiments under hydrodynamic condition at different rotation rates between 0 to 1300 rpm [Figures 6-10(d-f)]. An exponential increase in current density was observed with an increase in rotation rate for all Co_2B catalysts to achieve a diffusion limited current density. A higher diffusion limited current density of -4.9 mA cm^{-2} , half-wave potential of 0.83 V and a lower ring current (pointing towards low H_2O_2

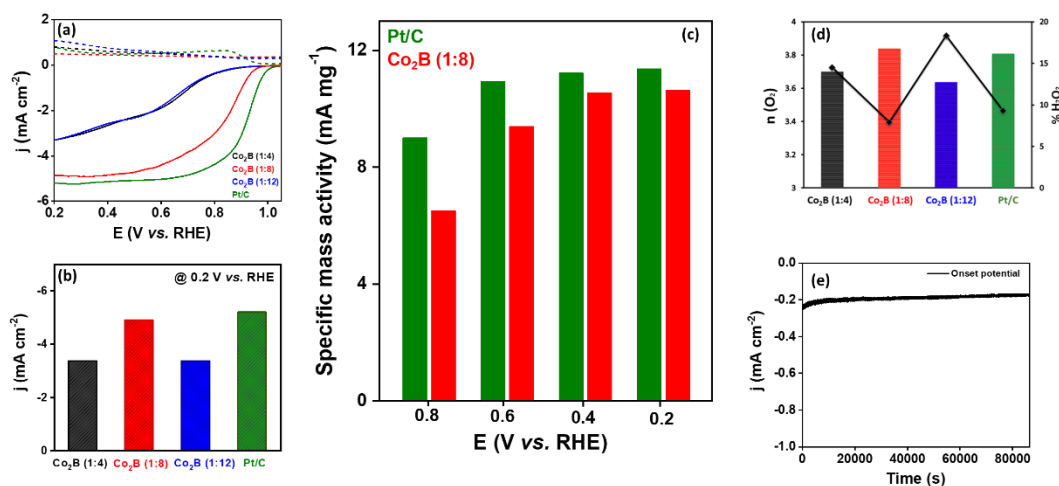


Figure 6-11. (a) Comparison of RRDE curves of Co_2B catalysts with state-of-art Pt/C catalyst. (b) Bar diagram comparison for diffusion limited current density during ORR. (c) Comparison of specific mass activity for Pt/C and Co_2B (1:8) at different potentials. (d) Bar diagram comparison of no. of electrons and H_2O_2 produced by catalysts @ 0.2 V. (e) Bar diagram comparison of no. of electrons and H_2O_2 produced by catalysts @ 0.2 V.

production) was achieved by Co₂B (1:8) catalyst at 1300 rpm with an onset potential of 0.98 V respectively, which was better than other catalyst variants (Table 6-6). Further upon comparison with state-of-art Pt/C catalyst with similar loading, almost equivalent ORR activity was witnessed in terms of onset potential, diffusion limited current density and specific mass activity [Figures 6-11(a-c)]. The Co₂B (1:8) catalyst demonstrated its ability to follow a direct 4e⁻ pathway during ORR to reduce oxygen to water as final product, upon quantification of peroxide and number of electrons transferred from RRDE curves [Figure 6-11d and Table 6-7]. At last, CA was executed at an onset potential of ORR by Co₂B (1:8) for 24 h which disclosed a constant current response, as displayed in Figure 6-11e. These conclusions authenticated the competence of Co₂B (1:8) to reduce

Table 6-6. ORR performance comparison of Co₂B catalysts in O₂-saturated 0.1 M KOH electrolyte solution.

Catalyst	Onset potential@-0.1 mA cm ⁻²	Half wave potential	Current density (at 0.2 V)
Co ₂ B (1:4)	0.89 V	0.69 V	-3.37 mA cm ⁻²
Co ₂ B (1:8)	0.98 V	0.83 V	-4.9 mA cm ⁻²
Co ₂ B (1:12)	0.86 V	0.66 V	-3.38 mA cm ⁻²

Table 6-7. Total number of electrons transferred and simultaneous H₂O₂ production during ORR by Co₂B catalysts.

Catalyst	no. of electrons transferred (n)				H ₂ O ₂ (%)			
	0 V	0.2 V	0.4 V	0.6 V	0 V	0.2 V	0.4 V	0.6 V
Co ₂ B (1:4)	3.6	3.7	3.71	2.892	20.19	14.51	14.07	55.38
Co ₂ B (1:8)	3.83	3.841	3.843	3.86	8.42	7.91	7.76	6.81
Co ₂ B (1:12)	3.63	3.637	3.65	3.71	18.34	18.35	17.02	14.4

O₂ to H₂O with enriched activity and stability, which is crucial for practical bids. Then the activity of Co₂B catalysts were determined for oxygen evolution for which we carried out LSV in 0.1 KOH electrolyte at a scan rate of 5 mV s⁻¹. As expected, Co₂B (1:8) also revealed a superior OER performance than other two parallel catalysts and even the benchmark RuO₂ catalyst (Figure 6-12a). The O₂ evolution started at 1.5 V over Co₂B (1:8) surface and became sturdy as the potential scan towards anodic potentials and achieved 100 mA cm⁻² at just 1.6 V (vs. RHE). A low overpotential (η) of 290 mV was required by Co₂B (1:8) to achieve 10 mA cm⁻² of current density that was lower than Co₂B (1:4) and Co₂B (1:12) with η value of 360 and 300 mV respectively (Table 6-8). This higher activity towards OER was attributed to the strain originated in Co₂B due to chemical hybridization of B 2p and Co vacant 3d-orbitals which could reduce the activation energy barrier for Co oxidation. This strong hybridization was reinforced by existence of M-B bond in B 1s deconvoluted XP spectra of Co₂B (1:8)

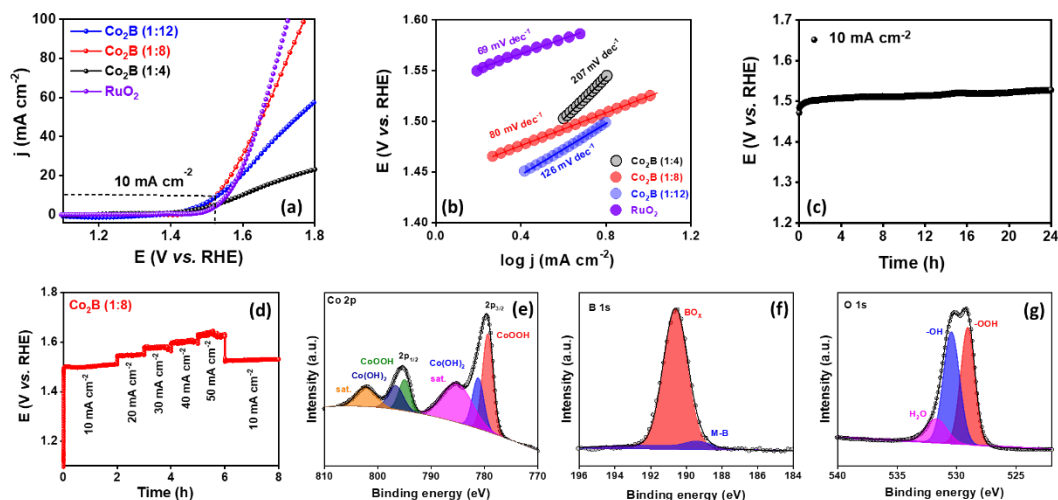


Figure 6-12. (a) LSV polarization curves during OER for variants of Co₂B and benchmark RuO₂ catalyst at 10 mV s⁻¹, (b) Tafel plots derived from LSV curves for different catalysts during OER. (c) Stability tests performed for Co₂B (1:8) for 24 h at 10 mA cm⁻² current density during OER and (d) Sequential chronopotentiometry performed at different current densities between 10-50 mA cm⁻² for Co₂B (1:8). XP deconvoluted (e) Co 2p, (f) B 1s and (g) O 1s spectrum of Co₂B (1:8) after OER stability tests.

which expedited the formation of OOH* intermediate and consecutively OER (M-OH/M-OOH species being an active site). The lower Tafel slope of the Co₂B (1:8) further supported the accelerated OER kinetics, which was found to be least when compared with other catalysts (Figure 6-12b). After the evaluation of OER activity by Co₂B (1:8) catalyst, the chronopotentiometric stability test were also acquired which didn't show any appreciable change in overpotential required to attain 10 mA cm⁻² even after 24 h of electrolysis (Figure 6-12c). Even upon changing the current densities from 10 to 50 mA cm⁻² a continuous increase in cell potential was observed with rapid stabilization, whilst the cell potential restored back when the applied current density came back to 10 from 50 mA cm⁻², specifying the remarkable durability of catalyst (Figure 6-12d).

Table 6-8. OER performance comparison of Co₂B catalysts in 0.1 M KOH electrolyte solution.

Catalyst	Overpotential (η at 10 mA cm ⁻²)	Current density (at 1.75 V vs. RHE)	Tafel slope (mV dec ⁻¹)
Co ₂ B (1:4)	350 mV	20 mA cm ⁻²	207
Co ₂ B (1:8)	290 mV	92.5 mA cm ⁻²	80
Co ₂ B (1:12)	300 mV	51 mA cm ⁻²	126

The actual active site for OER after stability measurements was inspected by XPS analysis [Figures 6-12(e-g)], which discovered the formation of Co-OOH species at 779.1 eV in Co 2p XP spectra. The deconvoluted B 1s XP spectra showed in Figure 6-12f presents the peak related to boron-oxo species (B-O), but the intensity of B peak related to boride was found out to be diminished presumably due to the shielding of catalyst surface by oxyhydroxide layer after OER. The B-O species could either stick onto the catalyst surface or dissolve in the electrolyte and further create pores to increase active sites during OER. During OER in alkaline electrolyte, either Co-OOH or B-O species could aid as active site. In one case, Co-

OOH may serve as major active site whilst borate may modulate the adsorption energies of reaction intermediates. While the other case could be the improved electron transfer between partially oxidized metal oxyhydroxide and current collector due to active non-oxidized metal boride centers. Hence, the remarkable electrocatalytic activity of Co₂B (1:8) towards both OER and ORR manifested it as an enormously proficient oxygen bifunctional catalyst. The oxygen polarization curves in Figure 6-13a represent the oxygen bifunctional activity of different catalysts and benchmark catalysts from which the potential gap, ΔE ($\Delta E = E_{@10 \text{ mA cm}^{-2}} - E_{1/2@ORR}$) value was calculated using the potential values amid OER (10 mA cm^{-2}) and ORR (half-wave potential). The Co₂B (1:8) catalyst presented a lower ΔE value of 0.69 V which approved the superior oxygen bifunctional activity than 0.89 V for (1:4) and 0.87 V for (1:12) ratio of Co₂B. The potential gap obtained for Co₂B (1:8) was even lower than those of obtained for benchmark catalysts, particularly, 0.73 V for Pt/C and 0.75 V RuO₂ respectively (Fig. 6-13b). The practical application of the outstanding oxygen bifunctional Co₂B (1:8) catalyst towards energy storage devices was appraised by assembling a homemade Zn–air

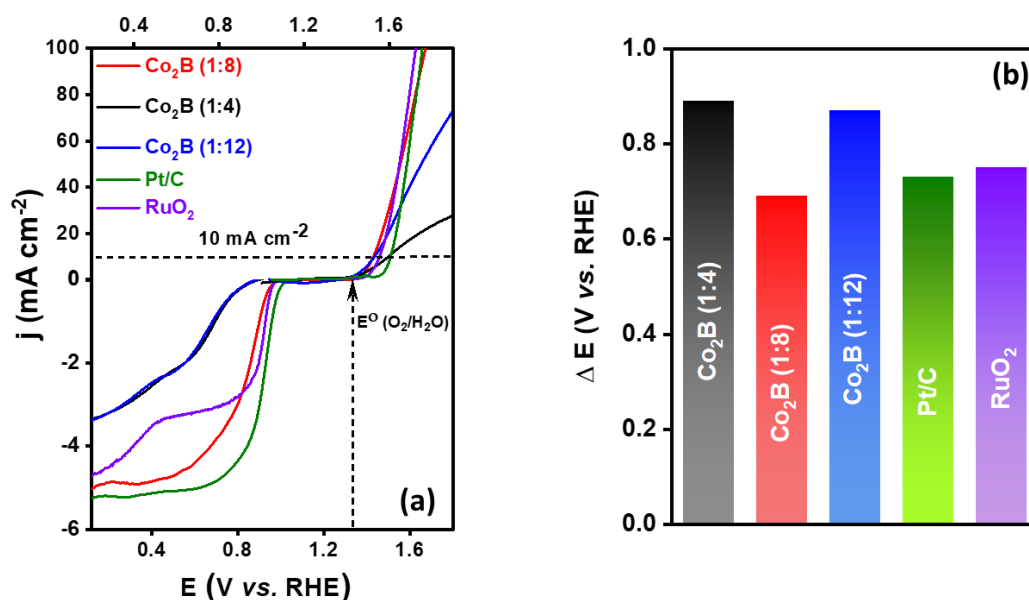


Figure 6-13. (a) Oxygen bifunctional activity of Co₂B catalysts and commercial benchmark catalysts and (b) comparison of potential gap for Zn-air battery.

battery employed with Co₂B (1:8) air-cathode, Zn foil anode, Whatmann separator and 6 M KOH + 0.2 M zinc acetate electrolyte. A high open circuit voltage of 1.45 V was perceived for the as-assembled battery that is almost similar to the OCP achieved by Pt/C + RuO₂ air cathode (1.48 V) with a similar mass loading of 2 mg cm⁻² (Figure 6-14a). More interestingly, the peak power density of Co₂B (1:8) equipped battery came out to be 500 mW cm⁻² which was way too higher than 200 mW cm⁻² obtained for Pt/C+RuO₂ equipped battery (Figure 6-14b). The Co₂B (1:8) air cathode also showed a small charge-discharge potential gap of 0.69 V than Pt/C+RuO₂ with a potential gap of 0.73 V (Figure 6-14c). Moreover, a stable response was observed for Co₂B (1:8) during discharge at 10 mA cm⁻² with a cell voltage of 1.27 V [Figures 6-14(d-e)] and a high specific capacity (889 mA h g⁻¹) and energy density (1078 W h kg⁻¹) than Pt/C + RuO₂ (748 mA h g⁻¹ and 860 Wh kg⁻¹, normalized w.r.t mass of lost zinc). The durability of the proposed Co₂B (1:8)

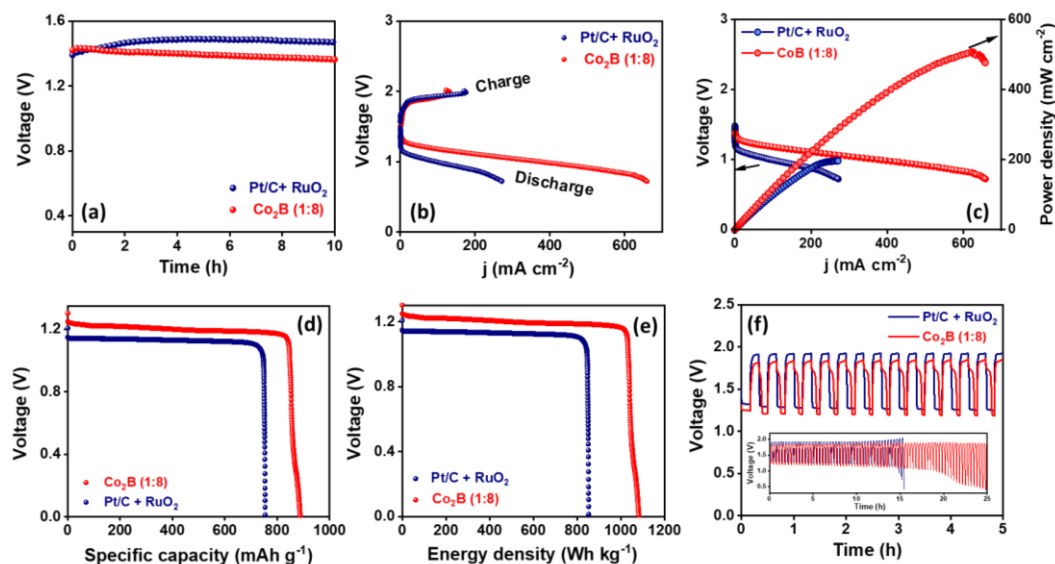


Figure 6-14. (a) Open circuit voltage, (b) charge-discharge polarization curves, (c) power density plots extracted from discharge polarization curve for Zn- air battery assembled using Co₂B (1:8) and Pt/C as air cathode respectively. (d) Corresponding specific capacity and (e) energy density curves obtained at 10 mA cm⁻². (f) Galvanostatic charge-discharge cycling stability curves for Co₂B (1:8) and Pt/C+RuO₂ at 10 mA cm⁻² current density (10 min. charging - 10 min. discharging).

air cathode was depicted by galvanostatic charge-discharge cycling of the battery at 10 mA cm^{-2} , which demonstrated an initial potential gap of 0.61 V which increased to 0.75 V for 17 h with each cycle having 10 min discharging and 10 min charging (Figure 6-14f). On the other hand, Pt/C + RuO₂ underwent severe degradation in potential gap (from 0.63 V to 1.6 V) within 45 cycles (15 h), most probably due to Ostwald ripening and carbon corrosion leading to the aggregation of noble metals. Further, the practicality of the intended battery was demonstrated by its ability to power a red LED (2.0 V) by connecting two Zn-air batteries in series (Figure 6-15a).

6-3.5 Self-powered ammonia synthesis: The primary target of designing a trifunctional catalyst was accomplished by powering the two electrode ammonia

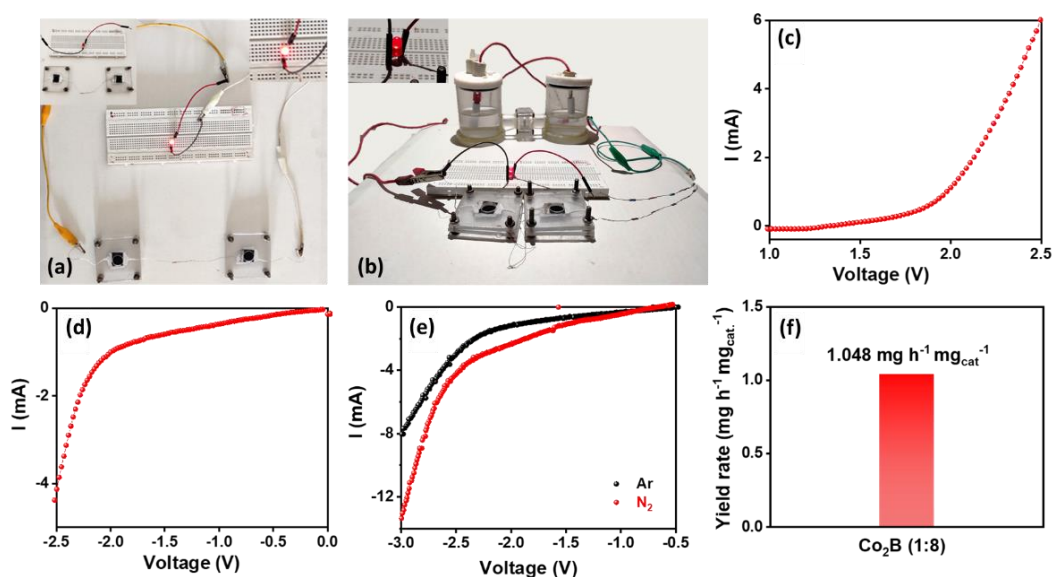


Figure 6-15. (a) Zn-air battery equipped with Co₂B (1:8) air cathode assembled in series to light a red LED of 2.0 V (Inset (left): no connection with battery; (right): lightened LED). (b) Photograph of Zn- air battery powered NRR full cell setup (Air cathode in battery: Co₂B (1:8); cathode and anode in NRR full cell: Co₂B (1:8)). LSV acquired under full-cell conditions for overall NH₃ synthesis (c) anodic sweep, (d) cathodic sweep, showing bifunctional activity of Co₂B (1:8) catalyst towards OER at anode and NRR at cathode. (e) LSV for full-cell equipped with Co₂B (1:8) for NH₃ synthesis, (f) NH₃ yield produced after 2 h of electrolysis by battery powered NH₃ production cell setup.

synthesis device by as-assembled Zn-air batteries connected in series (Figure 6-15b). During the integration of two Zn-air batteries (approx. voltage ~ 2.9 V) with the full cell NH₃ synthesis device, a resistor (300 Ω) was used to limit the excessive current supply to the cell which maintained the efficiency of the device to achieve the maximum NH₃ production yield rate. Two-electrode NRR cell was constructed by employing Co₂B (1:8) as a bifunctional catalyst at both anode and cathode. The bifunctional activity of catalysts towards NRR and OER under full-cell conditions was affirmed thru LSV. A steep increase in current density at 1.6 V witnessed in LSV curve showed in Figures 6-15(c-d) signified the onset potential of overall ammonia synthesis in full-cell. The increased current density in presence of N₂-saturated electrolyte than in Ar-saturated conditions further presented the successful nitrogen reduction to ammonia under applied potentials (Figure 6-15e). The 2 h electrolysis was then performed where in the full-cell NH₃ synthesis device was powered by two Zn-air batteries connected in series, which delivered an overall ammonia production rate of 1.05 mg h⁻¹ mg_{cat}⁻¹, as displayed in Figure 6-15f. These inferences defend the ability of the as-designed trifunctional Co₂B catalyst to be applied for self-powered ammonia synthesis. The outstanding trifunctional activity towards NRR/OER/ORR could possibly lead to a new pathway towards development of cost-effective catalysts for Zn- air battery and NH₃ synthesis and their implementation towards powering the ammonia production by sustainable and high power density rechargeable Zn- air batteries.

6-4 Summary

In summary, the synthesis of amorphous cobalt boride (Co₂B) catalyst was described in this work by the use of an environment friendly, reasonably priced plus less time consuming sonochemical method. A notable NRR activity in terms of high Faradaic efficiency as well as yield rate is realized which was ascribed to the strong M-B bond as well as the porous nanosheet morphology of Co₂B (1:8). Systematic DFT investigations were also carried out to analyse the NRR active site in Co₂B where in the Co acts was found to be the active site to adsorb and activate

strong N≡N triple bond and produce NH₃ via an associative distal pathway. When employed as a cathode catalyst for Zn- air battery, Co₂B (1:8) unveiled considerable oxygen bifunctional activity and endowed a reduced potential gap, enhanced reaction rate, and high stability. The assembled Zn- air battery was able to power NH₃ synthesis device with an appreciable NH₃ production yield of 1.05 mg h⁻¹ mg_{cat}⁻¹ after two continuous hours of electrolysis under full-cell configuration. Being inexpensive, synthesized via simplistic strategy and high trifunctional activity of Co₂B hold a great promise towards energy conversion and storage devices.

6-5 References

1. V. Kyriakou, I. Garagounis, A. Vourros, E. Vasileiou and M. Stoukides, *Joule*, 2020, **4**, 142-158.
2. M. Wang, M. A. Khan, I. Mohsin, J. Wicks, A. H. Ip, K. Z. Sumon, C.-T. Dinh, E. H. Sargent, I. D. Gates and M. G. Kibria, *Energy Environ. Sci.*, 2021, **14**, 2535-2548.
3. C. Smith, A. K. Hill and L. Torrente-Murciano, *Energy Environ. Sci.*, 2020, **13**, 331-344.
4. U. B. Shahid, K. Siddharth and M. Shao, *Curr. Opin. Electrochem.*, 2021, **30**, 100790.
5. H. Xu, K. Ithisuphalap, Y. Li, S. Mukherjee, J. Lattimer, G. Soloveichik and G. Wu, *Nano Energy*, 2020, **69**, 104469.
6. C. Zhao, S. Zhang, M. Han, X. Zhang, Y. Liu, W. Li, C. Chen, G. Wang, H. Zhang and H. Zhao, *ACS Energy Lett.*, 2019, **4**, 377-383.
7. G. Zhou, G. Liu, X. Liu, Q. Yu, H. Mao, Z. Xiao and L. Wang, *Adv. Funct. Mater.*, 2022, **32**, 2107608.
8. Q. Liu, Z. Pan, E. Wang, L. An and G. Sun, *Energy Storage Mater.*, 2020, **27**, 478-505.
9. Z. Zhao, X. Fan, J. Ding, W. Hu, C. Zhong and J. Lu, *ACS Energy Lett.*, 2019, **4**, 2259-2270.
10. X. Yang, K. Li, D. Cheng, W.-L. Pang, J. Lv, X. Chen, H.-Y. Zang, X.-L. Wu, H.-Q. Tan and Y.-H. Wang, *J. Mater. Chem. A*, 2018, **6**, 7762-7769.
11. G. Qing, R. Ghazfar, S. T. Jackowski, F. Habibzadeh, M. M. Ashtiani, C.-P. Chen, M. R. Smith III and T. W. Hamann, *Chem. Rev.*, 2020, **12**, 5437-5516.
12. N.-T. Suen, S.-F. Hung, Q. Quan, N. Zhang, Y.-J. Xu and H. M. Chen, *Chem. Soc. Rev.*, 2017, **46**, 337-365.
13. Z.-L. Wang, D. Xu, J.-J. Xu and X.-B. Zhang, *Chem. Soc. Rev.*, 2014, **43**, 7746-7786.
14. D. U. Lee, P. Xu, Z. P. Cano, A. G. Kashkooli, M. G. Park and Z. Chen, *J. Mater. Chem. A*, 2016, **4**, 7107-7134.
15. Y. Kong, Y. Li, B. Yang, Z. Li, Y. Yao, J. Lu, L. Lei, Z. Wen, M. Shao and Y. Hou, *J. Mater. Chem. A*, 2019, **7**, 26272-26278.
16. G. Fenya, L. Hongwei, Z. Mengzhe, X. Zhengqi, Z. Yueqing and L. Tingting, *Prog. Chem.*, 2020, **32**, 33.
17. K. Zeng, X. Zheng, C. Li, J. Yan, J. H. Tian, C. Jin, P. Strasser and R. Yang, *Adv. Funct. Mater.*, 2020, **30**, 2000503.
18. D. Liu, M. Chen, X. Du, H. Ai, K. H. Lo, S. Wang, S. Chen, G. Xing, X. Wang and H. Pan, *Adv. Funct. Mater.*, 2021, **31**, 2008983.

19. S. L. Foster, S. I. P. Bakovic, R. D. Duda, S. Maheshwari, R. D. Milton, S. D. Minteer, M. J. Janik, J. N. Renner and L. F. Greenlee, *Nat. Catal.*, 2018, **1**, 490-500.
20. X. Guo, H. Du, F. Qu and J. Li, *J. Mater. Chem. A*, 2019, **7**, 3531-3543.
21. Y. Sun, X. Liu, Y. Jiang, J. Li, J. Ding, W. Hu and C. Zhong, *J. Mater. Chem. A*, 2019, **7**, 18183-18208.
22. E. Marini, L. Jörissen and S. Brimaud, *J. Power Sources*, 2021, **482**, 228900.
23. S. Haller, V. Gridin, K. Hofmann, R. W. Stark, B. Albert and U. I. Kramm, *Energy Technol.*, 2021, **9**, 2001106.
24. Z. Lu, J. Wang, S. Huang, Y. Hou, Y. Li, Y. Zhao, S. Mu, J. Zhang and Y. Zhao, *Nano Energy*, 2017, **42**, 334-340.
25. S. Ghosh and R. N. Basu, *Nanoscale*, 2018, **10**, 11241-11280.
26. T. Meng, J. Qin, S. Wang, D. Zhao, B. Mao and M. Cao, *J. Mater. Chem. A*, 2017, **5**, 7001-7014.
27. J. Yang, X. Wang, B. Li, L. Ma, L. Shi, Y. Xiong and H. Xu, *Adv. Funct. Mater.*, 2017, **27**, 1606497.
28. Z. Pu, T. Liu, G. Zhang, X. Liu, M. A. Gauthier, Z. Chen and S. Sun, *Small Methods*, 2021, **5**, 2100699.
29. L. Yi, Z. Zeng, Y. Liao, Y. Tang, X. Li, N. Lv, Y. Xu, H. Li and Y. Wang, *Energy Fuels*, 2021.
30. R. K. Tripathy, A. K. Samantara and J. Behera, *Sustain. Energy Fuels*, 2021, **5**, 1184-1193.
31. S. Carenco, D. Portehault, C. Boissiere, N. Mezailles and C. Sanchez, *Chem. Rev.*, 2013, **113**, 7981-8065.
32. X. Ma, K. Zhao, Y. Sun, Y. Wang, F. Yan, X. Zhang and Y. Chen, *Catal. Sci. Technol.*, 2020, **10**, 2165-2172.
33. N. Xu, G. Cao, Z. Chen, Q. Kang, H. Dai and P. Wang, *J. Mater. Chem. A*, 2017, **5**, 12379-12384.
34. S. Gupta, M. K. Patel, A. Miotello and N. Patel, *Adv. Funct. Mater.*, 2020, **30**, 1906481.
35. V. Jose, J. M. V. Nsanzimana, H. Hu, J. Choi, X. Wang and J. M. Lee, *Adv. Energy Mater.*, 2021, **11**, 2100157.
36. Y. Xiao, C. Shen and T. Long, *Chem. Mater.*, 2021.
37. X. Guo, S. Lin, J. Gu, S. Zhang, Z. Chen and S. Huang, *Adv. Funct. Mater.*, 2021, **31**, 2008056.
38. G. Qin, Q. Cui, A. Du, W. Wang and Q. Sun, *ChemCatChem*, 2019, **11**, 2624-2633.
39. S. Qi, Y. Fan, L. Zhao, W. Li and M. Zhao, *Appl. Surf. Sci.*, 2021, **536**, 147742.
40. H. Zhang, S. Wang, H. Wang, B. Huang, S. Dong, Y. Dai and W. Wei, *Nanoscale*, 2021, **13**, 17331-17339.
41. H. Xu, B. W. Zeiger and K. S. Suslick, *Chem. Soc. Rev.*, 2013, **42**, 2555-2567.
42. B. Coşkun, A. Kantürk Figen and S. Pişkin, *J. Chem.*, 2014, **2014**.
43. Z. Li, T. Zhuang, J. Dong, L. Wang, J. Xia, H. Wang, X. Cui and Z. Wang, *Ultrason. Sonochem.*, 2021, **71**, 105384.

Chapter 7

Summary and future perspectives

7-1 Summary

With the aim of leading a sustainable life on mother earth, the development of the human race and its well-being, the three essential requirements are water, energy and food. Moreover, in an overpopulated country like India, food production and thus the fertilizer industry needs a boost of as high as 60-70% to feed the population by 2050. Ammonia (NH_3), being the starting point for production of nitrogen-based fertilisers, is an essential chemical to fulfil the food demands of a growing and global affluent population. But the bulk ammonia production via the Haber-Bosch process comes at a cost of earth's sustainability which accounts for 2% of global energy consumption, 20% of industrial natural gas demand, 5% of industrial coal demand and more than 2-3% of global CO_2 emissions in the environment. So, the world urges for more NH_3 production but cannot afford the emissions that accompany it. Hence, an efficient, sustainable, green and cost-effective alternative to the existing NH_3 production route have sparked research interest in recent years where electrochemical NH_3 synthesis from N_2 reduction is the most attractive approach. However, the thermodynamic stability of the N_2 molecule requires high energy for its activation and is thus hampered by a low NH_3 production rate, while the competition with hydrogen evolution reaction (HER) results in poor Faradaic efficiency. And therefore to put electrochemical ammonia production into practice, it is significant to improve the energy efficiency, conversion rate and durability which is only possible through the design of efficient and selective electrocatalysts. Here in the first part of our thesis, we have worked in the direction of designing different classes of electrocatalysts including noble metal-based, non-noble metal based and carbonaceous materials with well-defined morphology for nitrogen (N_2) reduction to ammonia (NH_3) *i.e.* NRR in aqueous electrolytes. While in the second part of this thesis, we have focused on the overall ammonia synthesis under full-

cell conditions by designing bifunctional catalysts. Besides, we have eliminated the use of an external power source to accomplish overall ammonia synthesis by powering it with rechargeable Zn-air batteries. All the catalysts designed in this thesis were synthesized via cost-effective and sustainable approaches and morphology tuning was carried out by varying the reaction parameters *viz.* temperature, time, precursor ratio as well as the synthesis route itself. Above and beyond, the major challenging quest in electrochemical ammonia synthesis is to trace and eliminate the false positives during the estimation of produced NH_3 . A rigorous analysis has been accomplished in this thesis to trace any N-contamination and simultaneously eliminating it from the system *i.e.* catalyst, electrolyte and gas supplies by qualitative and quantitative practices and isotope labelling experiments were executed to prove the externally purged N_2 as the actual NH_3 production source.

In Chapter 3, we have reported mono and bimetallic phosphate catalysts with silver (Ag) being the primary metal due to its less expensive nature amongst other noble metals, high conductivity and less sensitivity towards HER. Moreover, the choice of alkaline electrolyte was based on the suppression of HER near the cathode surface due to the increased kinetic overpotential for the dissociation of water to release protons. The strategy to combine it with an inorganic phosphate moiety was adapted due to the stability issues of Ag in alkaline conditions, which can also induce the partial positive charge over Ag metal and facilitate N_2 adsorption while a partial negative charge over PO_4^{3-} can accelerate the subsequent hydrogenation steps. In Chapter 3A we report a facile, one-pot complexation strategy for the synthesis of an Ag_3PO_4 catalyst where the morphology was tuned towards the NRR activity by varying the reaction time without the use of any expensive templates or structure-directing agents. The optimized catalyst with a cuboidal morphology exhibited a remarkable performance towards NRR with a F.E. of 26.7% and an NH_3 production yield rate of $456.4 \mu\text{g h}^{-1} \text{mg}_{\text{cat}}^{-1}$ at 0 V *vs.* RHE (overpotential: 92 mV). Afterward, Vanadium was incorporated as a secondary metal in Chapter 3B to increase the conductivity and accelerate the rate of electron transfer in metal

phosphates. The synthesis of $\text{Ag}_2\text{VO}_2\text{PO}_4$ was carried out via a green, less time-consuming and energy-efficient sonochemical route to obtain a rice grain-like morphology and the improved F.E. (38%) and NH_3 yield rate ($1.5 \text{ mg h}^{-1} \text{ mg}_{\text{cat}}^{-1}$) at -0.2 V (vs. RHE) was perceived. The NRR activity achieved in Chapter 3 surpassed the activity of the reported Ag-based catalysts and thus demonstrate metal phosphates as proficient NRR catalysts and pave a pathway for further improvisation of the metal phosphates concerning NRR.

Meanwhile, Ag is a noble metal and holds low geographic distribution, hence we targeted to explore earth-abundant transition metal-based and metal-free catalysts for NRR in chapter 4. Dual-heteroatom (B & N) containing carbon was synthesized in chapter 4A in two steps *i.e.* synthesis of heteroatom-containing MOF-ionic liquid composite followed by its pyrolysis. Interestingly, the nanotubular morphology was achieved when the precursor was pyrolyzed at 600°C which may facilitate the mass as well as electron transfer through its porous and conductive channels while the different N and B functionalities might preferentially adsorb N_2 and suppress HER. C-BN@600 catalyst achieved a high F.E. of 16.7% and a yield rate of $204 \text{ } \mu\text{g h}^{-1} \text{ mg}_{\text{cat}}^{-1}$ at -0.2 V in the neutral electrolyte ($\text{pH}=7$). The B-N bond was found to be an active site for NRR both experimentally as well as by theoretical investigations. In the other part of the same chapter, we have designed a cost-effective transition metal boride (TMB) catalyst modified with secondary transition metal in view of enhanced NRR performance. The Cu-modified Ni_4B_3 catalyst was synthesized via a sonochemical approach which gave a grape bunch-like morphology assembled by spherical particles and was thereafter applied for the cathodic NRR. The optimized configuration of the catalyst *viz.* Cu- Ni_4B_3 (1:2) revealed the maximum F.E. of 43.42% and NH_3 yield rate of $684 \text{ } \mu\text{g h}^{-1} \text{ mg}_{\text{cat}}^{-1}$ in $0.1 \text{ M H}_2\text{SO}_4$ electrolyte at -0.3 V (vs. RHE). This fortifies the fact that TMB catalysts would be the optimal choice for high NRR activity in aqueous conditions.

The second part of this thesis was constructed towards strategies to reduce the cost & complexity of overall ammonia synthesis and eliminate the dependence over renewable energy sources by designing bi- and trifunctional catalysts based on

earth-abundant TM via inexpensive, green and viable approaches. In Chapter 5A, we started our effort in the direction of the development of bifunctional electrocatalysts for overall ammonia synthesis which comprises NRR at the cathode and OER at the anode respectively. Since, TM borides (TMBs) have recently been shown to exhibit a high OER activity even superior to that of the benchmark catalysts, and in the previous chapter we have seen the impressive NRR activity of Cu-Ni₄B₃ catalyst, so we focused on employing TMBs as a bifunctional catalyst. Since Cu doesn't show significant OER activity so here only a Ni_xB_y catalyst with cotton-like morphology was synthesized by sonochemical synthesis which was able to deliver a low overpotential of 300 mV to achieve 10 mA cm⁻² during OER and a high F.E. and ammonia production yield rate of 47.9% and 1.55 mg h⁻¹ mg_{cat}⁻¹ respectively at -0.2 V vs. RHE in 0.1 M KOH electrolyte. The NRR-OER full cell assembly using Ni_xB_y as a bifunctional catalyst could initiate NH₃ production at just 1.7 V and can produce 1.08 mg h⁻¹ mg_{cat}⁻¹ of ammonia and 0.81 mg h⁻¹ mg_{cat}⁻¹ of O₂ respectively after 2 h of electrolysis at 1.9 V. These outcomes indicate that the TMB catalysts will provide a trail for the design of high-performance bi-functional electrocatalysts coupling OER and NRR in a full-cell configuration. Also, the sluggish kinetics of OER reduces the overall energy efficiency of the device and results in large cell voltages, and therefore it can be replaced with an alternative anode reaction with faster kinetics, and thermodynamically feasibility which can yield a value-added product. Another objective of our thesis was to replace the sluggish OER with a methanol oxidation reaction (MOR) at the anode during NH₃ synthesis in Chapter 5B. Metal phosphates exhibit good NRR activity as scrutinized in Chapter 3 and they also display high MOR activity owing to the easy generation of adsorbed OH species and tolerance towards poisoning intermediates. Hence, the development of earth-abundant metal phosphates was carried out in this work namely cobalt pyrophosphate (CoPPi) micro flowers assembled by uniform nanosheets via a surfactant assisted-sonochemical method and explored as a bifunctional catalyst for NRR-MOR coupled ammonia synthesis. By virtue of structural and morphological

advantages, the maximum Faradaic efficiency of 43.37% and yield rate of $159.6 \mu\text{g h}^{-1} \text{mg}_{\text{cat}}^{-1}$ were achieved at a potential of -0.2 V vs. RHE . In addition, a very high specific activity (100 mA mg^{-1} at 1.48 V) along with the production of value-added formic acid at the anode with a yield rate of $2.78 \mu\text{mol h}^{-1} \text{mg}_{\text{cat}}^{-1}$ and F.E. of 59.2% was perceived during MOR. The overall NH_3 synthesis was achieved at a reduced cell voltage of 1.6 V (200 mV less than NRR-OER coupled NH_3 synthesis) with a high yield NH_3 rate ($95.2 \mu\text{g h}^{-1} \text{mg}_{\text{cat}}^{-1}$) and HCOOH formation rate ($2.53 \mu\text{mol h}^{-1} \text{mg}^{-1}$). Thus the coupling of NRR and MOR can conceivably lead to a major improvement in the race of overall electrochemical NH_3 synthesis at lower overpotentials with an auxiliary benefit of generating value-added chemicals at both anode and cathode.

Although the electrochemical production of ammonia is considered to be the most sustainable method to transform the existing Haber-Bosch industry, its dependence on external power sources *viz.* wind energy, and solar energy increases the overall processing cost and limits the ammonia production hours. This prompted us to work in the direction of the development of integrated energy systems (IES) which can store the energy from the renewables during peak production hours and later use the stored energy anytime for the electrochemical ammonia production *i.e.* self-powered ammonia synthesis. Zn-air batteries (ZAB) have established themselves as a promising power source because of their abundancy, cost-effectiveness and environment-friendly nature plus their high theoretical energy density (1216 Wh kg^{-1}). Integration of ZAB in electrochemical NH_3 production can offer amassed efficacy over its individual device and eliminate the use of power supply for ammonia production. That's why, the last objective of our thesis was to design multifunctional catalysts for both ZABs and overall ammonia synthesis. Chapter 6 was focused on the development of a trifunctional catalyst which can effectively execute self-powered ammonia synthesis under full-cell conditions. The amorphous Co_2B catalyst was synthesised using a facile sonochemical approach under room temperature conditions which disclosed a decent NRR activity with F.E. of 20.45% and a remarkable yield rate of $2.98 \text{ mg h}^{-1} \text{mg}_{\text{cat}}^{-1}$ in alkaline media

at -0.3 V *vs.* RHE. When Co₂B was employed as an air-cathode catalyst for ZAB, an OCP of 1.45 V, a high power density of 500 mW cm⁻² and energy density of 1078 W h kg⁻¹ was attained which could power NH₃ synthesis (employed with Co₂B as bifunctional catalyst) with a production yield rate of 1.048 mg h⁻¹ mg_{cat}⁻¹ after 2 hours at 1.8 V.

7-2 Future perspective

This work has accomplished the designing of active and selective catalysts with morphology-dependent activity for application in ammonia synthesis and ZABs via facile, economical and less time-consuming synthetic approaches. This provides a viewpoint for scalable catalyst synthesis as per the commercial perspective. Moreover, the complexity, material processing costs, large cell voltage and requirement of external power supply during ammonia synthesis are overcome by designing multifunctional catalysts. Although this work has provided plenty of new findings in the pursuit of electrocatalyst development for electrochemical ammonia synthesis, still there is a lot of room for improvement and new beginnings in this field.

1. Chapter 3 presented the synthesis and employment of Ag-phosphates as a competent, selective and stable electrocatalyst for NRR and also highlighted the effect of morphology on the activity as well as the role of secondary metal to improve the activity further. In the future, the activity of the metal phosphate catalysts can be tuned by altering other reaction parameters during synthesis including temperature, metal-to-metal ratio, and doping of other secondary metals to enhance the activity towards NRR and simultaneous suppression of HER. Interestingly, no hydrazine formation was observed when NRR was catalysed with Ag₃PO₄ catalyst while upon addition of “V”, N₂H₄ production was observed, pointing towards the change in the NRR mechanistic pathway from associative distal to associative alternating based on the reported literature. This can also be an interesting area to have an in-depth understanding of the actual mechanism involved during NRR over Ag-phosphates to further increase the efficiency up to

the practical level by various *in-situ* and theoretical investigations.

2. TMBs have come across as the most efficient class of electrocatalyst for ammonia synthesis and demand more insights into its mechanism to reach the level of practical standards. This can be done by looking after more scalable synthesis methods for TMBs and optimizing their activity by variation of metals, metal-to-metal ratio, morphology, defects and structural phase in the near future.

3. Simultaneous power generation and value-added ammonia production by Zn-N₂ battery could be another interesting yet challenging future outlook. The electrochemical NH₃ synthesis can be piloted via aqueous Zn-N₂ batteries without the requirement of an external power source.

4. Study of kinetic parameters during overall ammonia synthesis is crucial and still underexplored which can be investigated under hydrodynamic conditions using a four-electrode system. To date, most of the research is focused on understanding the interfacial kinetics and competition with HER during NRR. But the local concentrations of reactive species have received less attention which can contribute towards the mechanistic understanding of competition between NRR and HER. The NRR activity measured under well-defined mass transport conditions *i.e.* hydrodynamic conditions can provide a new insight into the concentration gradients near the electrode surface and its impact on the competition with HER and NRR. Also, the micro electrochemical techniques *i.e.* scanning electrochemical microscopy (SECM) can be utilised for visualization and screening of local catalytic activity of catalysts.

5. In Chapter 5 we have introduced the replacement of alternative anode reaction (MOR) over OER and its coupling with NRR to produce ammonia at reduced cell voltage along with the production of value-added product on the anodic side as an added advantage. Other reactions of more commercial importance such as glycerol oxidation, oxidative valorization of biomass etc. can be a stimulating perspective.

6. In Chapter 6 we have eliminated the reliance on an external power supply for ammonia synthesis by powering it with rechargeable ZABs. But due to the certain limitations of ZAB such as Zn corrosion, limited cycle life, etc., one can look for

other potential energy storage devices to power NH_3 synthesis *e.g.*, battery-supercapacitor hybrid and nanogenerators-supercapacitor hybrid devices.

7. Last but not least, the electrocatalytic coupling of N_2 and CO_2 for value-added urea production would be an exciting but challenging perspective. Urea is the most significant N-fertilizer, but its commercial production is energy and capital-intensive. It is based on the reaction between NH_3 and CO_2 under harsh conditions of T and P which accounts for over 50% of NH_3 produced by the Haber-Bosch process and thus increase the global carbon footprint. Direct one-step co-reduction of N_2 and CO_2 for value-added urea production where the two industrial steps (NH_3 synthesis and urea synthesis) with high energy consumption and greenhouse gas emissions can be augmented into one single step electrocatalytic process.

CURRICULUM VITAE

Divyani Gupta

Ph.D. Scholar

Department of Chemistry

Indian Institute of Technology Ropar

Nangal Road, Rupnagar

Punjab-140001, India

Email ID: 2018cyz0010@iitrpr.ac.in

Contact No: +91-9805674547, +91-7018703626

**Research Interest**

Designing and development of the various classes of electrocatalysts (noble-metal, non-noble metal, metal-free) for application in overall electrochemical ammonia synthesis and Zn-air batteries. Interested in the field of electrocatalysis for development of new electrocatalysts for cost-effective and green ammonia production at reduced cell voltages and without any external power supply using Zn-air batteries.

Academic Profile

S.No.	Qualification	School/College/ University	Passing Year	Marks (%)
1.	Matric	D.A.V. Sr. Sec. School Una, HP, India	2010	87.57
2.	10+2	D.A.V. Sr. Sec. School Una, HP, India	2012	90
3.	B.Sc.	Govt. P.G. College Una, HP, India	2015	74.1
4.	M.Sc.	Lovely Professional University, Punjab, India	2017	9.04 (CGPA)
5.	Ph.D.	IIT Ropar, Punjab, India	2018-Present	-

Publications

1. Self-powered NH₃ synthesis by trifunctional Co₂B based high power density Zn-air batteries

D. Gupta, A. Kafle, S. Kaur, P. P. Mohanty, T. Das, S. Chakraborty, R. Ahuja and T. C. Nagaiah*, *J. Mater. Chem. A*, 2023, 11, 12223-12235.

2. Dinitrogen reduction coupled with methanol oxidation for low overpotential electrochemical NH_3 synthesis over cobalt pyrophosphate as bifunctional catalyst

D. Gupta, A. Kafle, T. C. Nagaiah*, *Small*, 2023, 19, 2208272.

3. Selective electrochemical conversion of N_2 to NH_3 in neutral media using B, N containing carbon with nanotubular morphology

D. Gupta, A. Kafle, S. Kaur, T. S. Thomas, D. Mandal, T. C. Nagaiah*, *ACS Appl. Mater. Interfaces*, 2023, 15, 3, 4033–4043.

4. High yield selective electrochemical conversion of N_2 to NH_3 via morphology controlled silver phosphate under ambient conditions

D. Gupta, A. Kafle, S. Kaur, P. P. Mohanty, T. Das, S. Chakraborty, R. Ahuja and T. C. Nagaiah*, *J. Mater. Chem. A*, 2022, 10, 20616-20625.

5. Sustainable ammonia synthesis through electrochemical dinitrogen activation using $\text{Ag}_2\text{VO}_2\text{PO}_4$ catalyst

D. Gupta, A. Kafle, T. C. Nagaiah*, *Faraday Discuss.*, 2023, Advance article. (Under themed collection “Sustainable nitrogen activation”)

6. Local electrocatalytic activity of PtRu supported on nitrogen doped carbon nanotubes towards methanol oxidation by scanning electrochemical microscopy

D. Gupta, S. Chakraborty, R. G. Amorim, R. Ahuja and T. C. Nagaiah*, *J. Mater. Chem. A*, 2021, 9, 21291-21301.

7. Recovery of High Purity Chlorine by Cu-Doped Fe_2O_3 in Nitrogen Containing Carbon Matrix: A Bifunctional Electrocatalyst for HCl Electrolysis

D. Gupta, A. Kafle, A. Chaturvedi, T. C. Nagaiah*, *ChemElectroChem*, 2021, 8, 2858.

8. Ultrasensitive electrochemical biosensors for dopamine and cholesterol: Recent advances, challenges and strategies

N. Thakur,† **D. Gupta**,† D. Mandal* and T. C. Nagaiah* († Equal contribution), *Chem. Commun.*, 2021, 57, 13084-13113.

9. Efficient CO_2 utilization and sustainable energy conversion via aqueous Zn- CO_2 batteries

S. Kaur, M. Kumar, **D. Gupta**, P. P. Mohanty, T. Das, S. Chakraborty, R. Ahuja and T. C. Nagaiah*, *Nano Energy*, 2023, 109, 108242.

10. Facile fabrication of NiFeB deposited flexible carbon cloth electrode towards overall water splitting in alkaline and saline solutions

A Kafle, **D. Gupta**, T. C. Nagaiah*, *Electrochim. Acta*, 2022, 141779.

11. Self-standing Fe₃O₄ decorated paper electrode as binder-free trifunctional electrode for electrochemical ammonia synthesis and Zn-O₂ batteries

A Kafle, **D. Gupta**, A. Bordoloi, T. C. Nagaiah*, *Nanoscale*, 2022, 14, 16590-16601.

12. Copper nanoparticles embedded in polyaniline derived nitrogen-doped carbon as electrocatalyst for bio-energy generation in microbial fuel cells

S. K. Dhillon, A. Chaturvedi, **D. Gupta**, T. C. Nagaiah, P. P. Kundu*, *Environ. Sci. Poll. Res.*, 2022, 29, 80787–80804.

13. Selective Electrochemical Production of Hydrogen Peroxide from Reduction of Oxygen on Mesoporous Nitrogen Containing Carbon

S. Mehta, **D. Gupta**, T. C. Nagaiah*, *ChemElectroChem*, 2022, 9, e202101336.

14. Tuning the polyoxometalate composites with carbonaceous materials towards oxygen bifunctional activity

T. C. Nagaiah*, **D. Gupta**, S. D. Adhikary, A. Kafle and D. Mandal*, *J. Mater. Chem. A*, 2021, 9, 9228-9237.

15. Activation free electroless deposition of NiFe over carbon cloth as self-standing flexible electrode towards overall water splitting

A. Kafle, M. Kumar, **D. Gupta** and T. C. Nagaiah*, *J. Mater. Chem. A*, 2021, 9, 24299-24307.

Awards

1. Received “**Best Oral Presentation award**” at ChemFest-2023 organized by Department of Chemistry, IIT Ropar.

2. Received “**Best Hackathon Team Award- 1st prize**” at International Conference on Energy Conversion and Storage (IECS-2023) with a **cash prize of 1.25 Lakhs**.

3. Received **Second prize for the oral presentation** at 2nd Conference on heterogeneous catalysis (ChemCatCon 2.0) organized by Indian Institute of Technology Gandhinagar, Gandhinagar during May 14 - 16, 2022, India.

4. Received “**Research excellence award**” in Chemical Engineering & Green Technology Section at 58th Annual Convention of Chemists, 2021 & International Conference on “Recent Trends in Chemical Sciences (RTCS-2021)” organized by the Indian Chemical Society, Kolkata during December 21 - 24, 2021, India. (*Oral Presentation*).

5. Received “**Research excellence award**” in Industrial & Applied Chemistry Section at 57th Annual Convention of Chemists, 2020 & International Conference on “Recent Trends in Chemical Sciences (RTCS-2020)” organized by the Indian Chemical Society, Kolkata

during December 26 - 29, 2020, India. (*Oral Presentation*).

Conferences/Workshops

- **Presented paper at Faraday Discussions event “Sustainable nitrogen activation”** organized by Royal Society of Chemistry during March 25 - 27, 2023 in London, United Kingdom.
- **Participated in Hackathon** organized by International Conference on Energy Conversion and Storage (**IECS-2022**) at Indian Institute of Technology Madras, Chennai, India on January 18 - 20, 2023.
- **Poster presentation** in Conference on “**Advances in Catalysis for Energy and Environment (CACEE -2022)**” organized by Tata Institute of Fundamental Research (TIFR), Mumbai, India during October 31 - November 04, 2022.
- Participated in **New Generation Ideation Contest 2022**, organized by Hindustan petroleum green R&D centre, Karnataka, India during September 2022- March 2023.
- **Oral presentation** at 2nd Conference on heterogeneous catalysis (**ChemCatCon 2.0**) organized by Indian Institute of Technology Gandhinagar, Gujarat, India during May 14 - 16, 2022.
- **Participated in Material Next 3.0 contest**, organized by Tata steel, India during September 2021- March 2022.
- **Participated in New Generation Ideation Contest 2021**, organized by Hindustan petroleum green R&D centre, Karnataka, India during September 2021- March 2022.
- **Oral presentation** at 58th Annual Convention of Chemists, 2021 & International Conference on “Recent Trends in Chemical Sciences (**RTCS-2021**)” organized by the Indian Chemical Society, Kolkata, India during December 21 - 24, 2021.
- **Oral presentation** at International Conference on “Advanced materials for better Tomorrow (**AMBT-2021**)” organized by the Indian Institute of Technology BHU, Varanasi & Society for Interdisciplinary Research in Materials and Biology (SIRMB), India during July 13 - 17, 2021.
- **Oral presentation** at 57th Annual Convention of Chemists, 2020 & International Conference on “Recent Trends in Chemical Sciences (**RTCS-2020**)” organized by the Indian Chemical Society, Kolkata, India during December 26 - 29, 2020.
- **Participated** in 1st Conference on heterogeneous catalysis (**ChemCatCon 1.0**) organized by Indian Institute of Technology Gandhinagar, Gujarat, India in online mode during July 11 – 12, 2020.
- **Attended** International Virtual Conference on “**Advanced Nanomaterials Applications (VCAN 2020)**” organized by Centre for Nanotechnology Research (CNR), Vellore Institute of Technology, Vellore, India during June 17 – 19, 2020.
- **Attended** Virtual Conference on “Materials for Energy Harvesting and Catalysis (**MEHC 2020**)” organized by Tata Institute of Fundamental Research (TIFR) Mumbai and Indian Institute of Science Education and Research (IISER) Kolkata, India during May 01 - 03, 2020.
- **Attended Research Conclave** organized by Indian Institute of Technology Ropar, Punjab, India during April 20 - 21, 2019.

Instrument hand on experience

- Electrochemical workstations (Biologic VSP-300 and Autolab 302N potentiostat/galvanostat).
- Battery cyclers (BCS-810, Biologic).
- *In-situ* spectro-electrochemical UV.
- X-ray Diffractometer (XRD).
- UV-Vis. spectrophotometer.
- FT-IR spectrophotometer.
- CHNS-O Elemental analyser.
- Scanning Electron Microscopy (SEM) and Energy Dispersive X-ray spectroscopy (EDS).

Teaching Assistantship/Project Mentorship

- **Teaching Assistant**, Practical for Masters (2019-2020), IIT Ropar (Instructor: Dr. Tharamani C.N. and Manoj Kumar Pandey).
- **Project Mentor**, Major M.Sc. Project entitled “POM-MOF composite towards electrocatalysis” by Ms. Pooja Kulashri (2019), IIT Ropar (Supervisor: Dr. Tharamani C. N.).
- **Project Mentor**, Major M.Sc. Project entitled “The electrochemical reduction of CO₂ to value added fuels and chemicals” by Ms. Bhawana Kumari (2021), IIT Ropar (Supervisor: Dr. Tharamani C. N.).
- **Project Mentor**, Major M.Sc. Project entitled “Bimetallic Cu-doped zeolitic imidazolate framework towards high yield electrochemical ammonia production” by Ms. Naina Goyal (2022), IIT Ropar (Supervisor: Dr. Tharamani C. N.).

References

Dr. Tharamani C. N. (Ph.D. Supervisor)

Associate Professor and Head

Department of Chemistry

IIT Ropar, Rupnagar, Punjab-140001, India

Phone: 01881-232058

Email: tharamani@iitrpr.ac.in

Declaration

I hereby declare that all the information given above is correct to the best of my knowledge.

Place: IIT Ropar

Divyani Gupta